Protein dynamics studied with neutron spectroscopy

Dissertation

der Mathematisch-Naturwissenschaftlichen Fakultät

der Eberhard Karls Universität Tübingen

zur Erlangung des Grades eines

Doktors der Naturwissenschaften

(Dr. rer. nat.)

vorgelegt von

Christian Beck

aus Calw (Deutschland)

Tübingen

2019

Gedruckt mit Genehmigung der Mathematisch-Naturwissenschaftlichen Fakultät der Eberhard Karls Universität Tübingen.

Tag der mündlichen Qualifikation: 31/01/2020

Dekan: Prof. Dr. Wolfgang Rosenstiel

1. Berichterstatter: Prof. Dr. Frank Schreiber
2. Berichterstatter: Prof. Dr. Martin Oettel

Preamble

The research for this thesis was carried out within the PhD programme of the Institut Max von Laue - Paul Langevin (ILL), Grenoble, France, jointly with the University of Tübingen, Germany, co-funded by the two institutes. The work was supervised by Dr. Tilo Seydel at the ILL, and by Prof. Dr. Frank Schreiber and Prof. Dr. Martin Oettel at the University of Tübingen.

List of Papers Being Part of the Thesis

- **Nanosecond Tracer Diffusion as a Probe of the Solution Structure and Molecular Mobility of Protein Assemblies: The Case of Ovalbumin**
  Christian Beck; Marco Grimaldo; Felix Roosen-Runge; Michal K. Braun; Fajun Zhang; Frank Schreiber; Tilo Seydel
  J. Phys. Chem. B 2018, 122, 35, 8343-8350
  Publication Date: August 14, 2018
  `https://doi.org/10.1021/acs.jpcb.8b04349`

- **Neutron Spectroscopy on Protein Solutions Employing Backscattering with an Increased Energy Range**
  Christian Beck; Markus Appel; Marco Grimaldo; Felix Roosen-Runge; Fajun Zhang; Bernhard Frick; Frank Schreiber; Tilo Seydel
  Physica B: Condensed Matter, 2019, 562, 31-35
  Publication Date: June 1, 2019
  `https://doi.org/10.1016/j.physb.2018.11.058`

- **Protein Short-Time Diffusion in a Naturally Crowded Environment**
  Marco Grimaldo; Hender Lopez; Christian Beck; Felix Roosen-Runge; Martine Moulin; Juliette M. Devos; Valerie Laux; Michael Härtlein; Stefano Da Vela; Ralf Schweins; Alessandro Mariani; Fajun Zhang; Jean-Louis Barrat; Martin Oettel; V. Trevor Forsyth; Tilo Seydel; Frank Schreiber
  J. Phys. Chem. Lett. 2019, 10, 8, 1709-1715
  Publication Date: March 21, 2019
  `https://doi.org/10.1021/acs.jpclett.9b00345`

- **Following Protein Dynamics in Real Time during Crystallization**
  Christian Beck; Marco Grimaldo; Felix Roosen-Runge; Ralph Maier; Olga Matsarskaia; Michal Braun; Benedikt Sohmen; Orsolya Czakkel; Ralf Schweins; Fajun Zhang; Tilo Seydel; Frank Schreiber
  Cryst. Growth Des. 2019, 19, 12, 7036-7045
  Publication Date: October 25, 2019
  `https://doi.org/10.1021/acs.cgd.9b00858`

Contents

Abstract

Proteins, as biological macromolecules, play an important role in biology. Being present in the entire range of organisms, they differ in shape, size, functionality and stability. Changes in the behavior of the protein can lead to serious disorders in the organism. Since a large fraction of proteins *in vivo* is either entirely surrounded by solution molecules or partly in contact with an aqueous environment, it is of great interest to study the properties of proteins in solution. For biological processes, *e. g.* enzymatic catalysis, the flexibility and controlled structural change of the protein are important to understand as well. To obtain further insights into the protein dynamics, *e. g.* based on simulations, the structure of the protein must be known. One common method to obtain high-resolution structural information of proteins is crystallography based on diffraction patterns of protein crystals. The bottleneck within this approach is often the production of high-quality crystals. Insights in the crystallization pathways might resolve some of these problems.

In this thesis, the diffusive dynamics of several proteins is investigated with quasi-elastic high resolution neutron spectroscopy. The work performed can be divided into two parts. In the first part, new experimental approaches are developed which enable to access higher energy transfers for neutron backscattering, allowing for a separation of different internal diffusive processes. In addition, approaches to reduce the measurement time by limiting the number of energy transfers investigated or by using advanced analysis methods were developed. This novel framework enables to follow the diffusive kinetics of samples which changes as a function of time.

The second part of this thesis investigates different protein systems by systematically changing control parameters such as temperature, protein concentration and salt concentration. The analysis of the data collected benefits from the development of the analysis frameworks.

First, the diffusion of proteins in biological systems is investigated by using deuterated lysate as an external crowding agent and analyzing its influence on the diffusive behavior of γ-globulin. Second, a crowding-induced cluster formation is described for ovalbumin solutions. Third, the cluster formation of bovine serum albumin in the presence of trivalent salts is investigated with neutron backscattering and compared with the macroscopic phase behavior. Finally, the crystallization of β-lactoglobulin is investigated in the presence of $ZnCl_2$. The crystallization process is followed by small-angle neutron scattering, neutron backscattering and neutron spin-echo spectroscopy. Additionally to the separation of the time-dependent internal and global self-diffusion, the fraction of proteins in the crystal can also be extracted from the backscattering data. Spin-echo measurements allow addi-

tionally to obtain information on the time-dependent collective diffusion of the proteins in solution and in the crystal.

Summing up, this thesis presents several studies which investigate different protein solutions using state of the art neutron spectroscopy techniques.

Deutsche Zusammenfassung

Als biologische Makromoleküle sind Proteine von großer Bedeutung für physiologische Prozesse. Sie sind in Organismen allgegenwärtig und variieren in ihrer Form, Größe und Funktionalität, sowie in ihrer Stabilität. Veränderungen der Proteineigenschaften können im Organismus zu schwerwiegenden Störungen führen. Da die meisten Proteine unter physiologischen Bedingungen entweder vollständig gelöst oder teilweise in Kontakt mit wässrigen Lösungen vorliegen, ist die Untersuchung von Proteineigenschaften in Lösungen von großem Interesse. Für biologische Prozesse, wie beispielsweise enzymatische Katalysen, sind zudem das Verständnis der Proteinflexibilität, sowie kontrollierter struktureller Veränderungen von Proteinen essentiell. Um ein tiefergehendes Verständnis der Proteindynamik z. B. durch Simulationen zu erlangen, muss die Struktur des Proteins bekannt sein. Eine häufig eingesetzte Methode stellt hierbei die Analyse von Diffraktionsdaten von Proteinkristallen dar. In der Kristallographie stellt die Herstellung qualitativ hochwertiger Kristalle jedoch häufig einen Engpass der Methode dar. Durch ein besseres Verständnis der Kristallisationsprozesse kann dieses Problem zumindest teilweise behoben werden.

In dieser Arbeit wird die Diffusionsdynamik unterschiedlicher Proteine mit quasielastischer hochauflösender Neutronenspektroskopie untersucht. Im ersten Teil der Arbeit werden neue experimentelle Ansätze entwickelt, mit denen höhere Energieüberträge der Neutronenrückstreuung zugängig gemacht werden. Hierdurch können verschiedene interne Diffusionsprozesse voneinander getrennt werden. Weiterhin erlaubt eine Beschränkung auf die Betrachtung weniger Energieüberträge, oder die Nutzung weiterentwickelter Analysemethoden eine Reduktion der Messzeit für einzelne Spektren, sodass zeitabhängige diffusive Eigenschaften der Proben beobachtet werden können.

Im zweiten Teil der Arbeit werden unterschiedliche Proteinsysteme untersucht, wobei Kontrollparameter wie Temperatur, Protein oder Salzkonzentration systematisch geändert werden. Die Analyse der Daten baut teilweise auf den oben genannten entwickelten Auswertungsmethoden auf.

Zunächst werden die diffusiven Eigenschaften von Proteinen in biologischen Systemen untersucht. Hierzu wird deuteriertes Lysat als externer makromolekularer Crowder eingesetzt und sein Einfluss auf die Diffusion von γ-Globulin analysiert. Die zweite Studie befasst sich mit der konzentrationsabhängigen Bildung von “protein clusters” in Ovalbumin-Lösungen. Drittens wird die durch trivalente Ionen induzierte Bildung von Aggregaten in Rinderalbumin Lösungen mit Neutronenrückstreuung untersucht. Schließlich wird die Kristallisation von β-Lactoglobulin in der Gegenwart von $ZnCl_2$ betrachtet. Der Kristallisationsprozess wird hier-

bei mit Neutronen-Kleinwinkelstreuung, Neutronen-Rückstreuung und Neutronen-Spin-Echo-Spektroskopie quantifiziert. Neben der zeitaufgelösten Trennung von interner und globaler Selbstdiffusion der Proteine kann gleichzeitig der Anteil der kristallisierten Proteine aus den Rückstreudaten bestimmt werden. Die Spin-Echo-Daten geben Aufschluss über die kollektive Diffusion der Proteine in Lösung und im Kristall.

Zusammenfassend beschreibt diese Arbeit die Untersuchung verschiedener Proteine in Lösung unter Einsatz verschiedener modernster Neutronenspektroskopietechniken.

Chapter 1

Introduction

Proteins play an essential role both within individual biological cells but also in the extracellular environment within the overall organism. To understand the complex processes of life, it is important to investigate the function and behavior of proteins. Depending on the type of protein, they can be responsible for transport mechanisms or structure formation, but they can also belong to signal transmission chains or play an important role in immune responses.

As proteins fulfill different functions in the organism, malfunction, absence or excess concentrations of single proteins can significantly impact the organism. An example is sickle cell anemia [1], where a point mutation leads to a different structure of hemoglobin. On the one hand, this mutation induces a deformation of the erythrocytes, changing their shape and their tendency to aggregate and therefore leading to problems in the blood system, to infections [2] and to hypoxia [3]. On the other hand, the modification of the erythrocytes also leads to a less harmful disease course in the case of a malaria infection [4]. This illustrates that protein interactions and properties and their influence within organisms can be extremely complex. Understanding the specific interactions and linking them to the structure of the involved proteins is therefore of great interest to explore mechanisms on a cellular and organismic level.

The eye lens cataract constitutes another example where proteins are involved into the course of a disease. It has been shown that the formation of crystalline clusters leads to an increased turbidity of aging eye lenses through protein cluster formation [5]. Such protein clustering can be induced by several factors. To find possible non-invasive therapies, or prevent such cluster formations, the interactions between the involved proteins, the clustering kinetics as well as cluster properties have to be studied. The specific types of clusters depend on the protein investigated and the properties of the co-solutes.

Only few techniques are available to determine the structure of proteins with atomic resolution. In crystallography, high quality protein crystals can be used to determine the protein structures based on diffraction patterns. Using X-ray or neutron scattering, where different atoms contribute to different extents to the scattering signal, these data can be combined and full structures can be obtained. The bottleneck of this technique is often a lack of the necessary high-quality crystals. Even if crystals can be grown, their quality is not always sufficient to obtain structures with atomic resolution. In addition, since proteins are not rigid particles, their structure in solution might differ from the one in the crystal. Therefore, techniques other than crystallography are also explored. For instance, in the last few years, cryo-electron microscopy experienced a "resolution revolution", now also allowing for the determination of structures comparable with those obtained by neutron and X-ray diffraction [6, 7]. The advantage of this technique is that proteins, such as membrane proteins [8] or ribosomes [7, 9], do not need to be crystalline. In addition, a smaller amount of sample is sufficient, but homogeneous solutions are needed for sample preparation, which implies the use of suitable buffers. However, the analysis of cryo-electron microscopy data is still challenging and linked to relatively expensive calculations [10]. It is therefore of interest to study the crystallization process and to understand the underlying processes for its control and modification.

Moreover, proteins are flexible particles, which might result in differing or non-unique structures observed by cryo-electron microscopy or by crystallography. Their internal flexibility might also change during the phase transition. Here, neutron scattering is a valuable tool to investigate sample solutions, because it allows to access both the global and the internal diffusive processes of the samples simultaneously.

In this thesis, the diffusive behavior of different proteins is investigated. By neutron scattering, unique time and length scales are accessed in order to measure protein self-dynamics. The overall aim is to understand protein assemblies in solution based on their short-time self-diffusive behavior. This information about the diffusive dynamics is crucial for the understanding of structurally changing systems.

This chapter offers a general introduction to proteins, their dynamics and their response to external control parameters, whereas specific introductions to the theoretical background and to the specific systems are provided in the following chapters.

1.1 Dynamics of Proteins

A simplifying description of proteins is that of a biological polymer composed of amino acid building blocks. Depending on the specific interactions within their chains, they favor specific spatial arrangements. However, if interactions between the amino acids are rather strong, the protein adopts a well-defined structure. Although within this structure dynamical processes are possible, its center of mass diffusion can then be described with approaches from colloid physics.

This section describes the different diffusive time scales and is based mainly on Refs. 11–13.

For a dilute colloidal suspension, several diffusive time-scales can be probed. Depending on the instrumental setup, its time resolution and observation time, different processes are investigated. A schematic drawing, representing the mean squared displacement (MSD) of the colloids, *i.e.* the averaged distance the particle has moved within time, as a function of time, is shown in Figure 1.1.

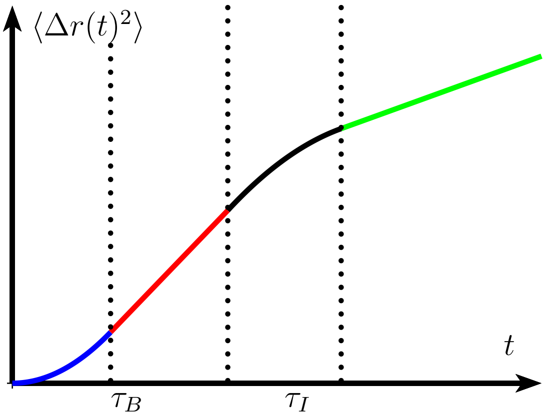

Figure 1.1: *Diffusive mean squared displacement (MSD) $\langle \Delta r(t)^2 \rangle$ as a function of time on a linear axes. Different time regions can be observed. For small times ($t < \tau_B$), the particles undergo a ballistic motion with a parabolic time dependence (blue). For times $t > \tau_B$, the MSD is governed by hydrodynamic interactions and follows a linear time dependence (red). For times comparable to the interaction time $t \approx \tau_I$, the time dependence of the MSD can be described by anomalous diffusion with $\langle \Delta r^2 \rangle \propto t^\alpha; 0 < \alpha < 1$ (black) before long-time diffusion takes place, which can be described by a linear relationship (green).*

For short times t, the colloid with a mass M, a radius R and a momentum $\vec{p}$ does not interact with other particles and the influence of the solvent is negligible. In this limit, a colloid does not change its momentum due to collisions with the solvent molecules. In this ballistic regime, the MSD $\langle \Delta r^2 \rangle$ can be written as

$$\left\langle \Delta r^2 \right\rangle = \frac{\vec{p}(0)\vec{p}(0)}{M^2} t^2 = \vec{v}(0)\vec{v}(0)t^2. \tag{1.1}$$

The time until the interactions with the solvent become relevant can be estimated using Stokes' friction coefficient γ_F

$$\begin{aligned} \gamma_F &= 6\pi\eta_0 R & (1.2) \\ t &\ll \tau_B = M/\gamma, & (1.3) \end{aligned}$$

where η_0 is the shear viscosity of the solution. For a protein such as bovine serum albumin (BSA) with a radius $R \approx 3.6\,\text{nm}$, the value of τ_B is on the order of some picoseconds. The corresponding time dependence of the MSD for the ballistic motion is shown in blue in Figure 1.1.

For longer observation times, the particles investigated interact with the solvent, which changes their diffusive behavior. If the diffusive process is mainly dominated by the interactions with the solvent, the MSD can be expressed as a function of time [11]

$$\left\langle \Delta r^2 \right\rangle = \hat{I} \frac{2}{\beta \gamma_F} t \tag{1.4}$$

with $\beta = \frac{1}{k_B T}$ and the unity matrix $\hat{I}$. Therefore, this diffusion process leads to a linear time dependence of the MSD. It is marked in red in Figure 1.1.

This linear relation is valid until the particle diffused far enough to interact with other colloids in the solution, *i.e.*, until an interaction time t_I. This interaction time can be estimated based on its radius and the translational diffusion coefficient D_t of the particles [12]

$$t_I = \frac{R^2}{D_t}. \tag{1.5}$$

For a BSA solution in the dilute limit at room temperature, the order of magnitude of τ_I is 100 ns. The diffusive process where only hydrodynamic forces influence the diffusion of the colloid, *i.e.* for observation times $\tau_B < t \ll \tau_I$, is denoted short-time diffusion.

For observation times $t \approx \tau_I$, marked in black in Figure 1.1, the colloid starts to interact with other colloids. This regime results in a time dependence which can be generally described by a power-law dependence [13]

$$\left\langle \Delta r^2 \right\rangle \propto t^{\alpha}; \quad 0 < \alpha < 1. \tag{1.6}$$

For observation times longer than τ_I, the diffusive behavior is dominated by the interactions with other colloid particles. Similar to the case where the diffusive behavior is dominated by hydrodynamics, the MSD can also be described by a linear time dependence. This so called long-time diffusion is shown in green in Figure 1.1.

1.2 Cluster Formation

In this thesis, different proteins are investigated under various conditions, such as changing salt concentration, protein concentration or the sample temperature. For some cases, cluster formation plays an important role. Therefore, different processes which might lead to formation of aggregates in solution are discussed in this section.

1.2.1 Crowding-Induced Cluster Formation

In cellular environments, significant volume fractions can be occupied by proteins. For *E.coli*, macromolecular concentrations up to 400 $\frac{\mathrm{mg}}{\mathrm{ml}}$ have been estimated [14]. While, for some techniques, studies on dilute systems might be favored for several reasons, such as sample homogeneity, focusing on specific interactions, expenses for sample preparation or solubility issues, it is important to investigate proteins at high volume fractions in order to mimic the biological environment.

Several enzymes have been shown to be activated under crowded conditions [15] and it has been demonstrated that equilibrium constants defining the speed of the enzymatic processes can change due to crowding [16].

In several protein systems, changes in the structural conformation were observed when the protein concentration was increased [17, 18]. These changes in structure might lead to a change in the overall interparticle potential. Additionally, the reduced average distance between proteins decreases at higher volume fractions and might send the system into a cluster-prone state. Since the proteins have an inhomogeneous surface charge distribution and vary in shape and size, a generalized theoretical description is difficult and depends strongly on the system investigated.

In this thesis, crowding-induced cluster formation is reported in the case of ovalbumin (OVA) (Chapter 7).

1.2.2 Cluster Formation due to Changes in Interparticle Interactions

Apart from the crowding-induced cluster formation presented in Section 1.2.1, clusters can be formed by changing the inter-particle interactions. The surface charge can be changed by adding monovalent salts, screening the protein surface charge, or by multivalent salts which can also induce a charge inversion at the surface. Additionally, changing the pH of the solution can modify the surface charge depending on the isoelectric point of the particles. In this section, some theoretical descriptions as well as previous studies on this topic are summarized.

DLVO Theory

If monovalent ions are present in a protein solution, an approximate description of the interactions between the proteins is given by the theory developed by Derjaguin, Landau, Verwey and Overbeek [19]. In the so-called DLVO theory, several forces contribute to the overall inter-particle potential.

A first contribution is the repulsion induced by the charges of the colloids. Since homogeneous samples are considered, the colloids have the same net charge. Depending on the shape of the colloids, the interaction changes slightly [20]. The electrostatic potential energy for two colloidal charged spheres with the charges z_1 and z_2 and the identical diameters σ separated by a distance r is given by [20]

$$V(r) = \frac{z_1 z_2 e^2}{4\pi\varepsilon\varepsilon_0 r}\frac{\exp(-\kappa(r-\sigma))}{(1+\kappa\sigma)} \tag{1.7}$$

with the elementary charge e, the relative permittivity ε of the solvent and the vacuum permittivity ε_0. The inverse Debye length κ takes into account the influence of the ions present in the solution. Its value can be calculated by summing up the contributions of the different ions j present in the solution [21]:

$$\kappa = \sqrt{\frac{e^2}{k_b T \varepsilon \varepsilon_0} \sum_j z_j c_j}. \tag{1.8}$$

While Equation 1.8 considers the different valencies z_j of the ions in solution, it should be mentioned that the model does not take into account ion-induced bridging effects, which can appear if multivalent ions are present in solution [22].

As a second contribution, the van der Waals forces contribute to the overall interaction potential. The mathematical description of this contribution is shape-dependent as well [20]. For two identical spheres, the expression can be written as

$$\begin{aligned} V_{vdW}(r) &= -\frac{A_H}{12}\left[\frac{\sigma^2}{r^2} + \frac{\sigma^2}{r^2-\sigma^2} - 2\log\left(\frac{r^2-\sigma^2}{r^2}\right)\right] && (1.9) \\ A_H &= \frac{3}{4}k_b T\left(\frac{\varepsilon_1-\varepsilon_2}{\varepsilon_1+\varepsilon_2}\right)^2 + \frac{3I}{16\sqrt{2}}\frac{(n_1^2-n_2^2)^2}{(n_1^2+n_2^2)^{3/2}} && (1.10) \end{aligned}$$

with the Hamaker constant A_H, the ionization potential I and the static dielectric constants ε_i and refractive indices n_i with $i = 1, 2$ representing the colloids and the solvent, respectively [20].

A schematic view of the interaction energy as a function of the particle distance of these two first contributions is given in Figure 1.2 for different surface charges and different Debye lengths. For increasing κ (or for a decreasing surface charge), *e.g.* due to increasing salt concentrations in the solution, the energy barrier decreases and a secondary minimum appears. The occurrence of this minimum, marked by points in corresponding curves (cyan and green) in Figure 1.2, is possible due to the different particle distance dependencies of the forces involved. If κ increases further (or the surface charge is reduced even more), the energy barrier vanishes and the potential becomes attractive for all particle distances.

As a last contribution, the DLVO theory also considers the hard-sphere repulsion. This contribution implies that two proteins cannot overlap. The corresponding potential is therefore infinite for interparticle distances smaller than the particle diameter.

Since the DLVO theory uses bulk properties of the solvent, it is no longer valid for particle distances close to the particle diameter. In this case, surface effects have to be taken into account.

In this section, the influence of salt ions on the interparticle potential was introduced. The screening effects as well as the influence of surface charge on the overall potential were discussed. In the case of multivalent ions, this description is limited to the case where the ions do not directly interact with the colloids. In case the

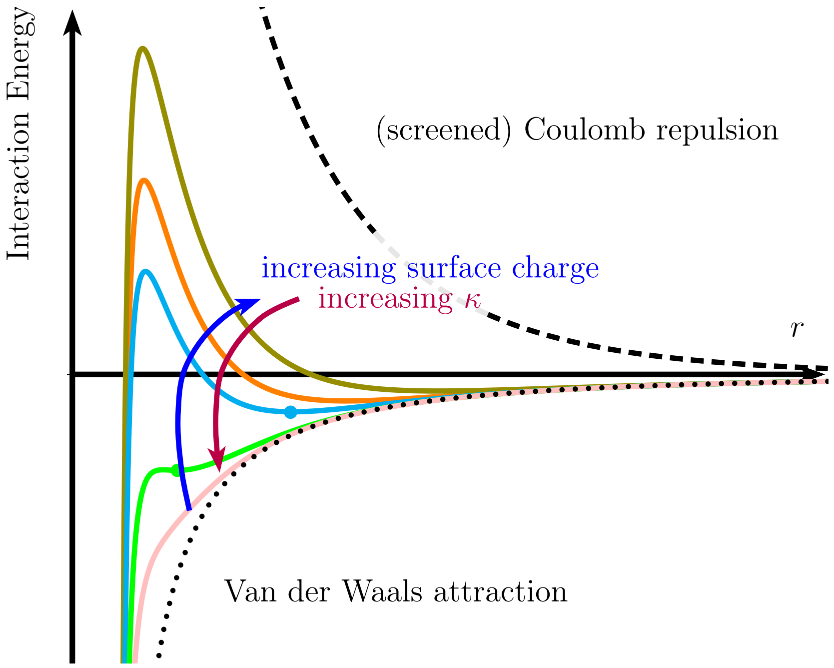

Figure 1.2: *Schematic representation of the interaction energy as a function of the particle distance. The dotted and dashed lines represent the van der Waals attraction and double layer repulsion, respectively. Colored lines represent the distance dependence described by DLVO theory for increasing inverse Debye length* κ *or decreasing surface charge, as indicated by the arrows. Figure reproduced based on Ref. 20 using Equations 1.7 and 1.9.*

ions bind to the surface, the surface charge is modified which might change the behavior of the system. These effects will be discussed in the next section.

Protein Solutions with Multivalent Ions

Several negatively charged proteins in aqueous solutions have recently been investigated in combination with several multivalent salts. The overall phase diagram (shown in Figure 1.3) is similar for the different systems.

At a constant temperature, the phase diagram shows that the protein solution is in a homogeneous and clear phase (Regime I) if the salt concentration c_s is below a certain critical concentration c^*.

If this critical salt concentration is crossed, the solution enters into Regime II, where protein clusters reach a size comparable to the wavelengths of visible light, which make the samples appear turbid. Under suitable conditions, the samples can undergo a liquid-liquid phase separation (LLPS). If the salt concentration is further increased, a second threshold c^{**} is crossed. Samples prepared in this regime (Regime III) appear clear again. With increasing multivalent salt concentration, a reentrant behavior can therefore be observed in BSA solutions.

The influence of different salts on the phase diagram has been investigated in several studies. In 2008, Zhang *et al.* reported the observation of the reentrant

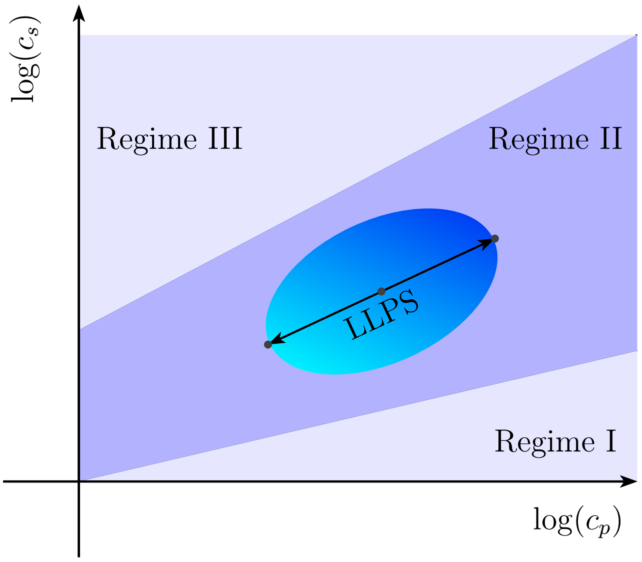

Figure 1.3: *Schematic isothermal phase diagram of negatively charged proteins with a protein concentration c_p in multivalent salt solutions with a salt concentration c_s. If a sample is prepared in the LLPS region, the sample phase-separates into a protein rich and protein poor phase as indicated by the arrows. Figure reproduced and modified from Ref. 23.*

phase diagram for BSA solutions with YCl_3 [22]. The study was expanded later to several proteins (BSA, human serum albumin (HSA), OVA, β-lactoglobulin (BLG), lysozyme) in the presence of several salts (YCl_3, $LaCl_3$, $FeCl_3$, $AlCl_3$, $SpeCl_4$)[24]. No reentrant behavior could be observed when lysozyme was used as protein with the salts mentioned. Also, $SpeCl_4$ did not induce macroscopically visible phase-separations for all investigated proteins. These two cases point out the high specificity of the investigated systems.

Fries *et al.* [25] observed the absorption of BSA in the presence of YCl_3 on surfaces in contact with the solution. The observed protein absorption as a function of salt concentration agrees well with classical density functional theory calculations with inhomogeneous density profiles.

Braun *et al.* investigated the influence of different anions on the phase diagram [26] at room temperature. It was shown that different anions can significantly change the second salt concentration threshold c^{**}. Additionally, the reduced second virial coefficient was obtained by small angle X-ray scattering (SAXS).

Matsarskaia *et al.* [27] focused on the influence of different cations ($HoCl_3$, $LaCl_3$, YCl_3) on BSA solutions and showed systematic differences between the different salts investigated in the second virial coefficient based on SAXS data. Furthermore, the temperature-dependent point of zero charge was obtained *via* ζ potential measurements.

Schubert *et al.* [28] investigated aqueous solutions of protein-coated (BSA) gold nanoparticles in the presence of several multivalent ions with ζ potential, ultraviolet - visible (UV-Vis) spectrophotometry measurements and transmission electron microscopy. In their study, the authors concluded that mainly the hydroxides rather than of hydrolyzed ions bind to the protein surface and therefore induce the surface charge inversion.

Soraruf *et al.* [23] and Beck [29] investigated the long-time collective diffusion with dynamic light scattering (DLS), approaching the first threshold concentration c^* at constant temperatures for aqueous BSA and HSA solutions with YCl_3, respectively. For both systems, two different contributions were identified in the autocorrelation function. They represent the diffusion of clusters and monomers in the solution, respectively. In both cases, the diffusion coefficient of the monomers as well as that of the clusters decreased while approaching Regime II. Pandit *et al.*[30] observed a similar trend for effective diffusion coefficients, obtained from one single exponential decaying function averaging over the different contributions for BSA-YCl_3 and BSA-$LaCl_3$ solutions. Within Regime II, they observed a minimum in the diffusion coefficient followed by an increase with increasing c_s entering into Regime III. Using time resolved photoluminescence, they observed systematic differences in the decay time of BSA for the different salts. It should be mentioned that the experimental set-ups as well as the analysis framework used for the DLS measurements by Pandit *et al.* [30] differs from the one used by Soraruf *et al.* [23] and Beck [29]. While the overall dependence on the salt concentration is consistent within the different studies [27, 30, 31], the dependence on the salt might be influenced by the batch variations or different fit models.

Braun *et al.* [32] investigated the isotope influence of the solvent with SAXS. The overall phase diagram as well as the second virial coefficients show systematic changes as a function of the D_2O fraction in the solvent. Thus, it has to be kept in mind that absolute values obtained from neutron backscattering (NBS) measured in D_2O might deviate from values obtained by techniques measuring in H_2O.

Previous studies by Grimaldo *et al.* [33] addressed the short-time self-diffusion of BSA at constant temperature with YCl_3 in D_2O approaching c^* at different fixed protein concentrations. A master curve, describing the universal slowing down of the normalized apparent diffusion coefficient, was observed as a function of salt ions per protein. By using the Flory-Stockmeyer theory to describe the cluster size distribution, a binding probability as a function of cations per protein was obtained.

In Chapter 8, the methods presented by Grimaldo *et al.* [33], Matsarskaia *et al.* [34] and Roosen-Runge *et al.* [35] are combined to analyze the temperature dependence of the master-curves obtained from different NBS spectra measured at the backscattering silicon spectrometer (BASIS), Oak Ridge, USA, on BSA solutions with YCl_3 and $LaCl_3$ in D_2O at different temperatures. Similar to the studies investigating the influences of the salt on the macroscopic phase diagram [26, 27, 36], also these quasi-elastic neutron scattering (QENS) studies, investigating the short-time microscopic level, point out consistent salt-dependent differences in the diffusion, allowing to link these microscopic results to the macroscopic ones.

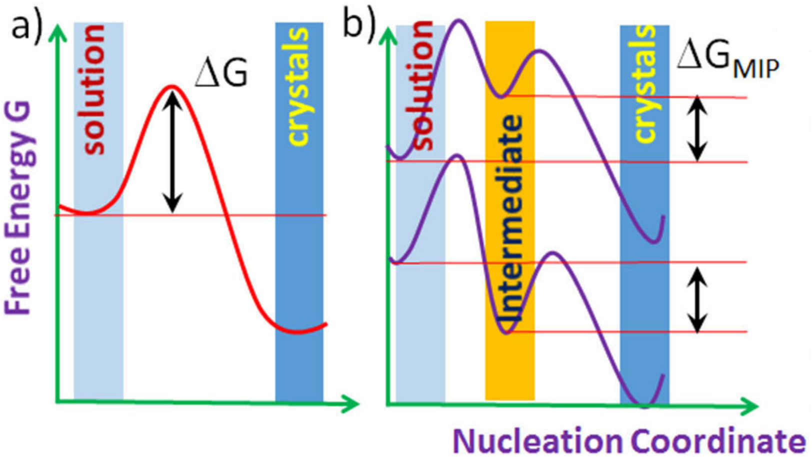

Figure 1.4: *Energy landscapes for different crystallization pathways. a) Energy landscape for a classical nucleation. b) Energy landscape for non-classical crystallization. In the lower case, the intermediate phase is preferred to the parent solution. Figure taken from Ref. [37].*

1.3 Crystallization

Under certain conditions, colloidal suspensions can form crystals. Various crystallization pathways have been proposed theoretically and observed experimentally for different systems. Obtaining high-quality crystals can help to determine the crystal structure by diffraction. Knowledge of the structure, in turn, can be crucial for the understanding of particle interactions.

In this section, some general theoretical approaches describing crystallization are reviewed. It is mainly based on the reviews by Zhang [37] and Karthika *et al.* [38].

The formation of crystals from supersaturated solution indicates that the sample has a free energy landscape with a local minimum representing the solution and a (global) minimum representing the crystalline state (Figure 1.4). These two minima are separated by an energy barrier (Figure 1.4a). If other local minima exist between the two mentioned minima, crystallization might take place passing through these different minima, which leads to intermediate phases (Figure 1.4b). In the latter case, the pathway is called non-classical.

To form larger assemblies of particles in a solution, the effective energy between the particles has to be attractive. However, the effective interaction between particles, which can be quantified using the reduced second virial coefficient, must not be too strong since this leads to aggregation, and a crystallization-prone orientation of the particles cannot take place.

In the case of negatively charged proteins in the presence of multivalent salts (schematic phase diagram shown in Figure 1.3), crystallization can be triggered if the protein and salt concentration as well as the temperature are well chosen. At a fixed protein concentration and at a low salt concentration the reduced second

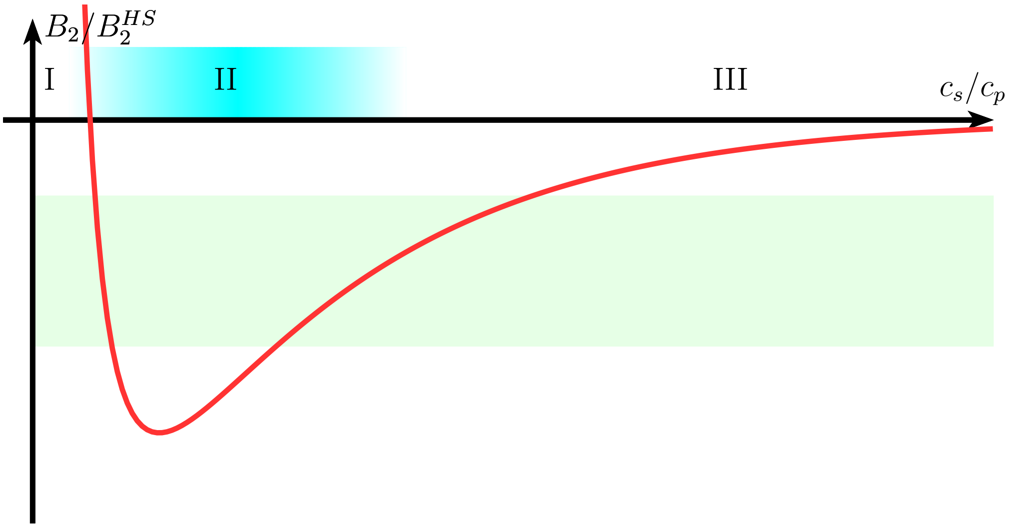

Figure 1.5: *Schematic representation of the reduced second virial coefficient of protein solutions as a function of multivalent ions per protein. Areas which favor crystallization are highlighted in green. Above the coordinate, the different regimes of the phase diagram (Figure 1.3) are displayed with roman numbers. Figure based on Refs. 34, 37.*

virial coefficient has positive or slightly negative values in Regime I, representing an overall repulsion of the particles (Figure 1.5). With increasing salt concentration, the electrostatic repulsion decreases and the charge inversion leads to an increasing attraction, which is represented by negative values of the second virial coefficient. With increasing salt concentration, the attraction favors the crystallization process up to a value where the proteins attract each other strongly, resulting in the formation of large, long-living clusters (Regime II). With even higher salt concentration, another concentration range can be found, in which the charges are balanced in such a way that the proteins form crystals. At very high salt concentrations, the overall charge of the protein is inverted. In this case, the solution mainly contains monomeric proteins and only small clusters, which results in a macroscopically clear solution (Regime III). The proteins still observe a slight attractive potential.

In the following, some general concepts are introduced to describe crystallization.

1.3.1 Classical Nucleation Theory

The classical nucleation theory, based on the framework presented by Gibbs in 1906 [39], describes the formation of crystals as a transition from a liquid to a solid state based on the surface energy and the chemical potential of the particles in solution and in the crystal. While the volume term ΔG_{vol}, containing the supersaturation ratio S of the chemical potentials, favors the formation of particles, the

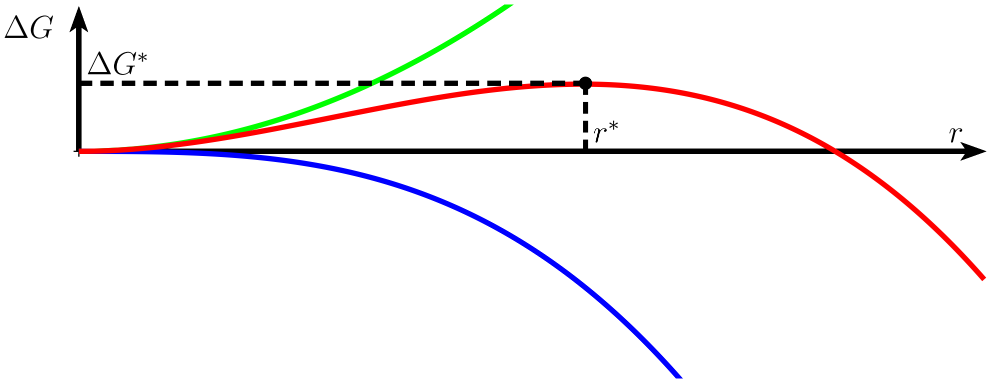

Figure 1.6: *Free energy as a function of particle radius based on the classical nucleation theory. The surface contribution (Equation 1.11), the volume contribution (Equation 1.12) and the total free energy (Equation 1.13), are displayed as green, blue and red curves, respectively. Figure reproduced from Ref. 38 based on Equations 1.11-1.13.*

surface term ΔG_{surf} favors their dissolution.

The total free energy ΔG can be expressed by a sum of these two terms [38]:

$$\Delta G_{\text{surf}} = 4\pi r^2 \sigma \tag{1.11}$$

$$\Delta G_{\text{vol}} = -\frac{4\pi r^3}{3\nu} k_B T \ln(S) \tag{1.12}$$

$$\Delta G = \Delta G_{\text{vol}} + \Delta G_{\text{surf}} \tag{1.13}$$

with the specific surface energy σ and the volume of a single molecule ν. The different contributions are displayed in Figure 1.6. The free energy has an energy barrier with the maximum value

$$\Delta G^* = \frac{16\pi\sigma^3\nu^2}{3k_B^2 T^2 \ln(S)^2} \tag{1.14}$$

at the critical radius $r^* = 2\sigma/(k_B T \ln(S))$. Once a particle passes this critical radius, the formation of the crystal is energetically favorable. If the radius of the particle is smaller, the dissolution is energetically favored. Thermal or density fluctuations or other perturbations are therefore necessary to induce crystallization. Classical nucleation theory describes the crystallization process based on the particle radius as the only reaction coordinate from supersaturated solutions.

It should be mentioned that the classical nucleation theory neglects several aspects. For instance, the surface free energy is assumed to be independent of the size of the particles and the growing crystal is assumed to be spherical. In addition, no specific interactions are taken into account.

A crystallization process, which might be described by classical nucleation, is presented in Chapter 9. Using QENS, the short-time self- and collective diffusion are investigated with NBS and neutron spin echo (NSE), respectively, during the crystallization process.

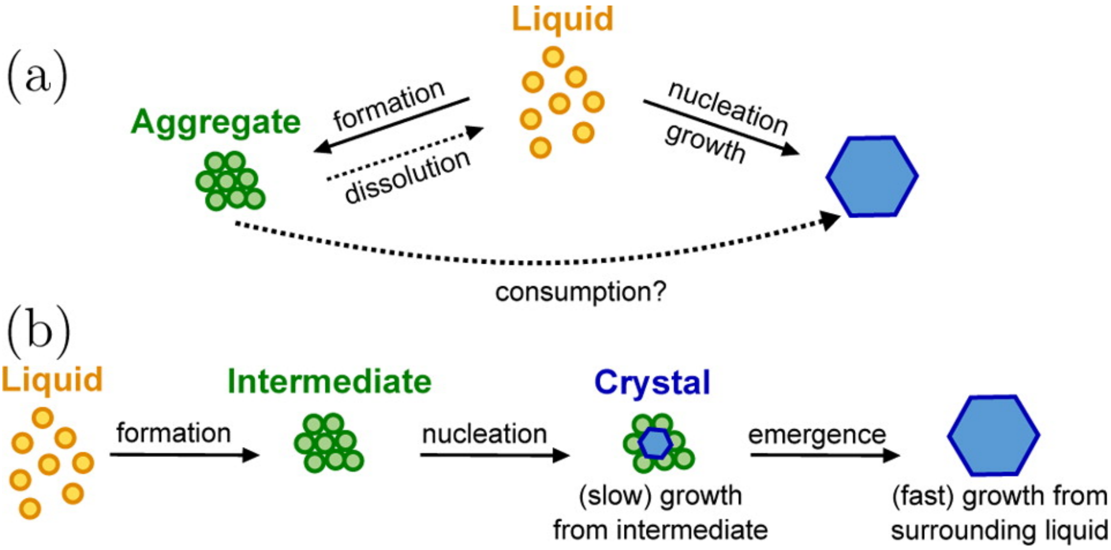

Figure 1.7: *Schematic representation of different non-classical crystallization processes. a) Crystals can grow from the liquid and clusters serve as protein reservoirs. b) From the liquid, aggregates form, which act as precursors for the crystals. Figure taken from Ref. 41.*

1.3.2 Non-Classical Crystallization

Besides the framework outlined in the previous section, describing the crystallization process only as a function of the radius of the particle in solution, different intermediate steps can occur if the free energy landscape characterizing the system contains minima besides the ones representing the solution and crystalline state. These intermediate states might be *e.g.* clusters or the separated phases of an LLPS. In the case of forming clusters or aggregates (represented by the upper energy landscape of Figure 1.4b)[40], they might either serve as reservoirs for the crystal and redissolve during the crystallization process or they might be precursors. In the latter case, the aggregates can serve as nuclei and the different proteins might reorganize into the correct position. A schematic representation of different crystallization processes is shown in Figure 1.7.

LLPS might also promote crystallization given the higher concentration within the dense phase (lower curve in Figure 1.4b). In this case, crystals can grow either at the interface between the two different phases, which might be a nucleation point, or they might grow within one of the two phases.

In Appendix A, non-classical crystallizing processes are investigated with NBS. The sample shows a significant part of non-diffusing particles at the very beginning of the process, which decreases as a function of time and increases again later with growing crystals. The presence of non-diffusing particles in the beginning of the crystallization process might be explained by relatively large aggregates in the sample investigated.

Chapter 2

Scattering Theory

The aim of this chapter is to provide a short introduction to scattering theory. The main equations relevant for the scattering techniques used within this thesis are derived to provide a theoretical background. For more detailed explanations, literature *e.g.* by Bée [42], Lovesey [43], Squires [44], Fitter [45], Lindner [46] or Schober [47] can be consulted.

The chapter starts with a general overview of the scattering geometry (Section 2.1). Section 2.2 provides information on the neutron as a probe used to study the samples, with a focus on its properties and its interaction with matter, offering unique possibilities to study the samples in different ways. Section 2.3 and Section 2.4 derive expressions for the elastic and inelastic scattering, respectively. In Section 2.5, the theoretical background for the description of the elastic incoherent structure factor (EISF) is provided.

In Section 2.6, different types of diffusion and the corresponding expressions for the scattering functions are explained. Finally, Section 2.7 describes the different contributions to the scattering function and how they can be separated.

2.1 The Scattering Geometry

This section is mainly based on Refs. 43 and 44.

Given the wave-particle duality, the kinetic energy E of a neutron can either be described as a particle by its mass m and its momentum $\hbar\vec{k}$ or as a wave with a wavelength λ:

$$E = \frac{\hbar^2 k^2}{2m} = \frac{h^2}{2m\lambda^2} \tag{2.1}$$

with the reduced Planck constant $\hbar = \frac{h}{2\pi} = 6.582119569\,\mu\text{eVns}$. If the neutron energy is characterized before and after the scattering process, it is possible to use its initial energy (E_i) and final energy (E_f) to calculate the energy transfer $\hbar\omega$ which took place during the scattering event:

$$\hbar\omega = E_f - E_i = \frac{\hbar^2\left(k_i^2 - k_f^2\right)}{2m}. \tag{2.2}$$

The corresponding wave vectors $\vec{k}_i$ and $\vec{k}_f$ can be used to describe the momentum transfer $\hbar\vec{q}$ with the scattering vector $\vec{q} = \vec{k}_f - \vec{k}_i$ (see Figure 2.1).

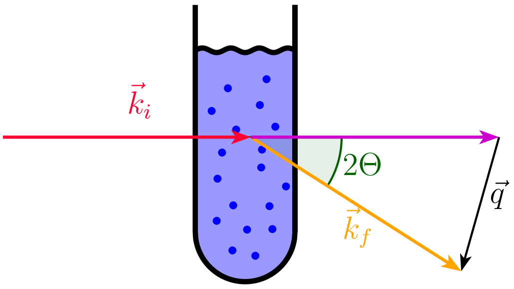

Figure 2.1: *Schematic representation of the scattering geometry in case of elastic scattering ($|k_i| = |k_f|$).*

For small energy transfers $\hbar\omega$, the absolute values of the wave vectors are comparable

$$\left|\vec{k}_i\right| = k_i \simeq k_f = \left|\vec{k}_f\right| \tag{2.3}$$

and the absolute value of the scattering vector q can be expressed using the scattering angle 2Θ:

$$q = |\vec{q}| = \frac{4\pi}{\lambda} \sin\left(\frac{2\Theta}{2}\right). \tag{2.4}$$

If the absolute values of the neutron momentum before and after the scattering process deviate significantly, the absolute value can be written as

$$q^2 = k_i^2 + k_f^2 - 2k_i k_f \cos(2\Theta). \tag{2.5}$$

To characterize a scattering system, the total scattering cross-section σ_{tot} can be defined as the total number of neutrons scattered per second normalized to the incoming flux Φ

$$\sigma_{tot} = \frac{total\, number\, of\, neutrons\, scattered\, per\, second}{\Phi}. \tag{2.6}$$

Since in experiments the total solid angle Ω is not entirely covered with detectors, it is important to define the differential cross-section $\frac{\mathrm{d}\sigma}{\mathrm{d}\Omega}$. Integrating over all directions yields σ_{tot}:

$$\sigma_{tot} = \int_{\text{all directions}} \left(\frac{\mathrm{d}\sigma}{\mathrm{d}\Omega}\right) \mathrm{d}\Omega \tag{2.7}$$

Up to now, no energy transfers are taken into account. In case the neutrons change their energy while interacting with the sample, the partial differential cross-section $\frac{\mathrm{d}^2\sigma}{\mathrm{d}\Omega \mathrm{d}E'}$ is used, which is defined as the fraction of neutrons with an energy in the energy interval $[E', E' + \mathrm{d}E']$. Integrating the partial differential cross-section over all energies thus results in the differential cross-section:

$$\frac{\mathrm{d}\sigma}{\mathrm{d}\Omega} = \int_0^\infty \left(\frac{\mathrm{d}^2\sigma}{\mathrm{d}\Omega \mathrm{d}E'} \right) \mathrm{d}E'. \tag{2.8}$$

In this section, the scattering geometry and cross-sections were introduced. In the next section, some properties of the neutrons, used as probes for the scattering process, will be discussed.

2.2 Properties of the Neutron

This section is mainly based on the textbook by Lovesey [43]. The neutron is an uncharged subatomic particle with a mass $m = 1.675 \cdot 10^{-27}\,\mathrm{kg}$. It has a spin $s = \frac{1}{2}$ and a magnetic dipole moment of $\mu_n = -1.913\mu_N$. The neutron decays *via* a β decay to a proton p^+ by emitting an electron e^- and an electron antineutrino $\bar{\nu}_e$

$$n \to p^+ + e^- + \bar{\nu}_e \tag{2.9}$$

with a mean lifetime $\tau = 881.5 \pm 1.5\,\mathrm{s}$. In contrast to X-rays, neutrons interact with the nuclei and not with the electron cloud since they are electrical neutral. Therefore, they penetrate deeply into the samples and are mainly scattered from the nuclei in the bulk [43] and not from interfaces. The interaction with the nuclei results in different scattering cross-sections, which do not follow a monotonous trend and even vary significantly between different isotopes and spin states. The significantly changing cross-sections between different isotopes of the same element allows to label specific parts of molecules for neutron scattering experiments *via* isotope exchange.

The neutrons used for the scattering experiments described in this thesis were obtained from thermal sources, *i.e.* their velocity distribution $\Phi(v)$ could be described using a Maxwellian distribution whose maximum is given by the moderator temperature T_M [47, 48]:

$$\Phi(v) \propto v^3 \exp\left(-\frac{mv^2}{2k_B T_M} \right) \tag{2.10}$$

Thermal neutrons, moderated by a moderator with $T_M = 293\,\mathrm{K}$, have a mean velocity of $v \approx 2.20\,\frac{\mathrm{km}}{\mathrm{s}}$ and a wavelength of $\lambda \approx 1.8\,\mathrm{Å}$ [44]. Since this wavelength is comparable to the interatomic distances of liquids and solids, thermal neutrons provide an ideal tool for probing the microscopic properties of these materials.

In addition, the energy of thermal neutrons is comparable to elementary excitations and can therefore be used to probe excitations, molecular vibrations, lattice excitations as well as atomic dynamics. Furthermore, their magnetic moment allows to study magnetic structures on a microscopic scale.

By combining the averaged thermal neutron velocity with the mean lifetime of the neutron, it is clear that the construction of instruments situated several hundred meters away from the neutron source is feasible. This offers the possibility to construct many instruments using one neutron source and to use *e.g.* curved neutron guides blocking the direct view from the instrument towards the reactor core and therefore reducing the background signal.

In the next sections, scattering functions are derived for elastic scattering of neutrons with one and several scatterers. Additionally, inelastic scattering is introduced.

2.3 Elastic Scattering

This section provides a short introduction to the theory of elastic neutron scattering. It is mainly based on the text books by Squires [44] and Lovesey [43].

2.3.1 Scattering Signal of a Single Nucleus

If a neutron, described by a wave ψ with a wave vector $\vec{k}$, is scattered elastically by an interaction potential $\hat{V}$, the transition probability $W_{k_i \to k_f}$ can be written using Fermi's Golden rule

$$W_{k_i \to k_f} = \frac{2\pi}{\hbar} \left| \int \mathrm{d}\vec{r} \psi^*_{\vec{k}_f} \hat{V} \psi_{\vec{k}_i} \right|^2 \rho_{\vec{k}_f}(E) \tag{2.11}$$

with $\rho_{\vec{k}_f}(E)$ the energy dependent density of final scattering states. By normalizing the wave functions to a box with size L, the differential cross-section can be calculated:

$$\begin{aligned}
\psi_{\vec{k}_j} &= \frac{1}{L^{\frac{3}{2}}} \exp\left(i\vec{k}_j \cdot \vec{r}\right) \qquad \vec{k}_j = \vec{k}_i, \vec{k}_f && (2.12)\\
\rho_{\vec{k}_f}(E) &= \left(\frac{L}{2\pi}\right)^3 \frac{\mathrm{d}\vec{k}_f}{\mathrm{d}E} && (2.13)\\
\mathrm{d}\sigma &= \frac{W_{\vec{k}_i \to \vec{k}_f}}{\Phi} && (2.14)\\
&= L^6 \left(\frac{m}{2\pi\hbar^2}\right)^2 \left| \int \mathrm{d}\vec{r} \psi^*_{\vec{k}_f} \hat{V} \psi_{\vec{k}_i} \right|^2 \mathrm{d}\Omega && (2.15)\\
\frac{\mathrm{d}\sigma}{\mathrm{d}\Omega} &= \left| \left\langle \vec{k}_f \middle| \hat{V} \middle| \vec{k}_i \right\rangle \right|^2 . && (2.16)
\end{aligned}$$

To calculate the cross-section for a bound nucleus at position $\vec{R}$, the potential $\hat{V}(\vec{r})$ is expressed by a Fermi pseudo-potential:

$$\hat{V}(\vec{r}) = \frac{2\pi\hbar^2}{m} b\delta\left(\vec{r} - \vec{R}\right) \tag{2.17}$$

with a scattering length b which corresponds to the radius of the nucleus. In case the nucleus is situated at the origin ($\vec{R} = 0$), the scattering cross-section can be expressed as

$$\left|\left\langle \vec{k}_f \middle| \hat{V} \middle| \vec{k}_i \right\rangle\right|^2 = \left(\frac{m}{2\pi\hbar^2}\right) \frac{2\pi\hbar^2}{m} bb^* \int \mathrm{d}\vec{r} \exp\left(-i\vec{k}_f \cdot \vec{r}\right) \delta\left(\vec{r}\right) \exp\left(i\vec{k}_i \cdot \vec{r}\right) = |b|^2 \tag{2.18}$$

The differential cross-section and total cross-section therefore can be expressed by

$$\frac{\mathrm{d}\sigma}{\mathrm{d}\Omega} = |b|^2 \tag{2.19}$$

and

$$\sigma = 4\pi\,|b|^2 . \tag{2.20}$$

It should be mentioned that the scattering length depends on the different isotopes present in the sample. While attractive potentials $\hat{V}$ require a positive b, repulsive potentials can be obtained with positive and negative values of b [44]. The scattering length b can also be complex. In this case, the imaginary part $\Im(b)$ represents the absorption of neutrons by the nucleus.

In this section, the expression describing the cross-section of a single nucleus was derived. The aim of the next section is to expand the expressions to obtain the descriptions for the scattering signal of multiple scatterers.

2.3.2 Coherent and Incoherent Scattering

In the previous section, the scattering signal was explained for a single nucleus. In this section, the effects of several scattering centers are presented.

If the scattering system is expanded to N non-moving scattering centers $j \in [1, N]$ at position $\vec{R}_j$, Equation 2.17 has to be modified to:

$$\hat{V}(\vec{r}) = \frac{2\pi\hbar^2}{m} \sum_{j=1}^{N} b_j \delta\left(\vec{r} - \vec{R}_j\right) . \tag{2.21}$$

Since the scattering lengths b_j depend not only on the element, but also on the isotope and on the total spin state of the nucleus-neutron system [42], the calculation of the differential cross section can be split up into several parts. The average over all b_j results in the coherent scattering length $b_j^{coh} = \bar{b_j}$, while the root mean squared deviation of b_j from the coherent scattering length is called incoherent scattering length $b_j^{inc} = \sqrt{\bar{b_j^2} - (b_j^{coh})^2}$. For unpolarized neutron beams, a nucleus with spin $I \neq 0$ results in a neutron-nucleus system which can have two different states $S^{\pm} = I \pm s = I \pm \frac{1}{2}$ with two different scattering lengths $b^{\pm}$. A single spin state is only obtained for isotopes with $I = 0$ ($I + s = \frac{1}{2}$) or if polarized neutrons are used. If the different $n^{\pm} = 2S^{\pm} + 1$ states have the same probability, the coherent and incoherent scattering lengths can be calculated [42]:

$$b^{coh} = \frac{1}{n^+ + n^-}\left[n^+ b^+ + n^- b^-\right] \tag{2.22}$$

$$b^{inc} = \frac{1}{2I+1}\left[(I+1)b^+ + I b^-\right] \tag{2.23}$$

The differential cross-section can then be written as a sum over the different scattering lengths including the phase shift given by the distances between the scatterers:

$$\frac{\mathrm{d}\sigma}{\mathrm{d}\Omega} = \sum_{j,j'=1}^{N} \exp\left(i\vec{q}\cdot\left(\vec{R}_j - \vec{R}_{j'}\right)\right)\overline{b^*_{j'} b_j} \tag{2.24}$$

The expression $\overline{b^*_{j'} b_j}$ represents the average over all isotopes and all nuclear states. For $j \neq j'$, the two scattering lengths belong to different nuclei and their values are uncorrelated. The average can therefore be rewritten as

$$\overline{b^*_{j'} b_j} = \overline{b^*_{j'}} \cdot \overline{b_j} = \left|\overline{b_j}\right|^2 \tag{2.25}$$

If $j = j'$, the expression simplifies to

$$\overline{b^*_{j'} b_j} = \overline{\left|b_j\right|^2} = \overline{|b|^2}. \tag{2.26}$$

Using Equations 2.25 and 2.26, Equation 2.24 can be rewritten as a sum of a coherent and an incoherent part as:

$$\frac{\mathrm{d}\sigma}{\mathrm{d}\Omega} = \left(\frac{\mathrm{d}\sigma}{\mathrm{d}\Omega}\right)_{coh} + \left(\frac{\mathrm{d}\sigma}{\mathrm{d}\Omega}\right)_{inc} \tag{2.27}$$

$$\left(\frac{\mathrm{d}\sigma}{\mathrm{d}\Omega}\right)_{coh} = \left|\bar{b}\right|^2 \left|\sum_{j=1}^{N} \exp\left(i\vec{q}\cdot\vec{R}_j\right)\right|^2 \tag{2.28}$$

$$\left(\frac{\mathrm{d}\sigma}{\mathrm{d}\Omega}\right)_{inc} = N\left(\overline{|b|^2} - \left|\bar{b}\right|^2\right) = N\overline{\left|b - \bar{b}\right|^2} \tag{2.29}$$

In Table 2.1, different experimentally determined cross-sections and the corresponding scattering lengths are listed for different elements. The different elements and different isotopes have coherent and incoherent cross-sections. Since the interactions of thermal neutrons are governed by interactions of their spins with unpaired electrons and, more importantly, with the nuclear force, which strongly depends on the nuclei structure and the resulting strong forces, a general theoretical description for the scattering lengths is missing [49]. It only exists for few simple scattering systems such as neutrons being scattered by deuterium [50]. Several methods were developed and studies were performed to increase the confidence values of the measured cross-sections[49, 51–53]. These differences in the coherent and incoherent scattering allows to enhance the scattering of specific parts of the sample by isotope exchange for both the coherent or incoherent scattering. If the resolution of the scattering instrument is not sufficiently high or if the length scales investigated are significantly higher than the interatomic distances, the scattering length density $\rho_b(\vec{r})$ can be defined as [47]

$$\rho_b(\vec{r}) = \frac{1}{V}\sum_{j=1}^{N} \bar{b}_j \delta\left(\vec{r} - \vec{R}_j\right). \tag{2.30}$$

The coherent cross-section from Equation 2.28 can thus be written as a Fourier transform of the real space scattering length density:

$$\left(\frac{\mathrm{d}\sigma}{\mathrm{d}\Omega}\right)_{coh} = \left|\bar{b}\right|^2 \left|\sum_{j=1}^{N} \exp\left(i\vec{q}\cdot\vec{R}_j\right)\right|^2 = \left|\int_V \mathrm{d}^3 r\, \rho_b\left(\vec{r}\right)\cdot \exp\left(i\vec{q}\cdot\vec{r}\right)\right|^2 \tag{2.31}$$

If solutions with N randomly oriented centrosymmetric particles with a volume V_p are investigated, Equation 2.31 can be written in such a way that the interference effects resulting from the shape of the particles are represented by a form factor $P(q)$.

If interparticle interactions cannot be neglected, the interferences of the different particles results in the so-called structure factor $S(q)$

$$\begin{aligned}
\left(\frac{\mathrm{d}\sigma}{\mathrm{d}\Omega}\right)_{coh} &= N\left(\Delta\rho\right)^2 V_p^2 P(q) S(q) && (2.32)\\
P(q) &= \frac{1}{V_p}\left|\int_{V_p} \exp\left(-i\vec{q}\vec{r}\right)\mathrm{d}\vec{r}\right|^2 && (2.33)\\
S(q) &= \frac{1}{N}\sum_{\alpha=1}^{N}\sum_{\beta=1}^{N} \exp\left(-i\vec{q}\left(\vec{r}_\alpha - \vec{r}_\beta\right)\right) && (2.34)
\end{aligned}$$

with $\Delta\rho$ being the scattering length density difference between the particles and the solvent. Different shapes of the particles result in different form factors. Examples can be found *e.g.* in Refs. 46, 54, 55. The structure factor contains information on the particle interactions and their distances.

In case the particles assemble into crystalline structures, the structure factor, and therefore also the scattering profile, features sharp Bragg peaks at well-defined scattering vectors $q_B = \frac{2\pi}{l}$, with l being the crystal lattice distance. If several randomly oriented crystals are present in the scattering volume, the differential cross-section has a well pronounced peak with radius q around the beam center if it is projected onto a two-dimensional detector. If less crystals are present, the powder average is not fulfilled and only discrete spots are visible on the detector image.

The incoherent part of the elastic scattering (see Equation 2.27) contains information about the self-diffusive dynamics of the investigated particles. A more detailed description is given in the following section and in Chapter 5.

This section introduced the elastic scattering from multiple scatterers and introduced as well the coherent and incoherent scattering. In the next section, the expressions are expanded and energy transfers between the neutron and the sample are taken into account.

Table 2.1: *Overview of the scattering lengths and bound scattering cross-sections for the different chemical elements predominantly present in the samples measured. If only one isotope is listed, the most prominent isotope is chosen. Shaded lines display the isotope-averaged values of the respective element. The nuclear notation* ${}^{A}_{Z}X$ *is used with* A, Z *and* X *being the atomic mass, atomic number and the chemical symbol of the element, respectively. Values are taken from Ref. 51. Scattering cross-sections and scattering lengths are given in* $\mathrm{barn} = 100\,\mathrm{fm}^2$ *and femtometers, respectively.*

	b_c	σ_{coh}	σ_{inc}	σ_{scatt}	σ_{abs}
H	-3.7409(11)	1.7568(10)	80.26(6)	82.02(6)	0.3326(7)
${}^{1}_{1}\mathrm{H}$	-3.7423(12)	1.7583(10)	80.27(6)	82.03(6)	0.3326(7)
$\mathrm{D}\hat{=}{}^{2}_{1}\mathrm{H}$	6.674(6)	5.592(7)	2.05(3)	7.64(3)	0.000519(7)
C	6.6484(13)	5.551(2)	0.001(4)	5.551(3)	0.00350(7)
${}^{6}_{12}\mathrm{C}$	6.6535(14)	5.559(3)	0	5.559(3)	0.00353(7)
N	9.36(2)	11.01(5)	0.50(12)	11.51(11)	1.90(3)
${}^{7}_{14}\mathrm{N}$	9.37(2)	11.03(5)	0.50(12)	11.53(11)	1.91(3)
O	5.805(4)	4.232(6)	0.000(8)	4.232(6)	0.00019(2)
${}^{8}_{16}\mathrm{O}$	5.805(5)	4.232(6)	0	4.232(6)	0.00010(2)
Na	3.63(2)	1.66(2)	1.62(3)	3.28(4)	0.530(5)
${}^{11}_{23}\mathrm{Na}$	3.63(2)	1.66(2)	1.62(3)	3.28(4)	0.530(5)
Al	3.449(5)	1.495(4)	0.0082(6)	1.503(4)	0.231(3)
${}^{13}_{27}\mathrm{Al}$	3.449(5)	1.495(4)	0.0082(6)	1.503(4)	0.231(3)
S	2.847(1)	1.0186(7)	0.007(5)	1.026(5)	0.53(1)
${}^{16}_{32}\mathrm{S}$	2.804(2)	0.9880(14)	0	0.9880(14)	0.54(4)
Cl	9.5792(8)	11.528(2)	5.3(5)	16.8(5)	33.5(3)
${}^{17}_{35}\mathrm{Cl}$	11.70(9)	17.06(6)	4.7(6)	21.8(6)	44.1(4)
V	-0.443(14)	0.01838(12)	5.08(6)	5.10(6)	5.08(4)
${}^{23}_{51}\mathrm{V}$	-0.402(2)	0.0203(2)	5.07(6)	5.09(6)	4.9(1)
Zn	5.680(5)	4.054(7)	0.077(7)	4.131(10)	1.11(2)
${}^{30}_{64}\mathrm{Zn}$	5.23(4)	3.42(5)	0	3.42(5)	0.93(9)
Y	7.75(2)	7.55(4)	0.15(8)	7.70(9)	1.28(2)
${}^{39}_{89}\mathrm{Y}$	7.75(2)	7.55(4)	0.15(8)	7.70(9)	1.28(2)
Cd	4.83(5)	3.04(6)	3.46(13)	6.50(12)	2520.0(50.0)
${}^{48}_{114}\mathrm{Cd}$	7.48(5)	7.1(2)	0	7.1(2)	0.34(2)
In	4.065(20)	2.08(2)	0.54(11)	2.62(11)	193.8(1.5)
${}^{49}_{115}\mathrm{In}$	4.00(3)	2.02(2)	0.55(11)	2.57(11)	202.0(2.0)
La	8.24(4)	8.53(8)	1.13(19)	9.66(17)	8.97(2)
${}^{57}_{139}\mathrm{La}$	8.24(4)	8.53(8)	1.13(15)	9.66(17)	8.93(4)

2.4 Inelastic Scattering

Previous sections derived expressions describing the elastic scattering from single and multiple scatterers. In this section, the expressions are expanded to consider also inelastic scattering processes. To calculate the differential cross-section for scattering events in which the probing neutron changes both its energy and its momentum transfer, the scattering potential has to be modified. Detailed calculations can be found, *e.g.*, in publications by Schober [47], Squires [44] and Lovesey [43]. The latter two references are used for this section.

If neutrons can exchange energy with the sample during the scattering process, the potential in Equation 2.16 becomes energy-dependent and the equation modifies to

$$\frac{\mathrm{d}\sigma_{\vec{k}_i\to\vec{k}_f,\lambda_i\to\lambda_f}}{\mathrm{d}\Omega} = m^2\left(\frac{2\pi}{\hbar}\right)^4\frac{k_f}{k_i}\left|\left\langle\lambda_f,\vec{k}_f\left|V\right|\lambda_i,\vec{k}_i\right\rangle\right|^2 \tag{2.35}$$

with the energy eigenstates λ_i of the system investigated. The equation can be rewritten in a differential way also considering the energy transfer respecting the conservation of energy

$$\frac{\mathrm{d}^2\sigma_{\vec{k}_i\to\vec{k}_f,\lambda_i\to\lambda_f}}{\mathrm{d}\Omega\mathrm{d}E_f} = m^2\left(\frac{2\pi}{\hbar}\right)^4\frac{k_f}{k_i}\left|\left\langle\lambda_f,\vec{k}_f\left|V\right|\lambda_i,\vec{k}_i\right\rangle\right|^2\delta\left(\hbar\omega-\left(E_{\lambda_i}-E_{\lambda_f}\right)\right) \tag{2.36}$$

$$\frac{\mathrm{d}^2\sigma_{\vec{k}_i\to\vec{k}_f}}{\mathrm{d}\Omega\mathrm{d}E_f} = m^2\left(\frac{2\pi}{\hbar}\right)^4\frac{k_f}{k_i}\sum_{\lambda_i,\lambda_f}p(\lambda_i)\left|\left\langle\lambda_f,\vec{k}_f\left|V\right|\lambda_i,\vec{k}_i\right\rangle\right|^2\delta\left(\hbar\omega-\left(E_{\lambda_i}-E_{\lambda_f}\right)\right). \tag{2.37}$$

In Equation 2.37, the equation was rewritten assuming that the energy eigenstates λ_i can be described using their statistical weights $p(\lambda_i)$ and that these weights are not changed by the interaction with the neutron.

Energy-sensitive scattering can probe the displacement of the scattering atoms and Equation 2.24 therefore has to be written as

$$\frac{\mathrm{d}^2\sigma}{\mathrm{d}\Omega\mathrm{d}E} = \frac{k_f}{k_i}\frac{1}{2\pi\hbar}\sum_{j,j'=1}^{N}\overline{b_j b_{j'}^*}\int\left\langle\exp\left(i\vec{q}\cdot\left(\vec{R}_j(0)-\vec{R}_{j'}(t)\right)\right)\right\rangle\exp\left(-i\omega t\right)\mathrm{d}t \tag{2.38}$$

Similarly to Equation 2.27, the double differential cross-section can be divided into a coherent and an incoherent contribution

$$\frac{\mathrm{d}^2\sigma}{\mathrm{d}\Omega\mathrm{d}E_f} = \left(\frac{\mathrm{d}^2\sigma}{\mathrm{d}\Omega\mathrm{d}E_f}\right)_{coh}+\left(\frac{\mathrm{d}^2\sigma}{\mathrm{d}\Omega\mathrm{d}E_f}\right)_{inc}. \tag{2.39}$$

To obtain an expression independent of the incident momentum $\hbar\vec{k}_i$ of the neutron and thus independent of the experimental setup, a scattering function $S(q, \omega)$ is defined, which can also be written as a sum of the coherent and incoherent parts:

$$\begin{aligned}\frac{\mathrm{d}^2\sigma}{\mathrm{d}\Omega\mathrm{d}E} &= \frac{k_f}{k_i} S(\vec{q}, \omega) && (2.40)\\ S(\vec{q}, \omega) &= \sum_{j \neq j'}^{N} \overline{b_j b_{j'}^*} S_c(\vec{q}, \omega) + \sum_{j=j'}^{N} \overline{b_j b_j^*} S_i(\vec{q}, \omega) && (2.41)\end{aligned}$$

The coherent scattering function can be linked to the intermediate scattering function $I(\vec{q}, t)$ and to the time correlation function $G(\vec{r}, t)$ *via* Fourier transforms:

$$\begin{aligned}S_c(\vec{q}, \omega) &= \frac{1}{2\pi\hbar} \int I_c(\vec{q}, t) \exp\left(-i\omega t\right) \mathrm{d}t && (2.42)\\ I_c(\vec{q}, t) &= \int G_c(\vec{r}, t) \exp\left(i\vec{q} \cdot \vec{r}\right) \mathrm{d}\vec{r} && (2.43)\end{aligned}$$

The collective time-dependent pair-correlation function $G_c(\vec{r}, t)$, linked to the coherent scattering function $S_c(\vec{q}, \omega)$, can be defined as

$$G_c(\vec{r}, t) = \frac{1}{N} \sum_{j,j'} \int \left\langle \delta\left(\vec{r'} - \vec{R}_{j'}(0)\right) \delta\left(\vec{r'} + \vec{r} - \vec{R}_j(t)\right)\right\rangle \mathrm{d}\vec{r'} \qquad (2.44)$$

It describes the probability that a particle j is found at position R_j at time t, in case the particle j' is located at position $\vec{R}_{j'}(0)$ at time $t = 0$. Its value at $t = 0$ is closely linked to the static pair distribution function $g(\vec{r})$, which is the Fourier transform of the structure factor (introduced in Equation 2.34):

$$\begin{aligned}g(\vec{r}) &= \sum_{j \neq 0} \left\langle \delta\left(\vec{r} - \vec{R}_j + \vec{R}_0\right)\right\rangle && (2.45)\\ G_c(\vec{r}, 0) &= \delta(\vec{r}) + g(\vec{r}) && (2.46)\end{aligned}$$

By integrating the pair correlation function over space, the total number of particles investigated, N, is obtained

$$N = \int G(\vec{r}, t) \mathrm{d}\vec{r} \qquad (2.47)$$

for all times t.

The second part of Equation 2.39 can be expressed similarly to the coherent part:

$$\begin{aligned} S_i(\vec{q},\omega) &= \frac{1}{2\pi\hbar}\int I_i(\vec{q},t)\exp\left(-i\omega t\right)\mathrm{d}t & (2.48)\\ I_i(\vec{q},t) &= \int G_s(\vec{r},t)\exp\left(i\vec{q}\cdot\vec{r}\right)\mathrm{d}\vec{r} \\ &= \frac{1}{N}\sum_j \left\langle \exp\left(-i\vec{q}\cdot\vec{r}_j(0)\right)\exp\left(-i\vec{q}\cdot\vec{r}_j(t)\right)\right\rangle . & (2.49)\end{aligned}$$

The self time-dependent pair-correlation function $G_s(\vec{r},t)$, linked to the incoherent scattering function $S_i(\vec{q},\omega)$ can be defined as

$$G_s(\vec{r},t) = \frac{1}{N}\sum_j \int \left\langle \delta\left(\vec{r'} - \vec{R}_j(0)\right)\delta\left(\vec{r'} + \vec{r} - \vec{R}_j(t)\right)\right\rangle \mathrm{d}\vec{r'}, \qquad (2.50)$$

describing the probability that the same particle j is found at position $\vec{R}_j(t)$ at time t, if it was at the origin at time $t = 0$. A spatial integration of G_s results in unity.

2.5 The Elastic Incoherent Structure Factor

This section is based on the textbook by Fitter *et al.* [45].

Investigating the self time-dependent pair-correlation function $G_s(\vec{r},t)$ from Equation 2.50 in the limit $t \to \infty$, two different contributions can be separated. If the investigated particle is free in space, it can diffuse to an arbitrary place. The corresponding correlation function therefore vanishes for $t \to \infty$. If, however, the particle can only diffuse within a confined volume, the correlation function does not vanish for the limit $t \to \infty$, but results in an asymptotic value $G_s(\vec{r},\infty) \neq 0$. Equation 2.50 can therefore be rewritten as

$$G_s(\vec{r},t) = G_s(\vec{r},\infty) + G'_s(\vec{r},t). \qquad (2.51)$$

By inserting Equation 2.51 into Equation 2.48 and Equation 2.49, the incoherent scattering function can also be written as a sum of two contributions

$$S_i(\vec{q},\omega) = S_i^{el}(\vec{q})\delta(\omega) + S_i^{in}(\vec{q},\omega). \qquad (2.52)$$

Resulting from the term $G_s(\vec{r},\infty)$ in Equation 2.51, the incoherent scattering signal $S_i^{el}(\vec{q})$ in Equation 2.52 contains structural information about the confinement. $S_i^{el}(\vec{q})$ is also described as elastic incoherent structure factor (EISF).

If both the total scattering function $S_i(\vec{q},\omega)$ and the incoherent scattering function describing the diffusion of the non-bound particles $S_i^{in}(\vec{q},\omega)$ are normalized, Equation 2.52 can be rewritten as:

$$S_i(\vec{q},\omega) = A_0(\vec{q})\delta(\omega) + (1 - A_0(\vec{q}))S_i^{in}(\vec{q},\omega). \tag{2.53}$$

with the EISF $A_0(\vec{q}) = S_i^{el}(\vec{q})$. Expressions for different confined motions have been derived. An overview is, *e.g.*, given by Fitter *et al.* [45].

Since the instruments used to measure the scattering functions have a finite energy resolution, the observation time of the instrument t_{obs} is limited by a factor proportional to the inverse energy resolution. The observed EISF therefore describes scatterers which are confined for $t > t_{obs}$. Investigating the same sample with different instruments, characterized by different energy resolutions, might therefore lead to different EISF.

2.6 Diffusion

The previous sections derived expressions describing the scattering process as a function of the momentum transfer and energy transfer. The aim of this section is to sketch a framework which describes different diffusive dynamics and how they influence the scattering signal. It is mainly based on publications by Milligen [56], Schober [47] and Grimaldo *et al.* [13], as well as on the book by Dhont [11].

2.6.1 Brownian Diffusion

In 1905, Einstein linked the Brownian motion quantitatively with the diffusion [57]. The atomic density $n(r,t)$ and the current $\vec{J}(\vec{r},t)$ are connected *via* the continuity equation:

$$\frac{\partial}{\partial t} n\left(\vec{r},t\right) + \vec{\nabla} \cdot \vec{J}\left(\vec{r},t\right) = 0 \tag{2.54}$$

Together with Fick's first law, the diffusion equation (Fick's second law) is obtained:

$$\begin{aligned} \vec{J}\left(\vec{r},t\right) &= \vec{\nabla} n\left(\vec{r},t\right) && (2.55)\\ \frac{\partial n\left(\vec{r},t\right)}{\partial t} &= D\vec{\nabla}\cdot\vec{\nabla} n\left(\vec{r},t\right) = D\Delta n\left(\vec{r},t\right) && (2.56) \end{aligned}$$

with D being the diffusion coefficient of the particles investigated. The isotropic solution can be written as

$$G\left(\vec{r},t\right) = \frac{1}{\sqrt{4\pi D\left|t\right|}^3} \exp\left(-\frac{r^2}{4D\left|t\right|}\right). \tag{2.57}$$

The correlation function describes the correlation of a particle with itself (self-correlation). Therefore, Equation 2.57 is a description of the time-dependent self-correlation function in the case of Brownian diffusion.

Combining Equation 2.57 with Equation 2.49, the incoherent intermediate scattering function can be calculated:

$$\begin{aligned} I_i\left(\vec{q},t\right) &= \int G\left(\vec{r},t\right) \exp\left(i\vec{q}\cdot\vec{r}\right) \mathrm{d}^3\vec{r} && (2.58)\\ &= \exp\left(-q^2 D\left|t\right|\right) && (2.59) \end{aligned}$$

resulting in an exponential decay. Using Equation 2.48, the incoherent scattering function can be described by a Lorentzian function $\mathscr{L}_\gamma$ with a half width at half maximum (HWHM) γ:

$$\begin{aligned} \gamma &= Dq^2 && (2.60)\\ S_i(q,\omega) &= \frac{1}{\pi\hbar}\frac{Dq^2}{\left(Dq^2\right)^2+\omega^2} = \frac{1}{\pi\hbar}\frac{\gamma}{\gamma^2+\omega^2} = \mathscr{L}_\gamma(\omega). && (2.61) \end{aligned}$$

The translational diffusion coefficient in the dilute limit (D_{t0}) can be linked to the hydrodynamic radius of the particles investigated *via* the Stokes-Einstein relation

$$D_{t0} = \frac{k_B T}{6\pi\eta R_H}. \tag{2.62}$$

If a particle has a radius R_H, it can also rotate around its origin. This rotational diffusion also contributes to the scattering function. Similar to the translational diffusion coefficient describing the translational Brownian diffusion (Equation 2.62), the rotational diffusion can be described by a rotational diffusion coefficient and can also be linked to the hydrodynamic radius.

$$D_{r0} = \frac{k_B T}{8\pi\eta R_H^3}. \tag{2.63}$$

The translational and rotational diffusion coefficients slow down if the particle concentration increases. For hard spheres, the volume fraction scaling can be described by

$$D_t(\varphi) = D_{t0}\cdot f_t(\varphi) \tag{2.64}$$

$$D_r(\varphi) = D_{r0}\cdot f_r(\varphi) \tag{2.65}$$

for the translational and rotational diffusion, respectively.

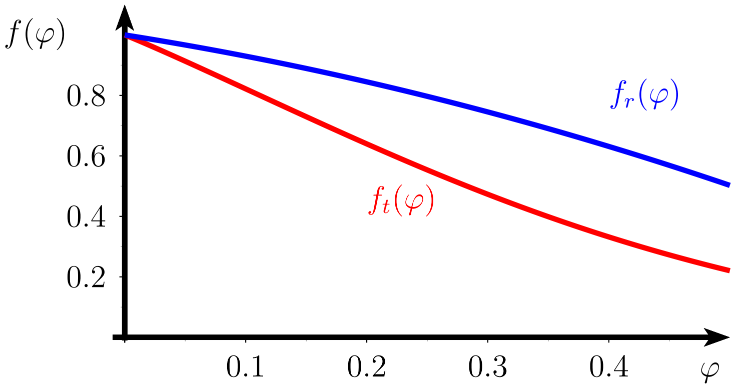

Figure 2.2: *Volume fraction dependence of the translational and rotational diffusion coefficients. The red and blue curve represent the volume fraction dependence* $f_t(\varphi)$ *(Equation 2.66) and* $f_r(\varphi)$ *(Equation 2.68) based on Ref. 59 and Ref. 58, respectively.*

Expressions for the volume fraction scalings are given by Refs. 58, 59

$$f_t(\varphi) = \frac{1}{1+\left(\frac{2b^2}{1-b} - \frac{c}{1+2c} - \frac{bc(2+c)}{(1+c)(1-b+c)}\right)} \tag{2.66}$$

$$b = \sqrt{\frac{9\varphi}{8}} \qquad c = \frac{11\varphi}{16} \tag{2.67}$$

$$f_r(\varphi) = 1 - 0.631\varphi - 0.726\varphi^2 + \mathscr{O}(\varphi^3). \tag{2.68}$$

The volume fraction dependencies are shown in Figure 2.2. The given expressions are obtained for hard spheres. If the properties of the particles vary, *e.g.* in shape or interactions, these dependencies might change [58, 60].

In contrast to the translational diffusion described with one single Lorentzian function, the incoherent scattering function for the rotation is described by an infinite sum of Lorentzian functions [61]:

$$S_i(q,\omega) = \sum_{l=0}^{\infty} B_l(q)\mathscr{L}_{\gamma_r}(\omega) \tag{2.69}$$

$$\gamma_r = l(l+1)D_r \tag{2.70}$$

$$B_l(q) = (2l+1)\int \rho_H(r) j_l^2(qr)\mathrm{d}r \tag{2.71}$$

with $\rho_H(r)$ and $j_l(x)$ being the hydrogen distribution of the particles investigated and the lth-order spherical Bessel functions.

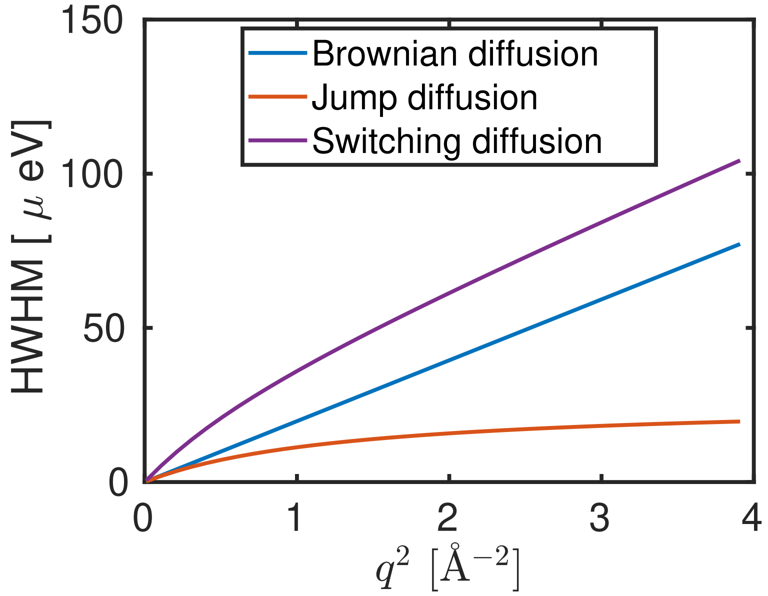

Figure 2.3: *HWHM of the scattering signal as function of q^2 for models describing different types of diffusion. The graphs are based on Equations 2.60, 2.73 and Equation 2.74-2.78 for Brownian diffusion (blue), jump diffusion (orange) and switching diffusion (purple), respectively.*

An apparent global diffusion, combining the translational and rotational diffusion, can be described with one single Lorentzian function with an apparent diffusion coefficient D_{app} fulfilling the condition [61]

$$\sum_{l=0}^{\infty} B_l(q) \frac{l(l+1)D_r + q^2(D_t - D_{app})}{(l(l+1)D_r + q^2(D_t + D_{app}))^2} = 0. \tag{2.72}$$

The HWHM of the Lorentzian describing the apparent global diffusion is described by $\gamma_{app} = D_{app}q^2$. In Figure 2.3, the HWHM of the scattering function $S_i(q,\omega)$ is displayed as a function of q^2 for different types of diffusion. For the case of Brownian diffusion explained in this section, an apparent diffusion coefficient of $D_{app} = 30\,\text{Å}^2\text{ns}^{-1}$ was used for the representation.

This section described the Brownian diffusion of particles. In the following subsections, different models accounting for other types of diffusion are explained.

2.6.2 Jump Diffusion

Singwi *et al.* [62] developed a model in which a particle can switch between two different diffusive states. The particle performs an oscillatory motion for a mean time τ_0 and then switches into a diffusive state with a diffusion coefficient D_j for a mean time τ_1. In the limit $\tau_0 \ll \tau_1$, the model results in the normal Brownian diffusion as described in Section 2.6. For $\tau_1 \ll \tau_0$ the authors derived a model in which the scattering function can also be described by a Lorentzian function. In contrast to Equation 2.60 the HWHM Γ is, in this case, described by

$$\Gamma = \frac{D_j q^2}{1 + D_j q^2 \tau_0}. \tag{2.73}$$

By investigating the q dependence of Γ (see Figure 2.3), it can, on the one hand, be seen that at high q the HWHM levels off to a value of $\frac{2\hbar}{\tau_0}$. On the other hand, the initial slope is identical to the one of the Brownian diffusion described in the previous section. To model the HWHM, the diffusion coefficient $D_j = 30\,\text{Å}^2\text{ns}^{-1}$ was chosen to be identical to the one of the Brownian diffusion presented in Section 2.6. The residence time was set to $\tau_0 = 0.025\,\text{ns}$.

2.6.3 Switching Model

Another model, developed by Roosen-Runge *et al.* [63], describes the internal diffusive dynamics taking into account several different diffusive states. The case of two different states has been applied to spectra of dissolved BSA collected by Grimaldo *et al.* [64]. The model can be described by two Lorentzian functions whose scaling parameters and widths are linked to each other by two diffusion coefficients $D_{1,2}$ and two residence times $\tau_{1,2}$:

$$\begin{aligned}
\Gamma_{1,2} &= D_{1,2} q^2 && (2.74)\\
\Lambda &= \sqrt{\left(\Gamma_1 - \Gamma_2 + \frac{1}{\tau_1} - \frac{1}{\tau_2}\right)^2 + \frac{4}{\tau_1 \tau_2}} && (2.75)\\
\lambda_{1,2} &= \frac{\Gamma_1 + \Gamma_2 + \frac{1}{\tau_1} + \frac{1}{\tau_2} \pm \Lambda}{2} && (2.76)\\
\alpha &= \frac{\tau_1 \Gamma_2 + \tau_2 \Gamma_1 + \frac{1}{\tau_1} + \frac{1}{\tau_2} - \lambda_1}{(\lambda_2 - \lambda_1)(\tau_1 + \tau_2)} && (2.77)\\
S(q,\omega) &= \alpha \mathscr{L}_{\lambda_1}(\omega) + (1-\alpha)\mathscr{L}_{\lambda_2}(\omega). && (2.78)
\end{aligned}$$

It should be noted that $\lambda_{1,2}$ and α are also q-dependent. Due to the increasing number of parameters, the q and ω dependence of the scattering data has to be fitted simultaneously using this model. The q dependence of the HWHM for this model is shown in Figure 2.3 with $D_1 = 30\,\text{Å}^2\text{ns}^{-1}$, $D_2 = 200\,\text{Å}^2\text{ns}^{-1}$, $\tau_1 = 0.025\,\text{ns}$ and $\tau_2 = 0.01\,\text{ns}$. Since the first diffusion coefficient is chosen to be identical to the one of the previous models, the slope at high q is similar to the one of the Brownian diffusion. At low q, a faster increase due to the second contribution is observed, resulting in an offset of the HWHM between the Brownian diffusion and the switching model presented.

2.7 Other Contributions to the Scattering Signal

The previous section described the influence of diffusive dynamics onto the scattering signal. In experiments, additional contributions to the signal can be observed. Its separation is described in the following. From Equation 2.38, which describes the scattering function as a sum over the different scatterers, it becomes visible that the scattering signal containing contributions from different particles can be written as a sum of the scattering signals of the different scatterers in a first approximation. The scattering signal of a protein solution can therefore be written as the sum of the scattering signal of the proteins and that from the solvent:

$$S(q, \omega) = S_{Prot}(q, \omega) + S_{D_2O}(q, \omega). \tag{2.79}$$

The scattering signal of the solvent can be measured separately. As shown by Grimaldo *et al.* [61], the solvent contribution has to be rescaled to the volume fraction $(1 - \varphi)$ occupied by the solvent. Qvist *et al.* [65] developed a model to describe the diffusive dynamics of water (H_2O). Two different Lorentzian contributions with an additional background were used to model the diffusion of water covering the center of mass diffusion as well as faster vibrational diffusive dynamics. While recent NBS spectrometers, such as cold neutron backscattering spectrometer (IN16B) or BASIS, access an energy transfer where diffusion can be described by one single Lorentzian function with a width fixed by time of flight (TOF) measurements [61], recent developments such as the Backscattering and Time of Flight Spectroscopy (BATS) option of IN16B [66], where higher energy transfers can be investigated, might imply a more detailed description of the water signal, *e.g.* using the model developed by Qvist *et al.* [65].

Similar to the separation of the protein and solvent scattering signal, the scattering signal of the sample holder can be separated from the total scattering function. The scattering signal of an empty sample holder can be measured. While in a first approximation, the scattering signal can be subtracted directly, correction terms can also be applied to subtract the scattering signal of the empty sample holder (also called empty can). As the aluminum sample holder is double-walled, several sample holder walls contribute to the scattering signal. In the case of a sample holder filled with a sample, the sample also scatters neutrons and thus reduces the neutron flux at the positions of the other walls of the sample holder. These walls thus contribute more to the scattering signal in the case of an empty can measurement. This effect is taken into account by using q dependent corrections proposed by Paalman and Pings [67]. A detailed description of the application in NBS is given by Hennig [68] and by Grimaldo *et al.* [33].

In recent high-resolution measurements performed with BATS [69], contributions of the cryofurnace used to control the sample temperature were visible also in the scattering signal. In the first BATS measurements, measured without an optimized neutron flux on the sample and presented in Section 4, the statistics of the collected spectra were not yet good enough to observe such a contribution.

A direct subtraction of the contribution similar to the one of the empty can or with correction factors has to be taken into account for future analysis. Due to the limited energy-transfer range or due to the slightly worse energy resolution, a similar subtraction of the empty cryofurnace signal is not significant for data collected on IN16B with a monochromator crystal installed on a Doppler machine or on BASIS, respectively.

In this chapter, the main theoretical concepts, necessary for the interpretation of the scattering data were presented. In addition, the different types of diffusion as well as their contributions to the scattering signal were discussed. The contribution of different scatterers as well as their separation was discussed in the last section.

Chapter 3

Materials and Methods

This chapter summarizes the materials and methods employed in this thesis. For detailed descriptions, specific literature is reviewed correspondingly.

In the first part of this chapter, the materials used and their characteristics are reviewed. In Section 3.1.1 to Section 3.1.3, the properties of the solvent, the proteins used and the multivalent salts are summarized. In the second part of this chapter, the different methods are described: In Section 3.2.1, the two methods mainly used to obtain neutron beams are explained. Finally in Section 3.2.2 to Section 3.2.4, the instrumental layouts for small angle neutron scattering (SANS) experiments, neutron spin echo (NSE) and neutron backscattering (NBS) measurements are explained, respectively.

3.1 Materials

All investigated samples were protein solutions with solutions containing different salts at different salt concentrations and different protein concentrations. This section will review the different properties of the components.

3.1.1 Solvents

Due to the fact that most studies used the incoherent scattering to access the short-time self-diffusion of the tracer particles, heavy water was used as solvent to reduce the incoherent scattering of the solvent. Besides the change in the cross-sections as explained in Section 2.3.2, the change to the ^{2}H=D isotope in the solvent results in some macroscopic differences in the behavior of the solvent. An overview is given in Table 3.1. The temperature-dependent viscosity is shown in Figure 3.1 for both liquids.

Table 3.1: *Comparison of different properties of H_2O and D_2O*

	H_2O	D_2O
Density at 25°C [70]	0.99704	1.1045
Melting point (101.325 kPa)	0.00° C[71]	3.802° C[72]
Boiling point (101.325 kPa)	100.00° C[71]	101.42° C[71]
Molecular Weight [g/mol]	18.0152[73]	20.02748[71]

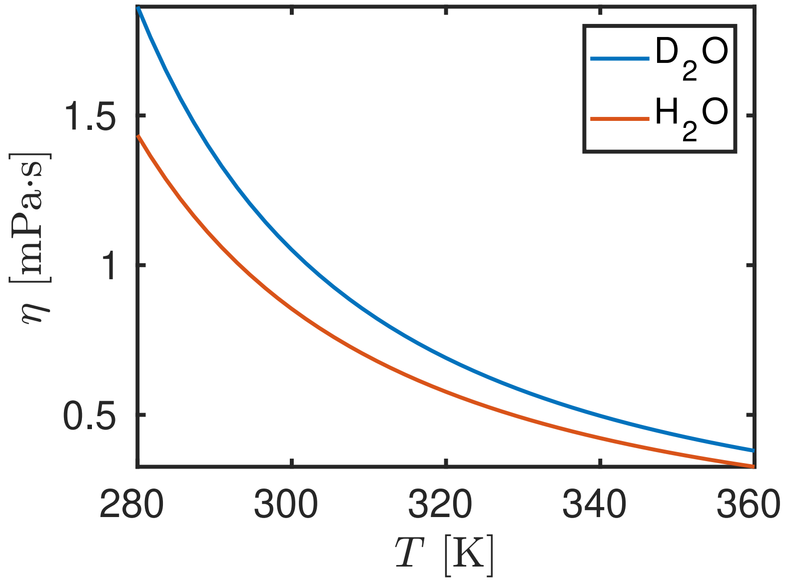

Figure 3.1: *Viscosity of H_2O and D_2O at ambient pressure as a function of temperature. The parametrization is obtained from Cho et al. [74]*

The H_2O - D_2O exchange is often assumed to be negligible and is therefore often used to profit from the differences mentioned above, such as contrast matching in SANS experiments [75, 76] or as a reduction of the solvent signal in NMR studies [77]. However, several studies pointed out that for specific systems, the solvent exchange might lead to significant changes in the phase behavior of the studied samples [32, 78, 79]. Hardy *et al.* [80] investigated water with different hydrogen isotopes and reported influences of this isotope exchange on the rotational and translational diffusion of the investigated molecules. Direct comparisons of samples prepared in H_2O with samples prepared in D_2O might therefore lead to systematic errors, if the system is solvent-sensitive and its response is not taken into account. Especially complex biological systems might react sensitively on the solvent exchange. Kushner *et al.* [81] compiled a review of the biological effects of deuteration. Remarkably, it was shown that deuteration can stabilize proteins [82–85] and render them more resistant against *e.g.* heat induced denaturation [86–88].

3.1.2 Proteins

Proteins are large biological molecules. Although based on the same building blocks called amino acids, their final structure and function can differ significantly depending on the sequence of the amino acids (also called the primary structure of the protein). Due to the chemical properties of the amino acids, specific sequences can arrange into specific three-dimensional structures (secondary structure) such

(a) Structure of BSA based on PDB 3v03 [90]

(b) Structure of BLG based on PDB 1cj5 [91]

(c) Structure of OVA based on PDB 1OVA [92]

(d) Structure of Ig based on PDB 1IGY [93]

Figure 3.2: *Cartoon plots of the monomeric proteins based on the PBD structures. Plots are generated with Jmol [94]. The different plots are not to scale. Different radii are listed in Table 3.2.*

as α-helices or β-sheets. These different secondary structures arrange in space and form the tertiary structure. If a protein contains more than one amino acid chain, the arrangement of these different chains is denoted quaternary structure.

While the majority of proteins has a well defined structure, other proteins, *e.g.* α-synuclein, possess an amino acid sequence, parts of which result in non-self-stabilizing structures. This leads to flexible domains of the proteins. These proteins are called intrinsically disordered. Roughly 10-35% of prokaryotic proteins are estimated to be at least partly disordered [89].

In contrast, the proteins used in this thesis have a stable structure. Schematic representations of the different proteins are displayed in Figure 3.2. The secondary structures α-helices and β-sheets are displayed in magenta and yellow, respectively. The different proteins have various properties which are described in the following. Some of their physical properties are listed in Table 3.2.

For the sample preparation, two different methods were applied. For samples which are considered to be in a stable state and do not change with time, a specified mass of protein m_p was obtained by using a balance. Afterwards, a volume V of

Table 3.2: Selected physical properties of the proteins.

	BSA	BLG	OVA	Ig
number of amino acids	433 [90]	162 [95]	386 [92]	434 [93]
Volume [nm^3] [96]	180.0	25.0	58.6	205.8
percentage of β sheets [96]	0	40	32	49
percentage of helices [96]	74	16	32	6
radius of gyration [nm]	2.76 [97]	2.04 [97]	2.31 [97]	2.60 [98]
isoelectric point	4.7 [99]	5.1 [100]	4.85 [101]	6.6-8.2 [102]

the solvent was added to dissolve the protein, resulting in a nominal concentration

$$c_p^{nom} = \frac{m_p}{V}. \tag{3.1}$$

In the case of solutions with salt, the protein was first dissolved in a volume V_1 while the volume $\Delta V = V - V_1$ is added from the salt stock solution. V_1 is chosen such that the desired salt concentration is obtained. In all cases, roller mixers were used to obtain homogeneous solutions.

For samples which evolve over time, protein stock solutions were used for preparation. This method is applied for the crystallizing samples analyzed in Chapter 9 and Appendix A. Their protein concentration was determined using UV-Vis spectroscopy. The obtained real protein concentration c_p^{real} is linked to the nominal concentration *via* the specific volume ν_p of the protein:

$$\varphi = c_p^{real} \cdot \nu_p = \left(\frac{c_p^{nom}}{1 + c_p^{nom} \nu_p} \right) \cdot \nu_p \tag{3.2}$$

with φ being the dry volume fraction. By using stock solutions, the sample preparation can be performed directly in the sample holder and no transfer of the sample into the sample holder is necessary. In this case, samples were homogenized by using a magnetic stirrer or by pipetting.

BSA

Bovine serum albumin (BSA) is a predominant protein in the blood serum of cattle. Having a high solubility, it acts as transport protein for molecules such as fatty acids, drugs and hormones but regulates also the osmotic pressure and the pH [103].

Due to its similarity to the human analogue (76% similarity [104]) and due to its good availability and low cost [103] it is often used as standard test protein.

Its interaction with metal ions has been extensively studied with different techniques. Alhazmi *et al.* [105] investigated binding sites of BSA for Ca^{2+}, Ba^{2+}, Ag^{+}, Ru^{3+}, Cu^{2+} and Co^{2+} using FT-IR Spectroscopy. Yu *et al.* [106] used the binding ability of BSA to Co^{2+}, Cu^{2+}, AuCl_4^- and Fe^{2+} to construct graphene based membranes which might be used in the future for water purification or ion detection. Guo *et al.* [107] recently reported changes in the secondary structure of BSA induced by binding of Ca^{2+} ions. Medda *et al.* [108] investigated the surface charge of BSA as a function of different monovalent salts.

Roosen-Runge *et al.* [109] investigated the volume fraction dependence of the short-time self-diffusion of BSA. A good agreement between theory and experiments was found assuming an effective volume fraction. The volume fraction dependence is shown in Figure 3.3a. Grimaldo *et al.* [33] investigated the short-time self-diffusion of BSA in the presence of YCl_3 with NBS. They found a salt-induced slowing down of the diffusion due to cluster formation which can be expressed as a function of salt ions per protein (Figure 3.3b). Soraruf *et al.* [23] observed a similar slowing down for the same system while investigating the long time collective diffusion with DLS.

Grimaldo *et al.* [64] and Hennig *et al.* [111] explored the short-time self-diffusion as a function of temperature crossing the denaturation temperature (see Figure 3.3c). At temperatures below the denaturation, the diffusion coefficient increases according to the Stokes-Einstein temperature dependence. Once the denaturation temperature is crossed, a significant slowing down can be observed in the diffusion coefficient, pointing to structural changes and network formation in the samples.

Fu *et al.* [88] investigated the influence of the solvent effect (D_2O, H_2O) on the denaturation of BSA by using circular dichroism. They observed an upshift of the denaturation temperature by 8 K when they changed from H_2O to D_2O indicating a stabilization of the protein at ambient temperatures. However, at elevated temperatures, they observed cluster formation in the case of D_2O as solvent, which was not observed in the H_2O samples.

In the presence of multivalent ions in the solution, BSA has a rich phase diagram including a reentrant phase separation as well as a temperature-dependent LLPS with a lower critical solution temperature (LCST). In several studies the effect of different salts [26, 27, 30] and temperature [34] were investigated.

Already in 1973, Kaneshina *et al.* [112] reported an increasing number of bound detergent ions to BSA with increasing hydrocarbon chains based on equilibrium dialysis and surface tension measurements. The interactions of BSA with different surfactants were studied with SAXS [113] and ultra-violet difference spectroscopy as well as with microcalorimetry [114]. Also the interaction with drugs [115] and other proteins [116] was studied.

Other studies focus on the interaction and on the properties of nano-particles in presence of BSA. Due the optical properties of the nano-particles, these approaches offer access to new applications in diagnostics and other pharmaceutical applications [28, 117, 118].

In addition, the protein absorption was studied on different surfaces and in presence of different cosolutes with different techniques [25, 119].

For the research presented in this thesis, BSA was purchased from Sigma-Aldrich (Merck A3059: heat shock fraction, protease free, essentially globulin free, pH 7, $\geq$ 98% purity) and used without further purification. In this thesis, BSA is used in Chapter 4, Chapter 5 and Chapter 8.

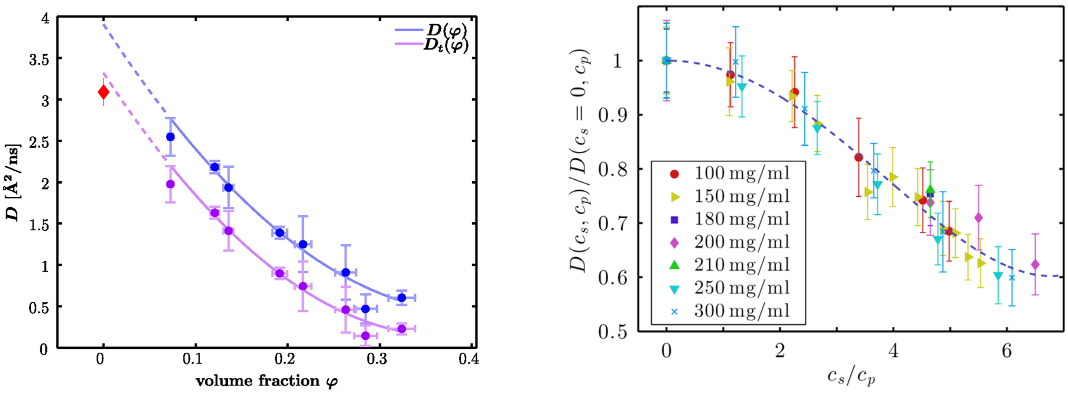

(a) *Short-time self-diffusion of BSA as a function of the volume fraction. Blue and purple points represent the experimental results of the apparent diffusion coefficient and the translational diffusion coefficient separated from the effective one by calculating the theoretical rotational diffusion coefficient, respectively. The red diamond represents the dilute limit of the translational diffusion. All points were measured at 280 K. Figure from Ref. [110].*

(b) *Normalized short-time self-diffusion coefficient as a function of salt ions (Y^{3+}) per protein. All measurements were performed at 295 K. As a normalization factor, the diffusion coefficient of dissolved BSA with the same protein concentration without salt was used. Figure from Ref. [33].*

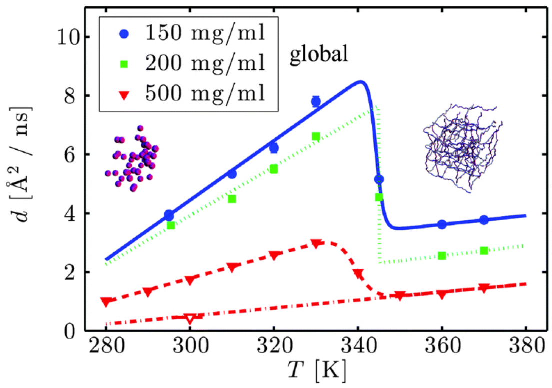

(c) *Short-time self-diffusion coefficient as a function of temperature crossing the denaturation temperature for different protein concentrations. Figure from Ref. [64].*

Figure 3.3: *Dependencies of the short-time self-diffusion of BSA on several control parameters.*

Ig

As an additional protein, γ-globulin from bovine blood (Ig) is used in this thesis. Igs are large proteins acting as antibodies in living organisms. Their quaternary structure consists of two light and two heavy chains which are connected *via* disulfide bridges and form a Y-shaped structure. As an antibody, it has the ability to bind specific antigens. As can be seen in Figure 3.2d, it consists mainly of β-sheets. It should be emphasized that the Ig used are not monoclonal but are a mixture of polyclonal different types of immunoglobulins. Since the overall structure of the different immunoglobulins is similar, their global dynamics can be investigated by assuming only one type of tracer molecule. Also, the overall internal dynamics should be comparable between different immunoglobulins. Besides its unambiguous role in the health system of mammals, specially designed antibodies can be used in medical applications such as targeting cancer cells or as vaccines.

Grimaldo *et al.* [120] investigated the short-time self-diffusion as a function of the volume fraction (Figure 3.4, top). Similar to the case of BSA [109], a good agreement with the translational short-time self-diffusion can be observed, if an effective volume fraction is used (Figure 3.4, bottom). No cluster formation is observed in this mixture of polyclonal Ig.

If polyethylene glycol (PEG) is added to the solution, the proteins can separate into a protein rich and a protein poor phase, due to depletion interactions [121]. At high temperatures, the solutions are homogeneous and phases separate if they are cooled down. This upper critical solution temperature (UCST) is therefore in contrast to the LCST behavior observed with multivalent salts and BSA, which were described in the previous subsection. If the temperature is quenched far enough into the phase separation regime, certain sample conditions can end up in an arrested state. The structural evolution can be followed with techniques such as USAXS and VSANS [121] or with X-ray photon correlation spectroscopy (XPCS) [122].

For this thesis, Ig was purchased from Sigma-Aldrich (Merck, G5009: $\geq$99% agarose gel electrophoresis) and used without further purification. Analyzed data is presented in Chapter 6 and Chapter 7.

BLG

Another protein investigated in this thesis is β-lactoglobulin (BLG). Similar to BSA, it serves as a transport protein and has several binding sites [123]. It is the major whey protein in milk of ruminants [124] and mainly involved in the transport of hydrophobic molecules [125]. A pH dependent structural change offers access to a binding site for retinol [124, 126, 127].

Anghel *et al.* [125] investigated the structural changes with SANS and SAXS of BLG as a function of pH and salt concentration (NaCl).

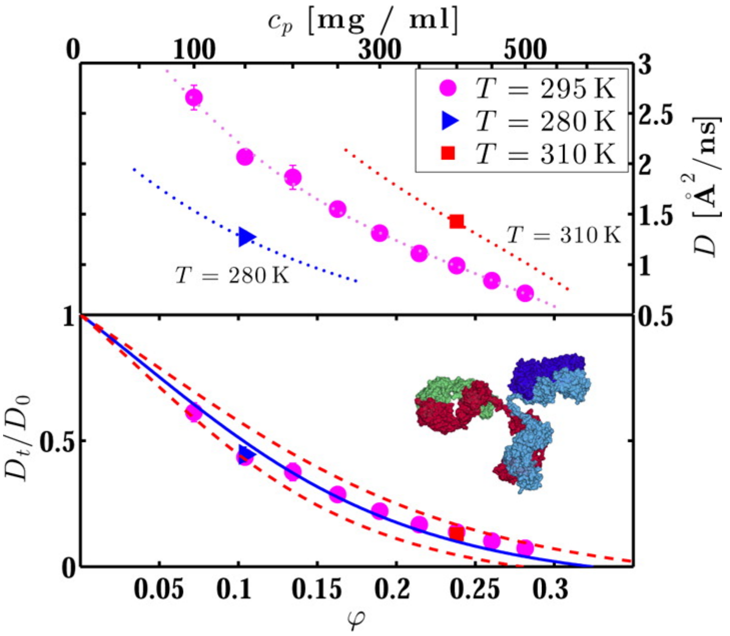

Figure 3.4: *Short-time self-diffusion coefficient of Ig as a function of the volume fraction. Figure from Ref. 120.*

Zhang *et al.* [123] investigated the simultaneous binding of different ligands to the protein. Sardar *et al.* [128] were able to control the aggregation behavior of BLG by adding silver nanoparticles. They observed a specific binding site for the nanoparticle inducing a rod-like aggregation.

A model describing the kinetic pathway of thermal denaturation was developed by Tolkach *et al.* [129]. They also investigated the influence of the heat treatment time onto the different states of the denaturation. Dumay *et al.* [130] investigated pressure induced unfolding of BLG and reported that the addition of sucrose to the solution stabilizes the protein.

Braun *et al.* [131] investigated the short-time self-diffusion as well as the short-time collective diffusion of BLG as a function of the volume fraction with NBS and NSE, respectively. By comparing the results with results from SAXS, a crowding induced cluster formation could be observed. By comparing the short-time self-diffusion with theoretical predictions, such a cluster formation is also already visible (Figure 3.5).

Similar to BSA, the system is characterized by a reentrant phase diagram, if multivalent salts (such as $CdCl_2$, $ZnCl_2$ or YCl_3) are added. In contrast to the LCST-LLPS observed for BSA, in the case of BLG, the system is characterized by a UCST [132]. In addition to the LLPS behavior, also crystallization can occur in these systems [41, 133, 134]. By carefully adapting the protein concentration, salt concentration and temperature, the crystallization pathway, its speed and also the final crystal structure can be modified. Within the framework of this thesis, different crystallization conditions in aqueous (D_2O) solutions in the presence of $ZnCl_2$

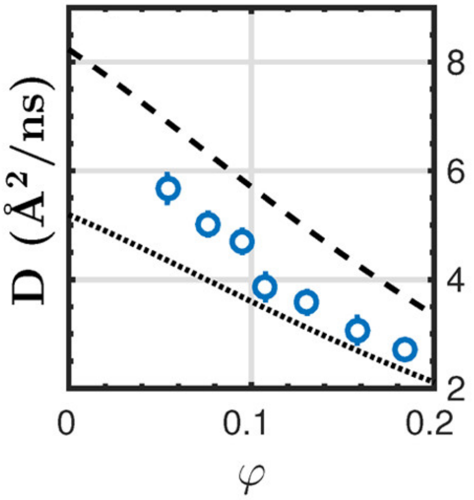

Figure 3.5: *Short-time self-diffusion coefficient of BLG as a function of the volume fraction. Dashed and dotted lines describe the volume fraction dependencies of dimers and tetramers, respectively. The measurements were performed at 295 K. Figure taken from Ref. 131.*

were determined to obtain sufficiently slow crystallizing samples for the neutron experiments. For some samples, it was found that the crystallization process could be triggered by lowering the temperature. One sample was stable at 295 K and crystallized when the temperature was lowered to 280 K. In the presence of $CdCl_2$, no such temperature dependence was observed. On the one hand, certain conditions (*e.g.* BLG $c_p = 100\,\frac{\text{mg}}{\text{ml}}$, $c_s = 35\,\text{mM}$ $ZnCl_2$) were found with crystals having the same Bragg peaks as the ones of BLG crystals grown in $CdCl_2$ solutions as already reported by Sohmen [135]. On the other hand, slight deviations on the salt concentrations (BLG $c_p = 100\,\frac{\text{mg}}{\text{ml}}$, $c_s = 20\,\text{mM}$) can result in different Bragg peak positions as the one presented in Chapter 9 (Ref. 136). Further studies might focus on the effect of salt concentration and temperature on the crystallization behavior. BLG, used in this thesis, was purchased from Sigma-Aldrich (Merck; L3908: $\geq$90% (PAGE), lyophilized powder) and used without further purification and was used in Chapter 7, Chapter 9 and Appendix A.

OVA

Ovalbumin (OVA) has early been subject of investigation due to the fact that it can be extracted from eggs as shown by Kekwick *et al.* [137]. Its self-diffusion has been investigated with NMR [138, 139]. The influence of pH on the volume of OVA [140] has also been investigated as well as the influence on the mobility determined with electrophoresis [141]. The influence of ionic strength on the diffusion was investigated with gel electrophoreses by Johnson *et al.* [142] and with SAXS by Ianeselli *et al.* [143]. In both cases the results were compared with data from BSA.

Scott *et al.* [144] investigated OVA solutions with different methods (DLS,

Table 3.3: *Properties of the different cations used in the thesis.*

Cation	Y^{3+}	La^{3+}	Zn^{2+}	Cd^{2+}
Charge in solution	3+	3+	2+	2+
Coordination number	8.0[155]	9.1[156]	6[155]	6[155]
Ionic radius [Å]	1.019 [155]	1.250[156]	0.740[155]	0.95
Used in Chapter	8,B	8	9	A

analytical ultracentrifugation and SAXS), after several SAXS studies reporting dimers [143, 145–147] published contradicting results from static light scattering (SLS) [148] and analytical ultracentrifugation [149–151] which observed monomeric OVA in solutions.

McKenzie *et al.* [152, 153] compared the urea induced denaturation of OVA with BSA by sedimentation, viscosity and diffusion measurements as well as with measurements of the optical rotation and gelation and UV absorption. Fourier Transform Raman Spectroscopy was used to study differently treated OVA (heat, pressure) and compared with the results of BLG [154].

OVA was purchased from Sigma-Aldrich (Merck; A5503: lyophilized powder, ≥98% (agarose gel electrophoresis)) and used without further purification. It was used in Chapter 7.

3.1.3 Multivalent Salts

In several studies multivalent salts were added to the protein solutions. Table 3.3 shows the salts used with some selected properties. Different multivalent salts interact in various ways with the proteins. General properties of the protein salt interactions and properties of the resulting phase diagrams are reviewed in Section 1.2.2 as well as in Chapter 8, Chapter 9 and Appendix A. Detailed comparisons of the trivalent salts are given by Matsarskaia [31]. The salts were purchased from Sigma Aldrich with guaranteed purities of 97% for $ZnCl_2$(96468), 99.99% for $CdCl_2$(202908) and 99.99% for YCl_3(451363). For the study in Chapter 8, YCl_3 (18682, 99.9% purity) and $LaCl_3$ (87911, anhydrous, 99.9% purity) were purchased from Alpha Aesar.

3.2 Instrumentation

The aim of this section is to give a short overview of the used techniques. A brief overview is given here, more detailed description can be found *e.g.* in Refs. 46, 48.

3.2.1 Neutron Production

Different neutron scattering techniques are employed in this thesis to investigate specific properties of the samples. Neutrons can be obtained from different sources in a sufficiently high flux for neutron scattering. The two principal methods, both used in this thesis, are presented in the following sections.

Reactor Based Neutron Sources

In reactor-based neutron sources, nuclear fission reactions are used to produce neutrons. Having absorbed a neutron, heavy nuclei decay into lighter fission products. Several fissile nuclei are known, such as ^{233}U, ^{235}U, ^{239}Pu or ^{241}Pu [157]. In the case of ^{235}U, used at the Institut Laue-Langevin (ILL), the uranium which has captured a neutron can decay to different fission products, *e.g.*

$$\mathrm{n}+{}^{235}\mathrm{U}\rightarrow{}^{236}\mathrm{U}^{*}\rightarrow{}^{134}\mathrm{Xe}+{}^{100}\mathrm{Sr}+2\mathrm{n}.$$

Alternative decays of ^{236}U* lead to an average release of 2.5 neutrons per decaying uranium isotope. The neutrons released by the fission process have a kinetic energy which is more than a factor 1000 too high to induce a new fission. To obtain a self-sustaining reaction, the neutrons have to be slowed down by collisions with other light atoms *e.g.* from graphite or from heavy water. The absorbed heat energy ($\sim$ 180 MeV per fission process) [48] has to be guided away from the core. The neutrons are thus slowed down and their energy distribution can be described by a Maxwell distribution (see Section 2.2) with an averaged moderator temperature of $T\approx$ 300 K. If neutrons are needed with different energy distributions, additional moderators can shift the Maxwellian distribution to lower temperatures (D_2, $T_M \approx$ 25 K) or higher temperatures (graphite, $T_M \approx$ 2000 K)[44].

Recent research reactors reach neutron fluxes up to $\Phi \approx 10^{15}\,\frac{\mathrm{neutrons}}{\mathrm{s\cdot cm^2}}$ [54, 158].

Spallation Neutron Sources

Since the neutron flux at reactors is limited by fundamental principal constraints such as the heat removal rate and operating safety considerations [157], pulsed sources can be constructed, which overcome some of these problems. The produced heat can be removed within the “dark time” where no neutrons are produced. By using either liquid or rotating targets, it is possible to obtain a significantly higher neutron peak flux. For the neutron production, protons coming from an accelerator are guided onto the target, often having a pulsed time structure. The metallic target, absorbing the neutron, “boils-off” particles. Among them, there are roughly 20 neutrons per fission process [159]. The different spallation products are separated from each other by different methods. Later, the neutrons are moderated similarly to the ones in the reactor based neutron source. Given the pulsed structure of the neutron beam, the instruments can be optimized by using the pulse as starting point for TOF-instruments.

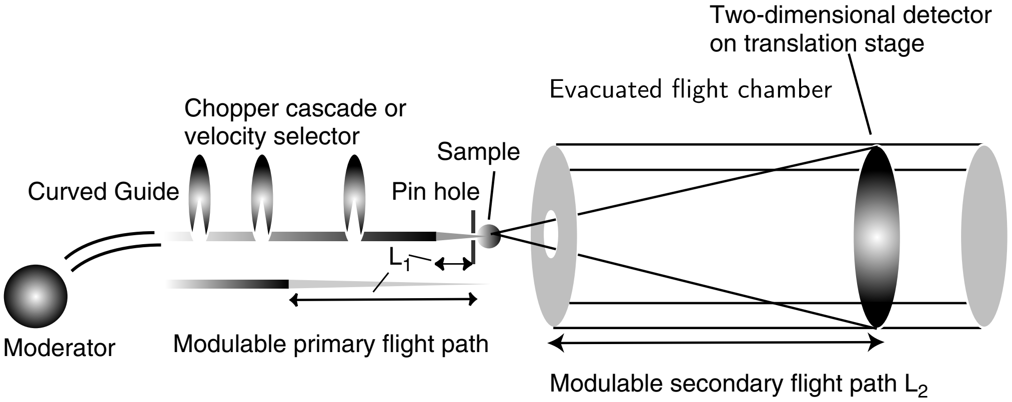

Figure 3.6: *Schematic setup of a SANS beamline. Figure modified based on Ref. 159.*

3.2.2 Small Angle Neutron Scattering

Small angle neutron scattering (SANS) probes the structure of inhomogeneities on the nanometer length scale and offers access to the size and shape as well as to the interactions between the particles [159]. In Figure 3.6, the general layout of a SANS instrument is shown. After being guided through a curved guide, blocking fast neutrons and γ-radiation from the reactor core, the thermal neutrons undergo a velocity selection *via* a chopper system or a velocity selector. The neutron beam is shaped by a collimation system and then guided onto the sample. After being scattered, the neutrons travel through an evacuated flight chamber before they hit the detector, where they are detected. By changing the sample-to-detector distance, the observed q range can be changed. While classical SANS measurements are preformed with a relatively well defined energy of the incoming neutrons, in a second mode, short pulses of a white neutron beam can be used to operate a SANS instrument in a so called TOF mode. By using the TOF in the secondary spectrometer, the neutron energy and therefore their wavelength can be determined. At the same detector pixel, different q values are then detected as a function of time. This mode offers access to larger q ranges without moving the detector. By using additional detector panels, the covered q range can be extended even further [160].

Since the interatomic distances are smaller than the investigated length scales by SANS, an averaged scattering length density $\rho(\vec{r})$ can be used. The scattered amplitude $A(\vec{q})$ can be expressed by integrating over $\rho(\vec{r})$ respecting its phase.

$$A(\vec{q}) = \int \rho(\vec{r}) \exp\left(-i\vec{q}\cdot\vec{r}\right). \tag{3.3}$$

The principal theoretical background is given in Section 2.3.2. For more detailed descriptions, literature *e.g.* by Kline *et al.* [161] or Baruchel *et al.* [158] can be consulted. SANS measurements are performed for the crystallizing samples presented in Chapter 9.

3.2.3 Neutron Spin Echo Spectroscopy

Neutron spin echo (NSE) spectroscopy, invented in 1972 [162] takes advantage of the neutron spin. By guiding a polarized neutron beam through a magnetic field $\vec{B}$ perpendicular to the magnetic moment of the neutron, the latter performs a Lamor precession with a Larmor frequency $\omega_l = \gamma_n B$ with the gyromagnetic ratio of the neutron $\gamma_n = -1.913\mu_n$ [163]. A schematic view of a NSE spectrometer is shown in Figure 3.7. Since neutrons passing the polarizer have a spin parallel to the propagation vector, a $\pi/2$ flipper is used to obtain a neutron beam with a polarization which is orthogonal to $\vec{k}$. A neutron which is guided through opposite magnetic fields before and after the scattering process with the sample will therefore have a phase shift φ of [164]

$$\varphi = \frac{B_1 l_1}{v_1} - \frac{B_2 l_2}{v_2} \tag{3.4}$$

with l_i being the length where the magnetic field B_i is applied. In the case of elastic scattering ($v_1 = v_2 = v$) and in the case of identical absolute magnetic fields ($l_1 = l_2 = l$ and $|B_1| = |B_2|$) the phase-shift returns to zero independently from the incoming energy. However, field inhomogeneities lead to a decay of the (elastic) scattering signal, resulting in observable Fourier times up to several hundred nanoseconds [166].

In case of an energy shift $\hbar\omega$, the phase shift results in

$$\varphi = \frac{\hbar\gamma_n B l}{m_n v^3}\omega. \tag{3.5}$$

By analyzing the scattered neutrons with another polarizer, the probability that the neutron passes the analyzer and reaches the detector is equal to $\cos(\varphi)$. Averaging over all energy transfers leads to the total measured scattering signal:

$$\langle\cos(\varphi)\rangle = \frac{\int \cos\left(\frac{\hbar\gamma_n B l}{m_n v^3}\omega\right) S(q,\omega)\mathrm{d}\omega}{\int S(q,\omega)\mathrm{d}\omega} = s(q,t). \tag{3.6}$$

NSE measures, thus, directly the intermediate scattering function with $t = \frac{\hbar\gamma_n B l}{m v^3}$. In the event that the neutron polarization changes during the scattering process, the given equation has to be modified [167]:

$$P_{NSE} = P_S\langle\cos(\varphi)\rangle = P_S\frac{\int \cos\left(\frac{\hbar\gamma_n B l}{m_n v^3}\omega\right) S(q,\omega)\mathrm{d}\omega}{\int S(q,\omega)\mathrm{d}\omega} \tag{3.7}$$

As shown by Williams [168], $P_S = -1/3P_0$ with P_0 being the polarization of the incident beam for incoherent scattering samples.

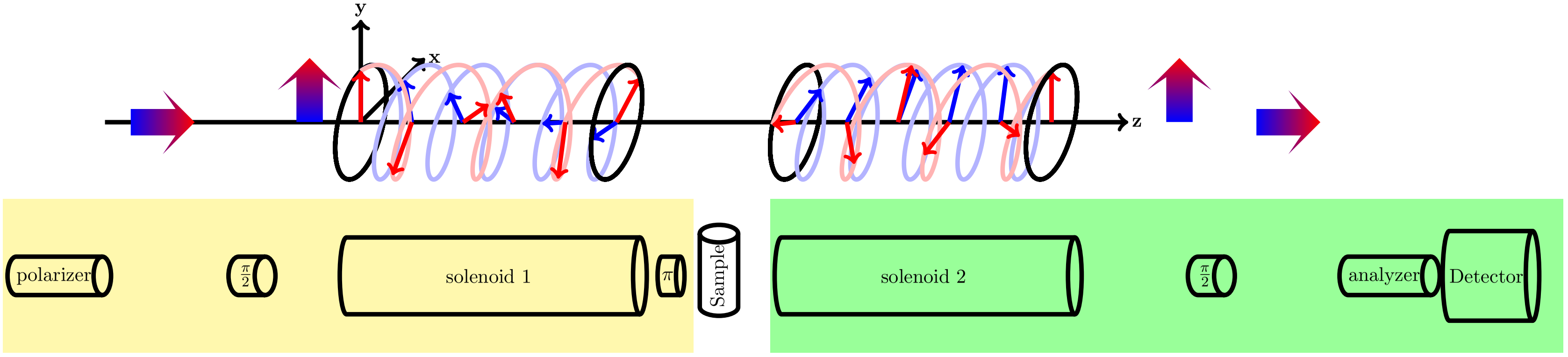

Figure 3.7: *Schematic view of a neutron spin echo spectrometer.*
The arrows in the upper part show the spin-state of different neutrons while passing the instrument. A polychromatic beam (indicated with the arrows with color-gradient) passes a polarizer, selecting only neutrons whose spin is parallel to the propagation direction. A $\frac{\pi}{2}$ *flipper rotates the spins in such a way, that they are orthogonal to the propagation direction. The neutrons then pass the first solenoid. Fast neutrons (color-coded in red) perform less Lamor precessions than the slower ones (blue). A* π *flipper rotates the spin for 180° before the neutrons interact with the sample. This allows to use a second solenoid behind the sample, whose magnetic field is oriented in the same direction as the one of the first solenoid. While at the sample position, no polarized beam exists, a (partly) polarized beam is achieved again after passing the second solenoid in the case of purely elastic scattered neutrons. A second* $\frac{\pi}{2}$ *flipper is used to flip the spin of the neutrons. In case of elastically scattered neutrons and similar solenoids, the initial polarization is obtained. A second spin selection similar to the one of the polarizer is used to analyze the neutrons with spin parallel to the propagation. The neutrons who have passed the analyzer are then detected in the detector.*
The lower part represents the different building blocks of the instrument. By rotating the secondary spectrometer (green shaded) around the sample position, different scattering vectors q *can be investigated. Figure reproduced and modified from Refs 164, 165.*

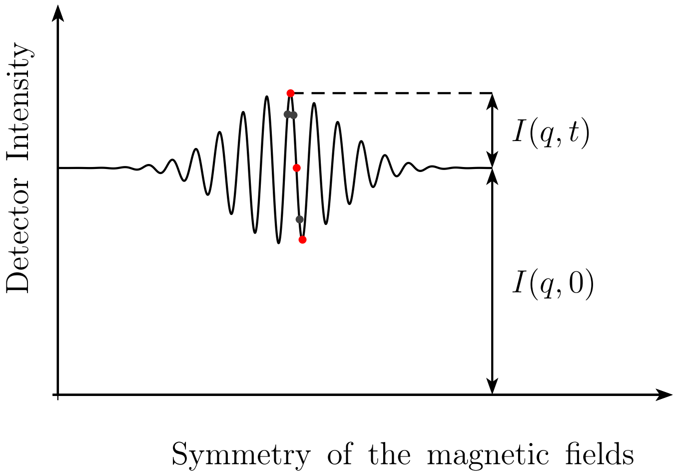

Figure 3.8: *Schematic representation of the spin echo group. To obtain one point of the intermediate scattering function, several points of the echo (marked in red) have to be measured. Several points (grey) can be added to be more robust against external influences. Reproduced and modified from Ref. 170.*

For $P_0 = 1$, the total detected scattering signal $s(q,t)$ therefore results in [169]

$$s(q,t) = \frac{S_{coh}(q,t) - \frac{1}{3}S_{inc}(q,t)}{S_{coh}(q,t=0) - \frac{1}{3}S_{inc}(q,t=0)}. \tag{3.8}$$

To measure the intermediate scattering function as a function of the scattering vector q, the secondary spectrometer (marked in green in Figure 3.7) is rotated around the sample. Due to the changing scattering angle, the corresponding scattering vector changes according to Equation 2.4. To investigate the time dependence, it is necessary to slightly change the symmetry of the magnetic field and therefore scan through the echo group (see Figure 3.8). At least two points have to be measured to obtain the intermediate scattering function. To be less sensitive to external influences, usually three or four measurements are performed [164]. Theoretical models to describe the intermediate scattering function are given in Section 2.4. The envelope of the echo signal is given by the Fourier transform of the wavelength distribution [169]. NSE measurements are used to access the collective diffusion during the protein crystallization described in Chapter 9 and in Appendix B investigating the collective diffusion of BSA with increasing YCl_3 concentration at constant temperature.

3.2.4 Neutron Backscattering

The previous section described a method which investigates the intermediate scattering function by profiting from the neutron spin. This section focuses on another type of instrument which can be used to investigate the QENS. Neutron backscattering (NBS), which uses mainly the neutron velocity, and therefore its energy, can also be used to probe the total scattering function. Different types of spectrometers are available for performing the NBS experiments. Their differences and characteristics are explained in this section.

General Layout

Similar to the NSE spectrometer, the NBS spectrometers can be divided into primary and secondary spectrometers. While the general layout of the secondary spectrometer is very similar for the different NBS spectrometers, the layout of the primary spectrometers differs and mainly influences the instrument properties. The primary spectrometer defines and varies the incoming energy of the neutrons on the sample, while the secondary spectrometer analyzes the neutron energy and only detects the neutrons with one specified energy. Knowing the energy difference between the incoming neutrons and the detected ones, it is possible to determine the energy transfer.

Different types of primary spectrometers are displayed in Figure 3.9 and will be discussed in the following paragraphs.

Backscattering Crystal Monochromator Primary Spectrometer

The first type of primary spectrometers defines the energy of the incoming neutrons with a monochromator using the Bragg reflection of a crystal. Having a certain divergence $\Delta\Theta$, the reflected neutron beam will have an energy resolution depending on this divergence as well as on the crystal lattice constant τ and its corresponding uncertainties. In addition, different flight paths L result in different flight times t_f influencing the final energy resolution [171, 172]:

$$\frac{1}{2}\frac{\Delta E}{E} = \frac{\Delta\lambda}{\lambda} = \frac{\Delta k}{k} = \sqrt{\left(\frac{\Delta\tau}{\tau}\right)^2 + (\Delta\Theta \cdot \cot\Theta)^2 + \left(\frac{\Delta t_f}{t_f}\right)^2 + \left(\frac{\Delta L}{L}\right)^2} \tag{3.9}$$

Simpler instrument geometries can be achieved by deviating from the perfect backscattering geometry ($\Theta = 90°$). As shown in Figure 3.9a, this deviation can be quantified by another angle ε. However, since Θ is replaced by $(\Theta + \varepsilon)$ in Equation 3.9, this deviation contributes to the energy resolution. By minimizing ε, the second term of Equation 3.9 vanishes. This geometry can only be achieved if a reflecting chopper is used as shown in Figure 3.9b. The chopper can also serve as a phase space transformer, which increases the divergence of the neutron beam, but simultaneously increases the neutron flux at the sample position [173]. While the layout represented in Figure 3.9a can be used with a continuous neutron flux at the sample position and analyzers are oriented in such a way that the detectors cannot capture neutrons directly scattered from the sample, the layout from Figure 3.9b already offers a pulsed beam at the sample position which can be used to select analyzed neutrons *via* TOF.

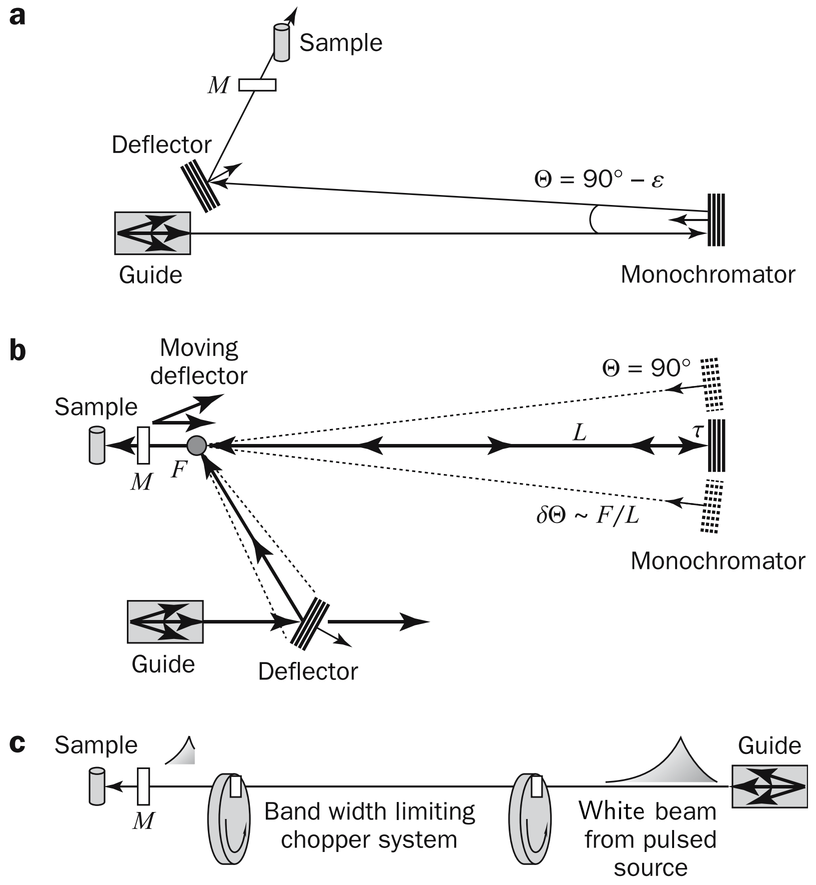

Figure 3.9: *Schematic drawings of different primary backscattering spectrometers for neutron backscattering instruments. Figure modified from Ref. 171.*

Time of Flight Primary Spectrometer

Besides the primary spectrometers which use crystals to obtain a monochromatic beam, the non-relativistic velocities of the neutrons can be used to obtain neutrons with a specified energy. Therefore, a first chopper system is used to obtain a pulsed white neutron beam. Due to the dispersion relation, the neutrons pass the distance to the second chopper with different flight times. By adapting the phase of the second chopper, it is possible to select only neutrons with a specified neutron energy. Since no monochromator crystal is used, the first two terms in Equation 3.9 do not exist for this type of primary spectrometer. At pulsed sources, the first chopper system is in principle already given by the source itself.

Secondary Spectrometer

The aim of the secondary spectrometer is to detect only neutrons with a specified energy. In addition, dependence of the scattering function on the scattering vector q is of great interest. To obtain the desired information, analyzer crystals

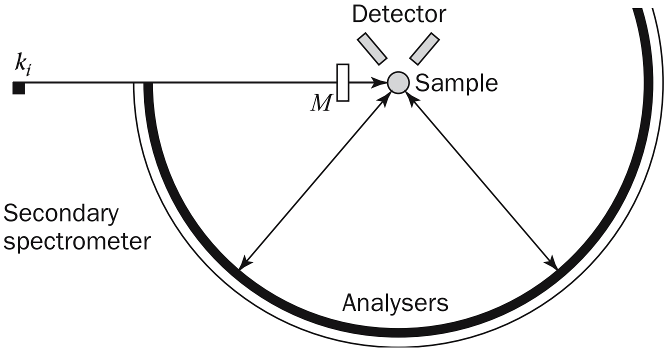

Figure 3.10: *Schematic drawing of a classical secondary backscattering spectrometer for neutron backscattering instruments. Typical sample to analyzer distances is in the order of two meters. Figure taken from Ref. 171.*

are positioned around the scattering sample covering a large fraction of the solid angle. By positioning the crystals on a spherical surface with the sample in the center (Figure 3.10), it is possible to approach the backscattering condition. In case of pulsed neutron beams, the backscattering condition can be fulfilled since neutrons being scattered directly into the detector can be separated from the analyzed ones by the time of flight. For continuous neutron beams the analyzers can be positioned in such a way that the neutrons do not pass a second time through the sample. The energy resolution of the secondary spectrometer can be described similarly to the primary spectrometer with Equation 3.9. Mainly the first two contributions are important for the secondary spectrometer. Depending on the desired resolution, the vertical temperature gradient has to be adapted to compensate the influence of gravity on the neutrons [174].

Types of Spectra

The different primary spectrometers result in various NBS spectrometers with their own characteristics. In the following section, different types of spectra are presented.

TOF-Spectra with Choppers: By using choppers to define the incoming neutron energy, it is possible to investigate non-centered energy transfer windows if the phases between the two choppers are varied [175]. In addition, the energy resolution can be adapted if different slit widths are available on the choppers [66]. By accepting slightly worse energy resolutions, it is possible to measure energy transfers up to the meV energy range. While spectrometers located at pulsed spallation sources can be optimized to use as many neutrons as possible and profit from the pulsed beam structure [172], spectrometers installed at continuous reactors can profit from the higher flexibility [66, 175].

Since the energy of the detected neutrons is fixed by the analyzer crystals, the flight-time of the neutron in the secondary spectrometer can easily be calculated. Given the pulsed structure of the beam, it is then also possible to determine the energy of the neutron before the scattering event and thus also the energy transfer. It is therefore crucial to obtain the time dependence of the detected neutrons with respect to the time t_0 defined by the choppers. TOF-backscattering spectra analyzed in Chapter 4 and in Chapter 8 are collected on BATS and on BASIS, respectively.

Spectra Using Monochromator Crystals: Alternatively to the use of choppers, crystals can be used to obtain a monochromatic neutron beam. If applied in the backscattering geometry, this option allows higher energy resolutions than primary spectrometers which only use choppers to define the incoming energy. To vary the incoming energy, several options can be used, which are presented in a schematic view in Figure 3.11.

1. If the monochromator crystal can be moved, the energy of the neutrons guided onto the sample can be modified by using the longitudinal Doppler effect [176, 177]. The neutrons are reflected on the moving crystal, where the effective crystal lattice of the crystal changes as a function of the crystal speed. Using a sinusoidal velocity profile, it is possible to observe a quasi-continuous QENS spectrum with energy offsets up to $\Delta E = 30\,\mu\text{eV}$ on IN16B [176]. At least one chopper is needed for the design to avoid frame overlaps in the spectra. This operating version is shown in blue in Figure 3.11. Data collected with this classical set-up of IN16B are analyzed in Chapter 7 and Chapter 9.

2. In case the monochromator crystal is not moved, elastic fixed window scans (EFWSs) can be performed by using identical crystals for the monochromator and for the analyzers. Compared to the full NBS spectra, significantly less information is contained in the measured spectra, but the measurement time is significantly reduced. To measure neutrons with one fixed energy transfer, i.e. by a so called inelastic fixed window scan (IFWS), the monochromator crystal can be moved with a zigzag-like displacement profile d_{mono}, resulting in a bimodal neutron velocity distribution centered around the energy characterizing the Bragg reflection on a non-moving crystal. The corresponding velocity profiles are shown in orange and green for the EFWS and IFWS in Figure 3.11, respectively. Methods for the analysis and some experimental examples are shown in Chapter 5.

3. IFWS can also be obtained by using a monochromator crystal with a different crystal lattice spacing. This constant energy offset is due to the different lattice constants. This option is represented in violet in Figure 3.11.

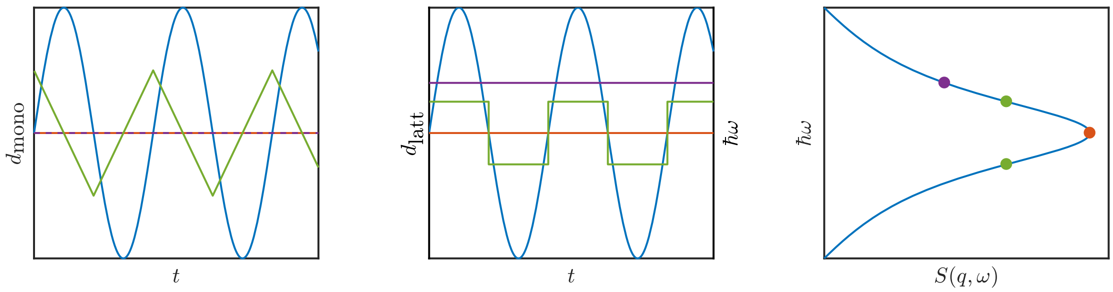

Figure 3.11: *Different operation modes for backscattering spectrometers using a movable monochromator crystal. Blue, violet, green and orange lines represent the operation mode with a sinusoidal velocity profile, a stationary heated monochromator crystal, as well as the ones for IFWS and EFWS respectively. The left subplot shows the displacement profile d_{mono} as a function of time. The effective lattice distance d_{latt} as well as the energy transfer observed by the reflected neutrons is shown as a time dependence in the middle graph. It is assumed to have the same crystals and orientations for monochromator and analyzer. The right subplot shows the detected scattering signal for the corresponding scenario.*

4. Thermal expansion of the crystals changes the lattice distance of the crystals. To measure different energy transfers, the crystal temperature has therefore to be changed. Instruments such as IN13 or the GaAs prototype option for IN16B, both located at the ILL, make use of this technique. Measuring quasi-continuous QENS spectra is therefore time consuming and limiting to discrete energy offsets is of interest. Similar to the method above, where the change in the crystal lattice was achieved by choosing another crystal, this method is represented in violet in Figure 3.11.

In the first part of this chapter, different materials used in this thesis were presented. In the second part of the chapter, the different instruments used and its different measurement techniques were explained.

Chapter 4

Neutron Spectroscopy on Protein Solutions Employing Backscattering with an Increased Energy Range

C. Beck *et al.* [96]

Chapter 4 is based on the following publication:

Neutron spectroscopy on protein solutions employing backscattering with an increased energy range

Christian Beck, Markus Appel, Marco Grimaldo, Felix Roosen-Runge, Fajun Zhang, Bernhard Frick, Frank Schreiber, Tilo Seydel

Physica B: Condens. Matter 562 (2019) 31

DOI:10.1016/j.physb.2018.11.058

Publication Date (Web): March 08, 2018

Contributions:

Research design	MA, BF, TS
Experiments	MA, BF, TS
Data Analysis and interpretation	CB, MA, MG, FRR, BF, TS
Paper Writing	CB, MA, MG, FRR, FZ, BF, FS, TS

Abstract

Novel cold neutron backscattering spectrometers contribute substantially to the understanding of the diffusive dynamics of proteins in dense aqueous suspensions. Such suspensions are fundamentally interesting for instance in terms of the so-called macromolecular crowding, protein cluster formation, gelation, and self-assembly. Notably, backscattering spectrometers with the highest flux can simultaneously access the center-of-mass diffusion of the proteins and the superimposed internal molecular diffusive motions. The nearly complete absence of protein-protein collisions on the accessible nanosecond observation time scale even in dense protein suspensions implies that neutron backscattering accesses the so-called short-time limit for the center-of-mass diffusion. This limit is particularly interesting in terms of a theoretical understanding by concepts from colloid physics. Here we briefly review recent progress in studying protein dynamics achieved with the latest generation of backscattering spectrometers. We illustrate this progress by the first data from a protein solution using the backscattering-and-time-of-flight option BATS on IN16B at the ILL and we outline future perspectives.

4.1 Introduction

Proteins in aqueous liquid suspensions are subject to a superposition of their center-of-mass diffusion and their internal diffusive molecular motions. These diffusive motions on the nanometer length scale can generally be well accessed by neutron backscattering spectrometers. When such a backscattering experiment probes protonated tracer proteins dissolved in heavy water (D_2O), the recorded signal from the incoherent scattering of the proteins informs on their self-diffusive dynamics. The complexity of this hierarchically superimposed center-of-mass and internal dynamics in dense aqueous protein solutions has been subject to numerous studies using neutron spectroscopy [33, 64, 96, 111, 120, 131, 178–182]. On the nanosecond time scale observed in a backscattering experiment, the measured protein center-of-mass diffusion corresponds to the colloidal short-time limit, on which protein-protein collisions are negligible and hydrodynamic interactions are dominant [109], providing one of the aspects of the useful complementarity of quasi-elastic neutron scattering (QENS) to nuclear magnetic resonance (NMR) measurements on protein solutions. The center-of-mass diffusion is represented by an observable apparent diffusion coefficient D which is an implicit function $D = D(D_t, D_r)$ of the translational D_t and rotational D_r diffusion coefficients [109, 110]. In the short-time limit, colloid physics models describing the diffusion of hard spheres [58] can be applied to quantitatively understand the dependence of $D_t = D_t(\varphi)$ and $D_r = D_r(\varphi)$ on the volume fraction φ occupied by the proteins in the sample solution [109]. Neutron backscattering experiments have already explored protein solutions in a wide range of protein concentrations from below 50 mg/ml up to above 500 mg/ml [109, 181]. Current topics of interest include for instance the investigation of protein cluster formation [33, 96, 131], the dynamics of intrinsically disordered proteins [179, 183], and thermal unfolding [64, 111]. Moreover, the effect of ion-induced charges in protein solutions has moved into the focus of current research, driven by a mutual inspiration of experiments on the phase behavior of protein solutions tuned by the presence of multivalent salts [23, 33, 184] and the theory of so-called patchy colloids (Refs. [35, 185] and references therein).

The quasi-elastic scattering signal $S(q,\omega)$ from a protein solution depending on the energy transfer ω and magnitude of the scattering vector q can be modeled by [64]

$$\begin{aligned} S(q,\omega) \;=\; & \mathscr{R}(q,\omega) \otimes \{\, \beta(q)\, [\;\; A_0(q)\mathscr{L}(\gamma(q),\omega) + \\ & (1 - A_0(q))\,\mathscr{L}(\Gamma(q) + \gamma(q),\omega)] \\ & + \beta_{\mathrm{D_2O}}(q)\,\mathscr{L}(\gamma_{\mathrm{D_2O}}(q),\omega) \;\; \}\,, \end{aligned} \tag{4.1}$$

where $\mathscr{R}$ is the spectrometer resolution function, β, $\beta_{\mathrm{D_2O}}$ and A_0 are scalars, and $\mathscr{L}$ Lorentzian functions. The symbol $\otimes$ represents the convolution. The Lorentzian widths γ, Γ, and $\gamma_{\mathrm{D_2O}}$ are associated with the center-of-mass and internal diffusion of the proteins and with the D_2O solvent contribution, respectively. $A_0(q)$ is the elastic incoherent structure factor (EISF). $\mathscr{L}(\Gamma(q) + \gamma(q),\omega)$ may be replaced by a more general function such as a generalized model of internal diffusivity [63, 64], the Fourier transform of a Kohlrausch [111, 182, 186, 187] or Mittag-Leffler [188–190] function, or the result of a molecular dynamics simulation, if applicable. In reported backscattering experiments on protein solutions, the apparent center-of-mass diffusion was consistent with simple Brownian diffusion, $\gamma(q) = D\,q^2$ [96, 109, 120, 131].

To best measure $S(q,\omega)$ (Equation 4.1), a good energy resolution to best capture $\gamma(q)$ as well as sufficient ranges in q and ω to access $A_0(q)$ and $\Gamma(q)$ are required, as discussed in the following section.

4.2 Progress in Backscattering Instrumentation

Cold neutron backscattering spectrometers outfitted with Silicon(111) analyzer crystals associated with the elastic wavelength $\lambda \approx 6.27\,\text{Å}$ are ideally suited to observe the short-time center-of-mass self-diffusion and the superimposed internal diffusion. For a good comparison of the experimental EISF to models, a high maximum q of nearly $2\,\text{Å}^{-1}$ as obtained with Si(111) analyzer crystals is very useful. An energy resolution on the order of $1\,\mu\text{eV}$ is required to measure the center-of-mass diffusion. To also access the internal dynamics, a sufficient energy range is additionally needed. Finally, the possibility to simultaneously measure both the center-of-mass diffusion of proteins in rather dilute aqueous solutions and the internal molecular motions of these proteins requires the high flux and good signal-to-noise ratios of the most recent backscattering spectrometers [172, 176, 191–194]. These spectrometers are located at the brightest cold neutron sources [195, 196] and are based on advances in neutron optics such as the phase space transformation in the case of exact backscattering [173] and modern neutron guide layouts [197].

So far, backscattering spectrometers have followed two complementary design concepts: (1) the concept of exact backscattering, where both the monochromator and analyzer single crystal reciprocal lattice vectors are oriented precisely parallel to the neutron optical axis and, thus, achieving the best energy resolution. These instruments are typically located at neutron sources that are continuous in time [191, 193, 198]. The excellent energy resolution in this design comes at the cost of a limited maximum energy transfer range given by the requirement that this transfer can with the current state-of-the-art only be reasonably achieved by carrying out the monochromatizing Bragg reflection in a mechanically moving reference frame. (2) The alternative design concept obtains the wavelength definition of the incident beam at the sample position by the spread with flight time of an initially very brief but polychromatic neutron pulse [172, 191, 199, 200]. This design increases the energy range and comes at the expense of a lower energy resolution compared to concept (1).

The spectrometer IN16B [191, 201] combined with its optional configuration denoted BATS (Backscattering-And-Time-of-flight Spectrometer) [66, 192] for the first time aims at providing both these concepts in one single instrument, where the BATS option represents concept (2). BATS notably provides the possibility to tune the energy range and resolution within certain ranges by changing the chopper settings [66]. For more detailed information we refer to the dedicated article on BATS within this proceedings volume. In the following section we report on the first application of the BATS option to record a QENS spectrum on a protein solution sample.

4.3 First QENS Signal from a Protein Solution using BATS

During the first ILL reactor cycle with IN16B operating in the BATS configuration (March/April 2018), we have recorded QENS data on a solution of BSA proteins dissolved in heavy water (D_2O). The sample was prepared by dissolving $m_p = 300\,\mathrm{mg}$ of BSA powder as purchased from Sigma-Aldrich (catalog number A3059, batch number SLBR6762V) without further purification in $V = 1.5\,\mathrm{mL}$ D_2O, such that the dry protein volume fraction in the sample solution amounted to $\varphi = m_p v_p/(V + m_p v_p) \approx 0.13$ with the specific volume of BSA $v_p = 0.735\,\mathrm{mL/g}$ [96, 109]. Part of the prepared sample solution was filled in a cylindrical Al sample holder with 7 mm outer diameter and 0.2 mm difference between the inner and outer cylinder walls. Pure D_2O reference data and empty can data were recorded using equivalent sample holders.

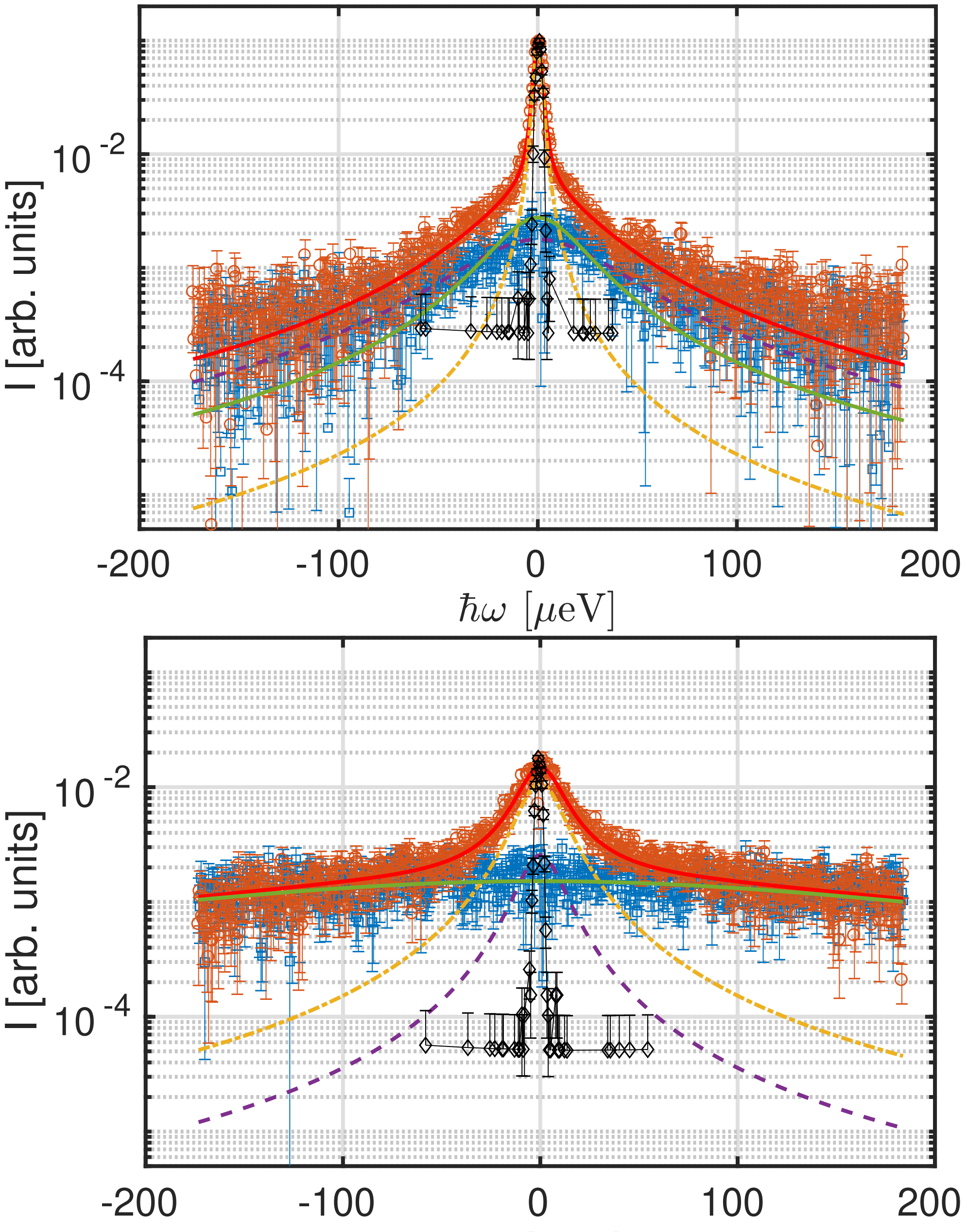

Figure 4.1: *First spectrum (circle symbols) from a bovine serum albumin (BSA) protein solution in* D_2O *recorded using the new BATS option of IN16B in a single tube of the position-sensitive detector (PSD); Top: PSD tube number 1,* $q = 0.44\,\text{Å}^{-1}$*; Bottom: PSD tube 14,* $q = 1.79\,\text{Å}^{-1}$*. The square symbols denote the corresponding pure* D_2O *solvent reference spectrum. The red solid line superimposed on the BSA/*D_2O *spectrum denotes the fit of Equation 4.1 consisting of the Lorentzian contributions with the widths* γ, Γ, *and* $\gamma_{\mathrm{D_2O}}$*, respectively, assigned to the global diffusion (dashed-dotted line), internal diffusion (dash line) and water contribution (solid line superimposed on the* D_2O *spectrum). The diamond symbols represent the resolution function measured using Vanadium.*

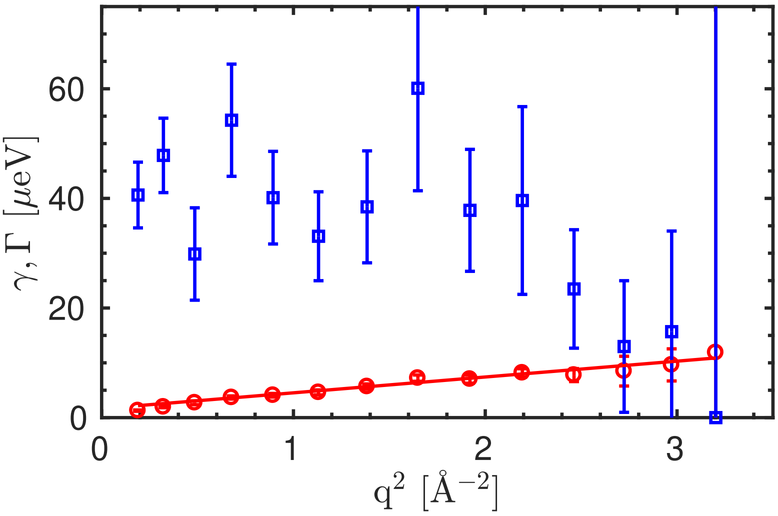

Figure 4.2: *Fit result for the Lorenztian widths γ (circle symbols) and Γ (squares) associated with the global and internal diffusive motions of the proteins, respectively, to the spectrum recorded on BSA in D_2O (Figure 4.1) according to Equation 4.1. The line superimposed on the circles is a fit of an affine function $\gamma = Dq^2 + const.$ (see text).*

The QENS data were measured at the temperature $T = 295\,\mathrm{K}$ thermostated by a cryofurnace. The energy resolution was measured with a cylindrical Vanadium foil with the slightly smaller diameter of $\approx 6\,\mathrm{mm}$ than the sample cell, thus resulting in a slightly better resolution than actually achieved on the sample itself. The resolution linewidth was found to be $(3.1 \pm 0.2)\,\mu\mathrm{eV}$ Gaussian full width at half maximum (FWHM) when fitting Vanadium spectra recorded in individual detectors. When summing the Vanadium spectra of all detectors, the thus obtained integrated resolution amounted to $\approx 3.3\,\mu\mathrm{eV}$ FWHM.

BATS was used in the “low repetition rate configuration” [66] with the first counter-rotating chopper-pair using the 20.5° slits and spinning at 79 Hz, *i.e.* serving as suppressor choppers, and the second pair set to 8° slits and 315 Hz, *i.e.* serving as the resolution-defining choppers. It is emphasized that during the reported test experiment the specific neutron optics for BATS, namely focus optics at the choppers and before the sample, was not yet installed. Therefore, the flux at the sample was substantially below the expected final flux. The neutrons were detected by a vertically position-sensitive detector (PSD) consisting of 16 vertical tubes used to obtain 16 discrete q-values in the horizontal scattering plane.

The thus obtained first spectrum from a protein solution is depicted in Figure 4.1 (circle symbols) for two q-values, along with the corresponding pure D_2O signal (square symbols) and fit result using Equation 4.1 (lines). The counting time for the BSA and the D_2O spectrum amounted to ≈ 6.5 hours each. The empty can contribution has been subtracted from the BSA/D_2O and pure D_2O signals. The Vanadium spectrum (diamond symbols in Figure 4.1) was measured

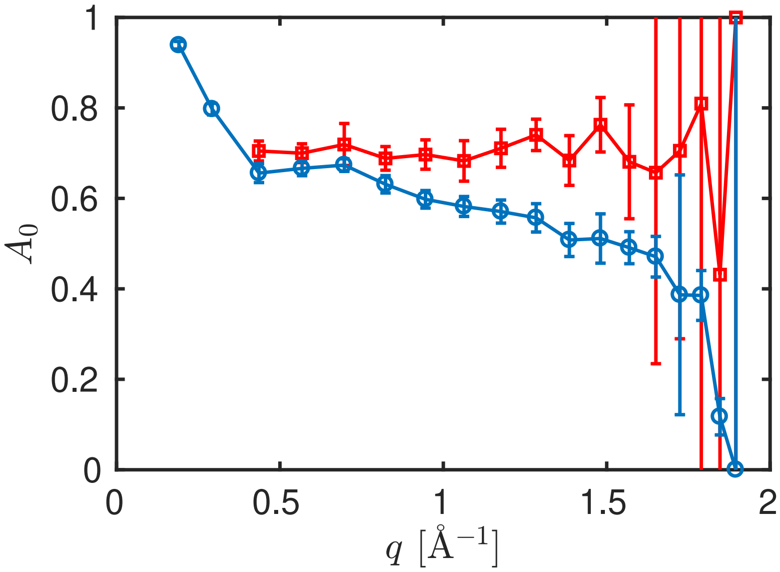

Figure 4.3: *EISF* $A_0(q)$ *of BSA in* D_2O *resulting from the fit of Equation 4.1 to the spectra displayed in Figure 4.1 (red square symbols). The EISF obtained from a fit of a spectrum recorded on IN16B in the exact-backscattering setup (energy resolution* $\approx 0.8\,\mu\text{eV}$*) is shown for reference (blue circle symbols). (Note that the detectors at the two smallest* q*-values visible in the IN16B results were not installed on BATS. The lines connecting the symbols are guides to the eye.)*

without a can. The Figure 4.1 illustrates the measured range in energy transfer of $-180\,\mu\text{eV} \leq \hbar\omega \leq +180\,\mu\text{eV}$, the good visibility of the solvent D_2O contribution on this range, and the convergence of the protein solution and solvent reference spectra for large absolute values of ω.

Specific IN16B/BATS software implemented in GNU Octave was used for the initial data reduction. The data analysis was carried out using software implemented in MATLAB (The MathWorks, Inc.) [61]. The fit of Equation 4.1 (lines in Figure 4.1) demonstrates the analysis of the first spectrum from a protein solution measured on BATS. This fit was carried out for the spectra at each q-value individually, *i.e.* without imposing any q-dependence in the fit. The width $\gamma_{\mathrm{D_2O}}$ of the Lorentzian describing the water contribution was fixed using tabled values for D_2O [61]. β_{D_2O} was fixed using the rescaled pure solvent signal to account for the volume occupied by the proteins [61].

The width $\gamma(q)$ (circle symbols in Figure 4.2) accounting for the global diffusion can be fitted by a straight line (superimposed on the circle symbols in Figure 4.2). The slope of this line results in an apparent diffusion coefficient $D = \gamma(q)/q^2 = (4.39 \pm 0.72)\,\text{Å}^2/\text{ns}$ consistent with earlier IN16B results ($D = (4.14 \pm 0.40)\,\text{Å}^2/\text{ns}$ [96]) on an equivalent sample. However, the offset $\gamma = Dq^2 + (1.6 \pm 0.6)\mu\text{eV}$ of this line is not yet understood. It might arise from a partial cross-talking of contributions from the global and internal diffusion due to the broader energy resolution compared to IN16B, from an insufficient description of the internal motions by only a single Lorentzian [64], from a possibly energy-dependent background contribution, and from the resolution data measured in a slightly different geometry.

The fit result for the linewidth Γ (square symbols in Figure 4.2) is consistent within the errors with previous results from IN16B in the intermediate q-range. The expected improved signal-to-noise ratio with the full implementation of the BATS neutron optics will substantially increase the accuracy of this information and allow for fitting more complex models. The EISF $A_0(q)$ (Figure 4.3) is reasonably close to a previous IN16B result. In view of the broader energy resolution of BATS, it is consistently slightly above the IN16B result by sampling more motions as “static” within the resolution.

Some uncertainties remain regarding this first test spectrum on a single sample and its interpretation, since the resolution was measured with a slightly different geometry and since an old batch of BSA proteins was used. Moreover, an energy-dependent background may be present in the measured data, which was not considered in the analysis. For these reasons, the present data and analysis cannot serve as quantitative reference for future studies. Nevertheless, these first data outline the promising possibilities with the large ω-range and the good energy resolution in a large q-range.

4.4 Conclusions and Outlook

In this proceedings article we have discussed the use of cold neutron backscattering spectrometers to study the superimposed center-of-mass and internal molecular diffusivities of proteins in aqueous solutions. We have shown the first commissioning data recorded employing the new instrument option BATS at IN16B on a liquid suspension of BSA proteins in D_2O. These data provide a proof of concept prior to the full implementation of all neutron optics in the BATS configuration and, thus, prior to the implementation of the full design neutron flux in the BATS configuration. Moreover, these data can already be quantitatively analyzed using established frameworks, thus pointing to the future possibilities when the full flux and optimized signal-to-noise ratio will be achieved on BATS. We have highlighted the need for versatile backscattering options with complementary energy ranges and resolutions to study the dynamics of proteins in water. Notably, IN16B and its BATS option will provide a choice of different energy resolutions and ranges that would otherwise require the use of several instruments. These new backscattering options open up perspectives for a systematic study of various topics such as the crowding effect in protein solutions, the formation of static or transient protein clusters, the self-assembly of protein aggregates, the thermal unfolding and denaturing of proteins, and the effect of salt-induced charges in protein solutions. These experiments will profit from the large and well-suited range in q – to access the EISF and the q-dependence of the diffusion processes – as well as ω – to access both the center-of-mass and internal molecular diffusion. The increased range in ω will benefit amongst other topics the experiments on more dilute protein suspensions as well as at elevated temperatures where the overall dynamics becomes too fast for the energy range covered by the exact backscattering configuration.

Acknowledgement

BATS was funded by the German Ministry for Education and Research (BMBF Verbundforschung grants 05K13WE1 and 05K16WEA). The research on protein solutions has been supported by the DFG and the ANR. C.B. acknowledges a PhD studentship grant co-funded by the University of Tübingen and the ILL. M.G. acknowledges support by the ANR (grant ANR-16-CE92-0009), and F.R.-R. by the Knut and Alice Wallenberg Foundation (project grant KAW 2014.0052). B.F., M.A., and T.S. are grateful for stimulating discussions at the QENS/WINS conference in Hong Kong 2018.

Chapter 5

Elastic and Inelastic Fixed Window Scans

This chapter will become part of a publication on methods for data analysis of elastic and inelastic fixed window scans.

5.1 Motivation

To collect classical neutron backscattering (NBS) spectra with a quasi-continuous energy transfer from highly concentrated protein solutions ($c_p \simeq 100\,\frac{\mathrm{mg}}{\mathrm{ml}}$) with good statistics, measurements of several hours are necessary. In the case of samples with low concentrations (*e.g.* $c_p \simeq 50\,\frac{\mathrm{mg}}{\mathrm{ml}}$), even longer measurement times are required to obtain full NBS spectra with comparable statistics. In addition to the efficient use of allocated beamtime, the interest in phase transitions and therefore in samples developing with time due to a change in control parameters such as temperature [64], pressure [202], illumination [203, 204] or chemical potential [33] has increased recently.

These features can be investigated thanks to recent technical developments of NBS spectrometers, which lead to higher signal-to-noise ratios up to 1:40000 [194]. New neutron guides and new focusing options also increase the neutron flux on the sample position, therefore allowing to observe changes in the short-time dynamics of the proteins on a kinetic time-scale of 15 minutes using a floating average [136]. More detailed explanations concerning this method are given in Chapter 9. However, floating averages smear out events that happen on a kinetic time-scale lower than the measurement time for one spectrum. Thus, to obtain a good time-resolved spectrum, high intensity measurements with good statistics are needed on shorter time scales. As the neutron flux is limited by the neutron source, the statistics for full spectra cannot be enhanced by increasing the neutron flux. Instead, the scattering signal can be obtained on shorter time scales by only investigating neutrons, which have passed a defined energy transfer $\hbar\omega$ during the scattering process. Using a primary spectrometer with a Doppler-driven monochromator crystal, such as present at the cold neutron backscattering spectrometer (IN16B), it is possible to collect scattering signals with fixed energy transfers up to $\hbar\omega = 10\,\mu\mathrm{eV}$ within less than ten minutes. As explained in Section 3.2.4, in this case the velocity profile of the monochromator crystal is changed in such a way that it passes a major part of the available distance with a constant speed, which results in a constant energy transfer of the neutrons finally detected. Spectra collected this way are called fixed window scans (FWSs). If the monochromator is not moving and is equipped with the same crystals as the analyzers (*i.e.* same orientation and temperature), the energy transfer observed is zero and the collected spectrum is called an elastic fixed window scan (EFWS). In the case of non-zero energy transfers, the spectra are called inelastic fixed window scan (IFWS).

Technically, as mentioned in Section 3.2.4, energy offsets might also be measured by another lattice distance by either changing the temperature of the monochromator crystal or by using a different crystal or a different crystal orientation.

As the observed energy interval is limited, this measurement type cannot provide the same amount of information as full quasi-elastic neutron scattering (QENS) measurements. Nevertheless, the possibility to investigate kinetic processes offers interesting new insights into short-time diffusive behaviors. Depending on the investigated sample, FWS might be the preferred measurement technique.

The aim of this chapter is to point out different methods to analyze the elastic and inelastic fixed window scan (E/IFWS) measured on protein solutions. Section 5.2 provides a short overview of some examples of elastic incoherent neutron scattering (EINS), *i.e.* EFWS which are dominated by the incoherent scattering, measured on protein solutions, while EFWS and IFWS are modeled in Section 5.3 based on the description of full QENS experimental spectra by Grimaldo *et al.* [64]. Using these modeled EFWS, influences of the chosen fit interval on the fit results are discussed and compared to experimental results obtained by L. Bühl [205] in Section 5.4. In Section 5.5 to Section 5.7, new approaches for analyzing EFWS combined with IFWS are explained based on the modeled data described in Section 5.3. The results are also compared with experimental values.

5.2 EINS of Dissolved Proteins

The majority of EINS measurements on proteins are performed on dry or on hydrogenated samples [206–208]. Only a limited number of studies on dissolved proteins at ambient pressure have been reported in the literature reviewed in [13]. Given the limited amount of sample points, the analysis of the spectra is mainly restricted to a mean squared displacement (MSD) averaging over the different hierarchical dynamics measurable on the time-scale given by the instrumental resolution [13]. Several examples with different fit approaches are reviewed in the following.

Wood *et al.* [208] suggested to combine the MSD obtained from EINS with information on global diffusion obtained from neutron spin echo (NSE) data to extract the internal diffusion of Ribonuclease A.

Hennig *et al.* [111] determined temperature-dependent MSD values from EINS. They used this temperature dependence together with the global diffusion obtained from full NBS spectra to extract the internal dynamics of bovine serum albumin (BSA) during thermal denaturation.

Caronna *et al.* [209] measured the temperature-dependent dynamics of hemoglobin with EINS. Using a deuterated glycerol-water mixture as a solvent, the authors investigated a larger temperature range than the one accessible with pure D_2O due to its freezing point. They found significant differences in the MSD obtained from EINS on the spectrometers IN13 and IN16 for temperatures $T > 250\,\mathrm{K}$, while below this value, the MSD observed were comparable. Given the significantly better energy resolution of IN16 (see also Section 5.6), this might be linked to the different observation times. In addition, the different q ranges accessed by IN13 and IN16 might influence the validity of the Gaussian approximation [210].

Al-Ayoubi *et al.* [202] investigated the enzymatic activity of lactate dehydrogenase in D_2O based TrisHCl buffer as a function of pressure and co-solvents. Due to the broader energy resolution of IN13 compared to IN16B the global diffusion is masked out. The measured EINS spectra therefore offer access to a MSD investigating mainly the fast internal dynamics.

This section provided a short review of EINS measurements of protein solutions. In the following sections, different methods for analyzing the FWS are reviewed and new methods are presented.

5.3 Modeling of FWS

For a better interpretation of the FWS, fit functions used to analyze full NBS spectra can be of help to model the FWS. By doing so, the different contributions to the FWS, *e.g.* contributions of global and internal diffusion, can be separated. When different contributions are known, several fit approaches can be tested on a data set and be compared to the initial parameter set. To model the FWS of protein solutions, fit results from experimental NBS spectra were used. As the experimental FWS were collected on BSA solutions, which were also used to compare the internal dynamics of different proteins, the results of this study can be compared to those shown in Chapter 7 and to those obtained by Grimaldo *et al.* [64].

The full NBS scattering function of the protein can be described by two Lorentzian functions $\mathscr{L}_{\sigma_l}(\omega)$ with σ_l being the half width at half maximum (HWHM). The Lorentzian function accounting for the apparent global diffusion can be described by Brownian diffusion, resulting in a HWHM $\gamma = D_{app}q^2$, with an apparent diffusion coefficient set to $D_{app} = 5\,\mathrm{\AA}^2\mathrm{ns}^{-1}$. The HWHM of the second Lorentzian function accounting for the internal dynamics can be described by a jump diffusion model developed by Singwi *et al.* [62]

$$\Gamma = \frac{D_{int}q^2}{1 + D_{int}q^2\tau_{int}} \tag{5.1}$$

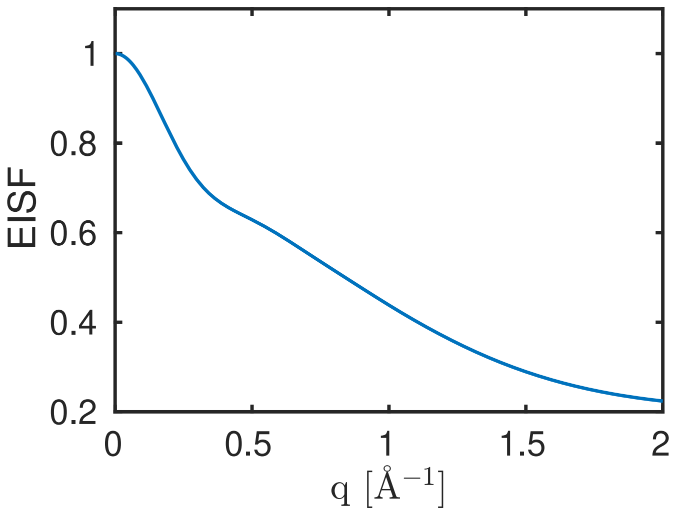

Figure 5.1: *Modeled q-dependence of the EISF based on experimental fit results.*

with an internal diffusion coefficient D_{int}, set to $30\,\text{Å}^2\text{ns}^{-1}$, and a residence time τ_{int}, set to 0.01 ns. The scattering function for the protein therefore equals

$$S(q,\omega) = A_0(q)\mathscr{L}_\gamma(\omega) + (1 - A_0(q))\mathscr{L}_{\gamma+\Gamma}(\omega) \tag{5.2}$$

with $A_0(q)$ being the elastic incoherent structure factor (EISF). It is described by the model used in Ref. 64:

$$\begin{aligned} A_0(q) &= p + (1-p)A_G(q,a)\left[sA_{sph}(q,R) + (1-s)A_{3j}(q,a_m)\right] && (5.3)\\ A_{3j}(q,a_m) &= \frac{1}{3}\left[1 + 2j_0(qa_m)\right] && (5.4)\\ A_{sph}(q,R) &= \left|\frac{3j_1(qR)}{qR}\right|^2 && (5.5)\\ A_G(q) &= \exp\left(-\frac{(qa)^2}{5}\right). && (5.6) \end{aligned}$$

Contributions from the rotation of hydrogens in methyl groups (Equation 5.4) with $a_m = 1.715$ Å, diffusion in a sphere (Equation 5.5) with a radius $R = 10$ Å, as well as a Gaussian radial profile $A_G(q)$ with an effective radius $a = 1.5$ Å (Equation 5.6) are used. The scaling parameters p and s from Equation 5.3 are set to $p = 0.2$ and $s = 0.35$, describing the fraction of immobile proteins as well as the fraction of mobile H-atoms diffusing within an impermeable sphere, respectively. The final q-dependence of the EISF is displayed in Figure 5.1. A flat background is added to approximate the water contribution to the scattering signal. Inspired by the experimental resolution function $\mathscr{R}^{exp}(q,\omega)$ measured on IN16B in a full QENS mode, the resolution function used is modeled by one Gaussian function $\mathscr{R}^{mod}_\sigma(\omega)$ with a q-independent full width at half maximum (FWHM) of $\delta E = 0.9\,\mu\text{eV}$ corresponding to a standard deviation of $\sigma = \frac{\delta E}{2\sqrt{2\log(2)}} \approx 0.38\,\mu\text{eV}$.

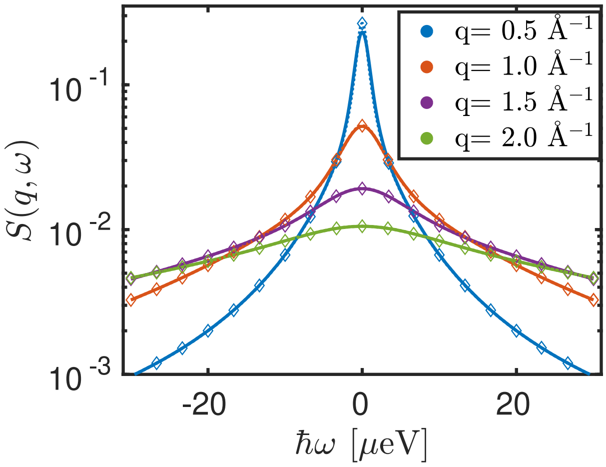

Figure 5.2: *Modeled QENS spectra based on experimental fit results. Different momentum transfers are color-coded as indicated in the legend. Dotted lines with diamonds represent the modeled scattering functions, solid lines represent the same scattering functions convoluted with the resolution function. When dotted lines are invisible, they agree with the solid ones.*

Figure 5.2 shows the fully modeled spectrum as a function of energy and momentum transfer before and after the convolution with the resolution function as dotted lines with diamonds and solid lines, respectively. The convoluted scattering function deviates from the modeled one mainly at small momentum transfers, where the HWHM of the scattering function is comparable to the one of the resolution. To extract the FWS $S_{mod}(q,\omega)$ at different energy transfers $\hbar\omega$, the convoluted model $S_{conv}(q,\omega)$ is evaluated at the desired energy transfer. As the scattering function is described by two Lorentzian functions $\mathscr{L}_\gamma(\omega)$ (see Equation 5.2) and the resolution function consists in a Gaussian function with a variance σ, their convolution can be written as a sum of two Voigt functions $\mathscr{V}_{\gamma,\sigma}(\omega)$:

$$S_{mod}(q,\hbar\omega) = S_{conv}(q,\hbar\omega) = A_0(q)\mathscr{V}_{\gamma,\sigma}(\hbar\omega) + (1 - A_0(q))\mathscr{V}_{\gamma+\Gamma,\sigma}(\hbar\omega) \tag{5.7}$$

In a different numerical approach, the modeled spectrum can be integrated over the resolution function.

$$S^{\mathscr{R}}_{mod}(q,\omega) = S(q,\omega) \otimes \mathscr{R}(q,\omega) = \int S(q,\omega)\mathscr{R}(q,\omega_0 - \omega)\mathrm{d}\omega_0 \tag{5.8}$$

In Figure 5.3, the two different approaches are compared. It was assumed that the resolution function at different energy transfers is similar to the one measured in the elastic case. The modeled energy offsets were chosen according to experimental ones, namely

$$\hbar\omega = 0; 1.3; 3; 6; 10\ \mu\text{eV}. \tag{5.9}$$

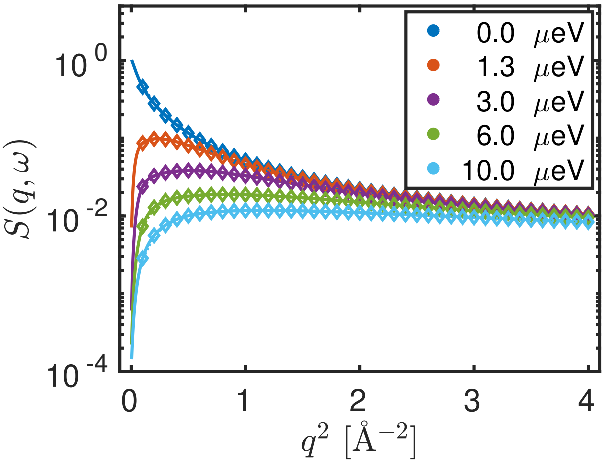

Figure 5.3: *FWS extracted from the modeled convoluted scattering function by evaluating Equation 5.7 at the given energy transfer (solid lines) and by integrating over the resolution function shifted to the corresponding energy transfer (dotted line with diamonds, Equation 5.8).*

As shown in Figure 5.3, the two different approaches lead to similar results. While the approach of Equation 5.8 can also be applied to models deviating from a Lorentzian shape, it is more expensive in terms of computational power. Therefore, as all the models presented here can be expressed by Lorentzian functions, the approach of Equation 5.7 is used for further analysis.

By modeling the FWS data, it is possible to display the contributions of different hierarchical dynamics. As both the global and internal diffusion of the protein and the EISF contribute to the q dependence of the E/IFWS, the modeling can offer insights into these contributions at different energy and momentum transfers. In Figure 5.4, FWS are plotted as a function of q^2 for the different energy transfers mentioned in Equation 5.9. Comparing the different plots of Figure 5.4 shows that the contributions dominate to different extents at given energy and momentum transfers. Due to the limited amount of points experimentally accessible, it is clear that it is not possible to extract all of the information if the analysis is limited to only one or a few energy transfers.

Nevertheless, obtaining information on the overall short-time dynamics of a system based on data obtained in a short measurement time is a valuable advantage of FWS. Different analysis methods are therefore discussed in more detail in the following sections.

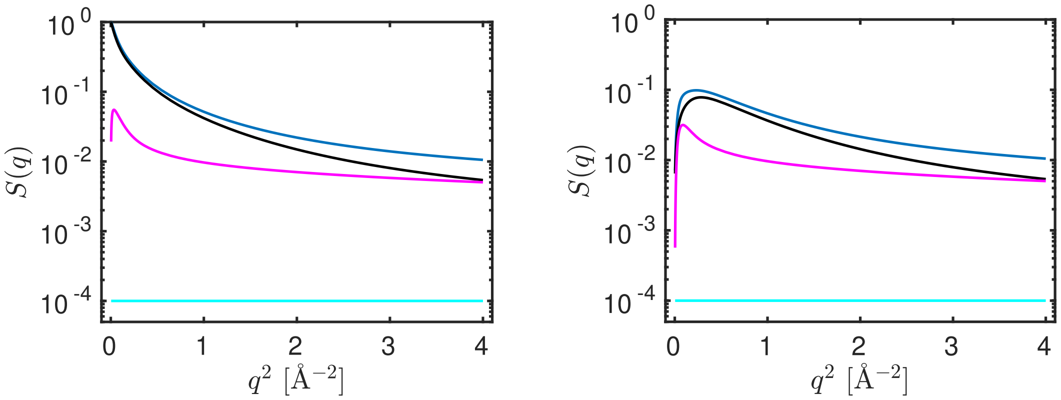

(a) *$\hbar\omega$ =0* µeV **(b)** *$\hbar\omega$ =1.3* µeV

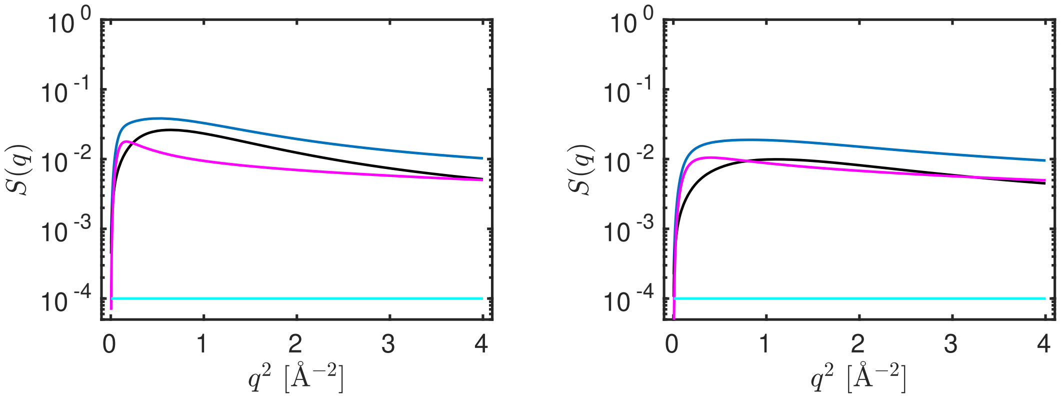

(c) *$\hbar\omega$ =3* µeV **(d)** *$\hbar\omega$ =6* µeV

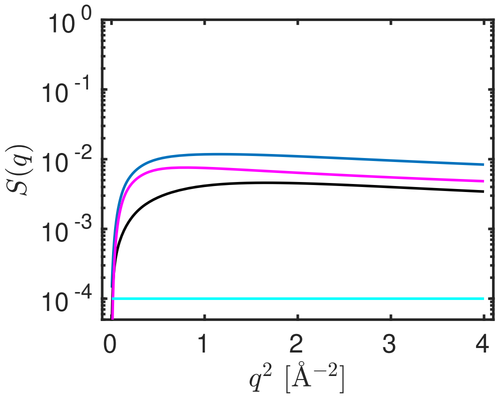

(e) *$\hbar\omega$ =10* µeV

Figure 5.4: *Modeled FWS as a function of q^2 for different energy transfers. Blue lines represent the total FWS scattering signal, while black, magenta and cyan lines represent the contributions of the Voigt function describing the global diffusion and the internal diffusion as well as the assumed background, respectively.*

5.4 Comparison of Modeled and Experimental Data

EINS measurements can be performed on different instruments characterized by their experimental setups as explained in Section 3.2.4. Since the instruments have specific instrumental energy resolutions, they also give access to different types of dynamics. There are several analysis frameworks for the EINS. A selection of different models is presented in this section.

5.4.1 Expanded Gaussian Approximation

FWS measurements on BSA solutions with different concentrations and additives were performed during heating ramps crossing the denaturation temperature. In a first approach, L. Bühl [205] analyzed EFWS collected during these measurements. Based on previous publications by Hennig [111], the normalized data was analyzed using a second order polynomial approach giving access to an overall MSD $\langle u^2 \rangle$ of the sample:

$$\log\left(S(q,\omega=0)\right) = -\frac{1}{3}\left(b + \left\langle u^2 \right\rangle q^2 + cq^4\right). \tag{5.10}$$

The underlying idea is to expand the Gaussian approximation and therefore cover a larger q range. While similar approaches, such as the one by Yi *et al.* [211] stay closer to the theoretical description by taking higher order contributions directly into account, the approach in Equation 5.10 has the advantage of being easily implemented and model-free. In addition, if required, the fit parameters of the different models can be linked to each other, if the approach of Equation 5.10 is assumed to be only a trunctation of a Taylor series.

One important result obtained by L. Bühl was the systematic characterization of the dependence of the fit results on the q range used for the fit. To judge if similar dependences are obtained with the FWS signal calculated with the model, similar fits were performed using the same q-values as those covered by the experiment. Figure 5.5 shows some fits over different q-ranges. The solid lines represent the fits in the fit interval and dotted lines show their extrapolation to higher q. Given the parabolic approach of the fit function, it is clear that the model used does not describe the data set entirely.

Figure 5.6 compares the influence of the q-interval used for the fits, on the extracted MSD from both experimental EFWS ($T = 300\,\mathrm{K}$ – Figure 5.6a) as well and modeled EFWS (Figure 5.6b). In both analyses, a qualitatively similar dependence on the q-range investigated can be observed. When a small q-range is chosen, the obtained MSD is high and decreases if the q-range is enlarged. Similar effects can be observed for the error bars. Their magnitude decreases with an increasing q-range. This effect can be explained by the increasing number of data points taken into account.

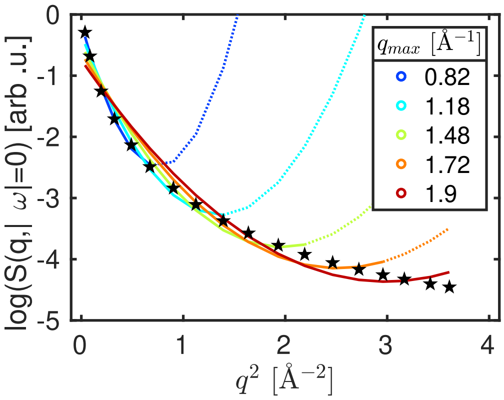

Figure 5.5: *Analysis of the modeled EFWS using the approach derived in Equation 5.10. Differently colored lines represent the fits over different q intervals with changing upper limit $[q_{min} = 0.19\,\text{Å}^{-1}, q_{max}]$. Solid lines represent the fits in the interval, dotted lines are extrapolations of the fit function, yielding clearly unphysical results.*

It should be emphasized that for the modeled data, no statistical errors were taken into account for the description of the scattering signal.

Similar observations were reported, *e.g.*, by Vural *et al.* and explained by the fact that dynamical heterogenity is ignored in the fit model [212].

In this section, the general consistency of the modeled data with the experimental data was shown. In addition, the limits of the Gaussian approximation were displayed. In the next section several models used to describe larger q-ranges, presented in the literature, are summarized.

5.4.2 Heterogeneous Models for EINS

The Gaussian approximation presented in the previous section assumes homogeneity and isotropy as well as harmonicity of the investigated particles [213, 214]. Deviations between the Gaussian approximation and the experimentally measured EINS spectra are often explained by heterogeneous motions in the sample [213, 215, 216]. To overcome this limitation, the scattering function can be generalized using different distributions ρ of the motions:

$$S(q, \omega = 0) = \int_0^\infty \rho(s) \exp\left(-q^2 s\right) \mathrm{d}s \tag{5.11}$$

with $s \propto \langle u^2 \rangle$. An overview of different distributions used for modelling the EINS is given in Ref. 216. Several distributions are summarized in Table 5.1. Comparing the model using a Gaussian distribution with Equation 5.10, it can be seen that for a correct normalization of the experimental data, the fit model used in Section 5.4.1 converges into the model used by Nakagawa [217].

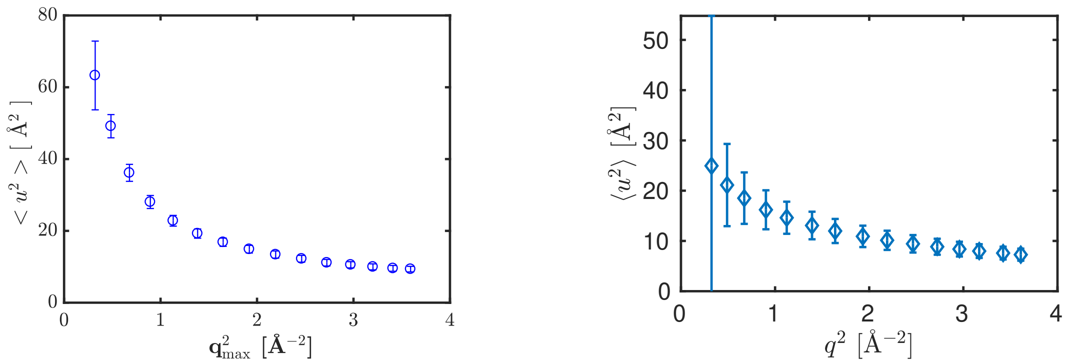

(a) *MSD as a function of the applied q interval obtained from experimental EFWS (Figure adapted from Ref. 205)*

(b) *MSD obtained from modeled EFWS*

Figure 5.6: *Comparison of the influence of the q interval on the MSD from experimental and modeled EFWS.*

Since the aim of this chapter is to explain different methods to analyze the FWS and not only EINS, detailed comparisons of different fit approaches are not provided here. They can be found in publications by Zeller [213] and by Nakagawa [217].

5.4.3 Models Describing the EFWS with Anharmonic Systems

Doster *et al.* [221] proposed a description of the elastic scattering based on a double-well potential. In each of the isotropic and harmonic wells separated by a free energy barrier ΔG and a distance d, the atoms are assumed to be homogeneous but anharmonic. The EINS can then be described by

$$S(q, \omega = 0) = \exp\left(-\frac{1}{3}q^2 \langle u^2 \rangle\right) \cdot (1 - p_{12}(1 - \mathrm{sinc}(qd))) \qquad (5.12)$$

with p_{12} being the product of the two probabilities p_1 and p_2, which represent the probability to find the atom in the ground state or excited state, respectively. The ratio between the two probabilities can be linked to ΔG by

$$\frac{p_2}{p_1} \propto \exp\left(-\frac{\Delta G}{RT}\right). \qquad (5.13)$$

Similar to the models presented in Section 5.4.1, this model is not fitted directly to experimental data collected during this thesis. A comparison of the different models can be found in other publications [213].

Table 5.1: *Overview of different MSD distributions used in different publications*

Author	distribution	mathematical expression
Nakagawa [217], Vural [212], Bicout [218]	bi-modal	$\rho_B(s) = p_1\delta(s - s_1) + p_2\delta(s - s_2)$
Nakagawa [217]	Gaussian distribution	$\rho_G(s) = \frac{1}{\sqrt{2\pi\sigma_G^2}} \exp\left(-\frac{\left(s-\langle s\rangle_{av}\right)^2}{2\sigma_G^2}\right)$
	exponential	$\rho_E(s) = A\exp\left(-As\right)$
Meinhold [219]	Weibull	$\rho_W(s) = \frac{\alpha}{\beta}\left(\frac{s}{\beta}\right)^{\alpha-1} \exp\left[-\left(\frac{s}{\beta}\right)^{\alpha}\right]$
Peters and Kneller [220]	Gamma distribution	$\rho_\Gamma(s) = \frac{\beta\exp(-\beta s)(\beta s)^{\beta-1}}{\Gamma(\beta)} \quad (\beta > 0)$

5.5 Analysis of EFWS Using Information from NBS Data

Based on the knowledge from full NBS spectra, EFWS can also be analyzed using Equation 5.7 evaluated at $\hbar\omega = 0\,\mu\text{eV}$ to describe the scattering signal of the protein:

$$S(q, \omega = 0) = A_0\mathscr{V}_{\gamma,\sigma}(0) + (1 - A_0)\,\mathscr{V}_{\gamma+\Gamma,\sigma}(0) \tag{5.14}$$

Given the small number of sampling points available, fitting this model leads to an ill-posed problem and no robust results can be obtained. Instead, an effective diffusion coefficient can be obtained by fitting one single Voigt function to the data:

$$S(q, \omega = 0) = \mathscr{V}_{D_{eff}q^2,\sigma}(0). \tag{5.15}$$

Similar to the approach presented in Section 5.4.1, which determines an overall MSD, the obtained effective diffusion coefficient D_{eff} averages over all hierarchical diffusive processes in the sample. Figure 5.7a displays the fit of Equation 5.15 to the modeled EFWS from Section 5.3.

The fit yields an effective diffusion coefficient $D_{eff} = (10.06 \pm 0.74)\,\text{Å}^2\text{ns}^{-1}$. The obtained fit describes the modeled data reasonably well. The effective diffusion observed is a combination of the global and internal diffusion. Similarly to the fits performed in Section 5.4, the fit also depends on the q interval employed (Figure 5.7b). To separate the internal and global contributions, more sampling points would be necessary. Since the number of q-values is limited by the instrument, more sample points can be obtained by additionally analyzing IFWS. In the next sections, different analysis frameworks for E/IFWS will be explained.

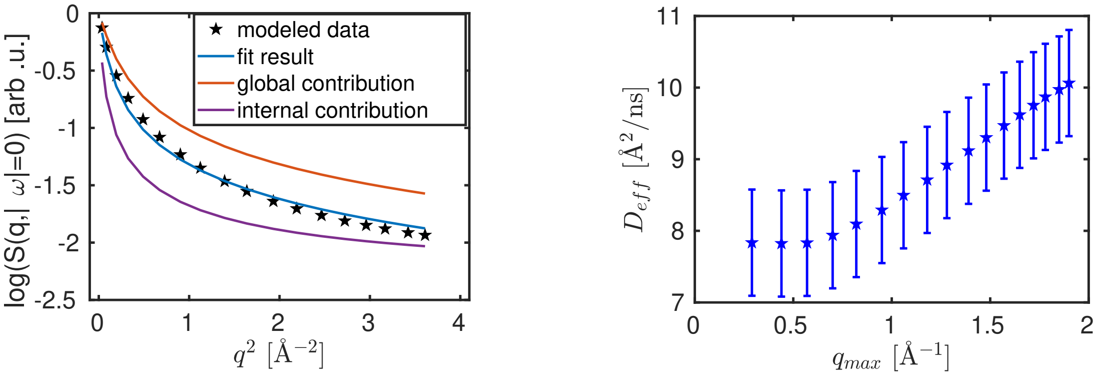

(a) *Fit of modeled EFWS using one single Voigt function (blue line) to the modeled data (black stars). The brown and violet curves represent the scattering signal of a Voigt function $\mathscr{V}_{\gamma,\sigma}(0)$ and $\mathscr{V}_{\Gamma,\sigma}(0)$ standing for the global and internal contribution, respectively. The scaling of the EISF is not included in the plot.*

(b) *q dependence of the effective diffusion coefficient D_{eff} obtained from the fit shown on the left hand side. The fits were performed over different q intervals $[q_{min} = 0.19\,\text{Å}^{-1}, q_{max}]$.*

Figure 5.7: *Fit and corresponding results of the modeled EFWS using one single Voigt function.*

5.6 Extracting Effective Diffusion Coefficients from EFWS and IFWS at Low Energy Transfers

The IFWS can be analyzed in a way motivated by the QENS analysis, but still using a model-free approach. The only assumption within this framework is that the observed diffusive process can be described by a Lorentzian function. Similar to the analysis of full NBS spectra, the analysis offers at the end a q-dependent HWHM. This is possible if the ratio between the elastic and an inelastic measurement is analyzed. The corresponding IFWS should therefore be chosen such that the mentioned assumption is valid. If this ratio is compared to a calibration curve calculating the same ratio for a Voigt function with a known HWHM, the HWHM of a Lorentzian function describing the global diffusion of the particles can be determined for each momentum transfer $\hbar q$ individually.

In Figure 5.8, the calculated ratio

$$C(\gamma) = \frac{\mathscr{V}_{\sigma,\gamma}(0\,\mu\text{eV})}{\mathscr{V}_{\sigma,\gamma}(1.3\,\mu\text{eV})} \tag{5.16}$$

is plotted as a function of γ for different assumed resolutions with FWHM δE. For this purpose, Gaussian functions, centered around the origin, were assumed for the

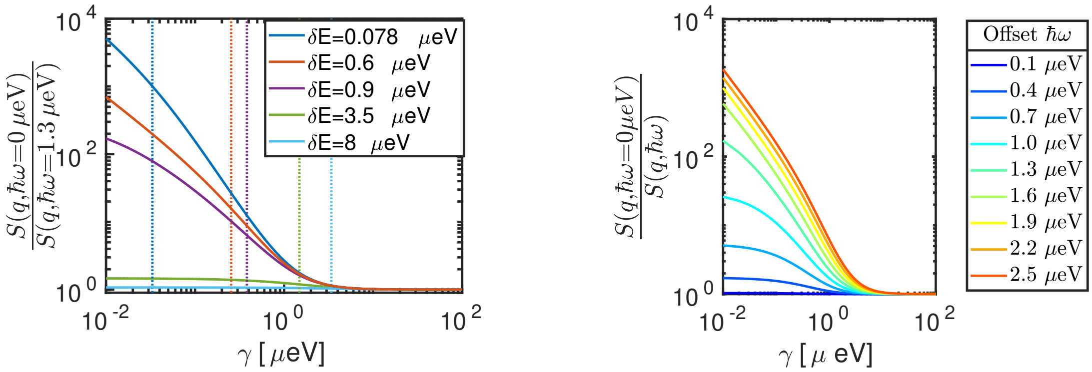

(a) *Resolution-dependent ratios as a function of γ with a fixed energy offset ($\hbar\omega = 1.3\,\mu\text{eV}$).*

(b) *Offset-dependent ratios as a function of γ with a fixed resolution of $\delta E = 0.9\,\mu\text{eV}$.*

Figure 5.8: *Ratio of the scattering function calculated with the values of the EFWS and the IFWS as a function of the HWHM of the Lorentzians. Solid and dashed lines represent the ratios as well as the resolution assumed for the calculations, respectively.*

resolution function with a standard deviation $\sigma = \frac{\delta E}{2\sqrt{2\log(2)}}$, leading to centered Voigt functions $\mathscr{V}_{\sigma,\gamma}(\hbar\omega)$. The FWHM were chosen to match the resolutions of backscattering spectrometers such as the one of the GaAs prototype of IN16B ($\delta E = 0.078\,\mu\text{eV}$ [222]), the one of SPHERES ($\delta E = 0.6\,\mu\text{eV}$ [193]), the one of the unpolished Si(111) version of IN16B ($\delta E = 0.9\,\mu\text{eV}$ [96, 222]), the one of backscattering silicon spectrometer (BASIS) or also of the IN16B Backscattering and Time of Flight Spectroscopy (BATS) option ($\delta E = 3.5\,\mu\text{eV}$ [66, 172, 223]) as well as the one of IN13 ($\delta E = 8\,\mu\text{eV}$ [224]).

This approach has several restrictions concerning the observable global dynamics. If the tracer particle moves too slowly, the ratio observed is mainly dominated by the resolution function and would appear to be an immobile particle contributing to a Dirac function. This is observed, *e.g.*, in the case of crystallizing samples (see Chapter 9). As can be seen in Figure 5.8a, the calibration curves slightly level off at low γ. If an experimental ratio with its corresponding errors close to this value should be translated into the corresponding γ, even a small error in the ratio would lead to a large error in γ. In the case of an ideal resolution ($\sigma = 0\,\mu\text{eV}$), the calibration curve $C(r)$ could be expressed using Lorentzian functions and could be described by

$$\lim_{\sigma\to 0} C(\gamma) = \frac{\hbar\omega}{\gamma^2} + 1 \tag{5.17}$$

with an energy transfer $\hbar\omega$. In the case of a non-negligible resolution function, the intersection point with the ordinate can be calculated since the Voigt function transforms into a Gaussian function if $\gamma = 0\,\mu\text{eV}$ and its intersection point is determined by

$$C(\gamma = 0) = \exp\left(\frac{1}{2}\left(\frac{\hbar\omega}{\sigma}\right)^2\right). \tag{5.18}$$

However, in case of too fast dynamics, the chosen energy offsets do not differ significantly and the ratio is close to unity. Additionally in this case, γ cannot be determined unambiguously anymore. In addition, the resolution can have influences on the observed parameters, such as the absolute values of the MSD [225].

If experimentally obtained ratios are above the theoretical limits, the used model should be revised. Such effects might be induced by non-moving scatterers. If the ratio is below unity, other contributions *e.g.* from the solvent as well as from the sample holder have to be re-investigated. Also inelastic scattering, which might appear, might influence the observed ratio. For values close to unity, internal diffusions might have to be respected as well.

After choosing a suitable resolution, the offset of the IFWS has to be set correspondingly. In Figure 5.8b, the ratios of the EFWS and IFWS are calculated as a function of γ for different offsets with a fixed energy resolution of $\delta E = 0.9\,\mu\text{eV}$. Even for offsets below the resolution, calibration curves can be obtained. The ratio increases with increasing offsets. This effect would suggest to measure the IFWS with the highest energy transfer possible. However, the systems studied are protein solutions with additional contributions due to internal dynamics. In addition the solvent becomes more dominant at higher energy transfers. To ensure that mainly the global dynamics are investigated, one is interested in measuring at low energy transfers, where the global dynamics dominate the QENS signal.

Depending on the system studied, it is therefore important to choose the right energy offsets as well as a suitable instrument, which determines the resolution function.

Based on the FWS modeled in Section 5.3, the corresponding ratio between the EFWS and the IFWS measured at $\hbar\omega = 1.3\,\mu\text{eV}$ was calculated. Figure 5.9 shows the different analysis steps going from the q-dependent E/IFWS (Figure 5.9a) over the q-dependent ratio (Figure 5.9b) to the q dependent γ (Figure 5.9c), which is then fitted with a Brownian diffusion model.

Already from the q-dependence of γ, it can be seen that the trend deviates from the Brownian diffusion. Since also contributions from internal diffusion are taken into account for the modeling of the scattering signal, the obtained diffusion coefficient based on a fit with $\gamma = D_{eff}q^2 + b$ over the total q-range is overestimated:

$$D_{eff} = (6.77 \pm 0.07)\,\frac{\text{Å}^2}{\text{ns}}. \tag{5.19}$$

In addition, it can be seen that neglecting the background leads to a non-zero intersection-point with the ordinate. Limiting the fit to $q < 0.8\,\text{Å}^{-1}$ where the EISF favors the Lorentzian function describing the global diffusion (see Figure 5.1) still leads to an overestimation of the diffusion coefficient

$$D_{eff} = (6.13 \pm 0.10)\,\frac{\text{Å}^2}{\text{ns}} \tag{5.20}$$

of around 22% compared to the diffusion coefficient of $D_{model} = 5\,\text{Å}^2\text{ns}^{-1}$ assumed for the modeling.

Modeling hard spheres without internal dynamics (Figure 5.9d), the method leads to the expected result of $D_{eff} = (5.0796 \pm 0.0789)\,\text{Å}^2\text{ns}^{-1}$ by applying a fit over the total investigated q-range. Further investigating the q-dependence might therefore offer information about the internal dynamics.

When investigating measured data, different resolutions at different q have to be taken into account. For this purpose, the data reduction scripts for FWS scans, written by L.Bühl [205], as well as analysis scripts written by L. Grabitz were expanded to analyze EFWS and IFWS at $\hbar\omega = 1.3\,\mu\text{eV}$ in the presented way. Figure 5.10 shows the results of the analysis of experimental data (BSA $c_p = 500\,\frac{\text{mg}}{\text{ml}}$) [226–228] with different NaCl concentrations. For each temperature, a q dependence of γ is obtained.

For each temperature, for each q value and for each protein concentration a new calibration curve was calculated to account for the different widths of the water signal, different resolutions and different scalings of the water signal (D_2O), respectively. The calibration curve $C(\gamma)$ was therefore calculated by

$$C(\gamma) = \frac{\mathscr{V}_{\gamma,\sigma}(0) + EC(0) + \beta_{D_2O} S_{D_2O}(q, 0, T)}{\mathscr{V}_{\gamma,\sigma}(1.3) + EC(1.3) + \beta_{D_2O} S_{D_2O}(q, 1.3, T)} \tag{5.21}$$

with EC and $S_{D_2O}(q, \hbar\omega, T)$ being the contribution from the empty can and the temperature-dependent water contribution, respectively. β_{D_2O} takes the volume fraction scaling into account [61]. Comparing the calibration curves from Figure 5.9b and 5.10b, the influence of the empty can and the solvent contribution can be observed. The calibration curves, used for the analysis of the experimental data, level off already at values above unity. Investigating the calibration curve in Figure 5.10b, it becomes apparent that the calibration curve is nearly flat for $\gamma \geq 2.5\,\mu\text{eV}$.

The first two data points at low q, detected by the single detector (SD), deviate from the trend. Since they are not in perfect backscattering geometry, they detect neutrons with a slight energy shift. In the case of full QENS spectra, this is not problematic, since the spectra can be realigned based on calibration measurements on vanadium. For FWS, however, this correction is not possible, since only one fixed energy transfer is observed.

The leveling-off of γ can be explained by the flattening of the calibration curve. Given this limit of the method, the temperature dependence of the residence time τ displayed in Figure 5.10e is probably not a characteristic of the sample but rather an indicator that the proposed method is not suitable anymore to investigate the sample at these temperatures elevated at an offset of $\hbar\omega = 1.3\,\mu\text{eV}$. Similar conclusions are obtained, if the errors of the diffusion coefficients are investigated (Figure 5.10d).

If the dynamics of the system are too fast and therefore the HWHM γ leads to an apparent flat signal with the chosen offsets, the dynamics cannot be resolved with this set of resolution and energy offset anymore given the statistical errors of the measurements. An example of a BSA solution with a protein concentration $c_p = 150\,\frac{\mathrm{mg}}{\mathrm{ml}}$ is shown in Figure 5.11. Due to the lower volume fraction, the sample is expected to have a higher global diffusion coefficient leading to larger values of γ. The observed decay of γ at higher q values clearly points out the limits of the technique presented here. Nevertheless it can be of value for the study of selected systems with relatively slow dynamics, but fast kinetics.

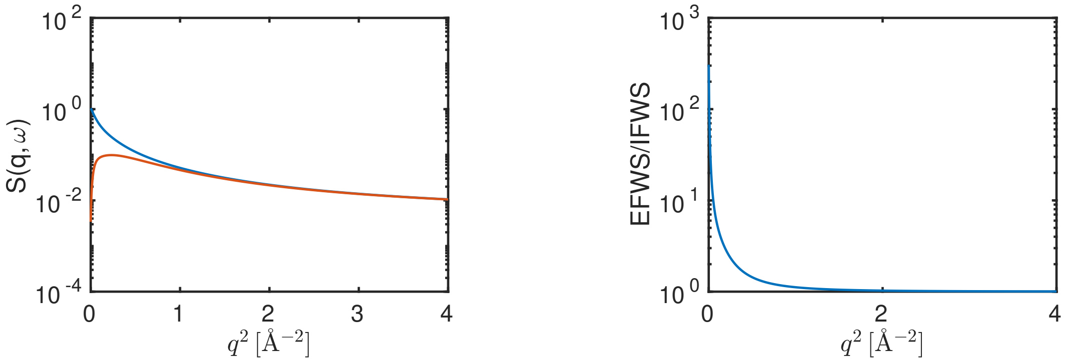

(a) *FWS as a function of the scattering vector q for the two investigated energy transfers. the blue and orange curves represent the EFWS as well as the IFWS at $\hbar\omega = 1.3\,\mu\text{eV}$, respectively.*

(b) *Ratio of the two FWS shown in Figure 5.9a.*

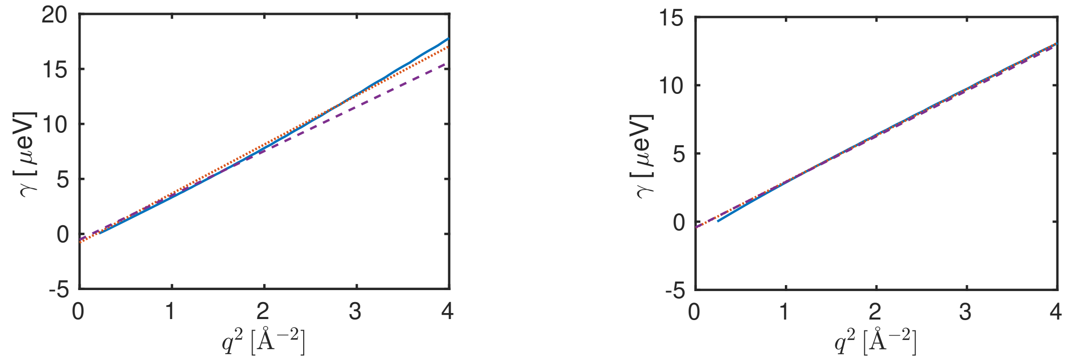

(c) *Extracted γ as a function of q^2 based on the presented analysis framework. The calibration curve $C(\gamma)$ was calculated using Equation 5.16. and is shown in violet in Figure 5.8a. The blue curves represent the data, while orange dotted and violet dashed curves represent fits ($\gamma = Dq^2 + c$) and their extrapolations for the q intervals q=[0,2] and q=[0,0.8], respectively.*

(d) *Result of the ratio analysis similar to the ones shown in Figure 5.9a-5.9c for hard spheres without internal dynamics. The HWHM γ can be well described by $\gamma = D_{eff}q^2 + b$ over the total investigated q-range.*

Figure 5.9: *Analysis of the modeled FWS using the ratio between the EFWS and the IFWS with $\hbar\omega = 1.3\,\mu\text{eV}$.*

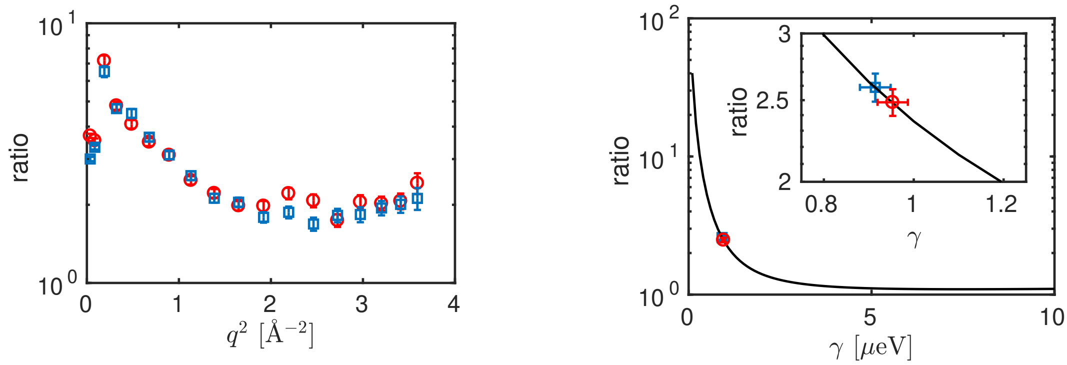

(a) *q dependence of the ratio between the EFWS and IFWS measured at* $T = 300\,\mathrm{K}$ *on the heating ramp.*

(b) *Calibration curve* $C(\gamma)$ *to calculate* γ *from the ratio (symobls) shown in Figure 5.10a. The plotted data points represent* $T = 300\,\mathrm{K}$ *and* $q \simeq 1\,\text{Å}^{-1}$ *measured during the heating ramp. The calculation of the calibration curve included the water and empty can contribution*

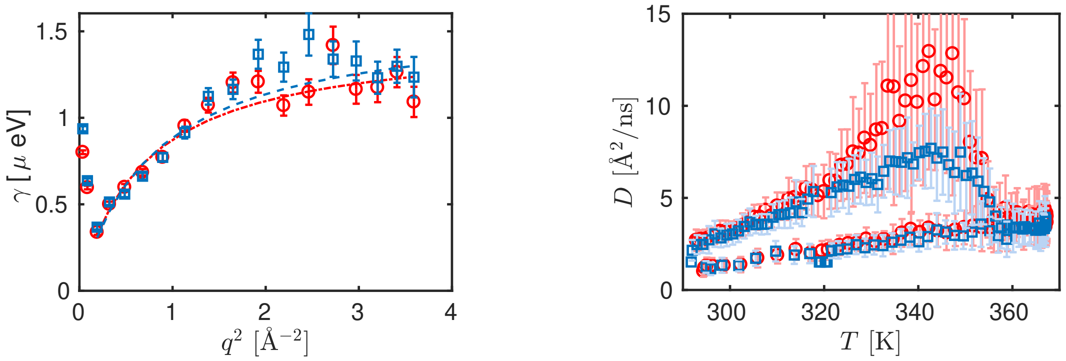

(c) *q-dependence of* γ *obtained from the ratio at* $T = 300\,\mathrm{K}$ *on the heating ramp. For each q value, an individual calibration curve was calculated.*

(d) *Temperature-dependent diffusion coefficients obtained from fitting the q dependence of* γ.

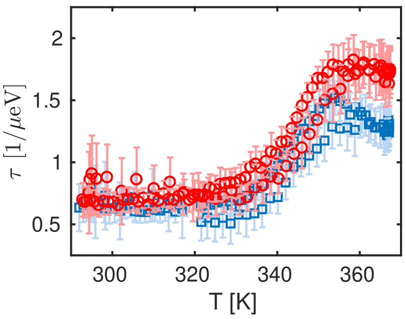

(e) *Temperature-dependent residence time* τ *obtained from fitting the q-dependence of* γ.

Figure 5.10: *Analysis of FWS measured on IN16B extracting diffusion coefficients from the ratio of EFWS and IFWS. The data shown were obtained for BSA solutions with* $c_p = 500\,\frac{\mathrm{mg}}{\mathrm{ml}}$. *Blue squares and red circles represent the sample without salt and with 150 mM NaCl, respectively.*

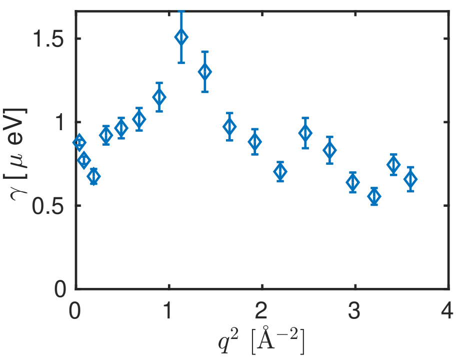

Figure 5.11: *γ as a function of q^2 of a BSA solution with $c_p = 150\,\frac{\text{mg}}{\text{ml}}$ at $T = 300$ K during the heating ramp. The decay of γ for $q^2 > 1.2\,\text{Å}^{-2}$ clearly points out the limits of the method presented.*

5.7 Analysis of FWS as Sparse QENS Signals

The previous Sections 5.4 and 5.5 focused on the evaluation of the EFWS. Apart from the EFWS, it is also possible to measure FWS with a fixed energy transfer $\hbar\omega$. In Section 5.6, an approach was presented which used the IFWS at $\hbar\omega = 1.3\,\mu\text{eV}$ in combination with EFWS to obtain an effective diffusion coefficient. While Section 5.4 described a model free approach, Section 5.5 and 5.6 already used knowledge and assumptions from the total QENS fits. This approach can be expanded by using a higher number of IFWS and therefore increase the number of independent sampling points. By doing so, either models approaching a model free analysis or more complex models offering access to more characterizing parameters can be used to describe the data. This section will show first approaches of sparse QENS fits based on FWS, which are recombined to QENS spectra with a very limited amount of energy transfers.

To evaluate these IFWS, the knowledge obtained from full QENS measurements can be used to construct a fit function. FWS performed in a sequential order can be grouped into a sparse QENS spectrum and can then be analyzed similarly to the QENS spectra.

While the polynomial approach presented above is a model-free approach to analyze the EFWS, the approach presented here is not model-free anymore but relies on existing knowledge from QENS results. On the one hand, it can allow to observe faster kinetic changes in the system (*e.g.* on a timescale of several minutes instead of several hours). On the other hand, it might lead to systematic errors if the system changes in a way that invalidates the model used.

Depending on the number of fit parameters used in the model and the energy transfers available, fits can either be performed similarly to the classical QENS analysis for each momentum transfer separately or they can be performed taking the energy and momentum transfers into account simultaneously. It is also possible to fit several spectra simultaneously, if appropriate models are used.

As a first step, the modeled data from Section 5.3 was evaluated at the energy offsets mentioned in Equation 5.9. The FWS obtained were regrouped to sparse QENS and were then fitted with the same model used to construct them (*i.e.* Equation 5.1-5.6). With this approach it can be tested if the offsets measured are sufficient to sample the features of the scattering function and to obtain reliable fit results.

Figure 5.12 shows the fit of the modeled sparse QENS spectra at $q = 1\,\text{Å}^{-1}$. The fit results are given in Table 5.2.

In a second approach, the model parameters describing the EISF are fixed to reduce the amount of fit parameters, which should render the fit more robust but might also introduce systematic errors. The fit results (shown in Table 5.2 for the different fit approaches) indicate that for the given offsets, the fit model is able to reproduce the data. It should be emphasized again that the modeled data set does not include statistical errors and solvent contributions are not accounted for.

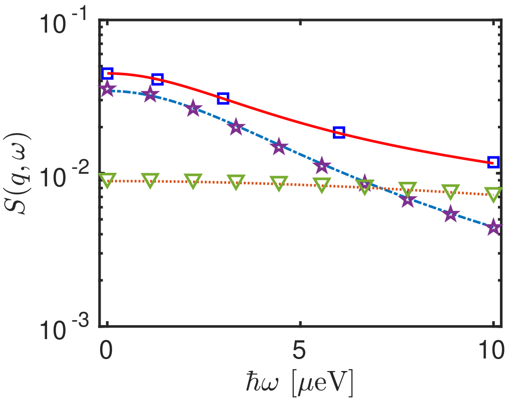

Figure 5.12: *Fit results of the global fits using the modeled sparse QENS spectra (blue squares) from Section 5.3. The shown data points represent the fit at* $q = 1\,\text{Å}^{-1}$*. The solid, dashed-dotted and dashed lines represent the total fit as well as the fitted global and internal diffusion, respectively. The fit results and the parameters used to model the scattering function are given in Table 5.2. Green triangles and violet stars represent the modeled values for internal and global diffusion, respectively.*

To test the model using experimental data, FWS measurements of BSA solutions during heating ramps ($280\,\text{K} < T < 370\,\text{K}$) are used. The model based on Equations 5.1-5.6 has to be expanded to respect the contribution of the solvent to describe the data. In addition, the detector efficiency has to be taken into account. Therefore, the model described in Equations 4.1 was used to fit the FWS obtained experimentally. The EISF was parametrized using Equation 5.3-5.6 and the parameters were fixed to $a = 1.5$ Å, $R = 10$ Å, $s = 0.35$ and $p = 0.2$ to reduce the number of fit parameters and to yield more reliable fit results. Since the different FWS were measured during one continuous heating ramp but no temperature corrections were performed, this method leads to a small systematic error. This error depends on the heating and cooling ramps. The fit handles three global parameters and one scaling parameter for each q, using the described model. An example of a fit result is shown in Figure 5.13. The temperature-dependence of the fit results is displayed in Figure 5.14. The temperature-dependent fit results of the global diffusion (Figure 5.14a) indicate that the fit has at least two minima. While the first minimum leads to fit results with small errors (brightly colored symbols), the other minimum yields fit results with significantly larger errors (lightly colored symbols). This might be due to the fixed parameters of the EISF since wrongly fixed parameters might induce minima in the χ^2 landscape. Another possible reason for these fit instabilities could be the limited number of sampling points. It should be mentioned that the fit results with the smaller errors, which would be normally assumed to be more reliable, are significantly lower than the parametrization obtained from full NBS spectra by Grimaldo *et al.* [64]. The results with larger errors, on the other hand, agree well with the previously determined parametriza-

Table 5.2: *Results of the fit of Equations 5.1-5.6 to the modeled sparse QENS spectra with and without fixed EISF. The different parameters used for modeling are also given.*

	D $\left[\frac{\text{Å}^2}{\text{ns}}\right]$	D_{int} $\left[\frac{\text{Å}^2}{\text{ns}}\right]$	τ_{int} [ps]
values used for modeling	5	30	10
free EISF	4.99±0.017	29.47±0.25	10.21±0.76
fixed EISF	5.01±0.006	29.83±0.13	10.88±0.22

	R [Å]	a [Å]	s	p
values used for modeling	10	1.5	0.35	0.2
free EISF	10.04±0.034	1.52±0.012	0.35±0.003	0.20±0.002
fixed EISF	-	-	-	-

tion. The temperature dependence of the residence time of the internal diffusion (Figure 5.14b) points out the limits of this fit approach. Since only a relatively small energy transfer interval is covered with the FWS ($\hbar\omega \leq 10\,\mu\text{eV}$), contributions with features mainly situated at higher energy transfers cannot be resolved and might contribute as apparent flat backgrounds.

To conclude, in this section, an alternative approach to analyze the FWS was described. On the one hand, a significantly higher time resolution was observed in the case of the FWS analysis. On the other hand, using the FWS implies a significant amount of modeling, while the analysis of the full QENS spectra can indicate a wrong choice in the model. In addition, the fit model might have to be significantly simplified compared to full QENS spectra analysis due to the smaller energy transfer interval investigated.

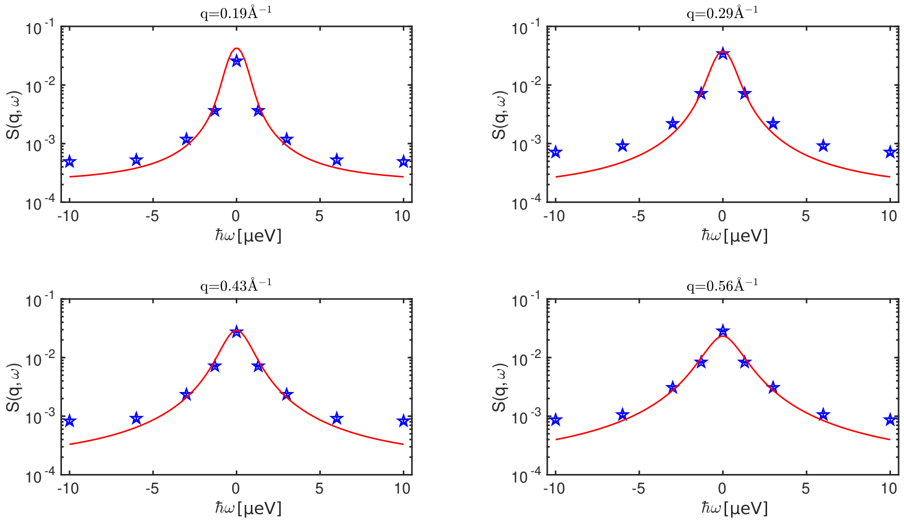

Figure 5.13: *Fit of the sparse QENS (blue diamonds) obtained from FWS collected during a heating ramp of a BSA solution ($c_p = 500\,\frac{\mathrm{mg}}{\mathrm{ml}}$) with $c_s = 150\,\mathrm{mM}$ NaCl. The EFWS was performed at $T = 300\,\mathrm{K}$. The subplots show different momentum transfers. Error bars are smaller than the symbols.*

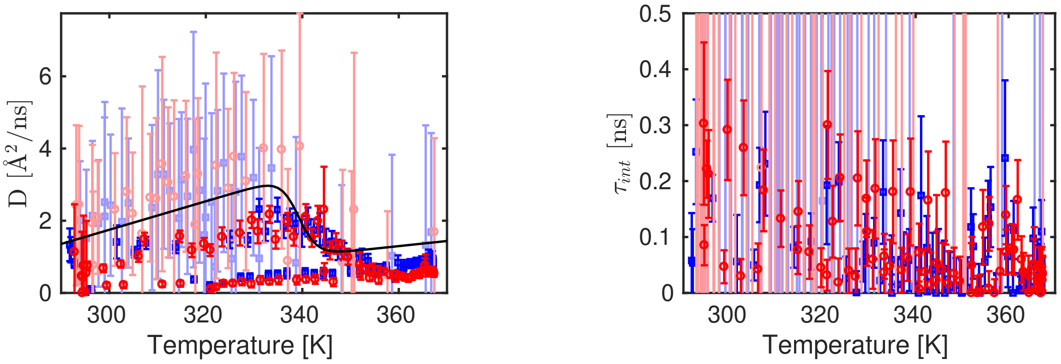

(a) *Temperature-dependent global diffusion coefficient from the sparse QENS fit. The solid line represents the parametrization obtained from full QENS spectra [64].*

(b) *Temperature-dependent residence time characterizing the assumed jump diffusion describing the internal diffusion.*

Figure 5.14: *Temperature-dependent fit results of the sparse QENS fit analysis. Blue squares and red circles represent the fit results of samples ($c_p = 500\,\frac{\mathrm{mg}}{\mathrm{ml}}$) with and without NaCl (150mM), respectively. Light and bright symbols represent fit results of the different fit minima.*

5.8 Generalized Mean Squared Displacements

Similar to the analysis performed in Section 5.4.1, the IFWS could be analyzed using a polynomial approach. As explained in Ref. 229, the generalized MSD can be extracted, corresponding to a Fourier transform truncated by the resolution function of the time-dependent MSD obtained from the EFWS.

Starting from the MSD, the generalized MSD decays with increasing energy transfers investigated. At a specific energy transfer, the generalized MSD is zero, before it gets negative at higher $\hbar\omega$. This transition point as well as the trend in $\hbar\omega$ depend on the type of diffusive process. Based on this knowledge, it is possible to extract information from the MSD about the type of diffusion as well as of its characterizing quantities. In addition, this method allows to extract information about the confinement of the diffusive processes.

To test this analysis approach, the modeled data was fitted using a first order polynomial function in q^2. The slope was then related to the generalized MSD:

$$\left\langle u^2 \right\rangle_\omega = -\lim_{q \to 0} \frac{3}{q^2} \log \left[\frac{S_{mod}(q,\omega)}{\hat{R}(\omega)} \right]. \tag{5.22}$$

The intersection point with the ordinate, kept as free fit parameter in this approach, might be fixed based on the resolution function, as it is visible in Equation 5.22. In Figure 5.15a, the logarithmic modeled data of the FWS are shown using the the q values available on IN16B as well as the offsets measured. To perform the linear fit, the first three q values were selected. While for the EFWS and for the IFWS at $\hbar\omega = 1.3\,\mu\text{eV}$, the q dependence can be described well by the linear approach and the fit range might be expanded, the sampling point density at the other offsets is not high enough, to obtain reliable results. This is also represented in the increasing errors shown in Figure 5.15b.

If the sample point density would be increased both in q and $\hbar\omega$, the modeled data offer access to the expected generalized MSD (see Figure 5.15c and Figure 5.15d.

Several points should be mentioned concerning this analysis. Decreasing the lower limit of the q range used for the fit is problematic, since at the present construction, the single detector (SD) covering the two lowest scattering vectors q have a slightly worse energy resolution and detect energy transfers with an offset compared to the ones of the position-sensitive detector (PSD). In addition, at low scattering vectors q, the coherent contributions have a non-negligible contribution which is not included in the model used to construct the fit function. These problems might be partly addressed by characterizing the energy offset between the SD and the PSD and by performing a global fit respecting these differences. Also, expansions of the fit models to higher q values will be of interest, since in this case, data colleced with the PSD could be used.

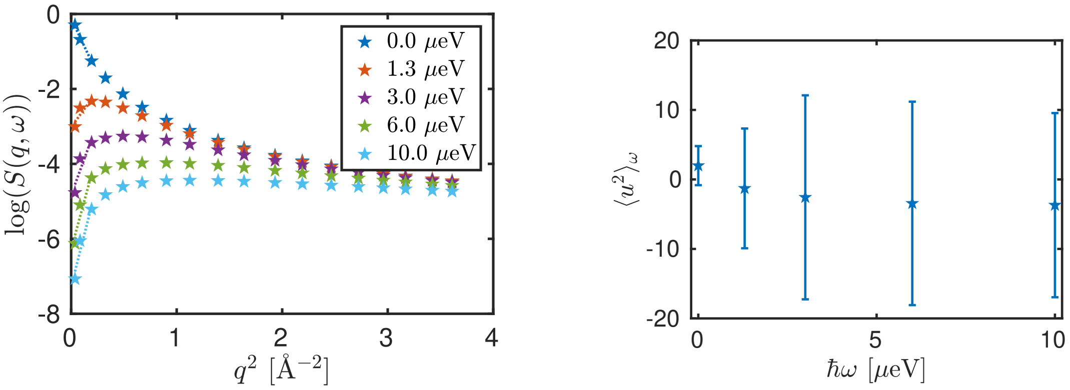

(a) *Modeled FWS with corresponding linear fits as a function of q using the experimentally available sampling points.*

(b) *Generalized MSD as a function of energy transfer obtained from fits using sampling points available in the experiment.*

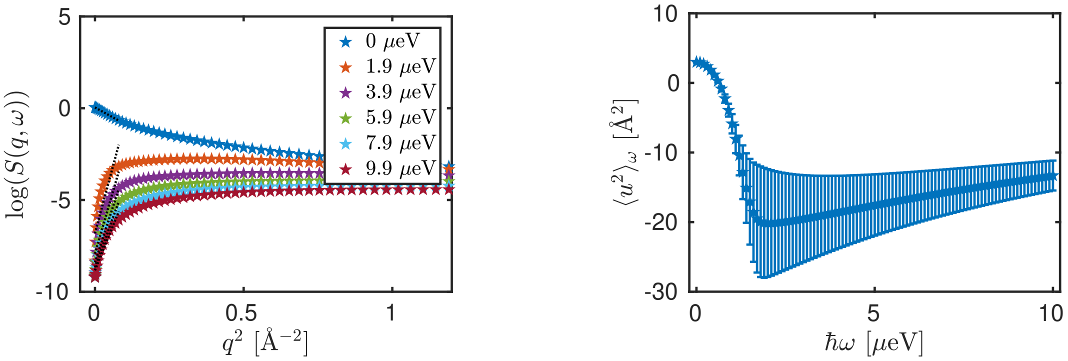

(c) *Modeled FWS with corresponding linear fits as a function of q using a higher sampling point density as experimentally. For reasons of clarity, not all fits (black dotted lines) are shown.*

(d) *Generalized MSD as a function of energy transfer obtained from fits in Figure 5.15c.*

Figure 5.15: *Analysis to obtain the generalized MSD using modeled FWS.*

5.9 Outlook

During the acquisition of EFWS, the monochromator crystal is in a well-defined position and its focus does not change. For IFWS, the monochromator crystal moves during the exposition and the detector integrates the signal. Therefore, the focus of the neutron beam changes during the acquisition. This results in two fundamentally different measurements, which might lead to systematic errors. Recent measurements showed that these effects are negligible for IN16B. Nevertheless, to avoid them, it might be of interest to measure very low energy transfers instead of EFWS. This approach is also of interest in the case of elastic contributions to the scattering signal, where the application of this method with using the EFWS would fail, since several contributions are predominant at the elastic position.

Nevertheless, by using two different non-zero offsets, the global diffusion as well as the fraction of immobile proteins could be determined. In a second step, this knowledge could be used to determine the contribution of immobile scatterers. If FWS are compared to full QENS spectra, no significant changes are observed in the monitor normalized data collected on the PSD. For the SD, significant deviations can be found between the FWS and the QENS spectra. Further tests are needed to understand these deviations.

For all analysis methods mentioned here, it should be emphasized that given the significantly lower amount of experimental data, less information can be extracted from the collected spectra compared to full QENS spectra. Therefore, more modeling, *e.g.* based on analysis of full QENS spectra, might be necessary.

Once a suitable model is found, FWS can be used to follow rather fast kinetic changes of the short-time diffusive properties. The analysis methods presented here, therefore, offer the possibility to address new scientific questions, *e.g.* to investigate the diffusion of proteins while crossing temperature or through pressure dependent phase boundaries.

Chapter 6

Protein Short-Time Diffusion in a Naturally Crowded Environment

Chapter 6 is based on the following publication:

Protein Short-Time Diffusion in a Naturally Crowded Environment

Marco Grimaldo, Hender Lopez, Christian Beck, Felix Roosen-Runge, Martine Moulin, Juliette M. Devos, Valerie Laux, Michael Härtlein, Stefano Da Vela, Ralf Schweins, Alessandro Mariani, Fajun Zhang, Jean-Louis Barrat, Martin Oettel, V. Trevor Forsyth, Tilo Seydel, Frank Schreiber

J. Phys. Chem. Lett. 10 (2019) 1709

DOI:10.1021/acs.jpclett.9b00345

Publication Date (Web): March 21, 2019

Contributions:

Research design	MG, CB, FRR, FZ, JLB, MO, VTF, TS, FS
Experiments	MG, CB, FRR, MM, JMD, VL, MH, SdV, RS, AM, FZ, VTF, TS
Theory/Simulations	HL, FRR, JLB, MO
Data Analysis and interpretation	MG, HL, CB, FRR, SdV, FZ, JLB, MO, TS, FS
Paper Writing	all authors

M. Grimaldo *et al.* [230]

The interior of living cells is a dense and polydisperse suspension of macromolecules. Such a complex system challenges an understanding in terms of colloidal suspensions. As a fundamental test we employ neutron spectroscopy to measure the diffusion of tracer proteins (immunoglobulins) in a cell-like environment (cell lysate) with explicit control over crowding conditions. In combination with Stokesian dynamics simulation, we address protein diffusion on nanosecond timescales where hydrodynamic interactions dominate over negligible protein collisions. We successfully link the experimental results on these complex, flexible molecules with coarse-grained simulations providing a consistent understanding by colloid theories. Both experiments and simulations show that tracers in polydisperse solutions close to the effective particle radius $R_{\mathrm{eff}} = \sqrt[3]{\langle R_i^3 \rangle}$ diffuse approximately as if the suspension was monodisperse. The simulations further show that macromolecules of sizes $R > R_{\mathrm{eff}}$ ($R < R_{\mathrm{eff}}$) are slowed more (less) effectively even at nanosecond timescales, which is highly relevant for a quantitative understanding of cellular processes. Living cells are filled with a polydisperse mixture of proteins and other macromolecules (including DNA, RNA and polysaccharides) suspended in water at high volume fractions (typically 10–40%). The varying crowding levels of proteins in living cells may affect their mobility, folding and stability, and thus the physical chemistry and physiology of cells [231–233]. Several experimental studies have addressed protein diffusion *in vivo* [178, 234–238] and *in vitro* [109, 120, 131, 239–245], mostly by means of NMR, fluorescence spectroscopy, and neutron scattering, and the topic has also been the subject of several computational studies [60, 246–249]. In general, protein diffusion was found to decrease with increasing crowding, although the details of how diffusion is modified by different cellular microenvironments are still unclear [246].

A quantitative theoretical understanding of diffusion is generally easier in connection with *in vitro* studies, which offer better control on many physical parameters such as types of crowding agents, macromolecular concentration, and temperature. Hence, they are better suited to systematic investigations regarding such parameters, although at the expense of simplifying the complex physiological environment, which is instead fully captured by *in vivo* studies. These, in turn, suffer from the lacking flexibility in changing specific cellular conditions. Here, we establish a framework combining both approaches with the use of tunable cell lysate. At the same time, in our simulations we go beyond standard colloidal modelling (using monodisperse crowders) and explicitly take into account the polydispersity of a cellular environment. In that way, we understand the influence of a cell-like crowded environment on the short-time diffusion of polyclonal γ-globulin from bovine blood (Ig), used as model nonspherical proteins, based on simple biophysical concepts. To perform a controlled experiment under rather realistic conditions, *Escherichia coli* cells were adapted to a fully deuterated environment as previously described [250]. The cells were then lysed and the membranes were removed. Subsequently, the cell material was collected and concentrated to produce the lysate (cf. Supporting Information (SI)). Perdeuterated lysate was used as a cytosol-mimicking polydisperse crowded environment. The concentrations c_{Ig} and c_{lys} of Ig and the lysate, respectively, were varied, covering a total volume fraction range $6\% \lesssim \varphi \lesssim 17\%$ and ratios $0.4 \lesssim \varphi_{\mathrm{Ig}}/\varphi \lesssim 0.8$ (φ_{Ig} is the Ig volume fraction) to systematically investigate the influence of different polydispersity. Macromolecular mass fractions of protein (82.5%), nucleic acids (14.5%), and lipids (1%) were experimentally estimated, and an additional 2% mass fraction of sugars was assumed [251]. An average partial specific volume $\nu_{\mathrm{lys}} = 0.66\,\mathrm{ml/g}$ for the macromolecular components of lysate was calculated accordingly [252, 253] (cf. Supporting Info (SI)). Small angle neutron scattering (SANS) [254], as well as (ultra) small angle X-ray scattering (USAXS/SAXS) [255] and static light scattering (SLS) were used to further characterize the lysate and qualitatively assess the batch-dependence of the lysate composition, as well as to check for potential aggregation of Ig in lysate (see the SI for details). The data indicate that, as expected, the lysate contains macromolecules and assemblies having a very broad range of shapes and length scales up to several micrometers, as seen by small angle X-ray scattering. The precise composition varied between the different batches used in this study. This polydispersity and variation of the lysate composition is important in testing the generality of the observations and the robustness of the results. It also contributes to having environments that are as realistic as possible. Solutions of the polyvalent Igs used in the present work were previously studied by Da Vela *et al.* [256], who found them stable at the concentrations considered here. Our additional SANS data show that Ig aggregation upon addition of lysate is negligible in our system.

Neutron backscattering (NBS) was employed to record incoherent quasi-elastic neutron scattering (QENS). This technique has, amongst others, the advantage of being label-free, non-invasive, and non-destructive. In this system, NBS probes predominantly the ensemble-averaged single-particle self-correlation function of the ^{1}H-atoms. The other types of atoms, including deuterium ($\mathrm{D} = {}^2\mathrm{H}$), possess a significantly smaller neutron scattering cross-section, and therefore contribute less to the total scattering intensity. In other words, only the use of heavy water (D_2O) and perdeuterated lysate sufficiently increases the contrast of the Igs of natural isotopic abundance with the background, allowing us to focus on the dynamics of the Ig tracers. Hence, neutrons are a unique probe for the determination of the self-diffusion (rotational and translational), or synonymously tracer diffusion, of the model proteins.

On the picosecond to nanosecond timescale and nanometer length scale probed by NBS, proteins typically do not diffuse sufficiently to collide with surrounding molecules, but naturally interact with the environment through hydrodynamic interactions (HI) in this regime of short-time diffusion. In addition to the experiments, we perform computer simulations providing accurate information on the diffusion of proteins in crowded environments [247, 248]. Simulations were recently successfully employed to interpret and rationalize neutron scattering experiments [78, 257]. Because of the timescales and the relevance of HI in our experiments, we perform simulations based on Stokesian Dynamics [258, 259] in which HI are considered explicitly and short-time properties can be calculated. Knowledge on the short-time diffusion as well as HI and its dependence on volume fraction is not only of fundamental intrinsic interest, but is also a prerequisite to quantitatively predict and correctly interpret the long-time diffusion [260–263] relevant for several biochemical processes [260], and being strongly influenced by protein-shape effects [264]. These processes include any diffusion-limited mechanism involving two or more macromolecules, such as the formation of protein complexes [265], the binding of enzymes to substrates [266], or protein aggregation [267], as well as the assembly of intercellular structures such as tubulin and actin filaments, and signal transduction [260].

To investigate the short-time self-diffusion of Ig in lysate, we employ QENS using IN16B [191]. With QENS, the scattering function $S(q,\omega)$ is recorded, where $\hbar\omega$ is the energy transfer and q is the scattering vector. A spectrum $S(q,\omega)$ of a mixture of Ig at a concentration of 67 mg/ml and lysate at 56 mg/ml at $q = 0.29\,\text{Å}^{-1}$ is shown in the insets of Figure 6.1 (red circles), after subtraction of the empty cuvette signal [67, 268] and of the lysate contribution as explained in the SI. The data can be well described by a sum of three Lorentzian functions $\mathscr{L}(\ldots,\omega)$ (green solid line, see eq. (6.1)) modeling a slow process with line broadening $\gamma(q)$ (blue dot-dashed line), a faster process with line broadening $\gamma(q)+\Gamma(q)$ (magenta dashed line), and the separately obtained solvent contribution (orange dotted line) with fixed values for both width $\gamma_{\mathrm{D_2O}}(q)$ and intensity $\beta_{\mathrm{D_2O}}(q)$ as explained in the SI:

$$\begin{aligned} S(q,\omega) = \mathscr{R} \otimes \{\beta(q)[A_0(q)\mathscr{L}(\gamma(q),\omega)\ldots \\ \cdots + (1-A_0(q))\mathscr{L}(\gamma(q)+\Gamma(q),\omega)]\ldots \\ \cdots + \beta_{\mathrm{D_2O}}(q)\mathscr{L}(\gamma_{\mathrm{D_2O}}(q),\omega)\}\ . \end{aligned} \tag{6.1}$$

In Equation 6.1, $\mathscr{R}$ represents the instrumental resolution function, $\beta(q)$ a scalar scaling factor, and $A_0(q)$ the elastic incoherent structure factor [61].

For the slower process, the relationship $\gamma(q) = Dq^2$ (red solid line in Figure 6.1) is not imposed, but arises naturally from independent fits of the spectra at each q. This q^2 scaling indicates that, on the timescale ranging from tens of picoseconds to a few nanoseconds accessible by NBS, immunoglobulins undergo a simple Fickian diffusion with apparent diffusion coefficient D (including both translational D_t and rotational D_r contributions [109]), even in the presence of lysate. For most samples, the dependence $\gamma \propto q^2$ holds well on the entire q-range. However, for the samples with the lowest signal-to-noise ratio, a stronger deviation is seen for $q^2 \gtrsim 1.5\,\text{Å}^{-2}$, presumably because the signal from this component weakens at high q. Hence, to avoid artifacts, we restrict the fit of $\gamma(q)$ to $q^2 < 1.5\,\text{Å}^{-2}$ for all samples.

The apparent diffusion coefficients D obtained from samples measured at temperatures $T = 293 \pm 2\,\text{K}$ are plotted versus φ in Figure 6.2. The grey Δ-symbols refer to suspensions of Ig in pure $\mathrm{D_2O}$, in the absence of lysate. In this case,

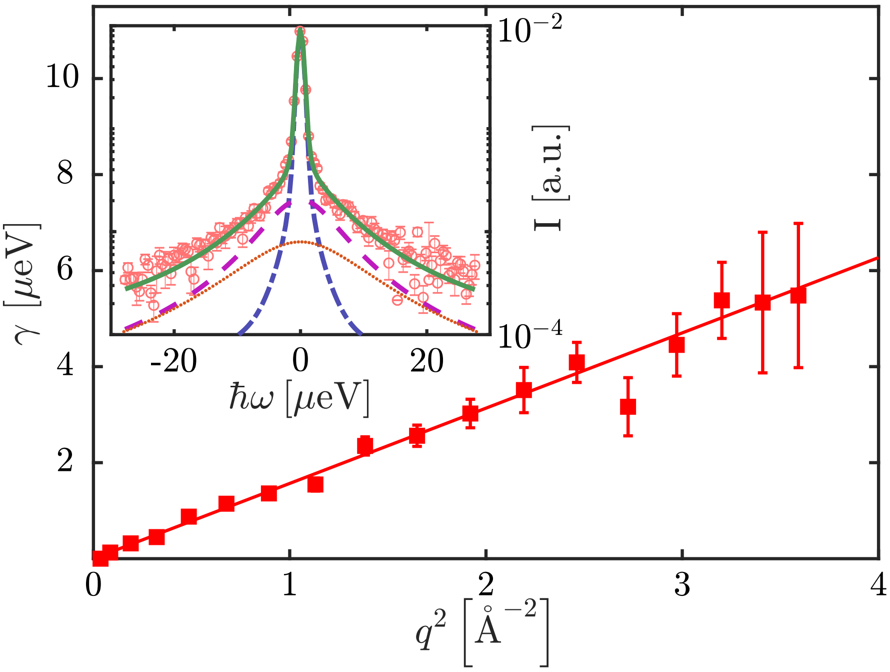

Figure 6.1: *Example of quasi-elastic neutron scattering data. Inset: Scattering function $S(q,\omega)$ (red circles) of Ig at a concentration of 67 mg/ml in E. coli lysate at 56 mg/ml at $T = 293\,K$ after subtraction of the lysate contribution, at $q = 0.29\,\text{Å}^{-1}$. The points were rebinned in the plot, for clarity. The lines depict the Lorentzian functions $\mathscr{L}(\gamma(q),\omega)$ (blue dot-dashed) $\mathscr{L}(\gamma(q)+\Gamma(q),\omega)$ (magenta dashed) and $\mathscr{L}(\gamma_{D_2O}(q),\omega)$ (orange dotted) in eq. (6.1). The green solid line superimposed on the data is the result of the complete fit using eq. (6.1). Main figure: Half width at half maxima γ (red squares) vs. q^2. The fit $\gamma(q) = Dq^2$ (solid red line) indicates a simple Brownian diffusive behavior. The fit range is restricted to $q^2 < 1.5\,\text{Å}^{-2}$.*

$\varphi = c_{\text{Ig}} \cdot \nu_{\text{Ig}}$, where c_{Ig} and $\nu_{\text{Ig}} = 0.739\,\text{ml/g}$ are the concentration and the partial specific volume of Ig [269], respectively. The dashed line depicts a polynomial fit to that data, providing an empirical function $D_p(\varphi)$ describing the effect of self-crowding on the apparent short-time self-diffusion of Ig.

The other symbols in Figure 6.2, each representing one lysate batch, show D of Ig in Ig-lysate mixtures as a function of φ. In this case, $\varphi = c_{\text{Ig}} \cdot \nu_{\text{Ig}} + c_{\text{lys}} \cdot \nu_{\text{lys}}$, where c_{lys} and ν_{lys} are the concentration and the partial specific volume of the lysate components, respectively.

Overall, D in the presence and absence of lysate decreases with increasing φ in a remarkably similar manner, despite the striking difference in the crowded environment. The physical reasons for this surprising result will become clear below. The value of the reduced mean squared deviation $\tilde{\chi}^2 \simeq 0.38$ of the data obtained in the presence of lysate from the fit $D_p(\varphi)$ for the data obtained in pure

Ig solutions quantitatively supports their excellent agreement. As translational-rotational coupling is strongly protein specific [243], we intentionally do not separate both contributions based on unsupported assumptions. The good agreement of $D(\varphi) = D(D_t(\varphi), D_r(\varphi))$ for the samples with and without lysate suggests that the type of crowder is unimportant for both of D_r and D_t.

This observation is further clarified in the inset of Figure 6.2, where D is plotted as a function of $D_p(\varphi)$: the Ig-lysate data points all lie close to the line $D = D_p(\varphi)$, with φ including the volume fraction of both Ig and the components of lysate. Within the experimental accuracy, no systematic influence on $D(\varphi)$ of the specific lysate batch is visible.

It is worth noting that the internal dynamics parameters of the function fitting the NBS spectra of Ig in the presence of lysate are found consistent with the self-crowded Ig solution (see SI). This finding suggests that the use of perdeuterated lysate may also be suitable for studies of protein internal fluctuations.

To gain further insight into the slowing down of the diffusion of Ig in lysate and the underlying physical mechanisms, we performed simulations based on Stokesian dynamics [258, 259] (see SI). The method adopted only includes translational velocity-force coupling (as in [248]), thus only translational short-time diffusion is considered in the simulations. To mimic the biomolecular crowded environment of the experiments, the simulated lysate solutions are represented by a set of spheres of different sizes. We study two models for the *E. coli* cytoplasm, by McGuffee and Elcock [247] (ME) and by Ando and Skolnick [248] (AS), respectively. Both models have a similar average radius, 3.53 nm for the ME model and 3.64 nm for the AS model, but they represent rather different size distributions as described by their polydispersity index α defined as the standard deviation normalized by the mean of the distribution. For the ME model $\alpha = 1.05$, while for the AS model $\alpha = 0.51$ (for details regarding the size distributions see the SI). This simulation model is still a gross simplification in the description of an Ig-lysate suspension. Notably, Ig and the components of lysate are non-spherical and also have some internal flexibility. Nevertheless, with this model we capture the correct size range and size distribution, which can be assumed to be the main factors influencing the hydrodynamic interactions.

Choosing two intracellular environments not only allows the evaluation of the effect of crowding on the diffusion of Ig but also of the sensitivity to the polydispersity of the solution. To reproduce the experimental conditions, tracers are added to the chosen lysate, and the short-time diffusion is calculated as explained in the SI. The parameter $y_{\mathrm{tr}} = \varphi_{\mathrm{tr}}/\varphi$ is defined, where φ_{tr} is the volume fraction occupied by the tracers and φ the total volume fraction in the simulations, *i.e.*, $\varphi = \varphi_{\mathrm{tr}} + \varphi_{\mathrm{lys}}$ with φ_{lys} the volume fraction of the lysate. In all cases, the number of particles of the lysate was fixed (1001 for the ME model and 1000 for the AS model), and the size of the simulation box and the number of tracer particles was varied.

The insets of Figure 6.3 and Figure S7 show D_{tr}/D_0 for a tracer of the size of Ig ($R_{\mathrm{tr}} = 5.5$ nm) as a function of D_{mono}/D_0 for the ME and AS lysate model, respectively, where $D_0 = k_B T/6\pi\eta R$ (η being the solvent viscosity) is the dilute limit translational diffusion coefficient, D_{mono} is the translational diffusion coefficient of the tracer particles in a monodisperse solution with same total φ. D_{tr} is the translational diffusion coefficient of the tracer particles in the polydisperse mixture. In both the ME and AS model, $y_{\text{tr}} = 0.3$, 0.5, and 0.7 (nearly coinciding symbols) are presented for $\varphi = 0.1, 0.2$, and 0.3. The deviations from the monodisperse situation are small, indicating that despite the rather complex composition of the suspensions, for a tracer of the size of Ig diffusing in a cellular-like environment only small differences should be expected when compared to an equivalent system (*i.e.* with the same φ) composed solely of Ig under the present conditions. Additional simulations performed with different tracer radii show that the size of the tracer determines whether the normalized short-time diffusivities decrease or increase compared to the monodisperse case. Figure 6.3 depicts the ratio $D_{\text{tr}}/D_{\text{mono}}$ for different φ and y_{tr} versus the normalized tracer radius (filled symbols). The normalization of the tracer radius by $R_{\text{eff}} = \sqrt[3]{\langle R_i^3 \rangle}$ (angle brackets denote an average over the entire distribution of spheres in the model) is based on diffusion theory of colloids [271]. The leading order hydrodynamic interactions for the translational self-diffusion between two classes of spheres A (radius R_A) and B (radius R_B) is given by [271]

$$D_{A0} - D_A \propto R_B^3 R_A \int_0^\infty \mathrm{d}r\, g_{AB}(r)/r^2 \,. \tag{6.2}$$

Therein, D_A is the translational diffusion coefficient of a sphere of class A at finite concentration and D_{A0} is its dilute limit. Thus, neglecting the effects encoded in the partial radial distribution function $g_{AB}(r)$ and higher-order lubrication effects, a rough measure for the effective radius of a polydisperse crowder solution would be based on the average of R_B^3 for all particles classes B, *i.e.* R_{eff}. Accordingly, a tracer of radius $R_{\text{tr}} \approx R_{\text{eff}}$ is expected to behave similarly to the monodisperse situation. Indeed, $D_{\text{tr}}/D_{\text{mono}} \approx 1$ for tracer radii around R_{eff} for all compositions, indicating diffusion in polydisperse solutions comparable to monodisperse solutions. For smaller and for larger tracer radii, the deviation $|D_{\text{tr}}/D_{\text{mono}} - 1|$ becomes larger. The same trend is observed for the spheres composing the model lysate (empty symbols in Figure 6.3), the smallest spheres being more strongly affected by the polydispersity than the large ones. Furthermore, it is noted that increasing the level of crowding results in larger deviations from the monodisperse case for particles of radius larger or smaller than R_{eff}. Similar results are also obtained for the AS model (Figure S7), showing that, despite the difference in the polydispersity between both lysate models, as indicated by their α values, the observed trend is not affected.

When comparing the hydrodynamic radius of Ig, R_{Ig}, to the effective radii of the lysate-protein solutions, a ratio $R_{\text{Ig}}/R_{\text{eff}} \approx 0.9 - 1.3$ is obtained, which explains the observed insensitivity to polydispersity. The simulation clearly indicates that this experimental observation is limited to proteins of a rather large size. We remark that, in the absence of the tracers, $R_{\mathrm{eff}} \simeq 3.95\,\mathrm{nm}$ and $4.68\,\mathrm{nm}$, for the ME and AS distribution, respectively. In both cases, R_{eff} is significantly larger than the mean radius of the distribution, and thus most macromolecules (ME $\approx 92\,\%$, AS $\approx 87\,\%$) are expected to diffuse faster in the cytoplasm than in a monodisperse system at the same volume fraction. However, *e.g.* ribosomes as a very abundant macromolecular complex in the cytosol [272] with a radius around 10 nm would be strongly slowed down compared to monodisperse conditions. The simulation results suggest that polydispersity in the cytosol causes the general trend to slow down larger macromolecules more strongly than smaller particles *via* hydrodynamic interactions already at nanosecond timescales, before proteins collide. This slowing down will then unavoidably affect also molecular mobilities and escape rates for the descriptions of long-time processes. Our results imply that the dynamical heterogeneity of a structurally heterogeneous system is significantly increased by crowding, which obviously has numerous implications for the understanding of the cellular machinery. We remark that our results based on the hydrodynamic interactions in the diffusive short-time limit cannot be directly transfered to the long-time regime, where other factors such as direct potential interactions might be comparable to the effect of polydispersity.

In summary, to gain a better understanding of the effect of macromolecular crowding on the picosecond to nanosecond protein self-dynamics under controlled but realistic conditions, a quasi-elastic neutron backscattering experiment was designed. In this study, the tracer diffusion of proteins of natural isotopic abundance in perdeuterated lysate mimicking the cellular environment was followed. In this way, we benefit from the incoherent contrast between tracer proteins naturally containing hydrogen and deuterated lysate and solvent (D_2O). In order to systematically investigate the influence of polydispersity on short-time diffusion, we vary the concentration of lysate and of the nonspherical model protein Ig and find its diffusive motion on a nanosecond timescale and nanometer length scale to be determined, within the current accuracy of the experiment, only by the volume fraction φ occupied by all macromolecules present (in this case $\varphi = \varphi_{\mathrm{Ig}} + \varphi_{lys}$). This observation is further corroborated by the fact that the different lysate batches with slightly different compositions lead to consistent results. Our experiments demonstrate the suitability of deuterated lysate as a tunable biomimicking crowding agent for neutron scattering experiments, which opens various opportunities for future systematic studies of the impact of a natural environment on protein global and internal dynamics.

The experimental results strengthen a conceptual connection of complex biological systems to quantitative accounts of statistical physics of colloids and coarse-grained simulations. We find that, for a crowder composition as in a living cell, the diffusion of tracers with a radius close to the ensemble effective radius $R_{\mathrm{eff}} = \sqrt[3]{\langle R_i^3 \rangle}$ is similar to a monodisperse system and weakly dependent on the tracer size. In contrast, for tracer radii differing significantly from R_{eff}, noticeable deviations are observed. The good qualitative agreement between experiments and simulations points to the major role of hydrodynamic interactions in determining the short-time protein diffusion, and shows that biophysical modelling based on colloid theory is capable of describing the macromolecular diffusion even in the more complex cellular environment. This outcome also confirms the generality of coarse-grained molecular dynamics simulations and allows to design simplified simulation setups for macromolecules in the cytosol.

Understanding how simple systems are slowed down by HI is essential to estimate the protein mobilities in different cellular compartments, and hence determine the time needed for a protein to come into contact with another protein, which is highly relevant for docking reactions and ligand transport. Our result that in a polydisperse system small proteins are slowed down less and larger particles more than in a monodisperse suspension is essential information for the understanding of the cellular physical chemistry and reaction pathways. In addition, this result is also relevant to the kinetics of the in-cell assembly of large structures.

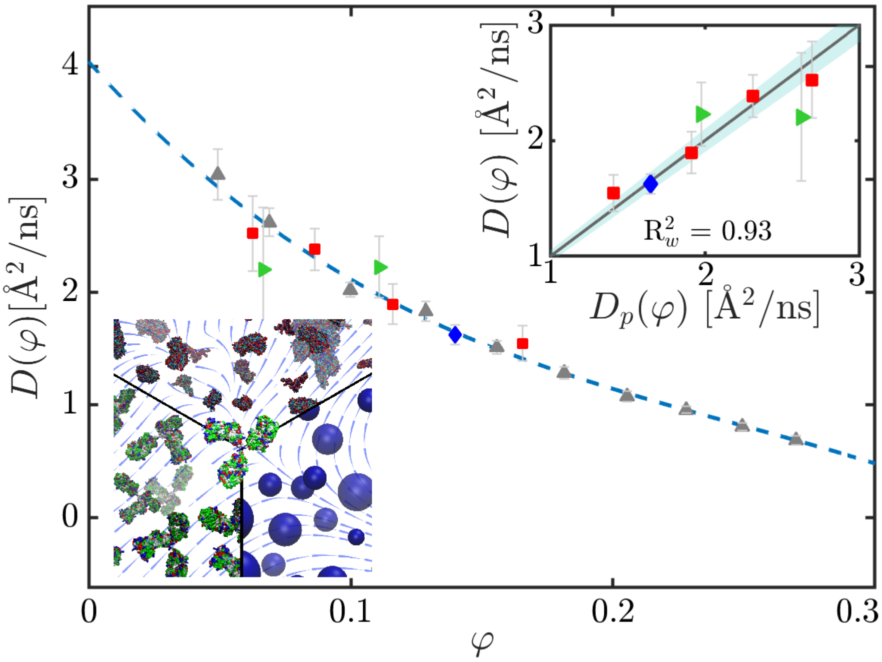

Figure 6.2: *Experimental agreement of immunoglobulin diffusion under polydisperse and monodisperse crowding. Main figure: Apparent diffusion coefficient* $D(\varphi)$ *as a function of the total volume fraction* φ, *i.e. the volume fraction of Ig and lysate combined. The symbols represent the experimental data recorded at* $T = 293 \pm 2\,K$. *Grey, pyramid symbols refer to samples of Ig in the absence of lysate, whereas other symbols and colors refer to Ig-lysate mixtures with different lysate batches (see the SI for the assignment of the batches). Finally, the dashed line depicts a polynomial fit* $D_p(\varphi)$ *of the diffusion of Ig in pure* D_2O. *Top inset: Apparent diffusion coefficient* $D(\varphi)$ *as a function of the polynomial function* $D_p(\varphi)$ *for the samples in the presence of lysate (*R_w^2 *is the weighted coefficient of determination [270]). The shaded area depicts a ±5% deviation of* $D(\varphi)$ *from* $D_p(\varphi)$. *Bottom inset: Artistic view of the two experimental systems (Ig-*D_2O, *bottom left, and Ig-lysate mixture, top) and of the simulations of hard-sphere suspensions (bottom right), all pointing out the importance of hydrodynamic interactions.*

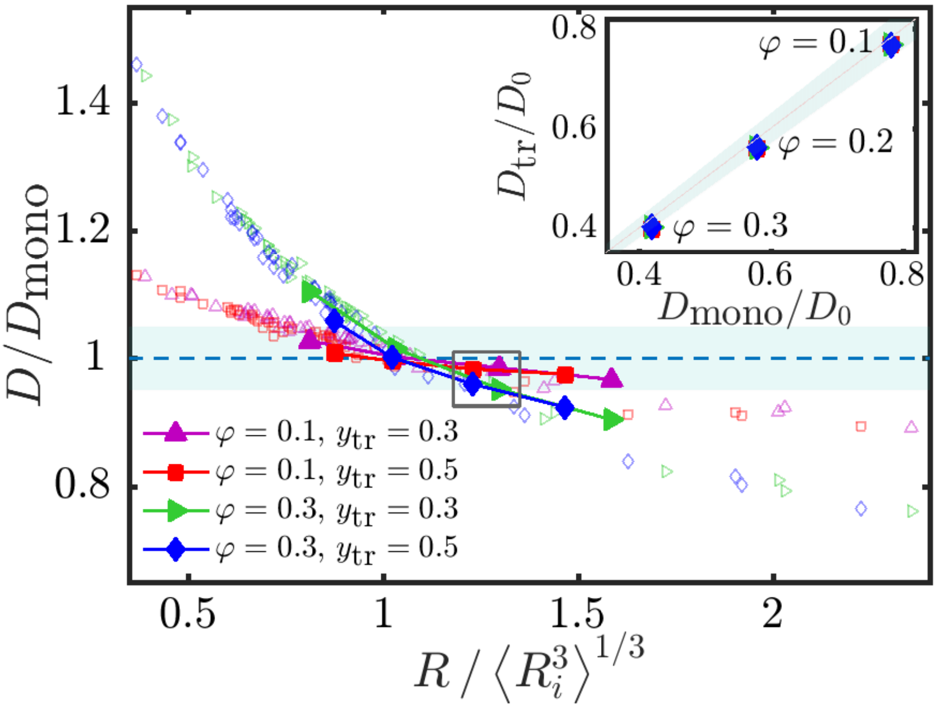

Figure 6.3: *Simulated difference (agreement for* $R \approx R_{\rm eff}$*) in particle diffusion between polydisperse and monodisperse crowding. Main figure: Normalized translational diffusion coefficient* $D/D_{\rm mono}$ *of spheres with radius* R*, plotted against the rescaled radius* $R/R_{\rm eff}$*.* $D_{\rm mono}$ *denotes the diffusion coefficient obtained in a monodisperse solution of spheres with radius* R *at similar volume fraction* φ*.* $R_{\rm eff}$ *is the effective radius* $R_{\rm eff} = \sqrt[3]{\langle R_i^3\rangle}$*, characterizing the crowding conditions in a mixture of spheres with radii* R_i*. The filled symbols depict the diffusion coefficients of the tracers at the ratios* $y_{\rm tr} = \varphi_{\rm tr}/\varphi$ *as specified in the legend, with the tracer volume fraction* $\varphi_{\rm tr}$*. In particular, the filled symbols within the grey rectangle refer to tracers with radius* $R_{\rm tr} = R_{\rm Ig}$*, as in the experiment. In this case, the deviations of the diffusion in the polydisperse environment from that in a monodisperse system are less than 5%. The empty symbols denote the diffusion coefficients of the crowders. These are plotted for the case* $R_{\rm tr} = R_{\rm Ig}$*. The plot refers to the ME lysate model. Inset: Reduced tracer diffusion coefficient* $D_{\rm tr}/D_0$*, where* D_0 *is the dilute limit diffusion coefficient, for a tracer of the size of Ig (*$R = R_{\rm Ig} = 5.5$ *nm) in a crowder from the ME model as a function of the reduced diffusion coefficient* $D_{\rm mono}/D_0$ *in the monodisperse suspension. The shaded areas (main figure and inset) depict a ±5% deviation of* $D_{\rm tr}$ *from* $D_{\rm mono}$*.*

Authors Information

Corresponding authors:
MG (grimaldo@ill.eu),
TS (seydel@ill.eu),
FR-R (felix.roosen-runge@fkem1.lu.se).

Note: The authors declare no conflict of interest.

Acknowledgments

We acknowledge support by the Partnership for Soft Condensed Matter (PSCM). We thank M. Braun, O. Matsarskaia, B. Sohmen for help during the experiments, as well as M. Hennig and V. Glenisson for discussion. We acknowledge financial support from the Deutsche Forschungsgemeinschaft (DFG 316738961) and the Agence Nationale de la Recherche (ANR-16-CE92-0009, ImmunoglobulinCrowding). This work was carried out using the laboratory facilities of Institut Laue-Langevin (ILL)'s Life Sciences group initially funded through EPSRC awards to VTF (grants EP/C015452/1, GR/R99393/01) for creation of the Deuteration Laboratory (D-Lab). FR-R acknowledges the Knut and Alice Wallenberg Foundation (project grant KAW 2014.0052).

Supporting information

The Supporting Information is available free of charge on the ACS Publications website at DOI: 10.1021/acs.jpclett.9b00345. Materials and Methods and following figures and tables:
Figure S1. Example spectra of pure lysate.
Figure S2. Comparison of spectra from pure lysate as well as mixtures.
Figure S3. Width of the Lorentzian function as a function q^2 for the different samples as well as example fits.
Figure S4. Influence of lysate subtraction on the diffusion coefficient rescaling the lysate spectra.
Figure S5. Influence of lysate subtraction on the diffusion coefficient interpolating between two different lysate spectra.
Figure S6. Fit parameters for the internal protein dynamics.
Figure S7. Fit results after direct subtraction of the empty cylinder (without Paalman-Pings corrections).
Figure S8. Broadening Γ associated with internal dynamics as a function of q^2.
Figure S9. Comparison of SAXS, USAXS and SLS intensity profiles $I(q)$ of lysate from different batches.
Figure S10. SANS scattering function of some mixtures of Ig and lysate.

Figure S11. Size distributions of the model cytoplasms by McGuffee and Elcock [247] and by Ando and Skolnick [248] used in the present study.
Figure S12. Diffusion coefficient D of spheres with radius R in the Ig-lysate mixture (AS lysate model [248]) normalized by the diffusion coefficient D_{mono} of spheres of the same size in a monodisperse solution as a function of R normalized by the effective radius $R_{\mathrm{eff}} = \langle R_i^3 \rangle^{1/3}$.
Table S1. Estimated lysate composition (mass fraction).
Table S2. Composition of the lysate ME model.
Table S3. Composition of the lysate AS model.

Data availability The data are avaliable at
`doi.ill.fr/10.5291/ILL-DATA.9-13-477`,
`doi.ill.fr/10.5291/ILL-DATA.8-04-759`,
`doi.ill.fr/10.5291/ILL-DATA.8-04-774`,
`doi.ill.fr/10.5291/ILL-DATA.9-13-620`,
`doi.ill.fr/10.5291/ILL-DATA.8-03-891`.

Chapter 7

Nanosecond Tracer Diffusion as a Probe of the Solution Structure and Molecular Mobility of Protein Assemblies: The Case of Ovalbumin

C. Beck *et al.* [223]

Chapter 7 is based on the following publication:

Nanosecond tracer diffusion as a probe of the solution structure and molecular mobility of protein assemblies: The case of ovalbumin
Christian Beck, Marco Grimaldo, Felix Roosen-Runge, Michal K. Braun, Fajun Zhang, Frank Schreiber, Tilo Seydel

J. Phys. Chem. B 122 (2018) 8343

DOI:10.1021/acs.jpcb.8b04349

Publication Date (Web): August 14, 2018

Contributions:

Research design	MG, FRR, FS, TS
Experiments	MG, FRR, TS
Data Analysis and interpretation	CB, MG, FRR, MB, TS
Paper Writing	CB, MG, FRR, FZ, FS, TS

Section 7.7 is not part of the publication.

Abstract

Protein diffusion is not only an important process ensuring biological function, but can also be used as a probe to obtain information on structural properties of protein assemblies in liquid solutions. Here, we explore the oligomerization state of ovalbumin at high protein concentrations by means of its short-time self-diffusion. We employ high-resolution incoherent quasi-elastic neutron scattering to access the self-diffusion on nanosecond time scales, on which interparticle contacts are not altered. Our results indicate that ovalbumin in aqueous (D_2O) solutions occurs in increasingly large assemblies of its monomeric subunits with rising protein concentration. It changes from nearly monomeric towards dimeric and ultimately larger than tetrameric complexes. Simultaneously, we access information on the internal molecular mobility of ovalbumin on the nanometer length scale and compare it to results obtained for bovine serum albumin, immunoglobulin and β-lactoglobulin.

7.1 Introduction

Protein assemblies such as clusters in liquid solutions are of fundamental interest regarding biological self-organization [273–275]. It is often difficult to understand such assemblies by solely employing static methods such as small-angle scattering, and experiments probing the protein dynamics are therefore performed in addition [276–280]. This observation holds in particular when protein assemblies are not static but dynamic or transient [281].

Self-assembled protein aggregates can be reasons for diseases such as eye cataract [5], sickle cell anemia [282], Alzheimer's disease and Parkinson's disease [283], but are also interesting for medical applications.

In this context, incoherent QENS allows to unambiguously access the self-diffusion of particles with nanometer hydrodynamic radii suspended in aqueous solutions. Using deuterated solvents, neutron backscattering spectroscopy becomes predominantly sensitive to the prevailing incoherent scattering from the protein tracer particles [61]. Systematic studies of the diffusive dynamics of protein solutions permit to address the effect of macromolecular crowding [78, 233] on both the global and internal motions of proteins [109, 120, 180]. It has been shown that these two contributions can be reliably separated using high-resolution QENS [33, 61, 109, 120]. Moreover, it has been shown that the translational center-of-mass diffusion of globular proteins as a function of the protein concentration in the solution can be quantitatively described in terms of the diffusion of colloidal hard spheres [109]. Besides macromolecular crowding, the diffusive dynamics also depends on control parameters such as the sample temperature [64, 111] and the charge state influenced by the possible presence of salt ions in the solution [33, 284]. Changes in the diffusive behavior due to structural changes induced by denaturation [64, 182] or by mutations [285] could also be investigated. These studies on simplified model systems composed of a single target protein in water complement other neutron spectroscopy studies on more complex systems which mimic *in vivo* conditions, including the diffusion of selectively labeled proteins in deuterated living cells [238]. By comparing spectra collected with deuterated and hydrogenated solvents, it is also possible to determine the dynamics of the solvent *in vivo* [286, 287].

Ultimately, the aggregation of proteins from a monomeric suspension into clusters caused by the presence of multivalent salt ions has been explored using high-resolution incoherent neutron spectroscopy [33, 131] and can be interpreted in terms of the theory of so-called patchy colloidal particles [34, 35]. This agreement points to the future perspective of quantitatively understanding and controlling dynamic processes governing the formation of protein clusters and larger protein aggregates.

A very useful observation made in several previous studies on the diffusion of model proteins in aqueous solutions is that the protein center-of-mass undergoes a strictly Brownian diffusion on the nanosecond and nanometer observation scales of QENS and even in "physiologically" crowded suspensions (*i.e.* at volume fractions of up to approximately 30%) [33, 61, 109, 120, 288, 289]. Importantly, this observation is made without imposing it as an assumption in the model fitting, implying that the dependencies of the different contributions from the global and internal motions of proteins are obtained independently from the same data set. The Brownian character of the center-of-mass diffusion has in particular been further corroborated on backscattering spectrometers with an intermediate resolution and broader energy transfer range. Due to the increasingly broad spectral contribution of the center-of-mass diffusion from dilute suspensions at high scattering vectors q, these spectrometers best access the high-q range. [33, 61]

The observed Brownian center-of-mass diffusion strictly obeys a Stokes-Einstein temperature dependence [64] and, importantly, as already indicated above, a dependence on the protein volume fraction in the solution that follows the model for the short-time diffusive properties of colloidal hard-sphere suspensions [109]. Given this previous observation, it is now possible to conversely infer the size of a macromolecular assembly, such as a protein cluster, *via* its effective hydrodynamic radius, which defines its Brownian center-of-mass diffusion [131]. In this way, a possible dependence of the formation of protein assemblies on external parameters, such as the protein concentration can be explored. Moreover, the observation time-scale of the employed spectrometer, given by the energy resolution of the instrument, provides information on the life time of such an assembly.

In addition to the information on the center-of-mass motion of the assemblies, the elastic incoherent structure factor (EISF) [290] and a characteristic linewidth associated with the internal molecular fluctuations, which can be compared between different proteins, are obtained.

Here, we present a high-resolution neutron backscattering study of ovalbumin (OVA) protein suspensions in heavy water (D_2O). We investigate the oligomerization based on the results of the global diffusion and we compare the internal dynamics to BSA, Ig, and β-lactoglobulin (BLG) protein solutions. The global diffusion of BSA, Ig and BLG was investigated by Grimaldo *et al.* in 2015 [64] and 2014 [120] and by Braun *et al.* [131], respectively. OVA is an approximately globular protein, and aqueous OVA solutions have been studied previously using small-angle scattering [143]. Its structure has been understood in terms of tetrameric assemblies that constitute the basic building blocks of OVA crystals studied in protein crystallographic experiments. In liquid solutions, it appears that the OVA tetramer may dissociate into dimers and monomers. However, this possible dissociation has been subject to debate, because small angle X-ray scattering (SAXS) measurements and other physicochemical measurements such as analytical ultracentrifugation resulted in conflicting results [144]. Our results using QENS suggest that the dissociation of ovalbumin tetramers may occur at sufficiently low protein concentrations.

7.2 Experiments and Methods

Chicken egg-white ovalbumin OVA (A5503, $\geq$ 98% purity), bovine serum albumin (BSA) (A3059, $\geq$ 98% purity), the polyclonal γ-globulin from bovine blood (Ig) (G5009 $\geq$ 99% purity), and β-lactoglobulin (BLG) (L3908, $\geq$ 90% purity) were obtained as lyophilized powders from Sigma-Aldrich and used without further purification.

Solutions were prepared by a direct dissolution of the mass m_p of protein powder in the volume V of D_2O, defining the observable nominal protein concentration $c_p := m_p/V$. The resulting dry protein volume fraction in the solution is calculated as [109]

$$\varphi = \frac{m_p \nu_p}{V + m_p \nu_p}, \tag{7.1}$$

where $\nu_p = 0.746\,\mathrm{ml/g}$ is the specific volume of ovalbumin at 25°C [291–293].

The dry volume fraction φ from Equation 7.1 can be linked to the real protein concentration $c_{p,\mathrm{real}} = \varphi/\nu_p$.

The experimental data were recorded on the neutron backscattering spectrometer IN16B at the Institut Laue-Langevin (ILL), Grenoble, France [191], using Si(111) monochromator and analyzer crystals, setting the elastic wavelength to 6.27 Å. A phase space transformer [173] was used to optimize the neutron flux at the sample position. The energy resolution function $\mathcal{R}(\omega)$ had an approximative width of ≈ 0.9 µeV FWHM and was described analytically by a fit of two Gaussian functions of the measured spectrum from a Vanadium sample [61]. The spectrometer chamber was kept in vacuum during the acquisition. The samples were filled into cylindrical, indium-sealed aluminum sample holders and held in a standard Orange cryofurnace during the data acquisition. In total, 18 detectors were used to cover a scattering vector q-range of approximately $0.2\,\text{Å}^{-1} \leq q \leq 1.9\,\text{Å}^{-1}$.

The data reduction and analysis followed previously published protocols [61, 120]. The employed model for the scattering function S depending on the scattering vector q and energy transfer $\hbar\omega$ was

$$\begin{aligned} S(q,\omega) = \;& \mathcal{R} \otimes \{\, \beta(q)\; [\, A_0(q)\, \mathscr{L}(\gamma(q),\omega) \\ & + \;(\, 1 - A_0(q)\,)\, \mathscr{L}(\gamma(q) + \Gamma(q),\omega)] \\ & + \;\beta_{\mathrm{D_2O}}(q)\, \mathscr{L}(\gamma_{\mathrm{D_2O}}(q),\omega)\;\; \}\,. \end{aligned} \tag{7.2}$$

Therein, $\mathcal{R} = \mathcal{R}(q,\omega)$ denotes the spectrometer resolution function, $\mathscr{L}(\gamma,\omega)$ represents a Lorentzian function with the width γ, $\beta(q)$ is an intensity scaling factor, and $A_0(q)$ the EISF of the proteins. Importantly, in the present study, two types of fits using this model, Equation 7.2, were carried out: (a) individual fits of the spectra for the different q-values ($q < 1.8\,\text{Å}^{-1}$) separately, and (b) fits of the spectra for all q-values simultaneously [64], denoted global fits. In the second case (b), the dependencies $\gamma(q) = D\,q^2$ and [62]

$$\Gamma(q) = \frac{D_{\mathrm{int}}\, q^2}{1 + D_{\mathrm{int}}\, q^2\, \tau} \tag{7.3}$$

were imposed. Thus, the global diffusion associated with $\gamma(q)$ was assumed to be Brownian, and the internal diffusion of the proteins associated with $\Gamma(q)$ was assumed to obey a so-called jump diffusion [62] with the internal diffusion coefficient D_{int} and the residence time τ. In contrast, the first approach (a) confirmed the validity within the errors of imposing $\gamma = D\,q^2$ and the jump diffusion determining $\Gamma(q)$, Equation 7.3, in accordance with earlier studies [33, 61, 109, 120].

Example data and fits using Equation 7.2 are depicted in Figure 7.1. In the plot, dash-dotted and dotted lines in the figure represent the result from the simultaneous fit of the spectra for all q at once, and solid lines report the result from the fits without imposing any q-dependence. We observe a good agreement of these two different fit approaches. The inset of Figure 7.1 displays the obtained $\gamma(q)$ for the case of the individual fits for each q (symbols). This inset illustrates that the center-of-mass diffusion for the ovalbumin solutions follows Brownian dynamics without imposing it. The small deviation of the fit results from $\gamma(q) = Dq^2$ at the highest q-values is presumably due to cross-talking of the signals from the Lorentzian contributions with the widths Γ and γ.

The EISF $A_0(q)$ resulting from the fit of Equation 7.2 was fitted by [120, 290, 294]

$$\begin{aligned} A_0(q) = p_0 + (1 - p_0)\; & [\, p_1\, A_{3-\mathrm{jump}}(q) \\ & + \;(1 - p_1)\, A_{\mathrm{sphere}}(q)\,]\,. \end{aligned} \tag{7.4}$$

Therein, p_0 denotes the fraction of hydrogen atoms that appear immobile on the observation time scale of our experiment. p_1 is the fraction of the mobile hydrogen atoms undergoing a jump diffusion between three sites.

The remaining hydrogen atoms, $(1 - p_0)(1 - p_1)$ are assumed to undergo a diffusion inside an impermeable sphere with the confinement radius R_s. $A_{3-\text{jump}}(q)$ and $A_{\text{sphere}}(q)$ are described as follows [120, 290, 294]:

$$A_{3-\text{jump}}(q) = \frac{1}{3}\left[1 + 2j_0(qa)\right] \tag{7.5}$$

and

$$A_{\text{sphere}}(q) = \left|\frac{3j_1(qR_s)}{qR_s}\right|^2, \tag{7.6}$$

where $j_0 = \sin(x)/x$ and $j_1(x)$ denote the spherical Bessel functions of the zeroth and first order, respectively. The three-site jump diffusion, Equation 7.5, is assumed to be due to the reorientation of methyl groups -CH_3, associated with a fixed jump distance $a = 1.715\,\text{Å}$ [120, 290, 294].

All data reductions and fits were performed using MATLAB (The MathWorks, Inc.), partly involving MATLAB “mex”-files employing the GNU Scientific Libraries for numerical integration and root finding [61, 109].

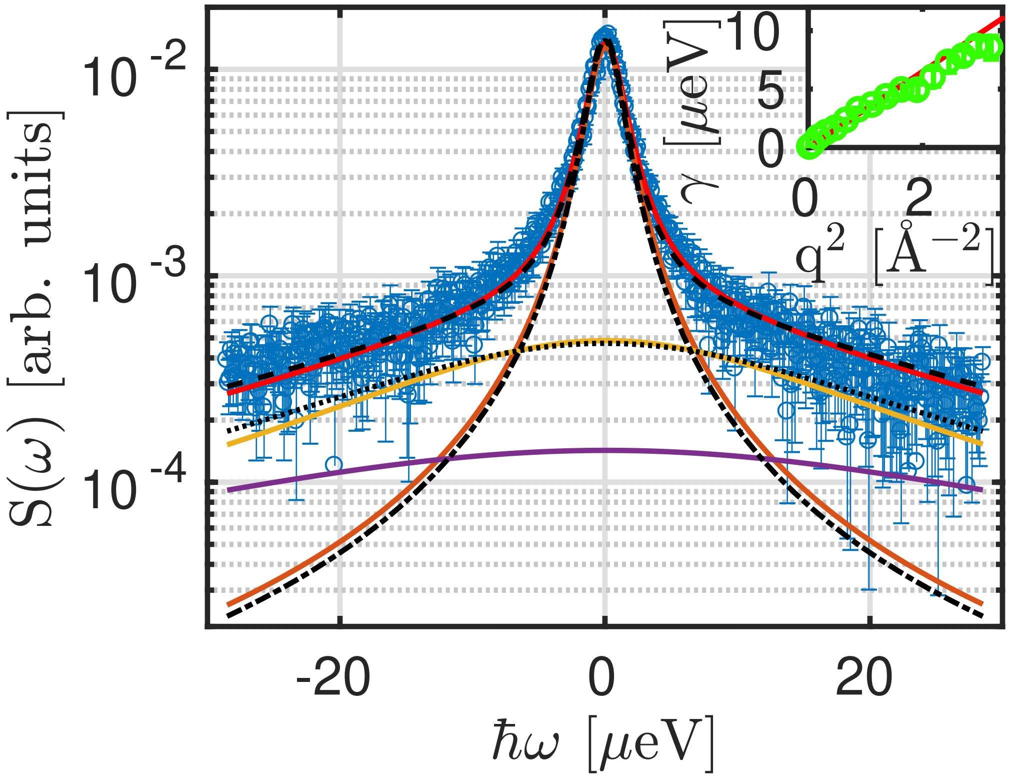

Figure 7.1: *Example spectrum of ovalbumin ($c_p = 200\,\frac{\mathrm{mg}}{\mathrm{ml}}$) in water ($D_2O$) (symbols) recorded on IN16B at $T = 295\,K$ and $q = 0.56\,\text{Å}^{-1}$. The solid lines denote the results from the fit of the individual spectrum according to Equation 7.2 without imposing any q-dependence. The red solid line superimposed on the symbols denotes the fit result composed of the Lorentzian with the width γ modeling the global diffusion (narrow brown line); the broader Lorentzian with the width Γ for internal dynamics (yellow line); and the nearly flat fixed water contribution (lower violet line). The dashed and dash-dotted lines superimposed on the solid lines depict the fit result and fit components in the case of the fit approach that imposes Brownian diffusion for the global motion and jump diffusion for the internal motion (see text). The water contribution is handled in the same way for both approaches. The inset shows γ versus q^2 from the q-dependent fit (symbols). The solid line in the inset reports a fit of $\gamma(q) = D\,q^2$.*

7.3 Theory and Modeling

From the tetrameric crystal structure ($N = 4$) of ovalbumin (PDB *1ova*, four chains) [92], we have extracted a dimeric structure ($N = 2$) by using only the closely-bound chains A and B from the tetrameric structure. For the monomer structure ($N = 1$) we used chain A.

For each of the three structures, HYDROPRO [295] was used to calculate the translational and rotational diffusion coefficients in the limit of infinite dilution, $D_{t0} = D_{t0}(N)$ and $D_{r0} = D_{r0}(N)$ as well as the radius of gyration $R_g = R_g(N)$, as summarized in Table 7.1.

The hydrodynamic radii $R_h(N)$ were calculated from the translational diffusion coefficients D_{t0} determined with HYDROPRO.

For consistency with the neutron data, the HYDROPRO calculations were performed using the viscosity and solution density of D_2O [74].

Moreover, the GROMACS [296] tool *pdb2gmx* was used to add the missing hydrogen atoms. Mathematica was used to extract the positions of the hydrogen atoms in these protein monomer, dimer, and tetramer structures. From the thus obtained hydrogen coordinates, the radial hydrogen density distribution functions $\rho(r, N)$ for these three structures were calculated (Figure 7.2).

The diffusion coefficients depend on the effective volume fraction

$$\phi = \varphi \cdot (R_h/R)^3 \tag{7.7}$$

with the effective sphere radius R calculated from the specific volume ν_P and the molar mass M_w [109, 120, 297, 298]:

$$R = \sqrt[3]{\frac{3}{4\pi}\frac{\nu_p M_w}{N_A}} \tag{7.8}$$

with the Avogadro constant N_A and the molecular weight of a monomer $M_w = 42.7\,\mathrm{kDa}$ [299].

By rescaling the volume fraction using an effective radius, anisotropy effects and influences due to the hydration layer are taken into account [109].

Established analytical expressions for hard spheres for $f_t(\phi)$ (Ref. [59] Eq. (11,12)) and $f_r(\phi)$ (Ref. [58] Eq. (21)) were used to rescale the translational and rotational diffusion coefficients, respectively, for the different protein oligomers, *i.e.* $D_t(\phi) = D_{t0} f_t(\phi)$ and $D_r(\phi) = D_{r0} f_r(\phi)$ which were then used to calculate the volume fraction dependent apparent diffusion coefficient.

The apparent diffusion coefficient D can be obtained from the solution of the implicit equation [61, 109]

$$\sum_{l=0}^{n} B_l(q) \frac{D_r l(l+1) + (D_t - D)q^2}{[D_r l(l+1) + (D_t + D)q^2]^2} = 0\,, \tag{7.9}$$

Table 7.1: *Table of properties of ovalbumin monomers, dimers, and tetramers calculated using HYDROPRO [295] for D_2O solutions (see text). The hydrodynamic radii R_h are calculated from the translational diffusion coefficients in the dilute limit $D_{t,0}$. D_0 is the apparent diffusion coefficient in the dilute limit calculated by Equation 7.9 with $D_t = D_{t,0}$ and $D_r = D_{r,0}$. R_g is the radius of gyration.*

	N	R_g [nm]	R_h [nm]	T [K]	$D_{t,0}$ [Å^2/ns]	$D_{r,0}$ [1/ns]	D_0 [Å^2/ns]
Monomer	1	2.28	2.8749	280	3.82	0.00341	4.74
				295	6.30	0.00562	7.80
				310	9.39	0.00838	11.60
Dimer	2	2.83	3.6029	280	3.05	0.00168	3.82
				295	5.02	0.00277	6.30
				310	7.49	0.00413	9.40
Tetramer	4	3.53	4.5944	280	2.39	0.000838	3.00
				295	3.94	0.00138	4.94
				310	5.88	0.00206	7.37

where n has to be chosen large enough to obtain convergence on the desired q-range [61]. For our case, we chose $n = 75$.

$B_l(q)$ in Eq. 7.9 is determined by the radial distribution of hydrogens $\rho(r, N)$ by

$$B_l(q) \quad = (2l+1) \int_0^\infty dr \rho(r, N) j_l^2(qr) \tag{7.10}$$

with the l^{th} order spherical Bessel functions of first kind, $j_l(x)$.

The values for D from HYDROPRO for the monomer are consistent with published results for native ovalbumin obtained using Dynamic Light Scattering in H_2O solutions, namely $D_0 = 8.7\,Å^2/\mathrm{ns}$ at $T = 25°\mathrm{C}$ [300] and $D_0 = 7.1\,Å^2/\mathrm{ns}$ at $T = 20°\mathrm{C}$ [301].

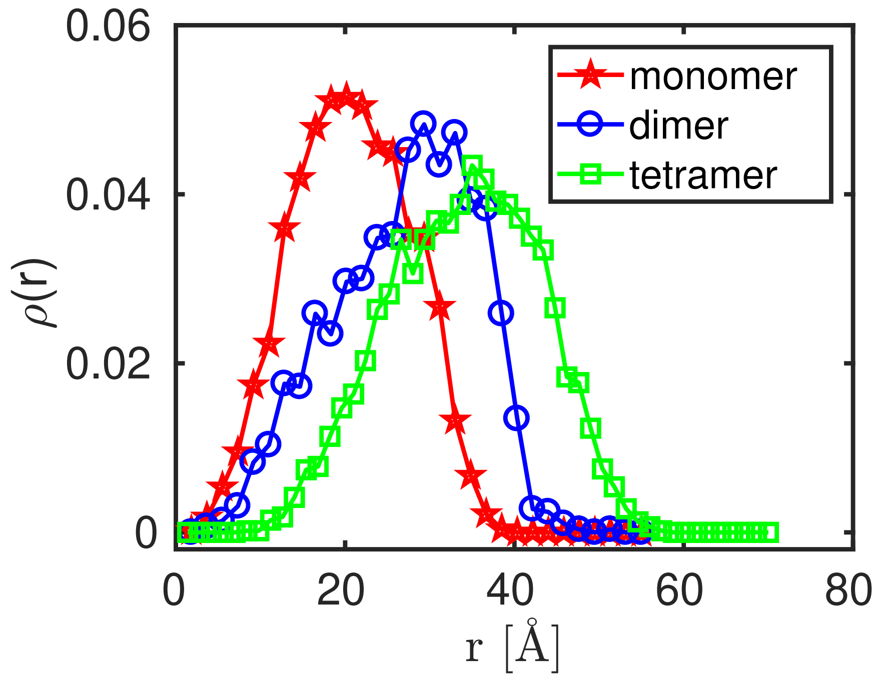

Figure 7.2: *Radial hydrogen density distribution functions $\rho(r, N)$ of the ovalbumin monomer (star symbols), dimer (circles), and tetramer (squares), obtained from the associated protein data bank (PDB) structure files as described in the text.*

7.4 Results and Discussion

7.4.1 Rotational and Translational Diffusion

The observable apparent diffusion coefficients D of ovalbumin given by $\gamma(q) = Dq^2$ with the fitted γ according to Equation 7.2 are depicted in Figure 7.3. The experimental values of D are depicted for the two distinct fit approaches explained in the Experiment and Methods section: (a) by a fit without *a priori* imposing $\gamma(q) = D\,q^2$ (star symbols); and (b) by a global fit imposing $\gamma(q) = D\,q^2$ and $\Gamma(q) = D_{\text{int}}\,q^2/(1 + D_{\text{int}}\,q^2\,\tau)$ (square symbols, cf. Experiments and Methods). The results for both approaches agree very well.

The observed apparent diffusion coefficients scale with the temperature and protein concentration as expected, *i.e.* the diffusion increases with rising temperature and decreases with rising protein concentration. For a better readability of the plot, the diffusion coefficients are normalized by the monomer diffusion coefficient in the dilute limit at the given temperature.

Figure 7.3 also reports an interpretation of these results for D by plotting the calculated apparent diffusion coefficients $D(\phi) = f(D_r(\phi), D_t(\phi))$ using Equation 7.9 for ovalbumin monomers (dash-dotted), dimers (dotted) and tetramers (solid) based on colloid models for the short-time self-diffusion of hard spheres.

This calculation is based on Equations 7.7 and 7.9 with the assumptions for $D_t = D_t(\phi, N)$, $D_r = D_r(\phi, N)$ and $\rho(r, N)$ (Figure 7.2) as explained in the Theory section. The samples are prepared with the nominal concentration c_p of the proteins in D_2O (lower x-axis in Figure 7.3), resulting in the dry protein volume fraction φ using Equation 7.1 (upper x-axis in Figure 7.3).

By comparing the experimental observation and theory, our results indicate that at $T = 295\,\mathrm{K}$ ovalbumin assemblies are, on average, nearly monomeric at $c_p = 100\,\frac{\mathrm{mg}}{\mathrm{ml}}$, approximately dimeric at $200\,\frac{\mathrm{mg}}{\mathrm{ml}}$, and tetrameric at $c_p = 350\,\frac{\mathrm{mg}}{\mathrm{ml}}$. The distribution may depend slightly on temperature as suggested by the slight spread of the symbols for $c_p = 150\,\frac{\mathrm{mg}}{\mathrm{ml}}$. We assume that a distribution of N-mers is present that increasingly shifts to a tetrameric assembly with rising protein volume fraction. Here we emphasize that in the present picture, the oligomers are seen as rigid assemblies in our experiment with an observation time in the order of one nanosecond.

The oligomers may be subject to internal fluctuations of the monomeric building blocks relative to each other, or be subject to a dissociation of these building blocks, on longer time scales. Moreover, a distribution of N-mers with different N may result in an average apparent N due to the limited accuracy and ensemble-averaging in our experiment.

7.4.2 Internal Diffusion

Simultaneously with the fit results for D, we obtain results on the internal molecular nanosecond relaxation motion of ovalbumin in D_2O. Our experiment observes these internal diffusive motions on a nanometer length scale, and, thus, displacements smaller than the protein radius. For the internal diffusion, we employ the individual fit approach for the spectra at each q separately, because the jump diffusion model, Equation 7.3, only constitutes an approximate model of the internal diffusion. This model has nevertheless been shown to be sufficiently suitable for proteins at physiological temperatures [63, 64, 120]. We obtain $\Gamma(q)$ and $A_0(q)$ (Equation 7.2) from this fit. Figure 7.4 depicts the resulting EISF $A_0(q)$ associated with the internal diffusive motions of the proteins and the fits of Equation 7.4. The resulting fit parameters for the EISF are given in Table 7.2. The EISF from the different proteins are nearly indistinguishable within the limits of the present experimental accuracy, as well as independent from the crowding. The latter observation is consistent with earlier findings [120]. The value for BSA is in good agreement with the value found at $T = 295\,\mathrm{K}$ in an earlier study using a different neutron spectrometer [64].

The confinement radius R_s does appear to have a systematic dependence on the protein size. We note, however, that the fit results for R_s sensitively depend on $A_0(q)$ at the lowest values for q, which are measured with the lowest two detectors. For these two detectors, we may have systematic errors, because the overall linewidth is small and thus approaches the resolution. Therefore, the results depend sensitively on the model of the resolution function. In addition, the intensity at low q might be affected by coherent scattering.

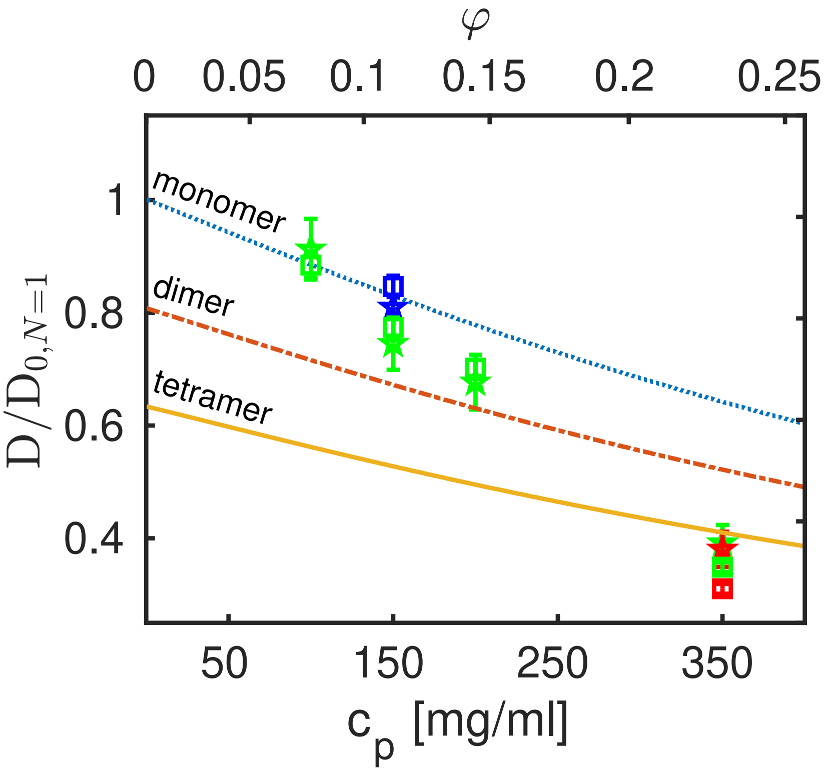

Figure 7.3: *Normalized apparent diffusion coefficients of ovalbumin (symbols) obtained from the fits. Square symbols denote results obtained from a global fit imposing the q-dependence of the global apparent diffusion* $\gamma(q) = Dq^2$ *and jump diffusion for the internal dynamics. Star-symbols denote results obtained by fitting* $\gamma(q) = Dq^2$ *to the fit results for* $\gamma(q)$*. The samples were measured at the temperatures* $T = 280, 295$*, and* $310\,K$ *(blue, red, and green symbols, respectively). The lower* x*-axis denotes the nominal protein concentrations* c_p *(Equation 7.1) from the sample preparation, i.e. the weighed dry protein powder mass per volume of* D_2O *that it was dissolved in, and the upper* x*-axis represents the calculated dry protein volume fraction* φ *(Equation 7.1). The lines indicate the theoretical apparent diffusion coefficients for ovalbumin monomers (dotted), dimers (dash-dotted), and tetramers (solid), respectively, calculated using Equation 7.9.*

Table 7.2: *Fit parameters for the EISF in Figure 7.4 and protein properties calculated with the 3V software [302] (surface and volume) and percentage of amino acids in helical structure and in* β*-sheet obtained from the PDB.*

	R_s [Å]	p_0	p_1	Surface [nm^2]	Volume [nm^3]	% of helix	% of β-sheet
OVA	9.87 ± 0.40	0.35 ± 0.04	0.54 ± 0.05	109.10	58.621	32	32
BSA	10.88 ± 1.86	0.30 ± 0.11	0.65 ± 0.11	357.77	180.032	74	0
Ig	8.84 ± 0.89	0.27 ± 0.08	0.59 ± 0.08	450.50	205.833	6	49
BLG	7.79 ± 0.90	0.35 ± 0.11	0.45 ± 0.16	58.95	24.996	16	40

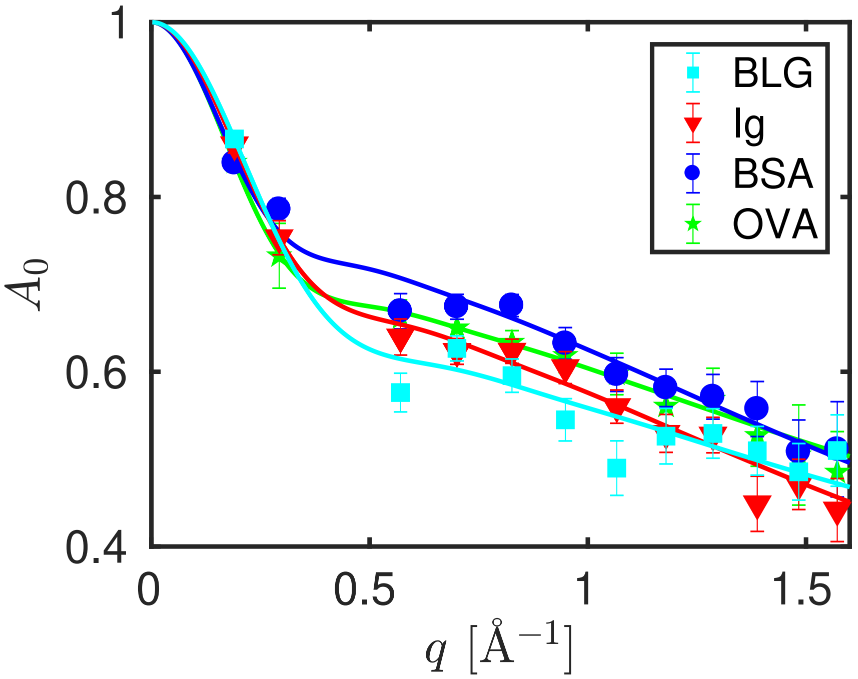

Figure 7.4: *Fit results (symbols) from Equation 7.2 for the EISF* $A_0(q)$ *at* $T = 295\,K$ *and* $c_p = 200\,\frac{\text{mg}}{\text{ml}}$ *(Ig, BSA, OVA) and* $c_p = 300\,\frac{\text{mg}}{\text{ml}}$ *(BLG), and fit of Equation 7.4 to these results (lines). Square symbols denote BLG, triangle symbols Ig, circle symbols BSA, and star symbols OVA, respectively.*

The values for the linewidth $\Gamma(q)$ associated with the internal dynamics are shown in Figure 7.5 for exemplary data sets. We subsequently fit Equation 7.3 to $\Gamma(q)$. The resulting fit parameters D_{int} and τ for all data sets are summarized in Figure 7.6 for different proteins with different concentrations measured at $T = 295\,\text{K}$.

Overall, the present results show that different proteins are characterized by remarkably distinct internal fluctuations. We have therefore looked for systematic correlations with properties of the proteins, namely the percentage of β-sheets or helices in the secondary structure of the protein, the protein surface and surface-to-volume ratio, as determined with the 3V software [302], by using the PDB structures 1OVA Chain A [92], 3V03 [90], 1IGT [303] and 4Y0P [304] for OVA, BSA, Ig and BLG, respectively. The corresponding values are also displayed in table 7.2.

We have not found a parameter that would link the results for all four investigated proteins in a monotonous way (see Figure 7.8), *i.e.* no obvious correlations were found.

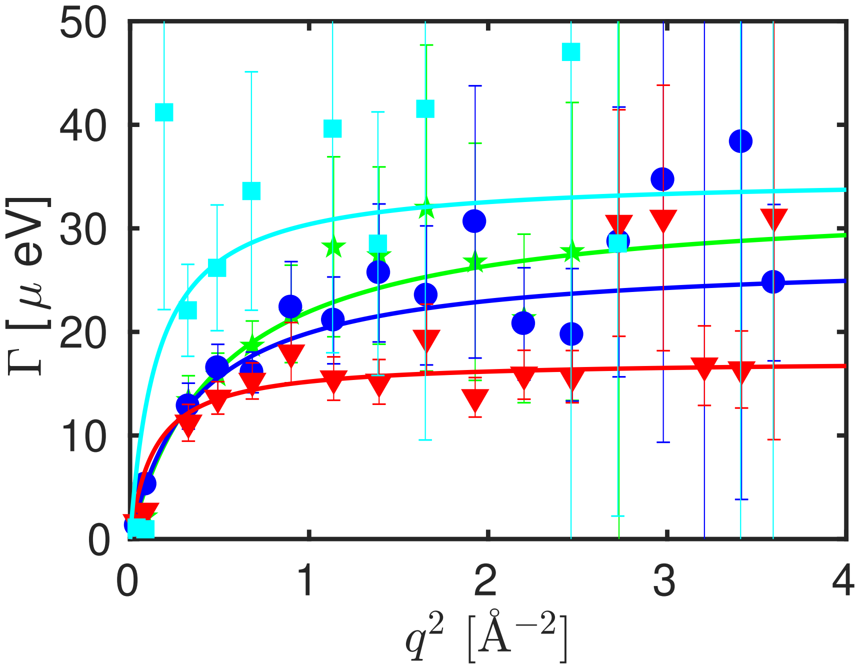

Figure 7.5: *Fit results for the linewidth of the Lorentzian contribution* $\Gamma(q)$ *associated with the internal molecular mobility of the proteins at* $T = 295\,K$ *and* $c_p = 200\,\frac{\mathrm{mg}}{\mathrm{ml}}$ *as a function of the scattering vector* q *(Equation 7.2), and fit of Equation 7.3* $(0.4\,\mathring{A}^{-2} < q^2 < 3.3\,\mathring{A}^{-2})$ *to these results (lines). Square symbols denote BLG, triangle symbols Ig, circle symbols BSA, and star symbols OVA, respectively.*

7.4.3 Limitations of the Current Analysis and Interpretation

We stress that all analysis presented in this work is subject to assumptions and modeling, and the interpretation of the results is subject to the validity of these assumptions, which we tentatively summarize here.

Regarding the analysis of the rotational and translational diffusion (Section 7.4.1), we used a colloidal hard-sphere model. In this context, the following issues have to be noted:

First, the excluded volume fraction φ by the proteins is calculated based on an effective sphere volume of compact clusters. In the case of less compact clusters, this assumption might not hold anymore, and a larger effective φ would be expected. Second, the theoretical φ-dependence of the diffusion of the oligomers is calculated based on the assumption of non-charged colloidal spheres [58, 59]. The validity of this approximation might break down in case of a strong interaction between the clusters, as well as for strongly non-spherical clusters. In fact, for attractive systems, a decay of D as a function of φ faster than expected for un-

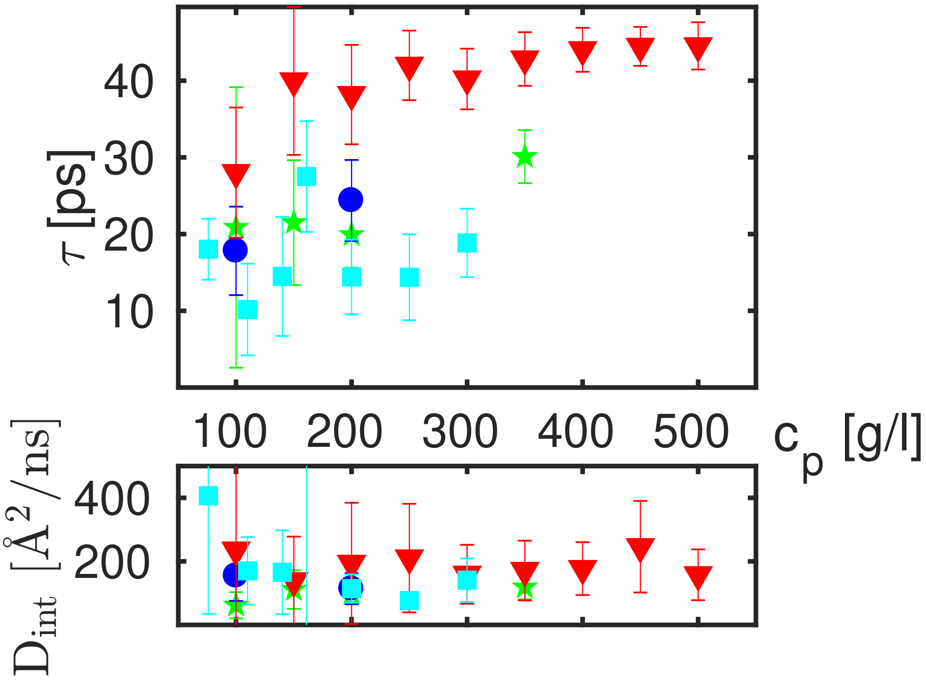

Figure 7.6: *Top: Residence times at $T = 295\,K$ associated with the internal protein motions as a function of the protein concentration c_p obtained from a fit of Equation 7.3 to the widths $\Gamma(q)$ (see Figure 7.5) based on q-dependent fits. Square symbols denote BLG, triangle symbols Ig, circle symbols BSA, and star symbols OVA, respectively. Bottom: Internal diffusion coefficients obtained from the same fits.*

charged hard spheres has been observed [78]. Third, since our QENS experiment accesses an ensemble-average, the clusters may be subject to a size distribution with unknown dispersity, but an average size that increases with φ (as previously observed in lysozyme solutions [279]).

For a full picture regarding the cluster formation, both comprehensive SAXS data and neutron spin echo data recorded under the same sample conditions (*i.e.* at the same protein concentrations in D_2O solutions without additional buffers) would be required in addition to our neutron backscattering data [131], ideally employing protein samples from the same production batch. In the absence of such comprehensive data, our interpretation of cluster formation may remain ambiguous.

Regarding the internal molecular diffusive motions we note: The possibility to observe the internal motions on IN16B is presently limited by the explored maximum energy range $|\hbar\omega| \leq 30\mu$eV. Moreover, the jump diffusion model, Equation 7.3, for the internal diffusion obviously constitutes an approximation of more complex motions [63, 64, 180]. More fundamentally, even the Lorentzian $\Gamma(q)$ in Equation 7.2 accounting for the internal motions in the fit constitutes an approximation only of a more complex scattering function. There is no strong physical but only a heuristic justification of the jump-diffusion model, because it reproduces the observed q-dependence of $\Gamma(q)$ quite well. Nevertheless, the residence time τ showing the main differences could also be extracted by taking an average of the asymptotic values at high q-values. Furthermore, the energy-landscape of a protein contains many local minima which the hydrogens have to overcome to get to a new position. It is therefore reasonable to assume that the atoms stay at one position during the residence time τ before performing a diffusive jump. For this reason, the jump diffusion model appears justified to some level. To identify the driving parameters leading to distinct dynamics in different proteins, backscattering spectrometers having a broader energy range but broader energy resolution may be employed in addition in further studies [64, 172, 192]. Moreover, the internal motions may in the future be further investigated by molecular dynamics simulations. A scattering function calculated from such simulation results would then replace $\Gamma(q)$ in the fits.

7.5 Conclusions

The ensemble-averaged short-time protein center-of-mass self-diffusion in aqueous (D_2O) ovalbumin solutions observed using neutron backscattering spectroscopy is not consistent with the picture of rigidly bound ovalbumin tetramers over the entire range of protein concentrations explored. In contrast, both ovalbumin monomers and dimers may be present at low concentration. The results for the nominal protein concentrations of 100 and 150 $\frac{\text{mg}}{\text{ml}}$, point to a suspension consisting predominantly of monomers and dimers, and solely of dimers at 200 $\frac{\text{mg}}{\text{ml}}$. At 350 $\frac{\text{mg}}{\text{ml}}$ tetramers or even larger aggregates appear to prevail. However, the aggregation state of ovalbumin may depend sensitively on various environmental parameters and even the specific protein batch explored. We also point out that our aqueous sample solutions were based on D_2O without any buffer, and results can differ if H_2O [32, 305] or if an additional buffer are used. Moreover, we used an effective hard sphere model to rescale the diffusion coefficients, obtained from the pdb structures in the dilute limit, to match the desired volume fraction.

Our results illustrate the general possibility and describe the methodological framework, using QENS, to infer on the assembly size and in this way, more generally, on solution structure properties. Since the scattering signal from the proteins in our samples is mainly incoherent, we unambiguously detect the self-diffusion, or, synonymously, tracer diffusion of the protein N-mers, clusters, or aggregates independent from their size. Moreover, another advantage of incoherent QENS over complementary scattering methods consists in the linear dependence of the scattering signal on the size of the assemblies, aggregates, or clusters, *i.e.* the possible presence of large aggregates at a comparatively small partial number density in a dispersed suspension would not “cover up” the scattering signal from any possibly prevailing monomers.

We emphasize that our current work addresses and illustrates the methodology of neutron backscattering data analysis, and our resulting picture of the cluster formation in the ovalbumin protein solution system is based on the observed global diffusion. For a complete picture, a combination of other experimental techniques including small-angle scattering and neutron spin-echo spectroscopy is required in addition to neutron backscattering [131], ideally complemented by simulations. Without such complementary information, ambiguities may remain regarding the interpretation of the results.

We simultaneously obtain information on the internal molecular mobility of the investigated proteins. By comparing those of OVA with the other model proteins BLG, BSA, and Ig, we observe clear differences, which do not correlate in an obvious manner with the structural properties of the protein such as the percentage of β-sheet or helices or the surface-to-volume ratio. Further studies will be needed to better understand how internal motions on the subnanosecond timescale are tuned in different proteins.

Supporting Information

The neutron data are permanently curated by the ILL and accessible *via* `http://dx.doi.org/10.5291/ILL-DATA.9-13-477` (OVA, Ig, and BSA), and `http://dx.doi.org/10.5291/ILL-DATA.8-04-724` (BLG).

The Supporting Information contains the diffusion coefficients calculated for spheres with equivalent hydrodynamic radii compared with the ones calculated for the different clusters and the averaged residence times as a function of the radii of gyration for different proteins. This information is available free of charge *via* the Internet at http://pubs.acs.org

Acknowledgements

This work was supported in part by the DFG and the ANR (contract no. ANR-16-CE92-0009-01) and the Knut and Alice Wallenberg Foundation (project grant KAW 2014.0052). C. B. acknowledges support by a studentship co-funded by the ILL and the University of Tübingen. We thank R. Ammer (ILL) for help during the IN16B experiment.

7.6 Supporting Information

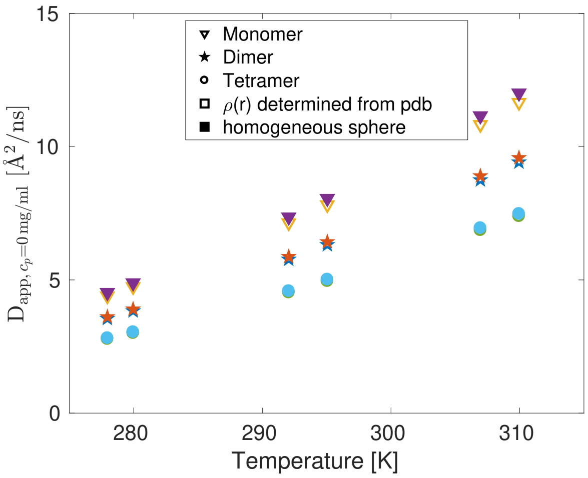

Figure 7.7: *Apparent diffusion coefficients D_{app} in the dilute limit ($c_p \to 0\frac{\text{mg}}{\text{ml}}$) calculated using the hydrogen distribution functions extracted from the pdb structure (open symbols) and the hydrogen distribution function from a homogeneous sphere (filled symbols). Triangles, stars and circles represent the diffusion coefficients of monomers, dimers and tetramers, respectively.*

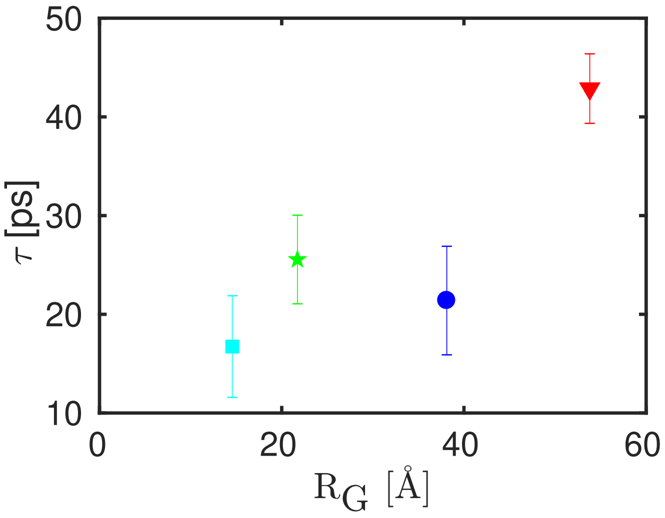

Figure 7.8: *Error-weighted average of the residence time τ (Equation 7.3) versus the radius of gyration R_{G}. No obvious correlation between residence time and the radius can be seen.*

7.7 Additional Analysis: Determination of the Number of Proteins within a Cluster by SAXS

Next to the data analysis based on the QENS data, structural information can be obtained by investigating SAXS data. We therefore extracted the peak positions q_c of the SAXS profiles from Ianeselli *et al.* [143] for different protein concentrations.

Following Refs. 131, 276, the number of clusters $n_{Cluster}$ can be calculated as follows:

$$n_{\text{Cluster}} = \frac{q_c^3}{\pi^3 4\sqrt{2}}. \tag{7.11}$$

From the real protein concentration $c_{p,\text{real}}$, as defined in Section 7.2, we calculated the number of proteins n_{Prot} in the solution:

$$n_{\text{Prot}} = \frac{c_{p,\text{real}} N_A}{M_W} \tag{7.12}$$

with the molar mass $M_W = 42.7\,\text{kDa}$ and the Avogadro constant N_A.

The averaged number of proteins per cluster N can then be calculated as:

$$N = \frac{n_{\text{Prot}}}{n_{\text{Cluster}}}. \tag{7.13}$$

(Note that Ianeselli *et al.* [143] use a different nomenclature for the protein concentration.) Figure 7.9 shows once more the diffusion coefficients in the upper graph, similar to Figure 7.7, but also the averaged number of proteins in the clusters obtained from the analysis of the SAXS data.

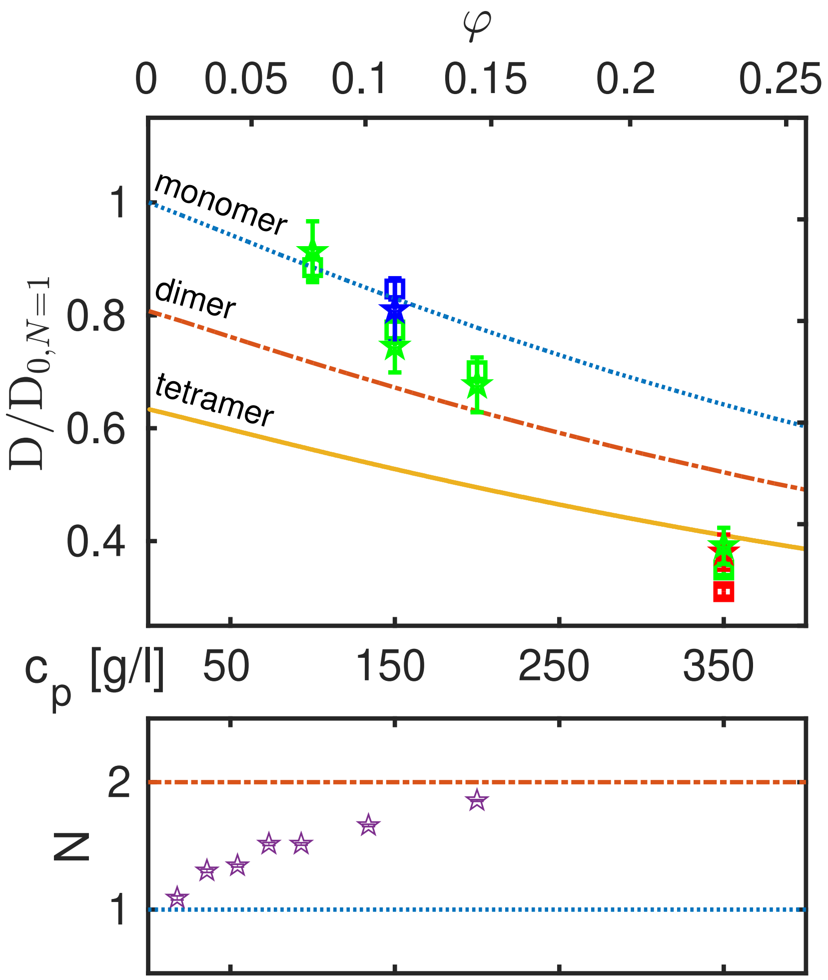

Figure 7.9: *Crowding dependent cluster formation: The upper plot reproduces Figure 7.3. The lower part shows the crowding-dependent averaged number of proteins per cluster.*

Chapter 8

Short-Time Self-Diffusion of Salt- and Temperature-Dependent Protein Clusters

This chapter constitutes a manuscript in preparation.
Contributing authors: Christian Beck, Marco Grimaldo, Olga Matsarskaia, Michal K. Braun, Lena Bühl, Niina H. Jalarvo, Fajun Zhang, Felix Roosen-Runge, Frank Schreiber, and Tilo Seydel

8.1 Abstract

Salt-induced charges in aqueous suspensions of proteins can give rise to complex phase diagrams including homogeneous solutions, large aggregates, and re-entrant dissolution regimes. Moreover, depending on the temperature, liquid-liquid phase separation (LLPS) may occur within the aggregation regime. Here, we systematically explore the phase diagram of the globular protein bovine serum albumin (BSA) as a function of temperature (T) and protein concentration (c_p) as well as of the concentrations of trivalent salts $\mathrm{YCl_3}$ and $\mathrm{LaCl_3}$ (c_s). By employing incoherent neutron spectroscopy, we unambiguously determine the short-time self-diffusion of the protein clusters depending on c_p, c_s and T. We determine the cluster size in terms of effective hydrodynamic radii as manifested by the cluster center-of-mass diffusion coefficients D. For both salts, we find a simple functional form $D(c_p, c_s, T)$ in the parameter range explored. The calculated inter-particle attraction strength, based on the short-time and microscopic properties, increases with salt concentration and temperature in the regimes investigated and can be linked to the macroscopic behavior.

8.2 Introduction

The quantitative understanding and the rational control of the formation of protein clusters in liquid suspensions is of interest for applications in the medical field since protein aggregation can play a role in diseases, such as cataract [5]. Moreover, drug delivery can be enhanced in several ways: For instance, proteins can be concentrated whilst still maintaining their functionality. This prevents the formation of irreversible protein clusters [306]. Alternatively, a triggered disassembly of reversible clusters can be used *e.g.* for drug delivery purposes [307]. Such fundamentally important contexts motivate the pursuit of a quantitative physical modeling of protein aggregation and dissolution.

The charge screening and, ultimately, charge inversion caused by an increasing concentration c_s of trivalent salts in aqueous solutions of globular proteins can result in complex phase diagrams. Theses phase diagrams have been observed for several different globular proteins, such as BSA [22], human serum albumin (HSA), ovalbumin and BLG[24] in combination with different salts such as YCl_3, $LaCl_3$, $FeCl_3$, $AlCl_3$ [24, 308], $HoCl_3$ [27, 36] as well as $Y(NO_3)_3$ and $La(NO_3)_3$ [26]. The phase diagrams depend on the salt concentration c_s, the protein concentration c_p, the temperature [34], the solvent [32] as well as on the salt cations [27] and anions [26] present in solution. The known phases comprise regimes that manifest themselves visually as transparent solution regimes and as turbid regimes, respectively. Within the turbid regime, in general, large protein clusters form. In most of the studied systems, a transparent solution regime can be observed at low salt concentrations $c_s \ll c^*$ as well as at very high salt concentrations $c_s \gg c^{**}$, where c^* and c^{**} denote the respective phase boundaries that depend on c_p. Within the range $c^* < c_s < c^{**}$, a so-called liquid-liquid phase separation (LLPS) can often be found. It is marked by emerging and ultimately microscopically visible protein-rich droplets embedded in a protein-depleted solution. At a given suitable (c_s, c_p) combination, the LLPS can be reversibly triggered by crossing a critical solution temperature. In the case of BSA, the LLPS is characterized by a lower critical solution temperature (LCST) [34], while in the case of BLG, an upper critical solution temperature (UCST) is observed [132]. Several theoretical descriptions, reproducing the experimental phase diagram, have been published [35, 309].

By employing incoherent QENS, the apparent center-of-mass diffusion D of the protein monomers or clusters is observed. The incoherent scattering is an intrinsic property of our experiment and not a model-based approximation. Therefore, the observable center-of-mass diffusion directly reflects the cluster size without requiring any assumption on the monomer-monomer or cluster-cluster correlation lengths.

In previous works, cluster formation of BSA in D_2O was observed upon approaching c^* for YCl_3. QENS spectra, measured at constant temperature (295K), were analyzed and a master curve depending only on the number of salt ions per protein was found, which describes the global short-time self-diffusion [33]. Here, we present a study expanding the parameter range by changing the temperature and choosing two different salts, namely, YCl_3 and $LaCl_3$. We find a temperature dependence of the cluster formation already from simple heuristic models and use a more advanced model, based on patchy-particle colloid physics, to determine thermodynamic parameters driving the cluster formation. Previous studies used a patchy-particle model [35] to describe the salt-induced protein adsorption on surfaces [25]. In addition, the patchy-particle model helped understand cation binding to BSA monitored by ITC and ζ-potential measurements [34].

8.3 Theoretical Description of the Scattering Function of a Solution with Clusters

Being a function of the energy transfer $\hbar\omega$ and the momentum transfer $\hbar q$, the quasi-elastic scattering signal $S(q, \omega)$ of protein solutions can be described by a sum of the contributions of the solvent $S_{\mathrm{D_2O}}(q, \omega)$ and the protein $S_{\mathrm{Prot}}(q, \omega)$ convoluted with the instrumental resolution function $\mathscr{R}$:

$$S(q, \omega) = \mathscr{R} \otimes \{\beta_{\mathrm{D_2O}} S_{\mathrm{D_2O}}(q, \omega) + \beta S_{\mathrm{Prot}}(q, \omega)\} \tag{8.1}$$

with the q-dependent scalars $\beta(q)$ and $\beta_{\mathrm{D_2O}}(q)$. To compare the water contribution in a concentrated protein solution to a pure solvent measurement, the signal has to be rescaled by a factor $\beta_{\mathrm{D_2O}}$ accounting for the protein volume fraction as explained in Ref. 61. Since proteins are not rigid bodies, their scattering signal can be divided into the scattering signal describing their global and internal dynamics:

$$\begin{aligned} S_{\mathrm{Prot}}(q, \omega) &= S_{\mathrm{Prot,global}}(q, \omega) \otimes \ldots \\ &[A_0(q)\delta(\omega) + (1 - A_0(q))S_{\mathrm{Prot,internal}}(q, \omega)] \end{aligned} \tag{8.2}$$

with a delta function $\delta(\omega)$ and the EISF A_0 accounting for the confined motions in the protein [33]. The EISF, containing information on localized motions, can be described with several contributions, such as three-site jump diffusion or diffusion in a sphere [33].

Depending on the nature of the protein studied, several models have been used to describe its internal dynamics, such as jump diffusion models [96, 203], descriptions based on energy landscapes [310], and models of switching diffusive states [33]. Within this study, we use a jump diffusion model as described by Singwi and Sjölander [62] with a diffusion coefficient D_{int} and a residence time τ_{int}. It has been shown that the model is able to describe the internal dynamics of BSA in the temperature range investigated here [33]. The scattering signal describing the internal dynamics of the protein can thus be written using a Lorentzian function $S_{\mathrm{Prot,internal}}(q, \omega) = \mathscr{L}_\Gamma(\omega)$ with the width

$$\Gamma = \frac{D_{int} q^2}{1 + D_{int}\tau_{int} q^2}. \tag{8.3}$$

Numerous QENS studies confirm a Brownian center of mass diffusion of the proteins in solution. The scattering function can then be described by one apparent diffusion coefficient D_{app}, which can, on the one hand, contain contributions from rotational and translational diffusion [61, 120], but on the other hand, also contributions of different particles with different sizes (e.g. clusters) [33, 96, 131]. The scattering function for the global diffusion can then be described by a Lorentzian function with the width $\gamma = D_{\mathrm{app}} q^2$:

$$S_{\mathrm{Prot,global}}(q, \omega) = \mathscr{L}_\gamma(\omega) \tag{8.4}$$

In a system that contains scatterers with N different sizes, which diffuse independently, the scattering function can be written as a sum of the individual contributions

$$S_{\text{Prot,global}}(q,\omega) = \sum_{j=1}^{N} w_j S_j(q,\omega) \tag{8.5}$$

with the relative weight w_j of particles of type j. In a cluster-forming system, the cluster size distribution, ρ_n, can be described by Flory-Stockmeyer theory as a function of the binding probability p_b, and the number of patches per particle m [33, 311]:

$$\rho_n = \rho(1-p_b)^m \left[p_b(1-p_b)^{m-2}\right]^{n-1} \frac{m(mn-n)!}{(mn-2n+2)!\,n!} \tag{8.6}$$

Assuming that a n-cluster can be modeled as a hard sphere of the combined volume of n monomers, the rotational and translational diffusion coefficients can be calculated with the Stokes-Einstein relations for the dilute limit and can then be rescaled to the corresponding volume fraction φ (Ref. 59, Eqns. 11 and 12) and (Ref. 58, Eq. 21):

$$D_t^n = \frac{k_b T}{6\pi\eta(T)R_n} f_t(\varphi) \tag{8.7}$$

$$D_r^n = \frac{k_b T}{8\pi\eta(T)R_n^3} f_r(\varphi) \tag{8.8}$$

with the temperature-dependent viscosity of D_2O $\eta(T)$ [74] and the cluster radius $R_n = n^{1/3} \cdot R_{\text{Monomer}}$. Grimaldo *et al.* [230] recently showed that in inhomogeneous mixtures, the short-time self-diffusion is mainly driven by the total volume fraction of the solute if the tracer particle radius R is comparable to the averaged radius $\sqrt[3]{\langle R_i^3\rangle}$ of the particles in solution.

The apparent diffusion coefficient is calculated as described in Ref. 109, for each n-cluster by assuming a hydrogen distribution of a sphere with radius R_n and minimizing the $\mathbb{L}^2$ norm:

$$||S_{r,t}(q,\cdot) - \alpha\mathscr{L}_\gamma(\cdot)||^2 = \int \left[S(q,\omega) - \alpha\mathscr{L}_\gamma(\omega)\right]^2 \mathrm{d}\omega \tag{8.9}$$

with the scalar α depending on q and $\gamma = D_{\text{app}} \cdot q^2$. The scattering function for the global diffusion, which can be described with one single Lorentzian $\mathscr{L}_\gamma(\omega)$ for a monodisperse solution, therefore results in [33]

$$\begin{aligned} S_{\text{global}}(q,\omega) &= \frac{\sum_n n\rho_n(m,p_b) \cdot \alpha(n,q) S_n(q,\omega)}{\sum_n n\rho_n(m,p_b)} \\ &= \frac{\sum_n n\rho_n \cdot \alpha\mathscr{L}_{D_{\text{app}}^n q^2}(\omega)}{\sum_n n\rho_n} \end{aligned} \tag{8.10}$$

In a first approximation, the scattering function can be approached by a Lorentzian function $\mathscr{L}_{\gamma_{\text{global}}}(\omega)$ with the width $\gamma_{\text{global}} = D_{\text{global}} q^2$ with

$$D_{\text{global}} \approx \frac{\sum_n n\rho_n(m, p_b) \cdot D_n}{\sum_n n\rho_n(m, p_b)} \tag{8.11}$$

The Wertheim theory for patchy particles with m bonding sites describes p_b, used in Equation 8.6, as a function of the attraction strength, ε_{AB}, between two particles A and B [35, 312, 313]:

$$\frac{p_b}{(1-p_b)^2} = \rho m \Delta_{AB} \tag{8.12}$$

$$\Delta_{AB} = 4\pi g_{HS}(\sigma) K_{AB} F_{AB} \tag{8.13}$$

$$F_{AB} = \exp\left(\frac{\varepsilon_{AB}}{k_b T}\right) - 1 \tag{8.14}$$

with K_{AB} defined by Chapman *et al.* [313] as an integral measuring the volume associated with the binding sites A and B. The attraction strength ε_{AB} is described *via* the chemical potential $\mu_s(c_s)$ depending on the free binding energy ε_b between a protein and a salt ion and on the free bridging energy ε_{uo} between an unoccupied and occupied patch of two different proteins as described by Roosen-Runge *et al.* [35]. The attraction strength ε_{AB} can also be linked to the second virial coefficient *via* an integral expression over the solid-angle averaged Mayer function [314, 315]. The two free energies can be expressed by entropic and enthalpic contributions [34]. It should be emphasized that the present study, performed at high protein concentrations and in D_2O, is not expected to yield the same results as previous studies [25, 34] due to the different solvent [32] and due to the fact that the high protein concentrations, used in the experiments, favor also the bridging event of two proteins, which was limited in previous studies by using low protein concentrations [34].

8.4 Experiment

BSA was obtained from Sigma Aldrich as lyophilized powder (A3059, 98% purity) and used without additional purification. YCl_3 (18682, 99.9% purity), $LaCl_3$ (87911, anhydrous, 99.9% purity) and D_2O (14764, 99.8% purity) were obtained from Alfa Aesar. The samples were prepared following the protocol established by Roosen-Runge *et al.* [109] using a 100 mM YCl_3 stock solution.

The experiment was carried out on the cold neutron backscattering spectrometer BASIS at the Spallation Neutron Source (SNS), using its Si(111) analyzers. BASIS provides an energy resolution of approx. 3.5 µeV FWHM and an energy range $-100\mu\text{eV} \leq \hbar\omega \leq +100\mu\text{eV}$ at a scattering vector range $0.4\ \text{Å}^{-1} \leq q \leq 1.9\ \text{Å}^{-1}$ [172]. The samples were measured in hermetically sealed double-walled cylindrical aluminum containers and kept in a closed-cycle cryostat during the experiment. The sample preparation followed the protocols previously described by Grimaldo *et al.* [33].

8.5 Results and Discussion

Previously published protocols were used to perform the data reduction and analysis [61, 120]. Taking into account the resolution function $\mathscr{R}(q,\omega)$, fitted with five non-centered Gaussians, it is possible to model the scattering signal by

$$\begin{aligned} S(q,\omega) = \mathscr{R} \otimes \{&\beta_{\mathrm{D_2O}}\mathscr{L}_{\gamma_{\mathrm{D_2O}}}(\omega) + \beta(q) S_{\mathrm{global}}(q,\omega) \otimes \;... \\ &[A_0(q)\delta(\omega) + (1 - A_0(q) S_{\mathrm{internal}}(q,\omega))]\} \end{aligned} \tag{8.15}$$

with the scattering functions $S_{\mathrm{global}}(q,\omega)$ and $S_{\mathrm{internal}}(q,\omega)$ describing the global and internal dynamics of the proteins, respectively. In all fits performed, the scattering signal contribution of D_2O was rescaled to take the specific volume of the BSA into account and modeled with one Lorentzian based on time-of-flight data [61].

In a first approach, the scattering functions describing the contribution of the global and internal dynamics to the quasi-elastic scattering function at ambient temperatures can be modeled by two Lorentzians $\mathscr{L}_\sigma(\omega)$ with a width σ [33, 33, 61, 120, 131].

$$\begin{aligned} S(q,\omega) = \mathscr{R} \otimes \{&\beta_{\mathrm{D_2O}}\mathscr{L}_{\gamma_{\mathrm{D_2O}}}(\omega) + \;... \\ &\beta(q)\left[A_0(q)\mathscr{L}_\gamma(\omega) + (1 - A_0(q)\mathscr{L}_{\gamma+\Gamma}(\omega))\right]\} \end{aligned} \tag{8.16}$$

An example spectrum with a corresponding fit of Equation 8.16 is displayed in Figure 8.1.

Without imposing any q dependence on the fit, the width γ of the Lorentzian $\mathscr{L}_\gamma(\omega)$, accounting for the global diffusion, can be described with the diffusion coefficient $D = \gamma/q^2$ (inset Figure 8.1) revealing a Fickian diffusion.

Figure 8.2 shows the normalized diffusion coefficients for different c_s/c_p ratios and temperatures obtained from the slope of the q-dependent γ for both salts investigated (YCl_3 and $LaCl_3$). The normalization of the diffusion coefficient by the one obtained from a salt-free sample at the identical temperature and protein concentration eliminates both the slowing-down due to the crowding [120] and the Stokes-Einstein temperature dependencies of the monomeric solution [33]. Changes in the diffusion coefficients can therefore be related to changes in the averaged hydrodynamic radii of the particles studied. For all temperatures, a universal slowing down is found in this renormalized representation. This salt-induced slowing-down of the diffusion is independent of the protein concentration. It only depends on the number of salt ions per protein and has already been reported at $T = 295\,\mathrm{K}$ by Grimaldo *et al.* [33]. Here we confirm the observation also for $T = 280\,\mathrm{K}$, $300\,\mathrm{K}$ and $325\,\mathrm{K}$, as well as for $LaCl_3$. This slowing-down can be described by a polynomial approach:

$$g(c_s/c_p) = 1 + a_2\,(c_s/c_p)^2 + a_4\,(c_s/c_p)^4 \tag{8.17}$$

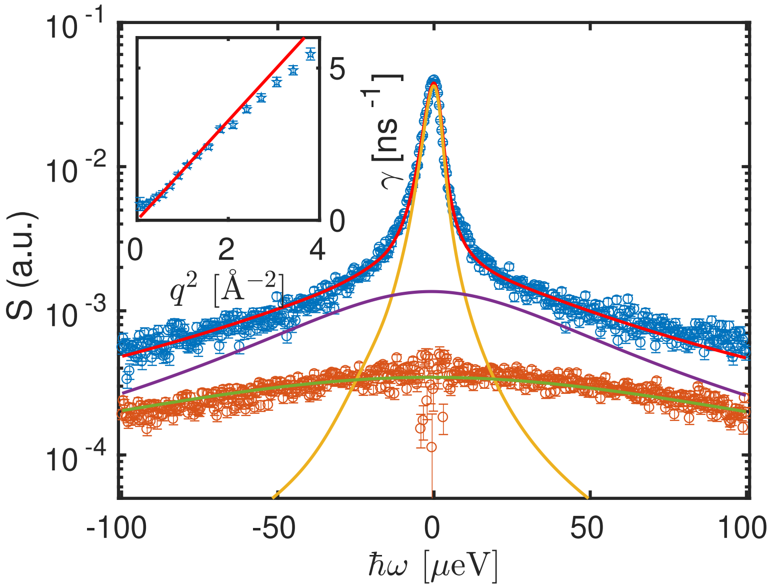

Figure 8.1: *Example spectrum (blue circles) with* $c_p = 200\,\frac{\mathrm{mg}}{\mathrm{ml}}$*,* $c_s = 15.1\,\mathrm{mM}$*,* $T = 280\,\mathrm{K}$ *at* $q = 1.15\,\mathrm{\AA}^{-1}$ *containing the rescaled* D_2O *signal (brown circles) fitted with Equation 8.16. Red, yellow, violet and green lines represent the fit result, the global and internal diffusion as well as the water contribution (*D_2O*), respectively. Inset: HWHM* γ *of the narrower Lorentzian function as a function of* q^2 *with the corresponding fit offering access to the apparent global short-time self-diffusion.*

The number of free parameters can be reduced if an exponentially decaying function with a squared argument is used:

$$g_1\left(\frac{c_s}{c_p}\right) = \frac{D(c_s, c_p)}{D(c_s = 0, c_p)} = \exp\left(a\left(\frac{c_s}{c_p}\right)^2\right) \tag{8.18}$$

For all temperatures investigated, the fit parameters of Equation 8.17 and Equation 8.18 show monotonous trends with increasing temperature (Figure 8.3), which indicates the formation of clusters.

As shown in Figure 8.2, the normalized diffusion coefficients obtained from the sample series containing $LaCl_3$ decay more slowly than the normalized diffusion coefficients of the samples with YCl_3. At the same c_s/c_p and at the time and length scales given by the experimental set-up, YCl_3 induces a cluster size distribution with a larger average cluster size than $LaCl_3$. In other words, in the case of YCl_3, the clusters approach already at smaller salt concentrations close to c^* sizes comparable to the wavelength of visible light and higher screening is necessary to dissolve the clusters around c^{**}. On the macroscopic level, this results in a broader second regime where clusters make the solution appear turbid [27].

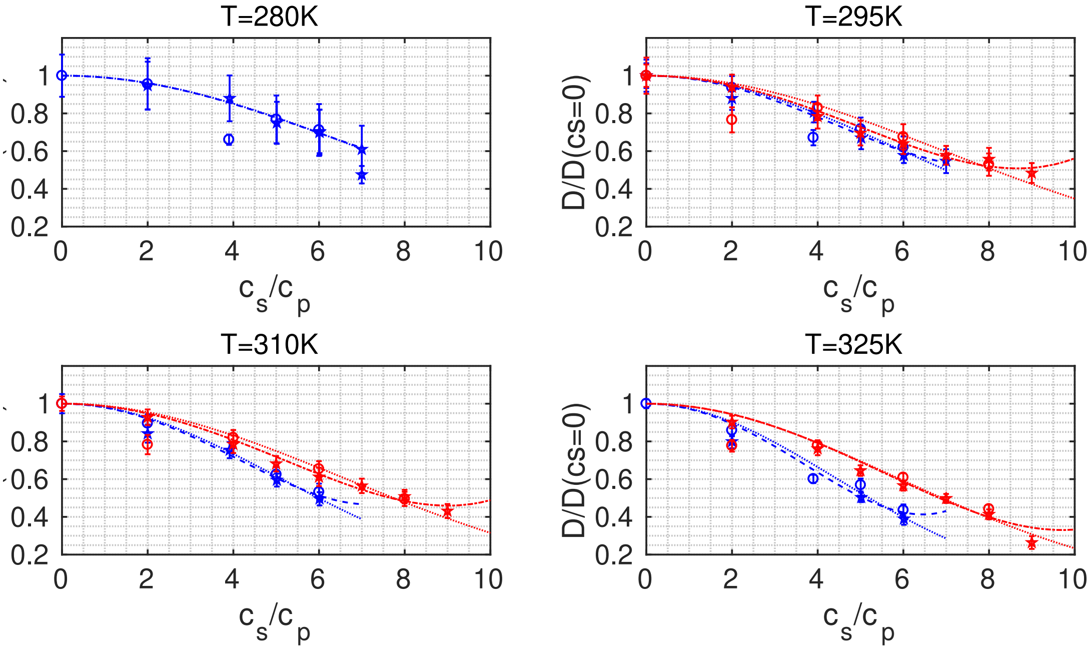

Figure 8.2: *Normalized observable center-of-mass diffusion coefficients* $D(c_s/c_p)/D(c_s = 0, c_p)$ *as a function of* c_s/c_p *for different temperatures (one subplot each). Diffusion coefficients of samples with* $c_p = 200\frac{\text{mg}}{\text{ml}}$ *and* $c_p = 300\frac{\text{mg}}{\text{ml}}$ *are denoted by stars and circles, respectively. Dashed and dotted lines are the results of Equation 8.17 and Equation 8.18, respectively. Red and blue symbols and lines represent* YCl_3 *and* $LaCl_3$*, respectively.*

The width Γ of the second Lorentzian function of Equation 8.16 accounts for all other motions on the time scale observable, *e.g.*, the dynamics within the protein and in the clusters. As explained above, we assume rigid but dynamic clusters.

To model the cluster formation using Equations 8.6 and 8.11-8.14, the given apparent global diffusion coefficients can be used to calculate the protein-protein binding probabilities as described by Grimaldo *et al.* [33]. Based on these, the corresponding attraction strength ε_{AB} can be calculated for each sample measured. In accordance with [34] we choose a total number of $m = 6$ patches per protein. While the binding probability still follows a temperature-dependent master curve (see Figure 8.4), the attraction strength ε_{AB} depends on the volume fraction due to the fact that the model in Equation 8.12 includes the protein number density.

For both salts, the calculated binding probabilities exceed the theoretical limit of $p_b^{max} = \frac{1}{m-1} = 0.2$. This might be explained by a deviation from the assumed cluster size distribution or by clusters which are not fully compact and are therefore bigger than assumed by the model.

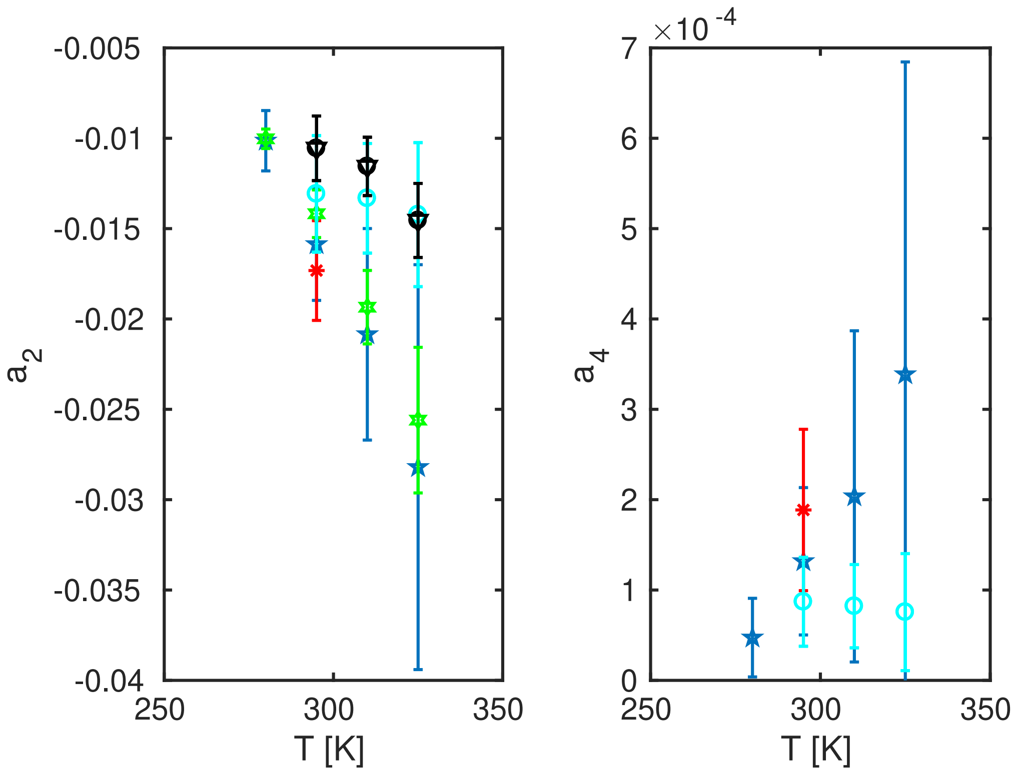

Figure 8.3: *Functional relationship of the parameters describing the master curve established at each temperature. Blue stars, cyan circles and red asterisks represent the temperature-dependent fit results of Equation 8.17 for* YCl_3*,* $LaCl_3$ *as well as the results previously published for* YCl_3 *[33] at* $T = 295\,\mathrm{K}$*, respectively. Green hexagrams and black triangles represent the fit results of Equation 8.18 for* YCl_3 *and* $LaCl_3$*, respectively. The reduced number of fit parameters reduces the errors.*

The calculated attraction strengths are shown in Figure 8.5. For both systems studied, the attraction strength increases with temperature and salt concentration, which is consistent with the LCST-LLPS phase behavior observed for these systems [27].

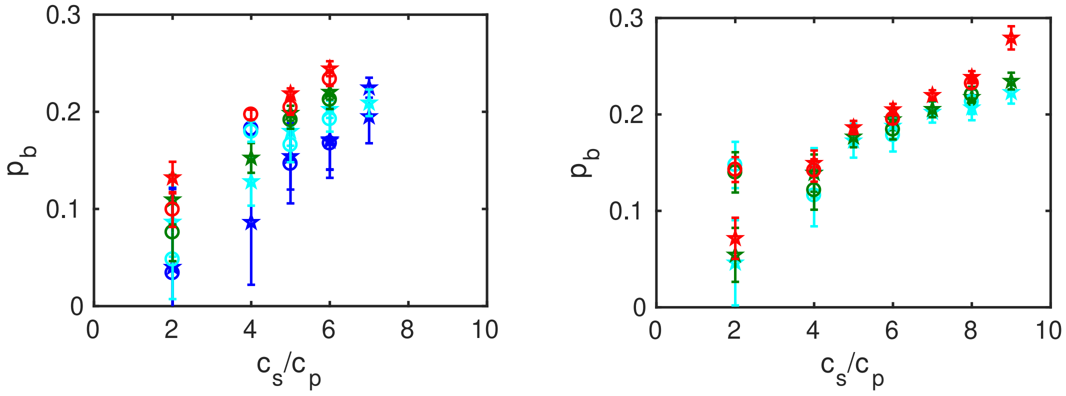

(a) *YCl_3* ***(b)*** *$LaCl_3$*

Figure 8.4: *Binding probability as a function of salt cations per protein for different temperatures. Stars and circles represent values of $c_p = 200\,\frac{\mathrm{mg}}{\mathrm{ml}}$ and $c_p = 300\,\frac{\mathrm{mg}}{\mathrm{ml}}$, respectively. Blue, cyan, green and red symbols represent values for $T = 280\,\mathrm{K}$, $T = 295\,\mathrm{K}$, $T = 310\,\mathrm{K}$ and $T = 325\,\mathrm{K}$, respectively.*

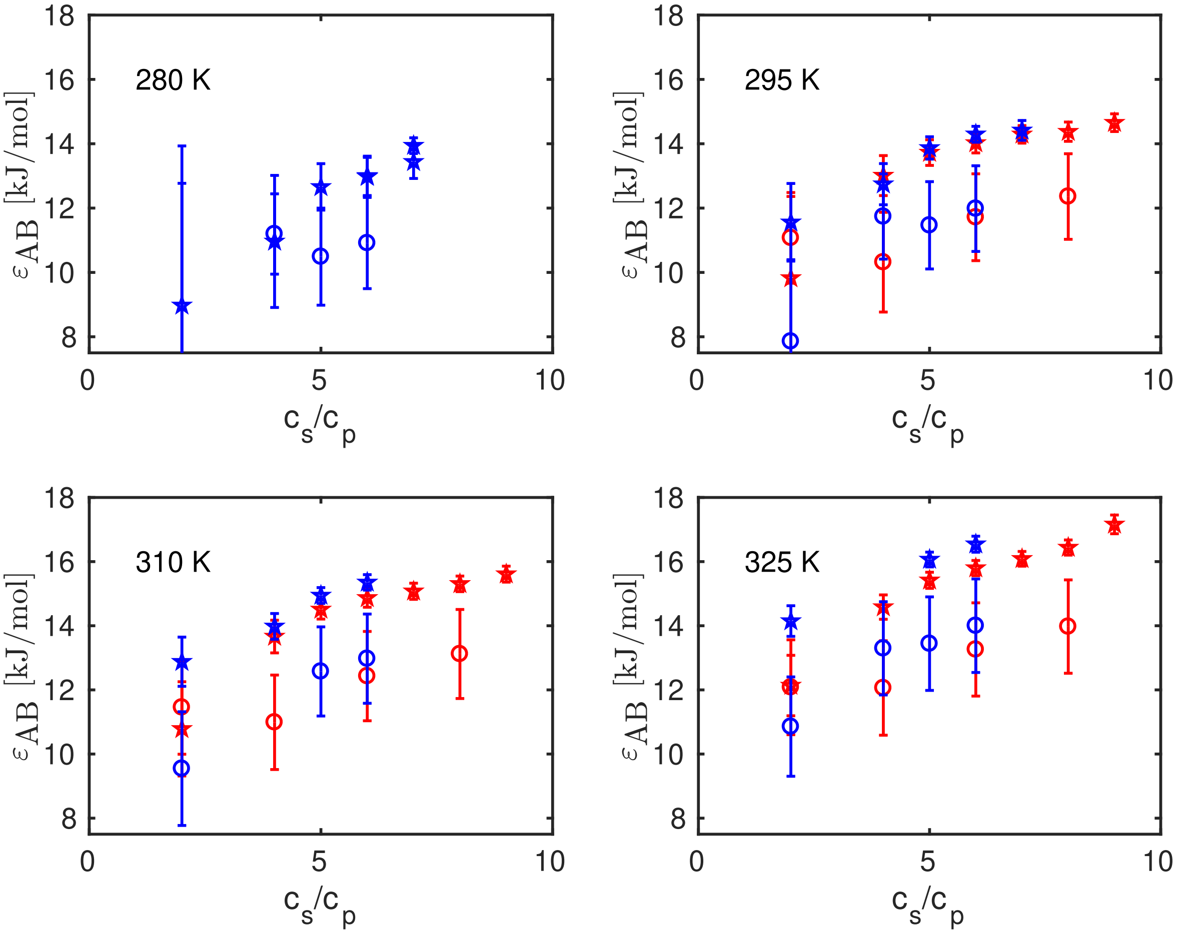

Figure 8.5: *Temperature-dependent protein-protein attraction strength as a function of c_s/c_p for the samples containing YCl_3 (blue) and $LaCl_3$ (red).*

8.6 Conclusion

We investigated the short-time self-diffusion of BSA solutions in the presence of different trivalent salts, approaching c^* at different temperatures. Apart from reproducing the previously investigated master-curve describing the salt-induced slowing down of the short-time self-diffusion at 295 K [33], we observed a change of this master curve with temperature. At higher temperatures, the master curve decays faster than at lower temperatures and salt-dependent effects become more pronounced. This can be explained by a temperature-induced cluster formation. From the normalized master curve describing the diffusion coefficients, the binding probability, showing also a consistent trend, was calculated. This allowed to calculate the attraction strength. Its dependence on the salt concentration, temperature and the type of cation is consistent with the macroscopic phase behavior. Especially at high temperatures, the attraction strength induced by the Y^{3+} ions was stronger than the one induced by La^{3+} ions.

Acknowledgement

This research used resources at the Spallation Neutron Source, a DOE Office of Science User Facility operated by the Oak Ridge National Laboratory. We thank the SNS, the Department of Energy DOE and the JCNS partner user program for allocation of beamtime on BASIS. CB thanks the ILL for studentships and a PhD studentship. We thank R. Moody, R. Goyette and E. Mamontov for support during the beamtimes and for fruitful discussions.

Chapter 9

Following Protein Dynamics in Real-Time during Crystallization

Chapter 9 is based on the following publication:

Following protein dynamics in real-time during crystallization

Christian Beck, Marco Grimaldo, Felix Roosen-Runge, Ralph Maier, Olga Matsarskaia, Michal Braun, Benedikt Sohmen, Orsolya Czakkel, Ralf Schweins, Fajun Zhang, Tilo Seydel and Frank Schreiber

ACS Cryst. Growth Des.19 (2919) 7036

DOI:10.1021/acs.cgd.9b00858

Publication Date (Web): October 25, 2019

Contributions:

Research design	CB, MG, FRR, FZ, TS, FS
Experiments	CB, MG, FRR, RM, OM, MB, BS, OC, RS, TS
Data Analysis and interpretation	CB, MG, FRR, TS
Paper Writing	CB, MG, FRR, FZ, TS, FS

C. Beck *et al.* [136]

9.1 Abstract

The process of protein crystallization from aqueous protein solutions is still insufficiently understood. During macroscopic crystal formation, occurring often on time-scales from a few hours to several days, protein dynamics evolves on the molecular level. Here, we present a proof of concept and a framework to observe this evolving diffusive dynamics on the pico- to nanosecond time-scale, associated with cluster or precursor formation that ultimately results in emerging crystals. We investigated the model system of the protein β-lactoglobulin in D_2O in the presence of $ZnCl_2$ which induces crystallization by electrostatic bridges. First, the structural changes occurring during crystallization were followed by small-angle neutron scattering. Furthermore, we employed neutron backscattering and spin-echo spectroscopy to measure the ensemble-averaged self- and collective diffusion on nanosecond time-scales of protein solutions with a kinetic time resolution on the order of 15 minutes. The experiments provide information on the increasing number fraction of immobilized proteins as well as on the diffusive motion of unbound proteins in an increasingly depleted phase. Simultaneously, information on the internal dynamics of the proteins is obtained.

9.2 Introduction

Protein crystallization is of great interest due to its crucial role for the determination of protein structures in crystallography as well as for applications such as drug design [21]. Despite its importance, a fundamental understanding of the mechanisms underlying protein crystallization is still missing [316, 317]. Under suitable conditions, protein crystals can grow from aqueous protein solutions. For instance, crystallization of negatively charged proteins from solution can be triggered by the presence of divalent salts such as $ZnCl_2$ or $CdCl_2$ [41, 134] or trivalent salts (YCl_3) [133]. Appropriate conditions can induce a liquid-liquid phase separation in the system [184, 318] which might promote crystallization *via* two-step nucleation pathways [133]. Generally, crystal growth resulting in macroscopic crystals proceeds on different time-scales [41] and may take several days.

The process of crystallization has been investigated employing various techniques such as differential scanning calorimetry [319–321], atomic force microscopy [322–324], transmission electron microscopy [324, 325], optical microscopy [41, 326, 327], dynamic light scattering [317, 325, 328], Fourier transform infrared spectroscopy [329], small angle X-ray scattering (SAXS) [41, 325], small angle neutron scattering (SANS) [330] and simulations [331, 332]. Notably, small-angle scattering can provide information on the proteins in solution, on the crystal structure and on protein-protein interactions during the crystallization [41]. The phase diagram and therefore also the crystallization process can be influenced by several parameters such as concentrations of both the proteins and co-solvents [26, 27], temperature [34, 333], vibrations [334], surfaces of the sample containers [335, 336], solvents and additives [32, 305, 326, 337, 338] and electric or magnetic fields [339]. Furthermore, different purification methods or different batches of the protein in question may result in different crystallization behavior.

While phenomenological observations and kinetic studies of the structure itself revealing both classical and non-classical crystallization pathways [37, 134, 327, 332, 339–342] are relatively frequent, only few studies are available on the molecular-level crystallization dynamics [41, 343]. Studies of the diffusive dynamics of dissolved proteins and the formation of protein clusters in solution [33, 64, 96, 109, 120, 131, 238, 277, 344] are more common. The lack of dynamical characterization is particularly puzzling, as diffusive motions are affecting assembly in essential ways, *i.e.* in the case of diffusion-limited aggregation or release from frustrated local configurations.

Here, we make a proof of concept and a first step towards establishing a framework to observe and analyze the ensemble-averaged pico- to nanosecond time-scale diffusive dynamics in protein solutions during crystallization in order to provide a complementary view on the process and inspire further theoretical work on the microscopic processes and dynamics. As a model system, we investigate aqueous (D_2O) solutions of protonated bovine BLG in the presence of $ZnCl_2$.

BLG, as the major protein in the whey of ruminant species, is also interesting for applications in the food industry [345, 346].

A study of the dynamics of the proteins throughout the nucleation and crystallization process can contribute to a complete overall picture. Having verified that the crystallization process appears on suitable time-scales using SANS and optical observation, we use quasi-elastic neutron backscattering spectroscopy (QENS) to access the self-dynamics of the proteins in the scattering vector range of $0.2\,\text{Å}^{-1} < q < 1.9\,\text{Å}^{-1}$ exploiting the prevailing incoherent scattering from their hydrogen atoms [13] Moreover, using neutron spin echo (NSE) spectroscopy, we access smaller q values ($q = 0.082\,\text{Å}^{-1} - 0.1\,\text{Å}^{-1}$), where the coherent scattering dominates and therefore enables an investigation of the collective dynamics of the proteins. Before crystallization, the collective dynamics observed at the Bragg peak ($q_{\text{Bragg}} = 0.082\,\text{Å}^{-1}$) [41, 134] provides information on the coordinated relaxation of concentration fluctuations with wavelengths comparable to the distances in the crystalline state. While the amount of proteins in the crystal increases, the signal at this q becomes dominated by the motion of the proteins in the crystalline state, whereas the off-peak scattering is essentially only originating from the proteins in solution throughout the process.

These neutron spectroscopy techniques thus access the evolution of the dynamics of individual proteins from their free diffusion in the supersaturated solution to their rearrangements during crystallization on different time- and length scales. It is important to note that neutron scattering as non-invasive technique is not influenced by sample turbidity (such as light scattering) and also does not lead to radiation damage, which can be a problem for X-ray scattering techniques.

Generally, we note that, although we did everything possible to ensure reproducible conditions, a complex kinetics experiment with nucleation events such as the presented one on different instruments cannot be expected to be 100% reproducible. Importantly, these neutron spectroscopic studies became only possible in the kinetic mode by significant improvements of the instrumentation in recent years.

This article focuses on the development of the experimental technique and on the data analysis and interpretation and displays a first step for exploiting systematically the dynamics throughout the crystallization process.

We emphasize that in this context certain aspects of the analysis are necessarily oversimplified, but that we believe that this helps to make the key features better visible.

9.3 Materials and Methods

9.3.1 Sample Preparation

Bovine BLG (purity of 90%, L3908), $ZnCl_2$ (purity $\geq 99.995\%$, 429430) and D_2O were purchased from Sigma-Aldrich, now Merck, and used without further purification. A BLG stock solution was prepared by dissolving 200 mg protein powder in 1 ml D_2O (nominal concentration $c_p = 200\,\mathrm{mg/ml}$). The BLG stock solution was mixed with appropriate amounts of D_2O and a 100 mM $ZnCl_2$ stock solution (in D_2O) to obtain a sample with a protein concentration $c_p = 100\,\mathrm{mg/ml}$ and a salt concentration of $c_s = 35\,\mathrm{mM}$. After mixing the components, the sample was vortexed to obtain a turbid, but macroscopically homogeneous solution. Photographs of the non-crystallized and crystallized sample are shown in the Supporting Information in Figure 9.9.

9.3.2 Small-Angle Neutron Scattering

Time-dependent SANS was performed at beamline D11 [347, 348] at the Institut Laue-Langevin (ILL) Grenoble, France. A freshly prepared sample was stored at 8 °C until first crystals were visible and then measured in a time series at room temperature. Neutrons with a wavelength of $\lambda = 6\,\text{Å}$ with $\Delta\lambda/\lambda = 9\%$ were used to measure for 2 min per run at a sample-to-detector distance of 2 m (with an incident beam collimation distance of 5.5 m) covering a q-range from $0.03\,\text{Å}^{-1} < q < 0.33\,\text{Å}^{-1}$. The scattering vector is defined by

$$q = \frac{4\pi \sin\theta}{\lambda} \tag{9.1}$$

with a scattering angle 2θ. A rectangular neutron beam of 10 mm height and 7 mm width was used to illuminate the samples which were filled into Hellma quartz cuvettes of 1 mm path length. The scattering intensity was recorded with a ^{3}He MWPC CERCA detector with 256×256 pixels of $3.75\,\mathrm{mm} \times 3.75\,\mathrm{mm}$ size. The two-dimensional scattering data were corrected pixel by pixel according to standard routines and then azimuthally averaged to obtain one-dimensional scattering curves as presented in Figure 9.1. For the data reduction the LAMP software available at the ILL was employed. Light water (H_2O, 1mm path-length) served as a secondary intensity calibration standard. Data were put on absolute scale by using the differential scattering cross-section of H_2O ($0.983\,\mathrm{cm}^{-1}$ for $\lambda = 6\,\text{Å}$).

9.3.3 Quasi-Elastic Neutron Backscattering

For the quasi-elastic neutron backscattering (QENS) measurements the sample was filled into a double-walled aluminum cylinder (23 mm outer diameter, 0.15 mm gap, *i.e.* difference between inner and outer radius), sealed against vacuum and inserted into the instrument at $T = 7\,^\circ\mathrm{C}$ for the measurement [349]. The experiment was carried out using the cold neutron backscattering spectrometer IN16B at the ILL [191]. The sample was inserted into a standard orange cryofurnace mounted inside the evacuated secondary spectrometer chamber. The instrument was used with unpolished Si(111) crystal monochromator and analyzers and a vertically position-sensitive detector (PSD) consisting of 16 ^{3}He detector tubes covering a scattering vector range of $0.57\,\text{Å}^{-1} < q < 1.94\,\text{Å}^{-1}$. In addition, two small-angle detectors with a slightly lower energy resolution (due to a small angular deviation from backscattering) were placed at $q = 0.19\,\text{Å}^{-1}$ and $0.29\,\text{Å}^{-1}$. An energy transfer range of $-30\,\mu\mathrm{eV} < \hbar\omega < 30\,\mu\mathrm{eV}$ was detectable in the so-called inverse geometry by Doppler-shifting the incident monochromatic neutrons using an AEROLAS Doppler drive operating with a sinusoidal velocity profile with an amplitude of 75 mm and maximum velocity of $4.5\,\mathrm{m/s}$. The flux at the sample was optimized by a phase space transformer (PST) chopper disk [173], carrying graphite mosaic crystals at its circumference and spinning at 7100 rpm during the experiment, corresponding to a crystal velocity of 243 m/s.

During the entire backscattering experiment, we recorded 15 minute frames at full energy range. By using a running average, the raw data was binned to obtain spectra which were collected over three hours with a time resolution of 15 minutes. Data reduction and fits were carried out using MATLAB R2017a (The MathWorks, Inc.). We normalized the measured intensities by the incident neutron flux and detector efficiency obtained from the vanadium measurement, and we subtracted an empty can signal from the protein solution spectra. Since the spectra collected are based on counting events, its errors are given by the Poisson statistics.

9.3.4 Neutron Spin-Echo Spectroscopy

A sample with identical concentrations was prepared and measured using the neutron spin-echo spectrometer IN11 at the ILL [349, 350]. The sample was filled into a 1 mm quartz cuvette and measured at $T = 7\,^\circ\mathrm{C}$ with a wavelength of $\lambda = 8\,\text{Å}$ iterating between the scattering angles 6° and 7.3°, covering the scattering vectors

$q_{\mathrm{Bragg}} = 0.082\,\mathrm{\AA}^{-1}$ and $q_{\mathrm{off}} = 0.1\,\mathrm{\AA}^{-1}$. Measurements were only performed at these scattering vectors to focus on the time dependence of the crystal growth.

Since the sample did not crystallize homogeneously over the entire cuvette, the sample was partially shielded with cadmium (around 41 hours after the sample preparation) to focus on the crystal growth once crystals were visible by eye. The resolution functions of the instrument were determined for the different experimental conditions using the elastic scattering of graphite, measured with the exact same Cd-mask as the protein sample. Each Fourier time point was measured for 45-90 s, resulting in a time resolution of around 80 minutes per scattering angle q. The data were normalized by the instrument resolution function and further analyzed with MATLAB.

9.4 Results and Discussion

9.4.1 Structural Characterization

SANS measurements were performed to investigate the time the sample needs to crystallize and to determine Bragg peak positions. Figure 9.1 shows the time dependent scattering signal of the sample. A sample prepared and measured at room temperature did not crystallize and served as a non crystallizing reference (black dotted line). By decreasing the temperature to T = 8 °C crystal growth could be triggered in a second sample. Once crystals were visible, they continued growing at room temperature and were measured by SANS. During the crystallization process, the overall scattering intensity decreases owing to the decrease of protein clusters in solution. Upon crystal formation Bragg peaks appear, which are used for the dynamic measurements later, whose intensity increases as the crystallization process evolves.

9.4.2 Model of the Scattering Function for Backscattering describing the Self-Diffusion

When hydrogenated proteins are measured in deuterated solvents, the incoherent scattering from hydrogen dominates in the q-range investigated with IN16B. In contrast to the coherent scattering containing structural information investigated in the previous section, the short-time self-diffusion is investigated with incoherent QENS [44].

In a crystallizing sample, at least two protein populations contribute to the scattering function: immobile proteins inside and mobile ones outside of the crystals. Besides, salt-induced [23, 33, 41, 134] as well as crowding-induced [96, 131] oligomeric populations may be present. While the global diffusion of proteins in crystals (as well as those in very large aggregates, diffusing so slowly that the energy transfers cannot be detected with the given energy resolution, see Section 9.4.3) should be negligible, we expect the “free” proteins to be well observ-

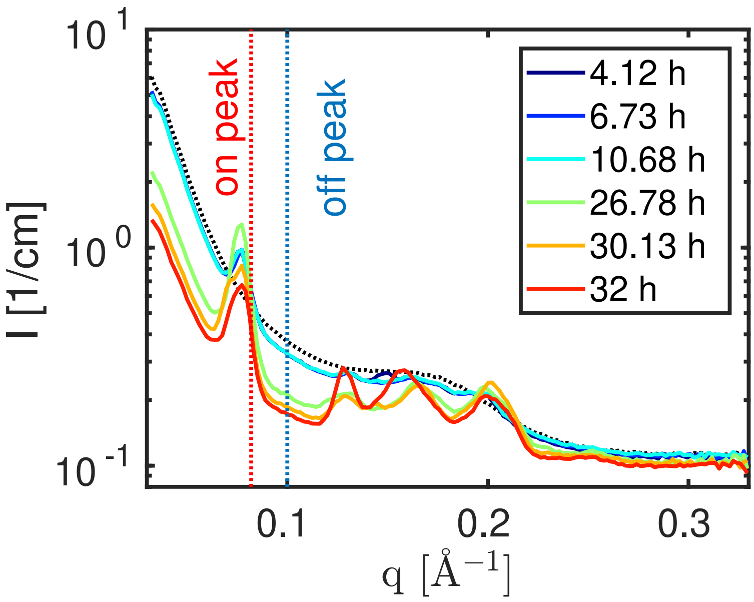

Figure 9.1: *SANS measurements of two different samples with the same concentration. The black dotted line shows the SANS profile of a non-crystalizing sample prepared at room temperature. Solid lines show the time dependence of a second sample which was followed after macroscopic crystals were already visible in the cuvette which was stored at 8 °C. The red and blue dotted vertical lines represent the q-values at which the NSE measurements were performed. All SANS measurements were performed at 20 °C. These data represent the best time resolution currently available for this sample condition, evidencing the course of crystallization on time scales of several hours.*

able within the accessible time-scale. Moreover, internal motions contribute to the recorded scattering function as well. In principle, internal dynamics could be different in crystals and in solution. Although a change of fast vibrational dynamics was observed by Raman spectroscopy upon lysozyme crystallization [351], nuclear magnetic resonance (NMR) studies suggest that differences on a pico- to nanosecond time-scale are absent or very limited [352, 353]. Hence, in order to keep the model as simple and robust as possible, *i.e.* to reduce the number of free parameters, we model the scattering function $S(q,\omega)$ as a sum of the contributions from non-diffusing proteins in crystals or large aggregates and diffusing proteins in solution with the same internal dynamics:

$$\begin{aligned} S(q,\omega) = \mathscr{R}(q,\omega) \otimes \{\beta(q)\times \\ [A_c\ [A_0(q)\delta(\omega) + (1-A_0(q))\mathscr{L}_\Gamma(\omega)] + \\ (1-A_c)\,[A_0(q)\mathscr{L}_\gamma(\omega) + (1-A_0(q))\mathscr{L}_{\gamma+\Gamma}(\omega)]\,] \\ +\beta_{\mathrm{D_2O}}\mathscr{L}_{\gamma_{\mathrm{D_2O}}}(\omega)\}\ . \end{aligned} \tag{9.2}$$

q denotes the scattering vector and $\hbar\omega$ is the energy transfer. We note that the assumption of identical internal dynamics of proteins in crystals and in solution may lead to systematic errors. In contrast, allowing for (slightly) different dynamics as well as considering additional contributions from protein clusters would render the fit ill-posed. We therefore prefer a simplified model. In Equation 9.2, A_c and $(1 - A_c)$ denote the fraction of non-diffusing and diffusing proteins, respectively, and $\delta(\omega)$ is a delta function accounting for immobile proteins. $\mathscr{L}_{\{...\}}$ denote Lorentzian functions accounting for diffusive (global and internal) dynamics with the index to this symbol denoting the respective half-width at half maximum. In particular, the linewidth γ accounts for the averaged global diffusion of monomeric and dimeric proteins as well as of small protein clusters in solution, whereas Γ describes the average internal dynamics. $\beta(q)$ is a scaling factor, while the so-called elastic incoherent structure factor (EISF) $A_0(q)$ provides information on the geometry of confinement of atoms within the protein [290]. Finally, the term $\beta_{D_2O}\mathscr{L}_{\gamma_{D_2O}}(\omega)$ accounts for the contribution of D_2O and is fixed during the fit, as explained in Ref. [61], and $\mathscr{R}(q,\omega)$ represents the resolution function of IN16B determined from the spectrum of a vanadium standard (width $\approx 0.9\,\mu\text{eV}$ full width at half maximum). In the fit algorithm, $\mathscr{R}(q,\omega)$ is described analytically by a sum of two Gaussian functions, and the convolution $\mathscr{R}(q,\omega) \otimes \{...\}$ is carried out analytically, yielding $\mathscr{R}(q,\omega) \otimes \delta(\omega) = \mathscr{R}(q,\omega)$ and Voigt functions consisting of $\mathscr{R}(q,\omega)$ and $\mathscr{L}_{\{...\}}$.

In a first step, the parameters $\beta(q)$, $A_0(q)$, γ and Γ are fitted q-wise, while A_c is set as a global, q-independent parameter. The errors of the fit results represent the 95% confidence bounds of the fit based on the inverse Jacobian matrix. Two examples of a fitted spectrum (first and last spectrum of the time-dependent measurement) are shown in the insets of Figure 9.2 with the main figure showing the time dependence of the scattering signal at $q = 1.48$ Å^{-1}. Already in the raw data, a reduction of the overall spectral width and an increase of the elastic contribution with time is visible. The widths γ obtained from a fit of Equation 9.2 are plotted as a function of q^2 in Figure 9.3.

The red triangles in Figure 9.3 corresponding to the sample 1.5 hours after preparation deviate slightly from a straight line (shown as black dotted line). We use a well-established formula to fit this apparent signature in q, as described by the Singwi and Sjölander jump-diffusion model [62]

$$\gamma = \frac{D\,q^2}{1 + \tau D\,q^2}\,, \tag{9.3}$$

where D is the jump-diffusion coefficient and τ denotes the residence time in the trapped state. The trend obtained from Equation 9.3 becomes even more pronounced at longer times, as noticeable from the flattening of γ at higher q. Three reasons may explain the deviations of γ at low q-values. First, due to the design of the instrument, the first two detectors have a broader energy resolution than the other 16 detectors. Second, the lowest detector covers the Bragg peak visible in

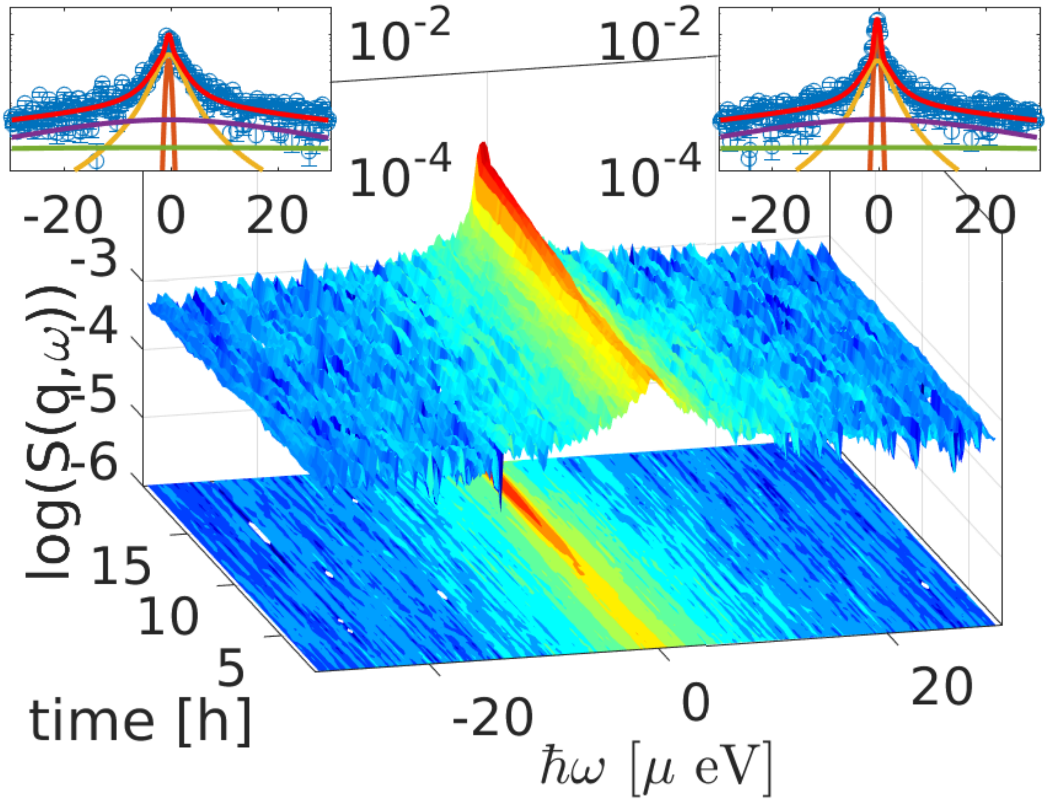

Figure 9.2: *Main figure: Time dependence of the backscattering signal at* $q = 1.48$ Å^{-1}*. The increase of the elastic contribution with time can already be seen in the raw data. The two insets show fits (red line) at the same* $q = 1.48$ Å^{-1} *for the first (left) and last (right) collected spectra. Brown, yellow, purple and green lines represent contributions of immobile proteins, global and internal diffusion, respectively. During the whole measurement, the sample was kept at* $T = 280\,\mathrm{K}$.

Figure 9.1. In the presence of crystals, the scattering signal at this detector therefore contains significant coherent contributions which are not accounted for in the model. Third, at low q, quasi-elastic broadenings are very small and close to the energy resolution and, as shown in Section 9.4.3, at longer times the contribution of diffusing proteins decreases, such that even small inaccuracies in the analytical description of $\mathscr{R}(q,\omega)$ may have a large influence on the fitting parameters.

Having verified that the q dependence of γ can be described by Equation 9.3, we impose this q-dependence in Equation 9.2 on D and τ to reduce their errors. Hence, we now fit $S(q,\omega)$ with A_c, D and τ as global parameters with the two latter parameters describing the global diffusion according to Equation 9.3. This slightly different procedure does not significantly change the values of any parameter (see Supporting Information, Figure 9.11 and Figure 9.12) but, as expected, increases the accuracy of A_c, D and τ.

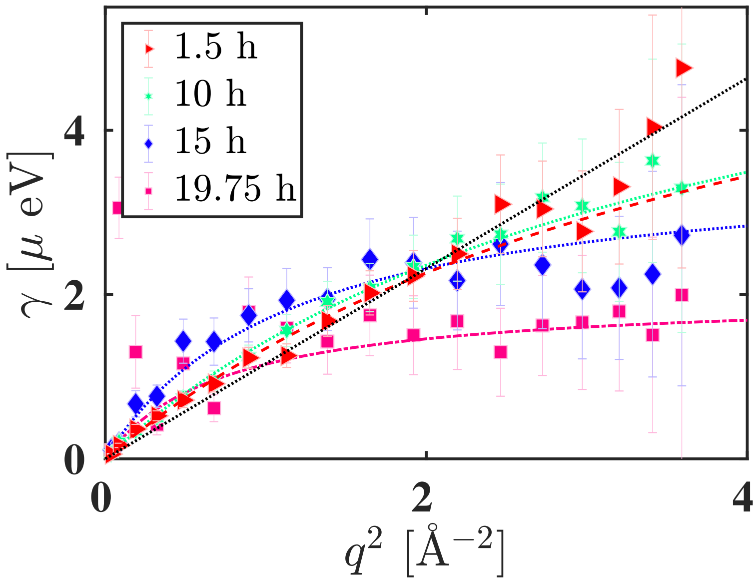

Figure 9.3: *Lorentzian linewidth γ (symbols) vs. q^2 characterizing the global diffusion obtained from the fits of Equation 9.2 to the backscattering spectra at four different times t after sample preparation. The fits with Equation 9.3 (lines) describe a jump-diffusion. At $t = 1.5\,\mathrm{h}$ and 10 h, γ deviates slightly from a straight line, which would indicate free Brownian diffusion, whereas at longer times the deviation from $\gamma \propto q^2$ is much more pronounced and a jump-diffusion-like behavior is clearly recognizable.*

As shown in the Supporting Information in Figure 9.13, the global diffusion coefficient exceeds the dilute limit, *i.e.*, the theoretical diffusion coefficient at infinite dilution calculated based on the protein structure (see Figure 9.13 in the Supporting Information) or the value extrapolated based on values determined by PFG-NMR ($D = 4.82\,\mathrm{Å}^2\mathrm{ns}^{-1}$ [354], rescaled to $T = 7°\,\mathrm{C}$ according to the Stokes-Einstein relation). Since the internal dynamics is assumed to be the same for proteins in solution and in the crystals, it should not change during the transition from a solvated protein to a crystal. The parameters should therefore also remain constant over time. Fixing the internal dynamics based on the first binned QENS spectrum leads to an apparent global diffusion coefficient which approaches the dilute limit but does not exceed it. This indicates that the Lorentzian function describing the global dynamics can no longer be unambiguously separated from the one describing the internal dynamics on the limited energy range investigated if all parameters have to be determined by the fit.

The results of this third fit with q-global fit parameters and fixed internal dynamics will be shown and discussed in the following sections.

9.4.3 Fraction of Immobilized Proteins

The coefficient A_c in Equation 9.2 describes the fraction of non-diffusing proteins on the time-scale accessible (up to a few nanoseconds) such as crystals and big aggregates and precursors. In fact, after opening the sample holder many crystals were found. However, the opening was possible only several hours after the experiment because of radiation protection regulations. The system might thus have first developed amorphous aggregates, which eventually crystallized (as it happens for non-classical crystallization [41, 133, 134]).

Figure 9.4 shows A_c as a function of time. The model indicates that $\sim 10\,\%$ of the proteins in the sample are immobile in the first analyzed spectrum, although they are not part of crystals, pointing to cluster formation immediately after the sample preparation, which is also supported by the turbidity of the sample after sample preparation (See Figure 9.9 in the Supporting Information). After about 7 hours, the fraction of non-diffusing proteins starts to increase, first slowly, then more quickly, going up to $\sim 65\%$. Hence, due to the crystallization process, the volume fraction of proteins in solution

$$\varphi_{free} = (1 - A_c)\ c_p\,\vartheta/(1 + c_p\,\vartheta) \tag{9.4}$$

decreases to $\varphi \simeq 0.025$, corresponding to a free protein concentration of $c_p^{free} = \frac{\varphi}{\vartheta - \vartheta\varphi} \simeq 34\,\frac{\mathrm{mg}}{\mathrm{ml}}$, calculated with a specific volume of $\vartheta = 0.75\frac{\mathrm{ml}}{\mathrm{g}}$ [354].

Given the experimental data, it cannot yet be determined if the clusters observed at the beginning are precursors of the crystallites or if they serve as protein reservoirs which redissolve again during the crystallization process [41].

Applying Equation 9.2 to pure protein solutions, A_c as well as τ are zero within the error bars as expected (see Supporting Information, Figure 9.14). Other protein systems with concentrations up to $c_p = 500\,\frac{\mathrm{mg}}{\mathrm{ml}}$ have already been investigated previously [64], still showing quasi-elastic contributions and no significant elastic contribution.

9.4.4 Global Diffusion

As explained in Section 9.4.2, Equation 9.3 is imposed on the global fit of $S(q, \omega)$ and the internal dynamics is fixed based on the first run. The obtained diffusion coefficients D and residence times τ are plotted as a function of time in Figure 9.5a and Figure 9.5b, respectively. The two trends are very similar to the one of A_c: for about 10 hours, D and τ remain almost constant and then increase up to $D \simeq 5\,\text{Å}^2/\mathrm{ns}$ and $\tau \simeq 0.3\,\mathrm{ns}$, respectively. More systematic measurements at different sample conditions are necessary to confirm and to extract reliable information on the time dependence of D and of τ, such as the small peak between 7 and 10 h and the shoulder at $\sim$ 14 h, respectively, and to link them to the crystallization progress.

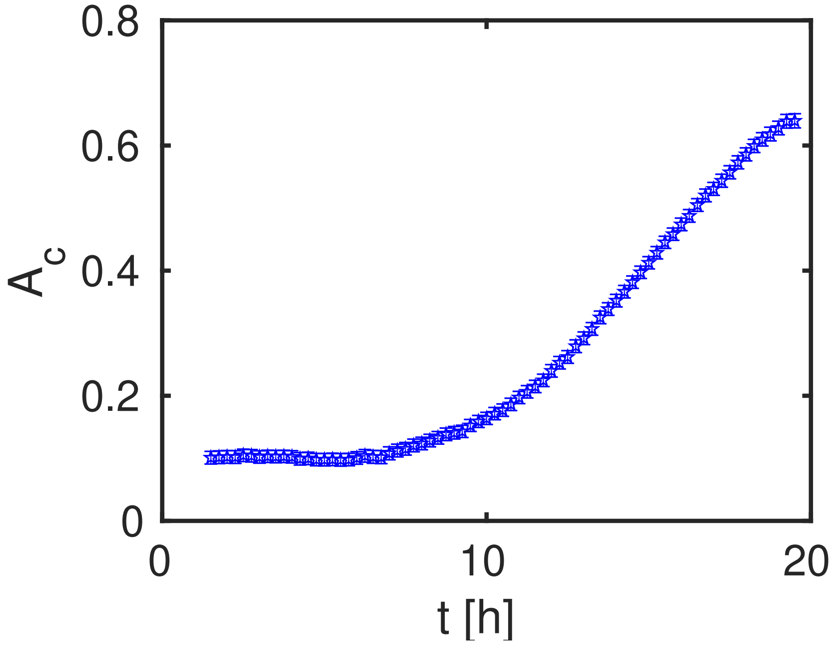

Figure 9.4: *Fraction of immobile proteins A_c as a function of time obtained from the QENS spectra applying fits based on Equation 9.2 with fixed internal dynamics.*

Several effects influence the global diffusion. First, since the amount of proteins bound in crystals increases, the volume fraction of proteins, which diffuse freely in solution decreases over time. As shown in several previous studies, this effective dilution leads to an increasing diffusion coefficient up to the dilute limit [96, 109, 120, 131] ($D = 5.95\,\mathring{A}^2\mathrm{ns}^{-1}$). With increasing global diffusion coefficients, the separation of internal and global diffusion becomes difficult due to the limited dynamic range of the instrument. To obtain reasonable values, this cross-talk in the fit is reduced by fixing the width for the internal dynamics. Second, the presence of multivalent ions in solution can lead to a salt-dependent slowing down of the apparent diffusion coefficient [23, 33]. Since the concentration of salt ions in the solution could not be measured during the experiment and the influence of $ZnCl_2$ on the short-time self-diffusion of BLG has not been studied systematically, the fraction of immobile proteins, A_c, cannot be quantitatively linked to the diffusion coefficient in a straight forward fashion. Nevertheless, although a quantitative connection cannot be established, the general trend can be compared directly. Different plots using different axes are displayed in the Supporting Information in Figure 9.10. We note that the jump-diffusion process observed might also be linked to low statistics in contributions of the scattering function due to the low protein concentration in solution.

9.4.5 Geometry of Confined Motions

Figure 9.6 shows the q-dependence of the EISF obtained from the fits with A_c as the only q-independent parameter for different times. Clearly, the EISF does not change much throughout the process, which gives an *a posteriori* justification for the same internal dynamics assumed for the two populations. The q-dependence of the EISF is described using a model containing a fraction p of non-diffusive contributions, three-site jump-diffusion processes $A_{3-j}(q)$ as well as diffusion in an impermeable sphere $A_{sph}(q)$ [64, 96, 120] for each time-step:

$$A_{3-j} = \frac{1+2j_0(qa_m)}{3} \tag{9.5}$$

$$A_{sph} = \left|3\frac{j_1(qR)}{qR}\right|^2 \tag{9.6}$$

$$A_0 = p + (1-p)\left[\Phi A_{3-j} + (1-\Phi)A_{sph}\right] \tag{9.7}$$

with the n^{th} order spherical Bessel function j_n and the jump distance of H-atoms in methyl groups $a_m = 1.715\,\text{Å}$. While Figure 9.6 displays the q dependence of the EISF, the inset shows the time dependence of the fit parameters p and Φ of Equation 9.7. The parameters agree within the error bars with the values of pure BLG solutions [96]. This observation also supports the assumption that the geometry of the confined motions and the internal dynamics is, to a good approximation, independent of whether the proteins are in solution or parts of aggregates or crystals.

9.4.6 Model for the Scattering Function in NSE

Similar to SANS, neutron spin-echo measurements can access the coherent scattering containing structural information. At different scattering vectors, the kinetics of different components involved in the crystallization process can be followed [41]. The dynamics of the same components during the crystallization process can be investigated *via* NSE measurements sampling the same scattering vectors. The red and blue vertical dashed lines in Figure 9.1 represent the q-values at which the NSE measurements are performed.

We emphasize that in the beginning, in the absence of crystals, the same information about the dynamics is obtained from the scattering functions collected at the different q-values. Only in the presence of crystals, the scattering function measured at q_{Bragg} and at q_{off} contains different dynamical contributions.

Selected examples of the intermediate scattering function $F(q,t)$ measured with NSE on and off the Bragg peak are shown in Figure 9.7. Clearly, the intermediate scattering function on-peak ($q_{\text{Bragg}} = 0.082\,\text{Å}^{-1}$) flattens while crystals grow, indicating that the average diffusion on this length scale decreases, while off-peak ($q_{\text{off}} = 0.1\,\text{Å}^{-1}$), the dynamics becomes faster, consistent with the results from backscattering.

As a simple model, we assume only two different contributions to the scattering function. By describing the off-peak intermediate scattering function *via*

$$F(q,t) = \exp\left[-D_c^f(q)\ q^2\right] \tag{9.8}$$

we describe mainly the collective diffusion of the fraction of proteins, which are in either monomeric state or in clusters. Hence, in Equation 9.8, $D_c^f(q)$ denotes the collective diffusion coefficient of free proteins in solution. At q_{Bragg}, instead, the intermediate scattering function is

$$F(q,t) = A_c \exp\left[-D_c^c(q)\ q^2\right] + (1 - A_c)\ \exp\left[-D_c^f(q)\ q^2\right]\ , \tag{9.9}$$

where $D_c^f(q)$ denotes again the collective diffusion coefficient of proteins in solution, $D_c^c(q)$ is the diffusion coefficient of crystallizing or crystallized proteins, and A_c is the fraction of proteins in crystals. If we furthermore assume that $D_c^f(q) = D_c^f$ is a q-independent parameter, we can first fit Equation 9.8 at q_{off} and then use D_c^f in Equation 9.9, leaving A_c and D_c^c as free parameters. The fits with Equations 9.8 and 9.9 are shown in Figure 9.7. The data thus seem to be consistent with this simple model.

9.4.7 Collective Dynamics studied at Different q

Figure 9.8a and Figure 9.8b show A_c and D_c as functions of time obtained from fitting Equation 9.8 and Equation 9.9 to data measured off-peak at $q_{\mathrm{off}} = 0.1\,\text{Å}^{-1}$and on peak ($q_{\mathrm{on}} = 0.08\,\text{Å}^{-1}$), respectively. Similar to the self-diffusion coefficient, the collective diffusion coefficient D_c^f also increases in parallel with A_c, which is consistent with a depletion effect. This observation also confirms that off-peak we obtain essentially only the signal from proteins in solution. Figure 9.8b also shows the collective diffusion coefficient D_c^c (red squares). We do not see any additional dynamics on the length scale of the Bragg peak within the time scales studied. With longer time scales as well as with more scattering vectors measured, a better separation between the different contributions would be possible. Given the negligible values of D_c^c, the model can be simplified using an apparent flat background within the correlation times presently accessible. Future NSE measurements with higher Fourier times might access the corresponding diffusive dynamics, which would then be described by the second exponential function.

We note that differences at the Bragg peak position were visible only several hours after crystals were observable by eye. If only few crystals are present at the beginning of the process, discrete Bragg reflections are visible. The powder average might therefore not be fulfilled at the beginning of the crystallization process. Since the detector of IN11A only covers a small fraction of the total solid angle, Bragg reflections might have been initially positioned outside of the detector area of IN11A and then moved into the detection range.

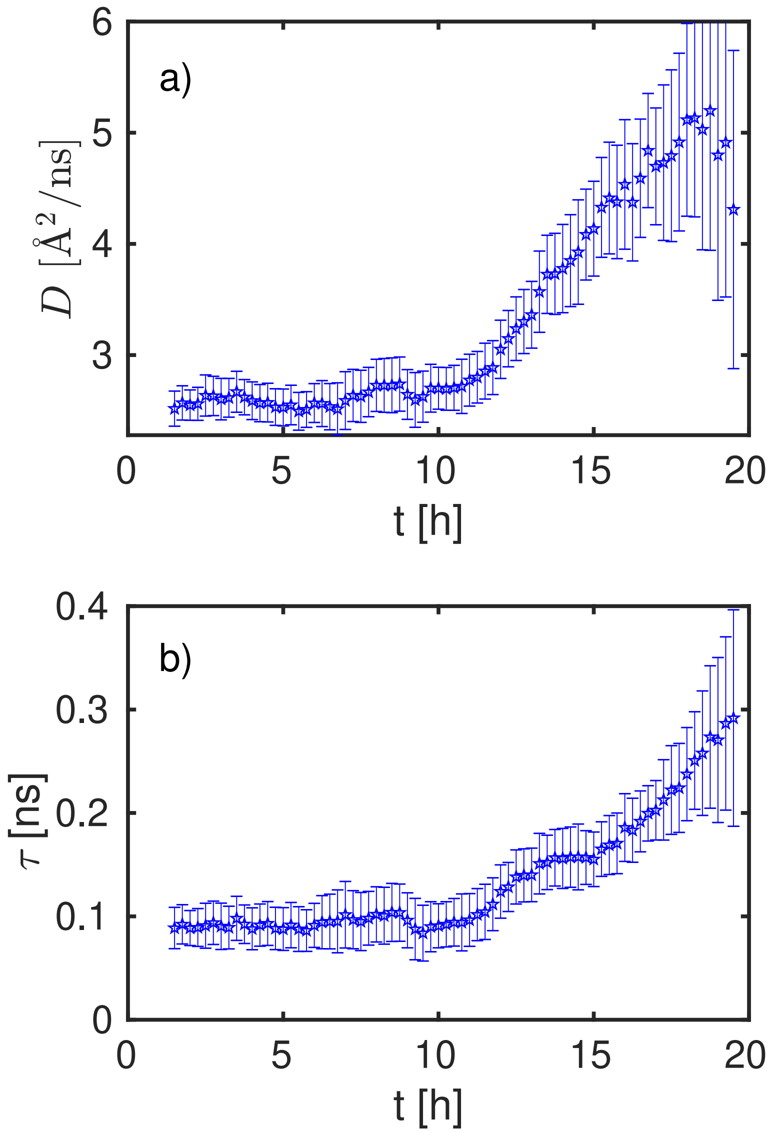

Figure 9.5: *Time dependence of the parameters characterizing the averaged global dynamics of the proteins in solution determined from the global fits of Equation 9.2 with fixed internal dynamics and Equation 9.3 describing the global diffusion as a function of time.*
Figure 9.5a displays the global short-time self-diffusion coefficient D as a function of time. For long times, the observed diffusion coefficient approaches the monomer dilute limit (see also Figure 9.13).
Figure 9.5b shows the time dependence of the residence time τ.

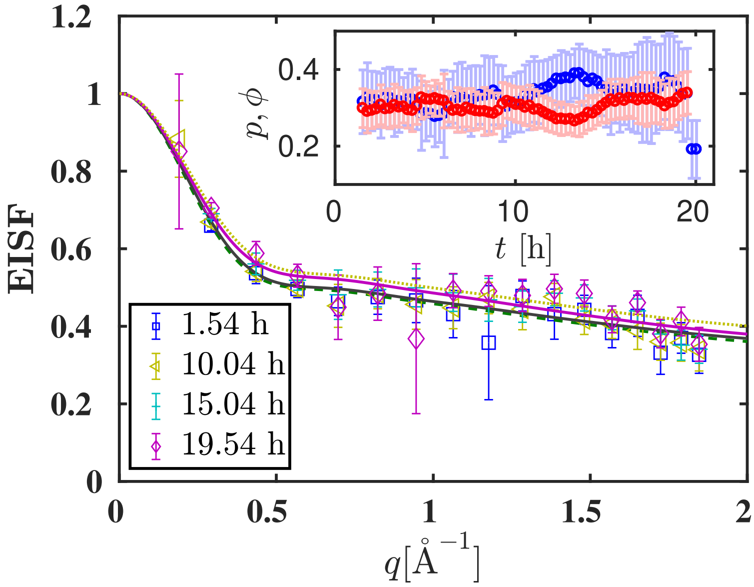

Figure 9.6: *Time dependence of the EISF $A_0(q)$ as a function of q describing the dynamics on a molecular length scale as obtained from the QENS spectra by fitting Equation 9.2 with free internal dynamics. Although a significant fraction of the proteins arrange into immobile assemblies, the EISF does not change significantly, which validates a posteriori the assumption that the internal dynamics does not change significantly between the different global arrangements. The time dependence of the different fit parameters (red: p ; blue: Φ) of the EISF from Equation 9.7 are shown in the inset. Within the errors, the parameters are constant in time.*

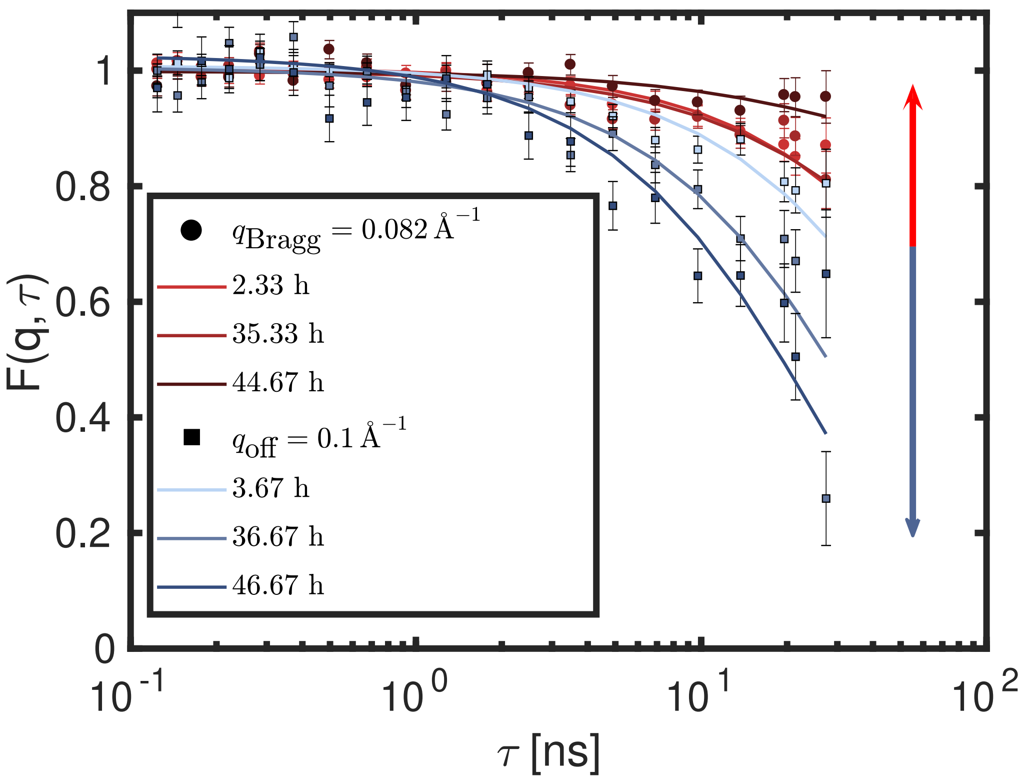

Figure 9.7: *Examples of the intermediate scattering functions measured at IN11 from BLG* $c_p = 100\,\frac{\mathrm{mg}}{\mathrm{ml}}$ *and* $c_s = 35\,\mathrm{mM}$. *Red circles and blue squares show measured data on and off the Bragg peak, respectively. The time steps are coded by the brightness of the points as shown in the legend. Solid lines show the fit results.*

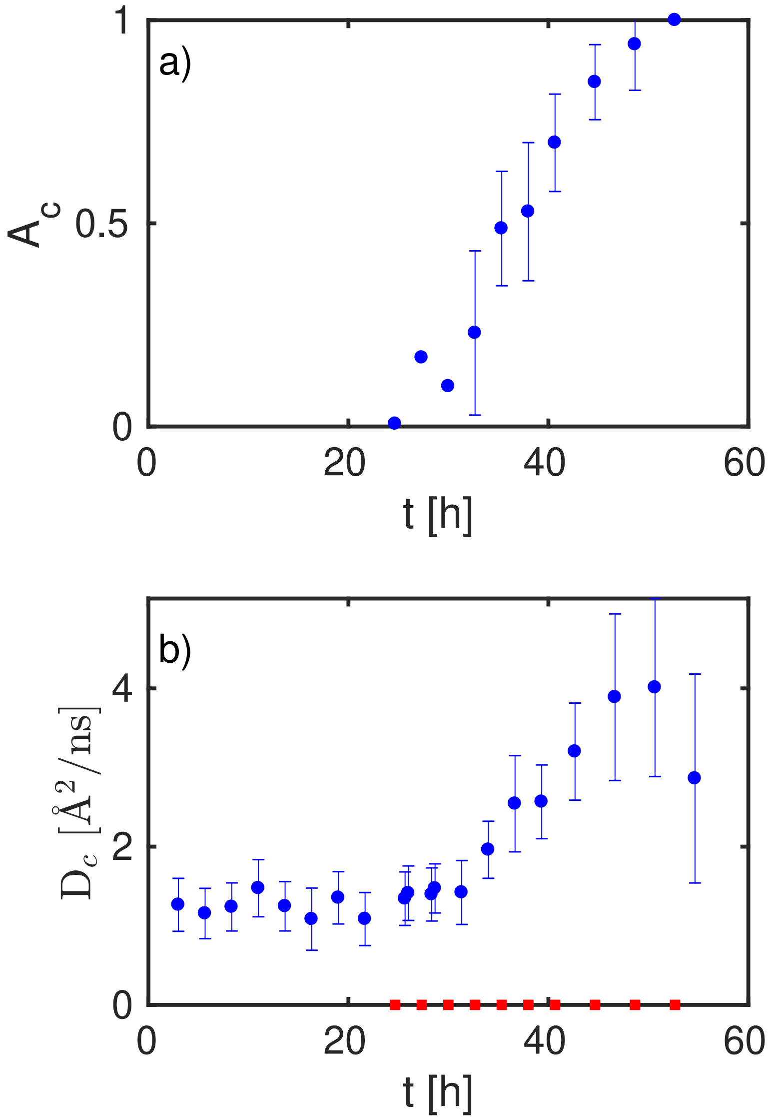

Figure 9.8: *Results of the analysis of the neutron spin-echo data based on Equation 9.8 and 9.9 shown in Figure 9.7.*
Figure 9.8a: The time dependence of the fraction of proteins within the crystals and of the diffusion coefficient of the dissolved proteins in solution agrees qualitatively with the results obtained from the QENS analysis shown in Figure 9.4 and 9.5.
Figure 9.8b: The obtained diffusion coefficients off-peak and on-peak are shown in blue circles and red squares, respectively. While the diffusion coefficient of the proteins in solution observed with NSE increases similarly to the one observed with QENS (see Figure 9.5a), no dynamics could be extracted from the proteins in the crystals.

9.5 Conclusions

We have presented a proof of concept and an analytical framework to investigate the process of protein crystallization in solution, proceeding on a time-scale of several hours, by measuring the short-time diffusive dynamics of proteins in solution and in aggregates and crystals on different time-scales such as on the nanosecond time-scale with QENS and on longer time-scales with NSE. By combining neutron spin-echo and backscattering spectroscopy, we access both the collective dynamics on the Bragg peak and the dynamics in the liquid phase at other scattering vectors. Due to the high scattering vector, corresponding to a nanometer observation length scale, and the absence of polarization analysis, backscattering accesses the self-diffusion of the proteins *via* their prevailing incoherent scattering. Notably, both experiments corroborate an onset of a slowly and continuously growing fraction of proteins that are immobile during the experimental observation or coherence time of a few nanoseconds in the backscattering experiment and a few tens of nanoseconds in the neutron spin-echo experiment. This immobility may be associated with emerging protein aggregates or later with crystallites forming in the sample. In parallel, a decreasing protein monomer concentration in the depleted phase manifests itself by monomer diffusion coefficients that increase as crystallization proceeds. This increase of the observable monomer center-of-mass diffusion can be partially explained by the decrease of the crowding effect by the freely diffusing proteins. Measuring more scattering vectors with NSE and up to higher energy transfers with QENS will allow in future studies to separate additional contributions such as from aggregates and will thus reveal more information about the crystallization pathways and the dynamical properties of the different species involved. The backscattering experiment simultaneously accesses the superimposed internal diffusive motions within the proteins. These motions seem to be nearly unaffected by the crystallization within the precision currently achievable, but may be further studied with improved setups. Our framework opens the perspective to systematically study the dynamics of protein crystallization of numerous protein solution samples. Given the time-dependent changes of the sample, the statistics of the scattering data is flux limited. Accessing several scattering vectors simultaneously using future NSE instruments and using future neutron sources with higher peak neutron fluxes or measuring slower crystallizing samples will offer access to the dynamics of the proteins in the different phases of the (multistep-) crystallization processes with higher accuracy. Future wide-angle NSE instruments may also permit to study the formation of single large crystals. The influence of different protein and salt concentrations on the kinetic changes of the diffusion can be systematically investigated in future studies. Such systematic studies will contribute to a better fundamental understanding of crystallization pathways, which will help to address the bottleneck of obtaining diffraction-quality crystals for applications in structural biology.

9.6 Supporting Information

The neutron data are permanently curated by the ILL and accessible *via* doi:10.5291/ILL-DATA.8-04-760 (Backscattering data and NSE)[349], and doi:10.5291/ILL-DATA.9-13-620 (SANS data)[348].

9.6.1 Photographs of the Sample Before and After Crystallization

In Figure 9.9 photos of the sample measured with NSE are shown before and after the crystallization process.

(a) *Photo taken 16 hours after sample preparation.*

(b) *Photo taken 58 hours after sample preparation.*

Figure 9.9: *Photos of the sample before and after protein crystallization.*

9.6.2 Comparison of Time Dependencies of Different Parameters

In Figure 9.10, the time dependence of the different fit results obtained from the QENS fits are presented. It is visible that both the fraction of the immobile proteins A_c as well as the parameters D and τ, describing the global diffusion as shown in Equation 9.3 in the main manuscript, follow, within the error-bars, the same time dependence.

9.6.3 Comparison of Different Fit Routines

Two fitting approaches were presented in Section 9.4.2. In the first approach, only the fraction of immobile proteins was fixed as a q-independent fit parameter, while the second approach directly fixed jump-diffusion as the model for the global dynamics. Figure 9.11 shows the results for the two different approaches. The different subplots show the fit results for A_c, D or τ as a function of time.

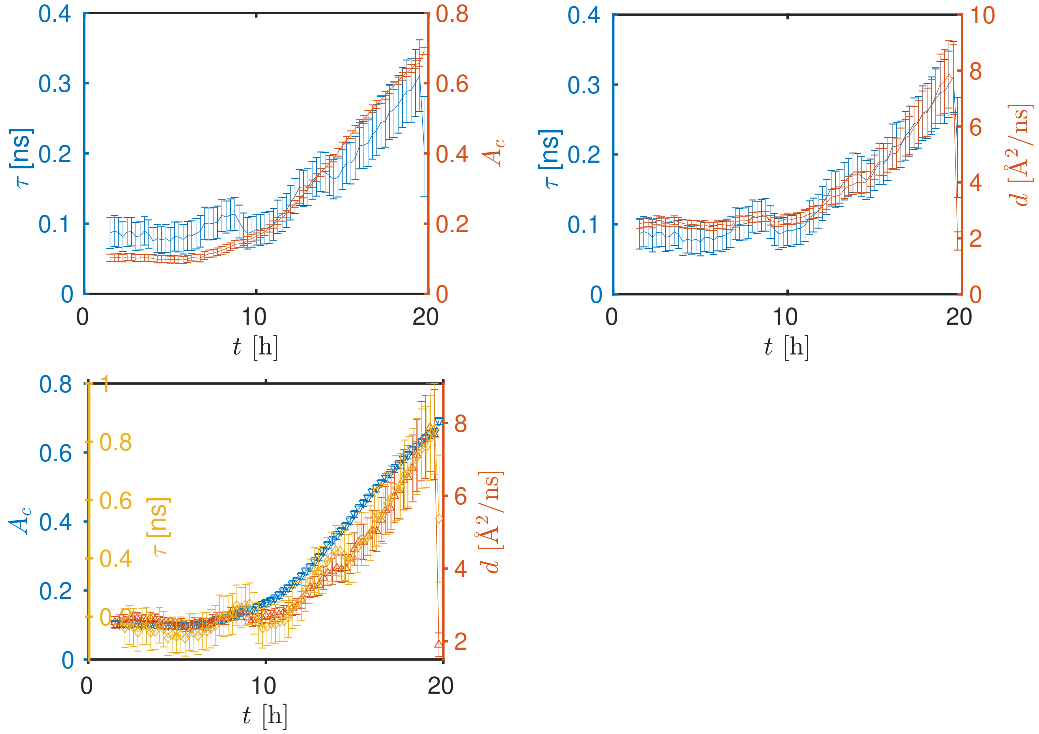

Figure 9.10: *Different combinations of two or three fit parameters with slightly rescaled and shifted ordinates to compare their time dependencies.*

Figure 9.12 shows the time dependence of the parameters characterizing the EISF (see Equation 9.7 in the main manuscript) for the two different fit approaches. The color coding is the same as in Figure 9.11. No significant differences are seen between the two approaches and as a function of time.

9.6.4 Influence of Fixed Internal Dynamics on the Apparent Global Diffusion Coefficient

In Figure 9.13, the time dependence of the apparent global diffusion coefficient is shown. For the fits with free internal dynamics (red symbols), the diffusion coefficient clearly exceeds the theoretical dilute limits for monomers (yellow dashed line) and dimers (brown dashed line). By fixing the width of the internal dynamics based on the first QENS-spectra measured (violet symbols), cross-talking can be avoided in the fit and the diffusion coefficients do not exceed the monomer limit anymore.

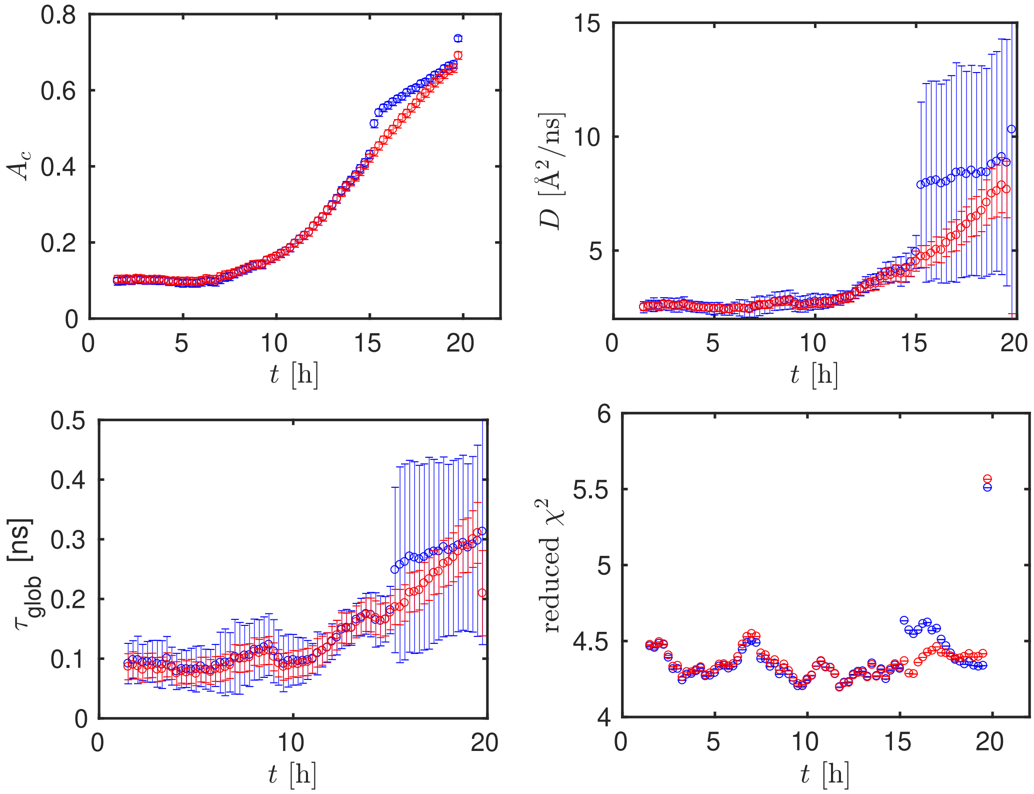

Figure 9.11: *Fit results obtained from the different fit routines. Blue points represent the fit results from the fits with only A_c as a q-independent fit parameter, the red points are obtained with D and τ as additional q-independent parameters.*

9.6.5 Comparison with Pure Protein Solutions

The fit model of Equation 9.2 to pure protein solutions without salt leads to A_c and τ being equal to zero within the errorbars. The diffusion coefficients obtained show the expected decrease due to crowding and cluster formation [131]. For different protein concentrations, the fit results are shown in Figure 9.14.

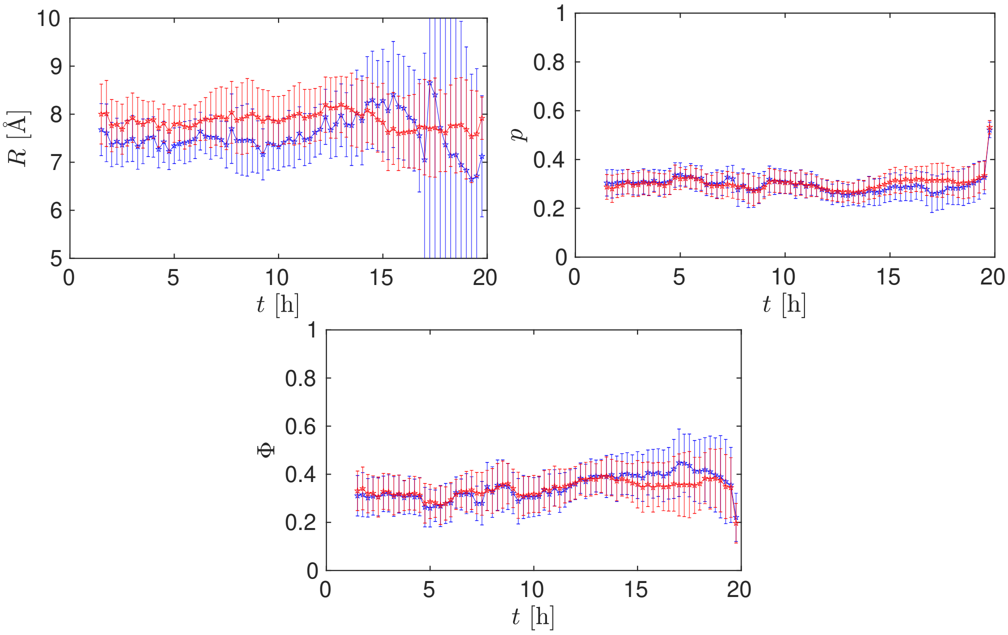

Figure 9.12: *Time dependence of the EISF fit parameters. Blue points represent the fit results from the fits with only A_c as q-independent fit parameter, the red points are obtained with D and τ as additional q-independent parameters.*

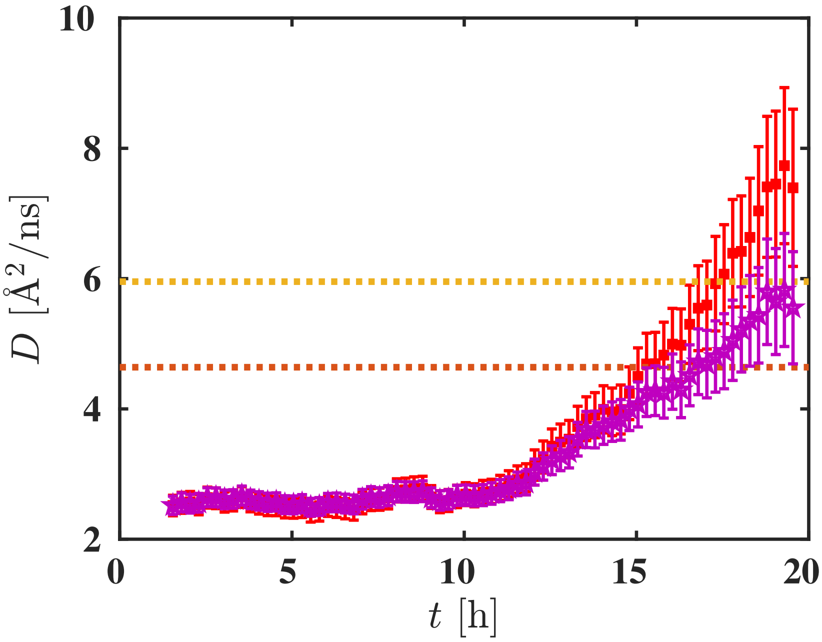

Figure 9.13: *Diffusion coefficients for fits with fixed (violet) and free internal dynamics contribution (red). The yellow and brown dashed lines represent the dilute limit for monomers and dimers, respectively.*

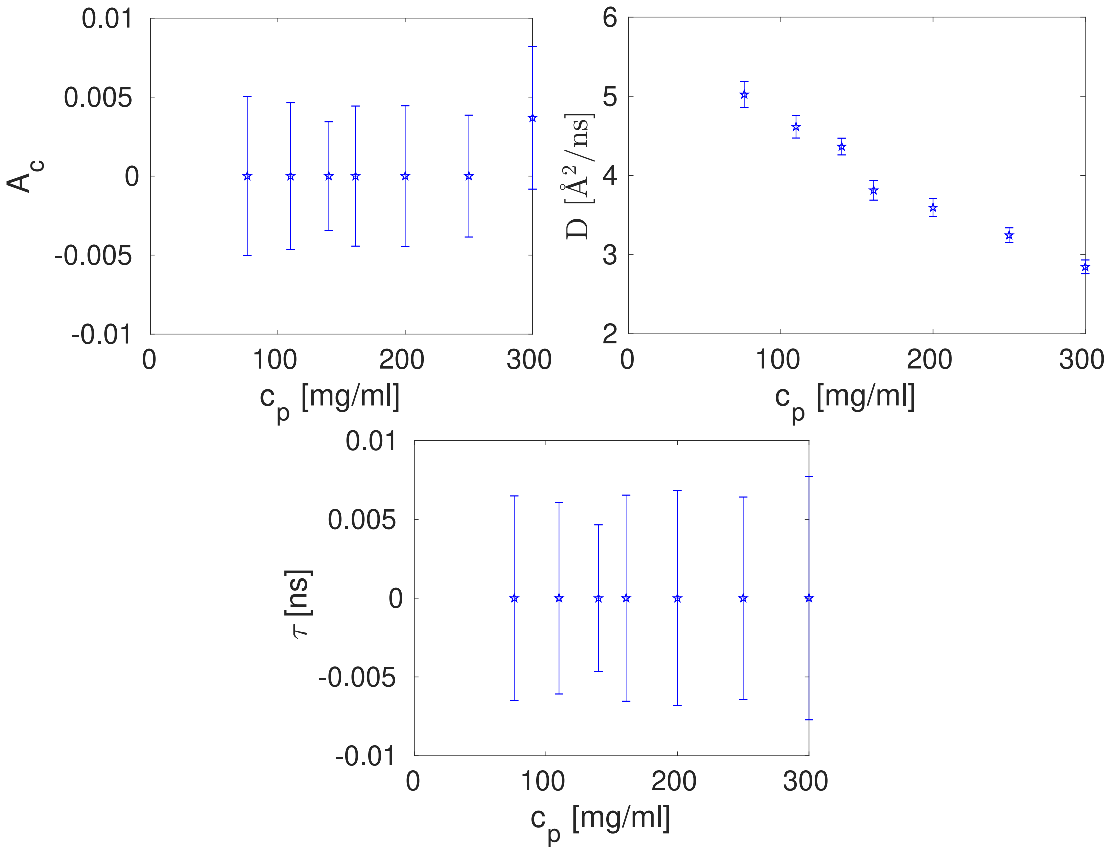

Figure 9.14: *Fit results of Equation 9.2 to pure protein solutions.*

Acknowledgments

This work was supported in part by the DFG and the ANR (contract no. ANR-16-CE92-0009-01) and the Knut and Alice Wallenberg Foundation (project grant KAW 2014.0052). C.B. acknowledges the support by a studentship co-funded by the ILL and the University of Tübingen. We thank Ingo Hoffmann, Andrea Sauter and Stefano da Vela for fruitful discussions and the PSCM (Grenoble) for sharing their laboratory resources.

Chapter 10

Outlook and Open Challenges

In this chapter, I give an outlook on possible follow-up projects based on the work presented in this thesis.

The present thesis systematically addresses different dynamic and static aspects of protein assembly in aqueous solutions, including cluster formation induced by crowding or multivalent salt ions, as well as crystallization. To this effect, frameworks were developed for the data analysis, notably including the access to the dynamics of kinetic processes on the molecular level using neutron spectroscopy (Chapter 5 and Chapter 9). These frameworks allow to access simultaneously both information on the global center-of-mass diffusion of the proteins - reflecting the size of a protein assembly - and the internal diffusive dynamics within the proteins (Chapter 7). The experiments were carried out at the most novel and advanced neutron spectrometers existing for this purpose, including IN16B and its BATS option (Chapter 4) at the ILL and BASIS at the SNS. The experiments involved prevailing incoherent neutron spectroscopy using neutron backscattering (NBS) (Chapters 4-9), as well as an access to coherent scattering using NSE spectroscopy (Chapter 9).

As explained in Chapter 2.7, for the BATS option of IN16B, it is necessary to perform additional, sophisticated background corrections to avoid systematic errors in the fit results due to the complexity of the time of flight mode. The broader energy range compared to IN16B in the setup using a monochromator crystal and the better energy resolution compared to the one of BASIS allows to to fit substantially more complex models. An analysis framework applying fits to more than one spectrum simultaneously and also considering further control parameters, is already developed for the analysis of the BASIS data presented in Chapter 8 and can be applied to future BATS data. The same framework can be applied to the FWS, if they are analyzed in terms of sparse QENS as presented in Section 5.7. For the BATS data, more complex models, including *e.g.*, several Lorentzian functions describing the internal dynamics of the proteins, can be used. In the case of the FWS, fitting different runs at several temperatures simultaneously with an appropriate model can avoid systematic errors.

Developments of cryostat center sticks and corresponding sample holders with two samples vertically above each other might allow to remotely switch between two samples without opening the cryofurnace. This would reduce the time between two measurements and might therefore increase the time-resolution of kinetic measurements similar to the one presented in Chapter 9, while the total amount of samples measured might be increased. It should be emphasized that such a sample holder would only be suitable for the standard IN16B setup and not for the BATS mode, since in the latter one the analyzers are situated in such a way that the analyzed neutrons pass below the sample holder before hitting the detector. In addition, due to the changing positions of the samples within the cryofurnace, the sample temperature might be influenced, which, in contrast, might affect the kinetic pathways.

Commissioning of a cryostat center stick with optical access to the sample will offer the possibility to collect information on optical properties of the sample simultaneously to the neutron data. Such information will be crucial to link changes occurring in the neutron data to macroscopic quantities or observations, such as turbidity of the sample. Possible applications might be temperature quenches into the LLPS regime. Here, information on the visual appearance of the sample can help to link the features observed in the measurements to macroscopic properties, such as the critical temperature of the LLPS.

In Chapter 6, the diffusive dynamics of proteins (Ig) were investigated in a naturally crowded environment. In spite of their heterogeneous environment, the investigated short-time self-diffusion of Ig can be described using the volume fraction dependence of purely monomeric solutions. However, the simulations performed by H. Lopez *et al.* showed that this slowing down depends on the tracer size and deviations from the scaling are expected for smaller proteins. NBS spectra were collected during beamtime 8-04-855 [69] with the BATS option of IN16B for proteins with different sizes to investigate this effect experimentally. Besides the global diffusion, the effect of the lysate on the internal dynamics of the proteins can be investigated. Due to the high energy transfer range of BATS, even small changes in the internal dynamics might be visible.

In addition to the protein diffusive dynamics in the natural environment, the recent technological developments allow to access shorter time scales and therefore faster kinetic processes. In future studies, specific interactions between enzymes and their products (*e.g.* lactose and lactase), as well as interactions between monoclonal antibodies with their corresponding antigens can be investigated. Besides measurements accessing mainly the incoherent scattering, NSE might be of interest here to obtain information about the structural dynamics. Well-established processes, such as the polymerase chain reaction (PCR), might be interesting subjects. By using isotope labeling, the signal from the DNA and the nucleotides might be reduced. Therefore, the dynamics of the polymerase can be investigated during the different steps of the PCR. The statistics necessary for reasonably good analysis cannot be collected with a sufficiently high time resolution. The PCR cycle will therefore have to be run several times and the corresponding signals will have to be binned together. Since the amount of DNA in the solution will increase with the number of cycles, different calibration measurements with different DNA concentrations will be necessary.

Theoretical models and methods to calculate the short-time diffusion coefficient for non-spherical particles might offer new approaches for fitting the data obtained from NBS.

For the salt-induced cluster formation approaching c^*, NSE measurements at constant temperature were performed during beamtime Inter-441 [355] (see Appendix B). The covered q range connects the q range investigated with NBS and the one accessible by dynamic light scattering (DLS). Since at low q the coherent scattering dominates, collective diffusion is investigated. The Fourier times investigated also expand the corresponding time scales and allow to connect the short-time diffusion with the long-time diffusion. To have comparable data, temperature-dependent DLS data were collected. The data set is expanded with temperature-dependent SANS data collected during beamtime TEST-3060 at D33. A temperature-dependent increase at low q is visible in the data, pointing towards a temperature-induced cluster formation. This data set also offers insight for theoretical descriptions since it offers data for transitions from short-time to long-time behavior, from self- to collective diffusion as well as from repulsive to attractive particles. The kinetic changes of samples, which phase-separate due to their LCST-LLPS behavior if their temperature is increased, were investigated with FWS during beamtime 8-04-804 [356]. The frameworks presented in Chapter 5 might be used to analyze these data in detail.

Several crystallization samples with BLG and $CdCl_2$ were measured during the beamtimes 8-04-810 and 8-04-853 with QENS and FWS [357, 358]. The system (BLG and $CdCl_2$) is known to have non-classical crystallization pathways. Some data are shown in Section A. Since in the elastic case, several diffusive contributions are present, the FWS data will have to be analyzed with modified routines. To obtain enough data points and to separate the different contributions, an additional offset was measured at $\hbar\omega = 0.6\,\mu\text{eV}$. Complementary SANS/SAXS and VSANS data, as well as microscopy data exist for these systems (partly collected during beamtime 8-04-853 [358]). Real-time DSC measurements as well as real-time viscosity measurements might complement the existing data set. In addition, it was found that temperature influences the crystallization dependence as well as the crystal structure. A systematic study of this control parameter should also be part of future studies.

The change in the crystal structure makes SANS or SAXS measurements unavoidable before NSE measurements are performed on IN11A or IN15, since for this approach, the Bragg peak position has to be known in advance. Future studies might be performed on NSE instruments covering simultaneously a larger q range (*e.g.* WASP at the ILL). Finally, higher Fourier times (such as the ones available at IN15) might be interesting to access the diffusive dynamics of the proteins within the crystal.

Acknowledgements

This research would not have been possible as a work of a single person. The research performed during the past three years at the ILL in Grenoble profited significantly from the expertise of several colleagues as well as from large experimental facilities, notably from the research reactor of the ILL and from the Spallation Neutron Source in Oak Ridge. It is a privilege to acknowledge these colleagues and facilities, as well as the funding for this thesis provided by the ILL Graduate School with co-funding by the university of Tübingen.

First, I would like to thank Frank Schreiber for supervising my thesis and for his support. I appreciated the different discussions and his openness for new ideas as well as his confidence. I appreciated that he offered me to gain research experience already during my studies in Tübingen in his group and to have offered me the thesis.

I am also very grateful to Tilo Seydel, my supervisor at the ILL. The main part of the knowledge about the functioning of IN16B and backscattering in general is due to the discussions with him. I enjoyed the scientific discussions about different methodological approaches and am very grateful for the confidence and the freedom I had to focus on the different projects independently on the one hand but also for the emphasis when the different projects approached a state where they could be published on the other hand.

I am thankful for fruitful discussions with Felix Roosen-Runge. The exchanges with him were always inspiring and helped answering questions on the theoretical approaches, simulations and on the experimental data as well as connecting them.

Here I am thankful to Marco Grimaldo without whom I would not have been able to understand the existing analysis frameworks that fast and who always had time when I had questions.

Moreover, I thank Bernhard Frick and Markus Appel for offering additional insights to the function of IN16B.

I am also grateful for the support from the research group from Tübingen. Discussions about different projects with Anita Girelli, Ralph Maier, Nafisa Begam, Anastasia Ragulskaya, Madeleine Fries, Daniel Stopper, Michal Braun, Fajun Zhang, Martin Oettel and plenty other persons who helped me to obtain a broader overview about the different experimental techniques, the behavior of similar or closely related samples under different conditions. In this context, it is important to thank also all the persons who always were helpful and without whom these three years would have been more difficult. Managing different administrative tasks, organizing events and providing IT resources as well as high precision sample holders are not trivial and are also necessary contributions to this thesis. Therefore special thanks to Hanna Maurer, Aleksandra Rötschke, Sandra

Matschke, Günter Bertsche, Bernd Hofferberth, Alexander Gerlach and to the machine shop of the University of Tübingen.

I also want to thank all the staff of the ILL for the discussions, support in the labs and during beamtimes. Thanks is also due to the life science group around Trevor Forsyth for the collaboration and for providing lysate. Special thanks also to Ingo Hoffmann, Ralph Schweins, Silvain Prevost and Robert Cubitt for internal beamtime at IN15, D11, D22 and D33. I also want to thank all the local contacts and technicians of IN11, IN15, IN16B, D11, D22 and D33 as well as the responsibles of the Partnership for Soft Condensed Matter (PSCM), mainly here David Hess, Martina Sandroni, Sandrine Verdon and Juliette Devos, for the support during the beamtimes and experiments and the related discussions.

I would like to thank the different student apprentices Lena Bühl, Frederieke Mey, Frank Hirschmann, Lara Grabitz and Ivan Musil. Their contributions as well as their questions and the related discussions contributed also in the understanding of the different subjects presented in this thesis.

I thank very much Olga Matsarskaia, Tilo Seydel, Nafisa Begam, Anita Girelli Ralph Maier and Fajun Zhang as well as Benedikt Sohmen, Marco Grimaldo, Lena Bühl, Aline Cissé and my family for proofreading and giving constructive critics improving this thesis.

I also acknowledge Richard Goyette, Niina H. Jalarvo and Rhonda L. Moody for support during the beamtimes at BASIS in 2016 and 2017 at the SNS, Oak Ridge national laboratory, Tennessee, USA. A portion of this research used resources at the Spallation Neutron Source, a DOE Office of Science User Facility operated by the Oak Ridge National Laboratory.

I am also indebted to the research group of Thorsten Hugel at the Institute of Physical Chemistry of the Albert-Ludwigs-Universität Freiburg, Germany. First analyses of the data collected with neutron spectroscopy on the samples prepared by them already show differences on the short-time diffusive behaviors. In this context, I also want to thank Benedikt Sohmen for the discussions we had and for making this project possible. I am looking forward to connect the results with the results of their single molecule measurements and the existing simulations.

Furthermore, I acknowledge funding by the ILL PhD program and its graduate school with co-funding from the University of Tübingen. The seminars as well as the discussions with Helmut Schober, Henry Fischer and other scientists of the ILL afterwards opened new insights in the applications of neutrons as well as the related theories. This work also profited from BMBF grants for the development of BATS and from fundings from the DFG and ANR.

I appreciate also the time I spent with a lot of different persons during my stay in Grenoble. I really enjoyed the different trips, hikes, visits and cycling trips. I was able to explore several places, which I would not have found on my own during the thesis. This includes different hikes organized by Tilo Seydel with various groups *e.g.* with Olga Matsarskaia, Frank Schreiber, Lena Bühl, Marco Grimaldo and Aline Cissé to mention some of them. Thanks also to Marco Grimaldo for several sports activities such as the *via ferrata* at the Funiculaire.

Especially, I would like to thank Olga Matsarskaia for her valuable advices in diverse subjects.

Special thanks I want to address to Aline Cissé for the support during my thesis. It is unnecessary to tell that I more than enjoyed the different excursions such as the trip to the Lac Robert. Thank you for passing all the time with me and for calming me down, when I started to be too much stressed.

Last but not least, I want to thank my parents and sisters for supporting me during the whole thesis. Knowing to have always their support, their confidence and their advice facilitated the three years a lot!

Appendix A

Real-Time Protein Crystallization: BLG with $CdCl_2$

In this chapter, first analysis results are presented of a crystallizing system following a non-classical crystallization path. As a model system, BLG solutions in the presence of $CdCl_2$ were used [37, 41, 133, 134]. In contrast to the measurements performed on the system presented in Chapter 9, not only time-dependent full QENS measurements but also E/IFWS were performed. This also allows to extract a MSD with a higher time resolution. An analysis with additional IFWS similar to the one presented in Chapter 5 is not possible without modifying the framework due to the fact that several contributions dominate in the elastic scan. The fit model has to be adapted correspondingly. The data were collected during beamtime 8-04-810 [357]. The sample was measured at $t = 295\,\mathrm{K}$ with a protein concentration $c_p = 84.4\,\frac{\mathrm{mg}}{\mathrm{ml}}$ and a $CdCl_2$ salt concentration of $c_s = 25\,\mathrm{mM}$.

The time-dependent EINS is shown in Figure A.1a. A decrease in the elastic intensity as a function of time can already be observed in the time-dependent raw data. Fits for different time steps using Equation 5.10 are shown in Figure A.1b.

The time-dependent MSD is shown in Figure A.2. The data mainly shows an increase of the MSD, which at first glance, is in disagreement with the behavior described in Chapter 9.

To analyze the QENS signal (example shown in Figure A.3), the same model as presented in Chapter 9 is used. The different time-dependent fit parameters are shown in Figure A.4. Also here, the diffusion coefficient and fraction of immobile proteins A_c agree with the time dependence of the MSD and disagree in a first glance with the results of Chapter 9. It should be mentioned that the macroscopic viscosity increases significantly after the preparation and decays later so that the samples first are in a "gel-like" state become liquid with time. When the samples became liquid, crystals were observable under the microscope.

Later measurements with other sample conditions (BLG $c_p = 84.4\,\frac{\mathrm{mg}}{\mathrm{ml}}$, $CdCl_2$ $c_s = 30\,\mathrm{mM}$, $T = 295\,\mathrm{K}$) performed during beamtime 8-04-853 [358] observed in the beginning a similar decay of the EFWS signal. Continuing the measurement (which was not possible due to limited beamtime for the previous sample) revealed another increase of the EFWS, pointing to the formation of crystals (Figure A.5). Other samples showing the same decay as the one presented previously could also be measured (BLG $c_p = 40\,\frac{\mathrm{mg}}{\mathrm{ml}}$, $CdCl_2$ $c_s = 25\,\mathrm{mM}$, $T = 295\,\mathrm{K}$). Further analyses are still necessary. The decrease of the EFWS signal, followed by an

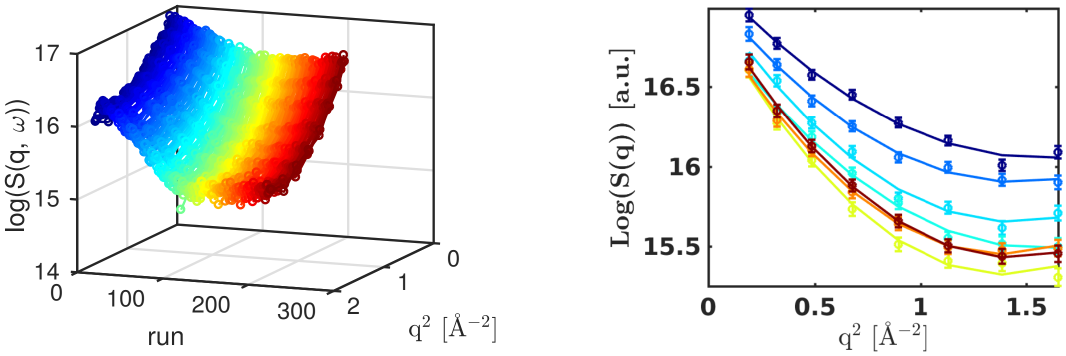

(a) *Time-dependent EFWS. The runs had a time offset of 5 minutes. The time interval covered corresponds to 56 hours.*

(b) *EFWS as a function of q^2 for different time steps. Solid lines represent fits using the fit model 5.10.*

Figure A.1: *Time-dependent scattering signal (EFWS) of dissolved BLG with CdCl$_2$ ($c_p = 84.4\,\frac{\mathrm{mg}}{\mathrm{ml}}$; $c_s = 25\,\mathrm{mM}$; $T = 295\,\mathrm{K}$) measured on IN16B.*

increase, indicates a non-classical crystallization pathway. In order to connect data investigating kinetics of the diffusive dynamics to those investigating the structure (such as SANS, SAXS or *via* microscope), further data analysis is necessary.

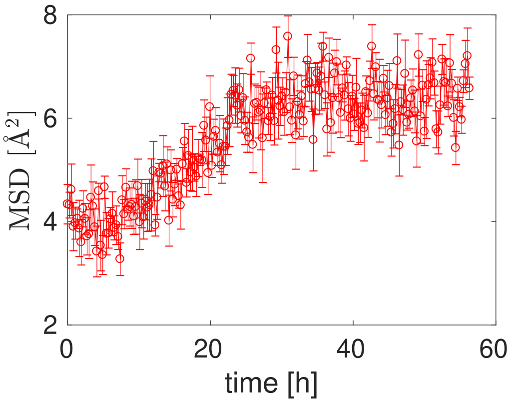

Figure A.2: *Time-dependent MSD of crystallizing BLG in the presence of* $CdCl_2$ *obtained from the analysis shown in Figure A.1b.*

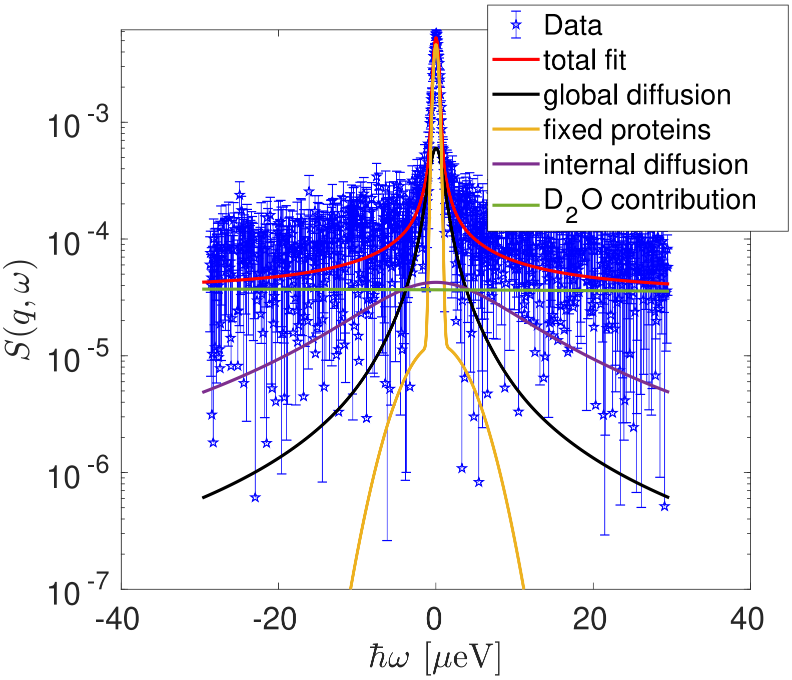

Figure A.3: *Example fit of the NBS spectra.*

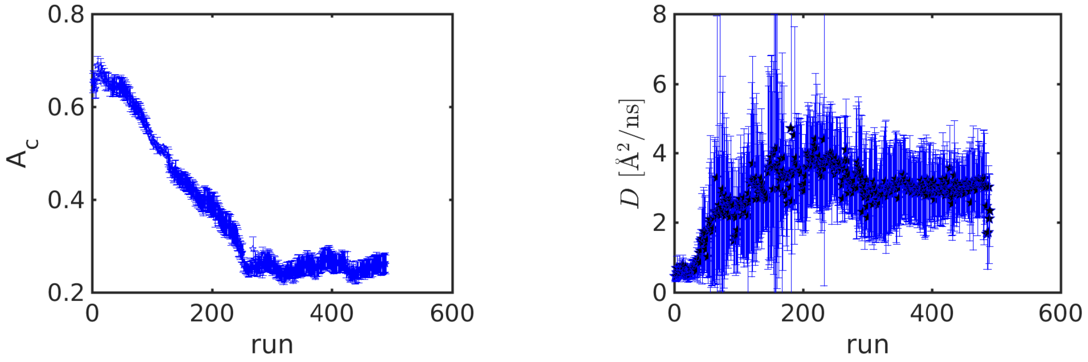

(a) *Time-dependent signal of the fraction of immobile proteins on the timescale observable*

(b) *Time-dependent global diffusion coefficient*

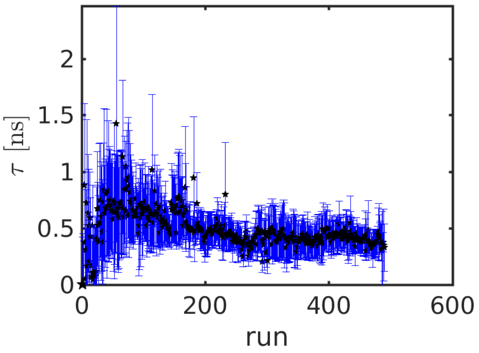

(c) *Time-dependent residence time of the global diffusion*

Figure A.4: *Time-dependent fit results of the non-classically crystallizing sample* ($c_p = 84.4\,\frac{\text{mg}}{\text{ml}}$; $c_s = 25\,\text{mM}$; $T = 295\,\text{K}$)*. In general, an opposite trend to the one found in the BLG-*ZnCl_2 *system (Chapter 9) can be observed. The time interval shown represents roughly 56 hours.*

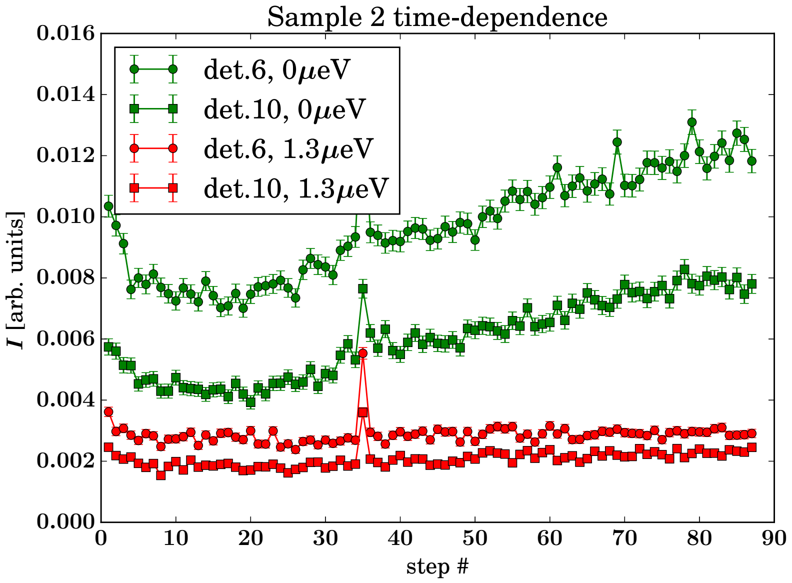

Figure A.5: *Time dependence of the FWS for different detectors for a sample measured during beamtime 8-04-853 [358]. The increase of the EFWS signal indicates crystal formation. The time interval shown represents a duration of 31 hours.*

Appendix B

Salt-Induced Protein Cluster Formation Investigated by NSE

During beamtime INTER-441, salt-induced cluster formation of dissolved BSA in the presence of YCl_3 was investigated with NSE at IN15 at the ILL. Using NSE offers the option to investigate low protein concentrations down to $c_p = 40\,\frac{\mathrm{mg}}{\mathrm{ml}}$. It is therefore possible to expand the protein concentration range investigated.

NSE accesses the intermediate scattering function. Given the time-scales as well as the q-range investigated, both, the short-time and also the long-time diffusive processes can be accessed. Also the self- and collective diffusion can be determined.

Similar to the study presented in Chapter 8, the number of salt cations per protein was changed systematically, thus changing from a repulsive system to an attractive one.

All samples were measured at $T = 295\,\mathrm{K}$ with three different scattering angles. Since the detector is position-sensitive, in total 12 different intermediate scattering functions at different q-values were collected for each sample. A detailed list of the measured samples is shown in Table B.1.

As a first approach, the intermediate scattering functions were analyzed for $\tau \leq 30\,\mathrm{ns}$. By investigating the extrapolation of the fit to higher Fourier times and comparing these to the experimentally measured data, deviations between the scattering data and the monoexponential decay can be observed (see Figure B.1). Simulations by Bleibel *et al.* of patchy particles already showed two different time-scales of the decays [185]. DLS studies by Soraruf *et al.* [23] observed also two decays in the long time collective diffusion and assigned these to the monomer and cluster diffusion. Limiting the fit range to small times allows to focus on the decay related to the diffusion of monomeric proteins.

As a fit function, a single exponential decay was applied. For each scattering vector q, the decay rate Γ was used to calculate the diffusion coefficient

$$D = \frac{\Gamma}{q^2}. \tag{B.1}$$

The q dependence of the diffusion coefficient D is shown in Figure B.2 for different salt concentrations for the samples with $c_p = 100\,\frac{\mathrm{mg}}{\mathrm{ml}}$.

The transition from repulsive to attractive systems show significant changes in the parameters observed.

Table B.1: *Overview of the measured samples on IN15 during beamtime INTER-441*

c_p $\left[\frac{\text{mg}}{\text{ml}}\right]$	c_s [mM]
100	0
100	3.4
100	5.1
100	7
60	0
60	3
60	4.2
40	0
40	2
40	2.8

In Figure B.3 and B.4, the normalized diffusion coefficients are shown as a function of salt ions per protein. Several observations can be made. At the high q limit of the NSE data, the measured normalized diffusion coefficients approach the results of the NBS study with a focus on the self-diffusion. For low scattering vectors q, the normalized diffusion coefficients differ more from the master curve. Additionally, the protein concentration dependence is more pronounced.

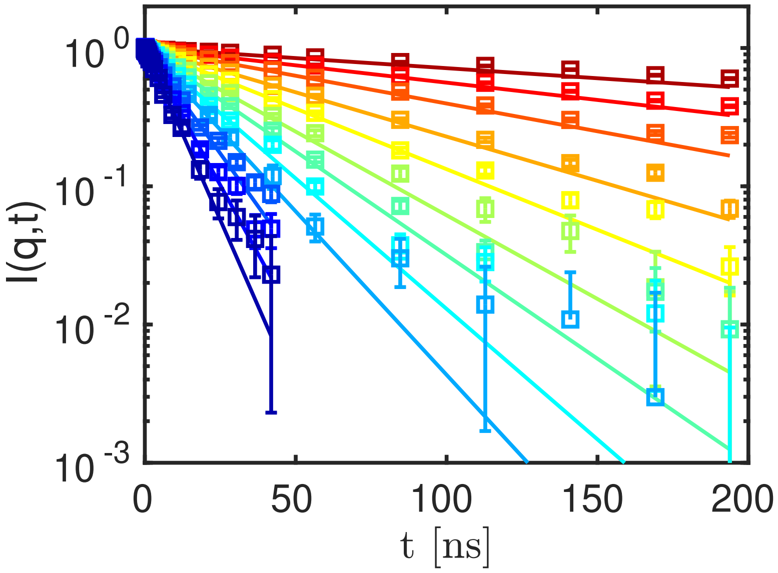

Figure B.1: *Intermediate scattering functions of protein solutions with BSA* $c_p = 40\,\frac{\mathrm{mg}}{\mathrm{ml}}$ *and* $c_s = 2.8\,\mathrm{mM}$ *as a function of* τ *for different scattering vectors* q*. Solid and dotted lines represent the fits of the scattering function for* $\tau \leq 30\,\mathrm{ns}$ *and the corresponding extrapolation. Colors code the increasing* q *values from dark blue (*$q \simeq 0.03\,\mathring{A}^{-1}$*) to dark red (*$q \simeq 0.16\,\mathring{A}^{-1}$*)*

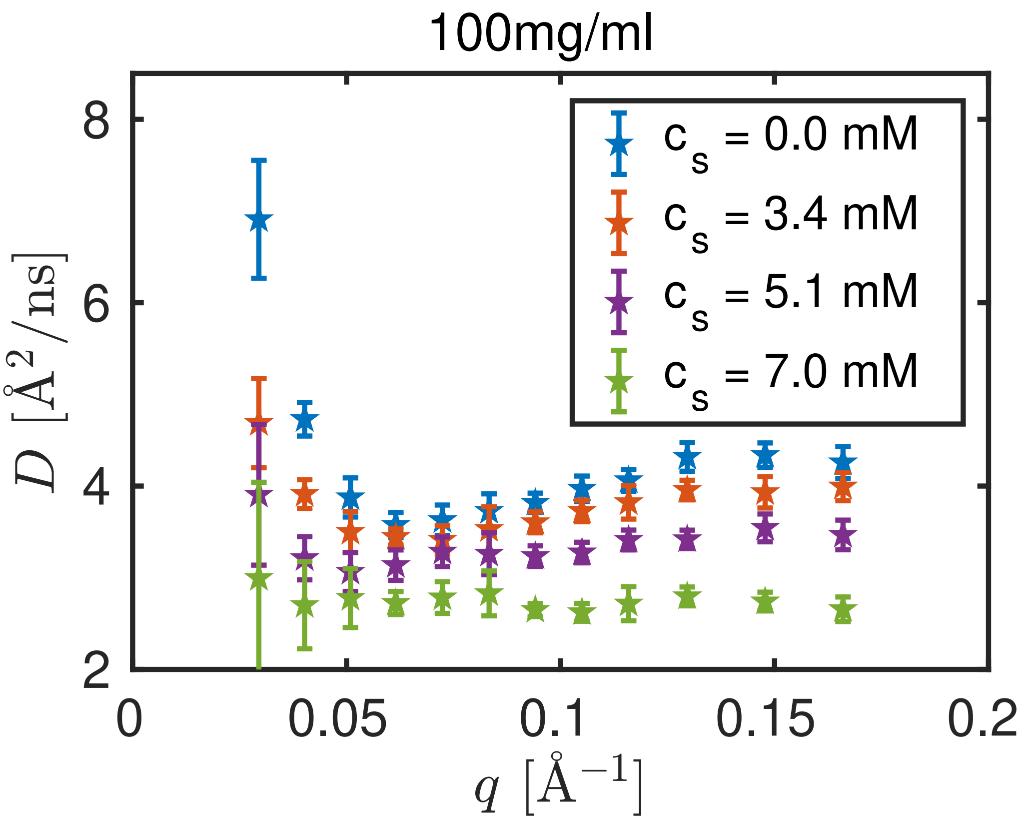

Figure B.2: *Diffusion coefficients as a function of the scattering vector* q *for different salt concentrations. The protein concentration of all shown data was* $c_p = 100\,\frac{\mathrm{mg}}{\mathrm{ml}}$ *and all samples were measured at* $T = 295\,\mathrm{K}$.

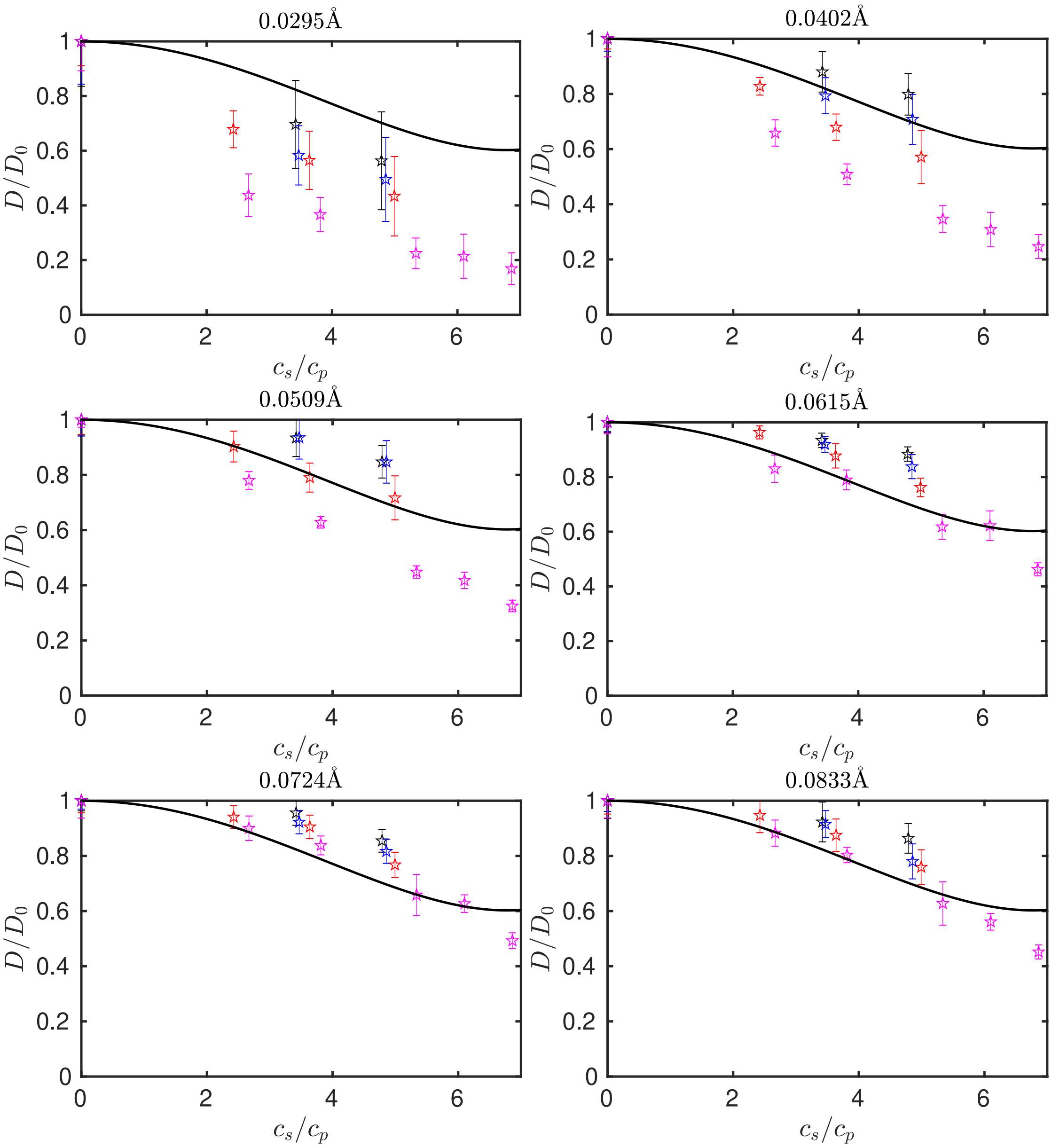

Figure B.3: *Normalized diffusion coefficients as a function of the number of salt cations per protein. Different protein concentrations are shown with different colors. The different scattering vectors are shown in the different subplots (see plot titles). The solid line represents the master curve obtained by Grimaldo et al. [33]. Black, blue, red and magenta symbols represent samples with nominal protein concentrations* $c_p = 40\,\frac{\mathrm{mg}}{\mathrm{ml}}$, $c_p = 60\,\frac{\mathrm{mg}}{\mathrm{ml}}$, $c_p = 100\,\frac{\mathrm{mg}}{\mathrm{ml}}$ *and* $c_p = 200\,\frac{\mathrm{mg}}{\mathrm{ml}}$*, respectively. The data with* $c_p = 200\,\frac{\mathrm{mg}}{\mathrm{ml}}$ *were reanalyzed to get an overview using the data by Hennig [68]. The higher* q *values are shown in Figure B.4.*

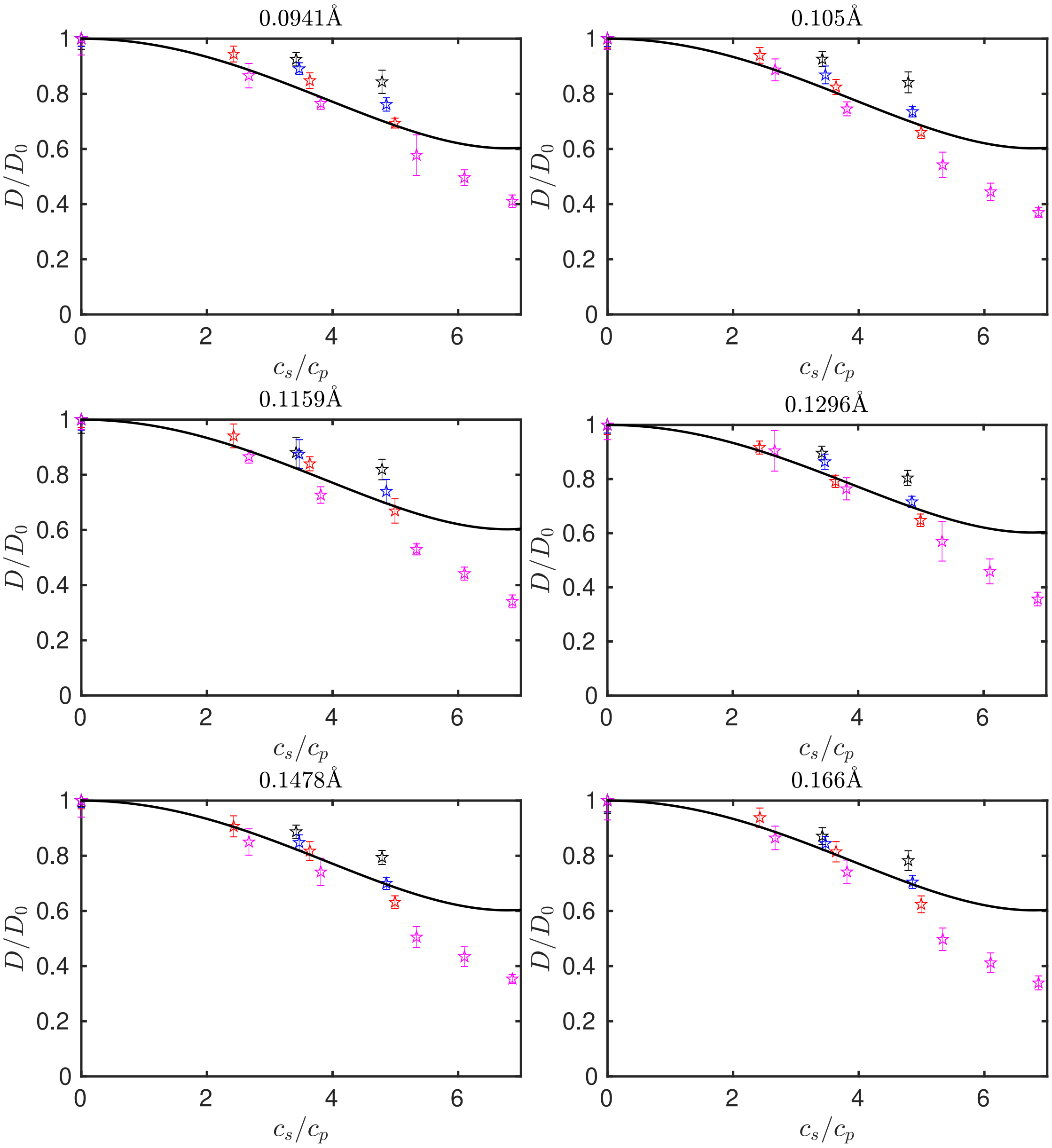

Figure B.4: *Continuation of Figure B.3.*

Appendix C

List of Neutron Scattering Experiments Performed

This chapter lists all beamtimes performed during the thesis.

1. **Characterizing the formation of liquid-liquid phase separation by tuning the system by using its lower critical solution temperature**
   Facility: ILL
   Experiment Number: 8-04-804
   Instrument:
   - IN16B (28/01/2017-31/01/2017)

   DOI: `http://doi.ill.fr/10.5291/ILL-DATA.8-04-804`
   Some data from this beamtime are shown in Chapter 5.6.

2. **Accessing the binding energy and entropy of protein clusters by QENS**
   Facility: SNS
   Experiment Number: 18578.1
   Instrument:
   - BL-2 BASIS (13/09/2017-18/09/2017)

   Data are shown in Chapter 8

3. **In situ real-time study of the diffusive dynamic arrest of proteins during crystallization**
   Facility: ILL
   Experiment Number: 8-04-810
   Instrument:
   - IN16B (06/04/2018-09/04/2018)

   DOI: `http://doi.ill.fr/10.5291/ILL-DATA.8-04-810`
   Data is shown in Chapter A

4. **On the structural dynamics of multi-domain proteins**
   Facility: ILL
   Experiment Number: 8-04-838
   Instrument:
   - IN16B (06/10/2018-08/10/2018)
   - IN15 (01/10/2018-04/10/2018)

   DOI: `http://doi.ill.fr/10.5291/ILL-DATA.8-04-838`
   Experiment in cooperation with Albert-Ludwigs-Universität Freiburg (Institute of Physical Chemistry; Prof. Dr. Thorsten Hugel; Benedikt Sohmen) Additional measurements on D11 (interal beamtime) and DLS/SLS measurements.

5. **Effects of salt-induced protein interactions on collective and self-diffusion**
   Facility: ILL
   Experiment Number: Inter-441
   Instrument:
   - IN15 (08/10/2018-11/10/2018)

   Data are shown in Chapter B. Additional DLS/SLS measurements were performed.

6. **Towards a realistic model of the cellular environment: Dynamics in 'naturally' crowded protein solutions**
   Facility: ILL
   Experiment Number: 8-04-855
   Instrument:
   - IN16B - BATS (03/07/2019-07/07/2019)

   DOI: `http://doi.ill.fr/10.5291/ILL-DATA.8-04-855`

7. **In situ real-time study of the diffusive dynamic arrest of proteins during crystallization**
   Facility: ILL
   Experiment Number: 8-04-853
   Instrument:
   - D11 (28/09/2019-30/09/2019)
   - IN16B (11/10/2019-15/10/2019)

   DOI: `http://doi.ill.fr/10.5291/ILL-DATA.8-04-853`

8. **Following LLPS formation with SANS by temperature changes**
   Facility: ILL
   Experiment Number: TEST-3060
   Instrument:
   - D33 (24/09/2019-25/09/2019)

   DOI: `http://doi:10.5291/ILL-DATA.TEST-3060`
   Complementary temperature dependent SANS to the data presented in Chapter 8.

Appendix D

Glossary

Abbreviations

BASIS	backscattering silicon spectrometer. 13, 36, 37, 57, 81, 133, 140, 167
BATS	Backscattering and Time of Flight Spectroscopy. 36, 57, 60, 62–67, 81, 167, 168, 172
BLG	β-lactoglobulin. 12, 41, 42, 45–48, 111, 112, 120–123, 125, 130, 143, 144, 152, 153, 157, 169, 175–178, 195
BSA	bovine serum albumin. 7, 8, 11–13, 35, 41–48, 53, 62–66, 71, 76, 83, 84, 86, 87, 89, 91, 111, 112, 119–123, 125, 129–131, 133, 134, 140, 181, 195
DLS	dynamic light scattering. 13, 43, 47, 169, 181
E/IFWS	elastic and inelastic fixed window scan. 70, 74, 79, 82, 175
EFWS	elastic fixed window scan. 57, 58, 70, 76–83, 85, 86, 88, 91–93, 175, 176, 179, 194
EINS	elastic incoherent neutron scattering. 70, 71, 76–78, 175
EISF	elastic incoherent structure factor. 19, 30, 31, 61, 65, 66, 72, 74, 80, 82, 88–90, 111, 113, 119–121, 131, 148, 153, 156, 161, 163
FWHM	full width at half maximum. 64, 72, 80, 81, 112, 133
FWS	fixed window scan. 70, 71, 73–76, 78, 82, 83, 85, 86, 88–94, 167, 169, 179, 194
HSA	human serum albumin. 12, 13, 130
HWHM	half width at half maximum. 32, 34, 35, 71, 73, 80, 81, 84, 85, 135
IFWS	inelastic fixed window scan. 57, 58, 70, 79–83, 85, 86, 88, 92, 93, 175

Ig	γ-globulin from bovine blood. 45, 96–102, 104–107, 111, 112, 120–123, 125, 168
ILL	Institut Laue-Langevin. 49, 58, 60, 62, 67, 106, 112, 145, 167, 169, 181
IN16B	cold neutron backscattering spectrometer. 36, 37, 57, 58, 60, 62, 63, 65, 66, 69, 71, 72, 81, 86, 92, 93, 98, 112, 115, 123, 125, 145, 146, 148, 167, 168, 176
LCST	lower critical solution temperature. 43, 45, 46, 130, 137, 169
LLPS	liquid-liquid phase separation. 11, 12, 17, 18, 43, 46, 129, 130, 137, 168, 169
MSD	mean squared displacement. 6–8, 70, 71, 76, 78, 79, 82, 92, 93, 175, 177, 194, 197
NBS	neutron backscattering. 13, 16, 18, 36, 39, 43, 46, 53, 54, 56, 57, 69, 71, 79, 80, 89, 97, 98, 100, 167–169, 177, 182, 195
NSE	neutron spin echo. 16, 39, 46, 51, 53, 54, 70, 143, 147, 153, 154, 158–160, 167–169, 181, 182
OVA	ovalbumin. 9, 12, 41, 42, 47, 48, 111, 112, 120–123, 125
PCR	polymerase chain reaction. 168
PSD	position-sensitive detector. 63, 64, 92, 94, 145
PST	phase space transformer. 145
QENS	quasi-elastic neutron scattering. 13, 16, 53, 57, 58, 60, 62, 64, 70, 72, 73, 80, 82, 83, 88–91, 94, 97, 98, 110–112, 123, 124, 127, 130, 131, 161, 167, 169, 175
SANS	small angle neutron scattering. 39, 40, 45, 50, 97, 142–144, 147, 153, 169, 176
SAXS	small angle X-ray scattering. 12, 13, 43, 45–48, 112, 123, 127, 142, 169, 176
SD	single detector. 83, 92, 94
SLS	static light scattering. 48, 97
SNS	Spallation Neutron Source. 133, 140, 167
TOF	time of flight. 36, 49, 50, 54
UCST	upper critical solution temperature. 45, 46, 130

Appendix E

List of Figures

Appendix F

List of Tables

Bibliography

[1] L. Pauling, H. A. Itano, S. J. Singer, and I. C. Wells, “ Sickle Cell Anemia, a Molecular Disease,” *Science*, vol. 110, no. 2865, pp. 543–548, 1949.

[2] S. Sheth, M. Licursi, and M. Bhatia, “ Sickle cell disease: time for a closer look at treatment options?,” *British Journal of Haematology*, vol. 162, no. 4, pp. 455–464, 2013.

[3] K. Sun and Y. Xia, “ New insights into sickle cell disease,” *Current Opinion in Hematology*, vol. 20, no. 3, pp. 215–221, 2013.

[4] T. N. Williams, T. W. Mwangi, D. J. Roberts, N. D. Alexander, D. J. Weatherall, S. Wambua, M. Kortok, R. W. Snow, and K. Marsh, “ An Immune Basis for Malaria Protection by the Sickle Cell Trait,” *PLOS Medicine*, vol. 2, no. 5, 2005.

[5] G. B. Benedek, “ Cataract as a Protein Condensation Disease: The Proctor Lecture.,” *Invest. Ophthalmol. Visual Sci.*, vol. 38, no. 10, pp. 1911–1921, 1997.

[6] A. Bartesaghi, A. Merk, S. Banerjee, D. Matthies, X. Wu, J. L. S. Milne, and S. Subramaniam, “ 2.2 Åresolution cryo-EM structure of -galactosidase in complex with a cell-permeant inhibitor,” *Science*, vol. 348, no. 6239, pp. 1147–1151, 2015.

[7] Z. Liu, C. Gutierrez-Vargas, J. Wei, R. A. Grassucci, M. Sun, N. Espina, S. Madison-Antenucci, L. Tong, and J. Frank, “Determination of the ribosome structure to a resolution of 2.5 Å by single-particle cryo-EM,” *Protein Science*, vol. 26, no. 1, pp. 82–92, 2017.

[8] M. Liao, E. Cao, D. Julius, and Y. Cheng, “ Structure of the TRPV1 ion channel determined by electron cryo-microscopy,” *Nature*, vol. 504, no. 7478, pp. 107–112, 2013.

[9] G. S. Allen, A. Zavialov, R. Gursky, M. Ehrenberg, and J. Frank, “The Cryo-EM Structure of a Translation Initiation Complex from Escherichia coli,” *Cell*, vol. 121, pp. 703–712, June 2005.

[10] D. Lyumkis, “ Challenges and opportunities in cryo-EM single-particle analysis,” *Journal of Biological Chemistry*, vol. 294, no. 13, pp. 5181–5197, 2019.

[11] J. Dhont, *An Introduction to Dynamics of Colloids.* ISSN, Elsevier Science, 1996.

[12] T. Seydel, “ Neutron Scattering - Applications in Biology, Chemistry, and Materials Science: Chapter 2 - Dynamics of Biological Systems,” vol. 49 of *Experimental Methods in the Physical Sciences*, pp. 77 – 134, Academic Press, 2017.

[13] M. Grimaldo, F. Roosen-Runge, F. Zhang, F. Schreiber, and T. Seydel, “ Dynamics of Proteins in Solution,” *Q. Rev. Biophys.*, vol. 52, p. e7, 2019.

[14] S. B. Zimmerman and S. O. Trach, “ Estimation of Macromolecule Concentrations and Excluded Volume Effects for the Cytoplasm of Escherichia Coli,” *Journal of Molecular Biology*, vol. 222, no. 3, pp. 599 – 620, 1991.

[15] J. Klinman and S. Schiffer, *Dynamics in Enzyme Catalysis.* Topics in Current Chemistry, Springer Berlin Heidelberg, 2013.

[16] A. P. Minton, “ How can biochemical reactions within cells differ from those in test tubes?,” *Journal of Cell Science*, vol. 128, no. 6, pp. 1254–1254, 2015.

[17] M. S. Cheung, D. Klimov, and D. Thirumalai, “ Molecular Crowding Enhances Native State Stability and Refolding Rates of Globular Proteins,” *Proc. Natl. Acad. Sci. USA*, no. 13, pp. 4753–4758, 2005.

[18] R. N. Frese, J. C. Pàmies, J. D. Olsen, S. Bahatyrova, C. D. van der Weijde Wit, T. J. Aartsma, C. Otto, C. N. Hunter, D. Frenkel, and R. van Grondelle, “ Protein Shape and Crowding Drive Domain Formation and Curvature in Biological Membranes,” *Biophysical Journal*, vol. 94, no. 2, pp. 640–647, 2008.

[19] E. J. W. Verwey, “ Theory of the Stability of Lyophobic Colloids.,” *The Journal of Physical and Colloid Chemistry*, vol. 51, no. 3, pp. 631–636, 1947.

[20] D. Leckband and J. Israelachvili, “ Intermolecular Forces in Biology,” *Q. Rev. Biophys.*, vol. 34, no. 2, p. 105267, 2001.

[21] J. Gunton, A. Shiryayev, and D. Pagan, *Protein Condensation: Kinetic Pathways to Crystallization and Disease.* Cambridge University Press, 2007.

[22] F. Zhang, M. W. A. Skoda, R. M. J. Jacobs, S. Zorn, R. A. Martin, C. M. Martin, G. F. Clark, S. Weggler, A. Hildebrandt, O. Kohlbacher, and F. Schreiber, “ Reentrant Condensation of Proteins in Solution Induced by Multivalent Counterions,” *Phys. Rev. Lett.*, vol. 101, p. 148101, 2008.

[23] D. Soraruf, F. Roosen-Runge, M. Grimaldo, F. Zanini, R. Schweins, T. Seydel, F. Zhang, R. Roth, M. Oettel, and F. Schreiber, “ Protein Cluster Formation in Aqueous Solution in the Presence of Multivalent Metal Ions–A Light Scattering Study,” *Soft Matter*, vol. 10, no. 6, pp. 894–902, 2014.

[24] F. Zhang, S. Weggler, M. J. Ziller, L. Ianeselli, B. S. Heck, A. Hildebrandt, O. Kohlbacher, M. W. A. Skoda, R. M. J. Jacobs, and F. Schreiber, “ Universality of Protein Reentrant Condensation in Solution Induced by Multivalent Metal Ions,” *Proteins: Struct., Funct., Bioinf.*, vol. 78, no. 16, pp. 3450–3457, 2010.

[25] M. R. Fries, D. Stopper, M. K. Braun, A. Hinderhofer, F. Zhang, R. M. J. Jacobs, M. W. A. Skoda, H. Hansen-Goos, R. Roth, and F. Schreiber, “ Multivalent-Ion-Activated Protein Adsorption Reflecting Bulk Reentrant Behavior,” *Phys. Rev. Lett.*, vol. 119, p. 228001, 2017.

[26] M. K. Braun, A. Sauter, O. Matsarskaia, M. Wolf, F. Roosen-Runge, M. Sztucki, R. Roth, F. Zhang, and F. Schreiber, “ Reentrant Phase Behavior in Protein Solutions Induced by Multivalent Salts: Strong Effect of Anions Cl^- Versus NO_3^-,” *J. Phys. Chem. B*, vol. 122, no. 50, pp. 11978–11985, 2018.

[27] O. Matsarskaia, F. Roosen-Runge, G. Lotze, J. Möller, A. Mariani, F. Zhang, and F. Schreiber, “ Tuning Phase Transitions of Aqueous Protein Solutions by Multivalent Cations,” *Phys. Chem. Chem. Phys.*, vol. 20, pp. 27214–27225, 2018.

[28] J. Schubert, C. Radeke, A. Fery, and M. Chanana, “ The Role of pH, Metal Ions and Their Hydroxides in Charge Reversal of Protein-Coated Nanoparticles,” *Phys. Chem. Chem. Phys.*, vol. 21, pp. 11011–11018, 2019.

[29] C. Beck, “Protein Cluster Formation in Solution Induced by Multivalent Salts Studied by Light Scattering,” Bachelor Thesis, Universität Tübingen, 2015.

[30] S. Pandit and S. Kundu, “ Optical Responses of BSA Protein under Reentrant Condensation in Presence of Trivalent Ions,” *J. Mol. Liq.*, vol. 276, pp. 954 – 960, 2019.

[31] O. Matsarskaia, *Multivalent Ions for Tuning the Phase Behaviour of Protein Solutions.* PhD thesis, Eberhard Karls University Tuebingen, 2018.

[32] M. K. Braun, M. Wolf, O. Matsarskaia, S. Da Vela, F. Roosen-Runge, M. Sztucki, R. Roth, F. Zhang, and F. Schreiber, “ Strong Isotope Effects on Effective Interactions and Phase Behavior in Protein Solutions in the Presence of Multivalent Ions,” *J. Phys. Chem. B*, vol. 121, no. 7, pp. 1731–1739, 2017.

[33] M. Grimaldo, F. Roosen-Runge, M. Hennig, F. Zanini, F. Zhang, M. Zamponi, N. Jalarvo, F. Schreiber, and T. Seydel, “ Salt-Induced Universal Slowing Down of the Short-Time Self-Diffusion of a Globular Protein in Aqueous Solution,” *J. Phys. Chem. Lett.*, vol. 6, no. 13, pp. 2577–2582, 2015.

[34] O. Matsarskaia, M. K. Braun, F. Roosen-Runge, M. Wolf, F. Zhang, R. Roth, and F. Schreiber, “ Cation-Induced Hydration Effects Cause Lower Critical Solution Temperature Behavior in Protein Solutions,” *J. Phys. Chem. B*, vol. 120, no. 31, pp. 7731–7736, 2016.

[35] F. Roosen-Runge, F. Zhang, F. Schreiber, and R. Roth, “ Ion-activated Attractive Patches as a Mechanism for Controlled Protein Interactions,” *Sci. Rep.*, vol. 4, p. 7016, 2014.

[36] O. Matsarskaia, S. Da Vela, A. Mariani, Z. Fu, F. Zhang, and F. Schreiber, “ Phase-Separation Kinetics in Protein- Salt Mixtures with Compositionally Tuned Interactions,” *J. Phys. Chem. B*, vol. 123, no. 9, pp. 1913–1919, 2019.

[37] F. Zhang, “ Nonclassical Nucleation Pathways in Protein Crystallization,” *J. Phys.: Condens. Matter*, vol. 29, p. 443002, 2017.

[38] S. Karthika, T. K. Radhakrishnan, and P. Kalaichelvi, “ A Review of Classical and Nonclassical Nucleation Theories,” *Cryst. Growth Des.*, vol. 16, no. 11, pp. 6663–6681, 2016.

[39] J. W. Gibbs, *The scientific papers of J. Willard Gibbs*, vol. 1. Longmans, Green and Company, 1906.

[40] P. G. Vekilov, “ The Two-Step Mechanism of Nucleation of Crystals in Solution,” *Nanoscale*, vol. 2, pp. 2346–2357, 2010.

[41] A. Sauter, F. Roosen-Runge, F. Zhang, G. Lotze, R. M. J. Jacobs, and F. Schreiber, “ Real-Time Observation of Nonclassical Protein Crystallization Kinetics,” *J. Am. Chem. Soc.*, vol. 137, no. 4, pp. 1485–1491, 2015.

[42] M. Bée, *Quasielastic neutron scattering: principles and applications in solid state chemistry, biology, and materials science.* Adam Hilger, 1988.

[43] S. Lovesey, *Theory of Neutron Scattering from Condensed Matter.* No. vol. 2 in International series of monographs on physics, Clarendon Press, 1986.

[44] G. L. Squires, *Introduction to the Theory of Thermal Neutron Scattering.* Cambridge University Press, 2009.

[45] J. Fitter, T. Gutberlet, and J. Katsaras, *Neutron Scattering in Biology.* Springer Berlin Heidelberg, 2006.

[46] T. Zemb and P. Lindner, *Neutrons, X-Rays and Light: Scattering Methods Applied to Soft Condensed Matter.* North-Holland delta series, Elsevier, 2002.

[47] S. Helmut, " An Introduction to the Theory of Nuclear Neutron Scattering in Condensed Matter," *J. Neutron Res.*, vol. 17, no. 3-4, p. 109357, 2014.

[48] T. Brückel, G. Heger, D. Richter, G. Roth, and R. E. Zorn, *Neutron Scattering: Lectures of the JCNS Laboratory Course held at Forschungszentrum Jülich and the Research Reactor FRM II of TU Munich in Cooperation with RWTH Aachen and University of Münster*, vol. 39 of *Schriften des Forschungszentrums Jülich. Reihe Schlüsseltechnologien / key technologies.* Jülich: Forschungszentrum, Zentralbibliothek, 2012.

[49] J. Dawidowski, J. R. Granada, J. R. Santisteban, F. Cantargi, and L. A. R. Palomino, "Experimental Methods in the Physical Sciences – Neutron Scattering Lengths and Cross Sections," pp. 471–528, Elsevier, 2013.

[50] D. G. Hurst and N. Z. Alcock, "The Scattering Lengths of the Deuteron," *Canadian Journal of Physics*, vol. 29, pp. 36–58, Jan. 1951.

[51] V. F. Sears, " Neutron Scattering Lengths and Cross Sections," *Neutron News*, vol. 3, no. 3, pp. 26–37, 1992.

[52] L. Koester, H. Rauch, and E. Seymann, " Neutron Scattering Lengths: A Survey of Experimental Data and Methods," *Atomic Data and Nuclear Data Tables*, vol. 49, pp. 65–120, Sept. 1991.

[53] V. F. Sears, " Local-Field Refinement of Neutron Scattering Lengths," *Zeitschrift für Physik A Atoms and Nuclei*, vol. 321, pp. 443–449, Sept. 1985.

[54] D. Sivia, *Elementary Scattering Theory.* Oxford University Press, 2011.

[55] J. Oberdisse, " Introduction to Soft Matter and Neutron Scattering," *EPJ Web Conf.*, vol. 188, p. 01001, 2018.

[56] B. P. van Milligen, B. A. Carreras, and R. Sánchez, " The Foundations of Diffusion Revisited," *Plasma Phys. Controlled Fusion*, vol. 47, no. 12B, pp. B743–B754, 2005.

[57] A. Einstein, " Ü ber die von der Molekularkinetischen Theorie der Wä rme Geforderte Bewegung von in Ruhenden Flü ssigkeiten Suspendierten Teilchen," *Ann. Phys. (Berlin, Ger.)*, vol. 322, no. 8, pp. 549–560, 1905.

[58] A. J. Banchio and G. Nägele, " Short-Time Transport Properties in Dense Suspensions: From Neutral to Charge-Stabilized Colloidal Spheres," *J. Chem. Phys.*, vol. 128, no. 10, p. 104903, 2008.

[59] M. Tokuyama and I. Oppenheim, “ Dynamics of Hard-Sphere Suspensions,” *Phys. Rev. E*, vol. 50, pp. R16–R19, 1994.

[60] J. S. Myung, F. Roosen-Runge, R. G. Winkler, G. Gompper, P. Schurtenberger, and A. Stradner, “ Weak Shape Anisotropy Leads to a Nonmonotonic Contribution to Crowding, Impacting Protein Dynamics under Physiologically Relevant Conditions,” *J. Phys. Chem. B*, vol. 122, no. 51, pp. 12396–12402, 2018.

[61] M. Grimaldo, F. Roosen-Runge, N. Jalarvo, M. Zamponi, F. Zanini, M. Hennig, F. Zhang, F. Schreiber, and T. Seydel, “ High-Resolution Neutron Spectroscopy on Protein Solution Samples,” *EPJ Web Conf.*, vol. 83, p. 02005, 2015.

[62] K. Singwi and A. Sjölander, “ Diffusive Motions in Water and Cold Neutron Scattering,” *Phys. Rev.*, vol. 119, no. 3, pp. 863–871, 1960.

[63] F. Roosen-Runge, D. Bicout, and J.-L. Barrat, “ Analytical Correlation Functions for Motion through Diffusivity Landscapes,” *J. Chem. Phys.*, vol. 144, no. 20, p. 204109, 2016.

[64] M. Grimaldo, F. Roosen-Runge, M. Hennig, F. Zanini, F. Zhang, N. Jalarvo, M. Zamponi, F. Schreiber, and T. Seydel, “ Hierarchical Molecular Dynamics of Bovine Serum Albumin in Concentrated Aqueous Solution Below and Above Thermal Denaturation,” *Phys. Chem. Chem. Phys.*, vol. 17, pp. 4645–4655, 2015.

[65] J. Qvist, H. Schober, and B. Halle, “ Structural Dynamics of Supercooled Water from Quasielastic Neutron Scattering and Molecular Simulations,” *J. Chem. Phys.*, vol. 134, no. 14, p. 144508, 2011.

[66] M. Appel, B. Frick, and A. Magerl, “ A Flexible High Speed Pulse Chopper System for an Inverted Neutron Time-of-Flight Option on Backscattering Spectrometers,” *Sci. Rep.*, vol. 8, no. 1, pp. 1–8, 2018.

[67] H. Paalman and C. Pings, “ Numerical Evaluation of X-Ray Absorption Factors for Cylindrical Samples and Annular Sample Cells,” *J. Appl. Phys.*, vol. 33, no. 8, pp. 2635–2639, 1962.

[68] M. Hennig, *Dynamics of Globular Proteins in Crowded Electrolyte Solutions.* PhD thesis, Eberhard Karls University Tuebingen, 2011.

[69] M. Grimaldo, M. Appel, C. Beck, S. Da Vela, J. M. Devos, T. Forsyth, M. Haertlein, V. Laux-Lesourd, O. Matsarskaia, M. Moulin, F. Roosen-Runge, F. Schreiber, T. Seydel, and F. Zhang, “ Towards a Realistic Model of the Cellular Environment: Dynamics in 'nNaturally' Crowded Protein Solutions,” 2019. doi.ill.fr/10.5291/ILL-DATA.8-04-855, Institut Laue-Langevin (ILL).

[70] M. Vedamuthu, S. Singh, and G. W. Robinson, “ Simple Relationship between the Properties of Isotopic Water,” *J. Phys. Chem.*, vol. 100, no. 9, pp. 3825–3827, 1996.

[71] D. Lide, *CRC Handbook of Chemistry and Physics, 84th Edition.* CRC HANDBOOK OF CHEMISTRY AND PHYSICS, Taylor & Francis, 2003.

[72] V. K. la Mer and W. N. Baker, “ The Freezing Point of Mixtures of H_2O and D_2O. The Latent Heat of Fusion of D_2O,” *J. Am. Chem. Soc.*, vol. 56, no. 12, pp. 2641–2643, 1934.

[73] J. Kestin, J. V. Sengers, B. Kamgar-Parsi, and J. M. H. Levelt Sengers, “ Thermophysical Properties of Fluid H_2O,” *J. Phys. Chem. Ref. Data*, vol. 13, no. 1, pp. 175–183, 1984.

[74] C. H. Cho, J. Urquidi, S. Singh, and G. Wilse Robinson, “ Thermal Offset Viscosities of Liquid H_2O, D_2O, and T_2O,” *J. Phys. Chem. B*, vol. 103, no. 11, pp. 1991–1994, 1999.

[75] M. Adamo, A. S. Poulos, R. M. Miller, C. G. Lopez, A. Martel, L. Porcar, and J. T. Cabral, “ Rapid Contrast Matching by Microfluidic SANS,” *Lab Chip*, vol. 17, pp. 1559–1569, 2017.

[76] A. Huang, H. Yao, and B. D. Olsen, “ SANS Partial Structure Factor Analysis for Determining Protein- Polymer Interactions in Semidilute Solution,” *Soft Matter*, vol. 15, no. 37, pp. 7350–7359, 2019.

[77] J. G. Kempf and J. P. Loria, “ Protein Dynamics from Solution NMR,” *Cell Biochem. Biophys.*, vol. 37, no. 3, pp. 187–211, 2002.

[78] S. Bucciarelli, J. S. Myung, B. Farago, S. Das, G. A. Vliegenthart, O. Holderer, R. G. Winkler, P. Schurtenberger, G. Gompper, and A. Stradner, “ Dramatic Influence of Patchy Attractions on Short-Time Protein Diffusion under Crowded Conditions,” *Sci. Adv.*, vol. 2, no. 12, p. e1601432, 2016.

[79] F. Gabel, D. Bicout, U. Lehnert, M. Tehei, M. Weik, and G. Zaccai, “ Protein Dynamics Studied by Neutron Scattering,” *Q. Rev. Biophys.*, vol. 35, no. 4, p. 327367, 2002.

[80] E. Hardy, A. Zygar, M. Zeidler, M. Holz, and F. Sacher, “ Isotope Effect on the Translational and Rotational Motion in Liquid Water and Ammonia,” *J. Chem. Phys.*, vol. 114, pp. 3174–3181, 2001.

[81] D. J. Kushner, A. Baker, and T. G. Dunstall, “ Pharmacological Uses and Perspectives of Heavy Water and Deuterated Compounds,” *Can. J. Physiol. Pharmacol.*, vol. 77, no. 2, pp. 79–88, 1999.

[82] L. C. Antonino, R. A. Kautz, T. Nakano, R. O. Fox, and A. L. Fink, “ Cold Denaturation and ^2H_2O Stabilization of a Staphylococcal Nuclease Mutant,” *Proc. Natl. Acad. Sci. U. S. A.*, vol. 88, no. 17, pp. 7715–7718, 1991.

[83] R. Guzzi, L. Sportelli, C. La Rosa, D. Milardi, and D. Grasso, “ Solvent Isotope Effects on Azurin Thermal Unfolding,” *J. Phys. Chem. B*, vol. 102, no. 6, pp. 1021–1028, 1998.

[84] P. Cioni and G. B. Strambini, “ Effect of Heavy Water on Protein Flexibility,” *Biophys. J.*, vol. 82, no. 6, pp. 3246 – 3253, 2002.

[85] G. I. Makhatadze, G. M. Clore, and A. M. Gronenborn, “ Solvent Isotope Effect and Protein Stability,” *Nat. Struct. Biol.*, vol. 2, no. 10, p. 852, 1995.

[86] M. J. Parker and A. R. Clarke, “ Amide Backbone and Water-Related H/D Isotope Effects on the Dynamics of a Protein Folding Reaction,” *Biochemistry*, vol. 36, no. 19, pp. 5786–5794, 1997.

[87] Y. M. Efimova, S. Haemers, B. Wierczinski, W. Norde, and A. A. v. Well, “ Stability of Globular Proteins in H_2O and D_2O,” *Biopolymers*, vol. 85, no. 3, pp. 264–273, 2007.

[88] L. Fu, S. Villette, S. Petoud, F. Fernandez-Alonso, and M.-L. Saboungi, “ H/D Isotope Effects in Protein Thermal Denaturation: The Case of Bovine Serum Albumin,” *J. Phys. Chem. B*, vol. 115, no. 8, pp. 1881–1888, 2011.

[89] P. Tompa, “ Intrinsically Disordered Proteins: A 10-Year Recap,” *Trends Biochem. Sci.*, vol. 37, no. 12, pp. 509 – 516, 2012.

[90] K. A. Majorek, P. J. Porebski, A. Dayal, M. D. Zimmerman, K. Jablonska, A. J. Stewart, M. Chruszcz, and W. Minor, “ Structural and Immunologic Characterization of Bovine, Horse, and Rabbit Serum Albumins,” *Mol. Immunol.*, vol. 52, no. 3, pp. 174 – 182, 2012.

[91] K. Kuwata, S. Era, M. Hoshino, V. Forge, Y. Goto, and C. A. Batt, “ Solution Structure and Dynamics of Bovine β-Lactoglobulin A,” *Protein Sci.*, vol. 8, no. 11, pp. 2541–2545, 1999.

[92] P. Stein, A. Leslie, J. Finch, and R. Carrell, “ Crystal Structure of Uncleaved Ovalbumin at 1.95 Å Resolution,” *J. Mol. Biol.*, vol. 221, pp. 941–959, 1991.

[93] L. J. Harris, E. Skaletsky, and A. McPherson, “ Crystallographic Structure of an Intact IgG1 Monoclonal Antibody,” *J. Mol. Biol.*, vol. 275, no. 5, pp. 861 – 872, 1998.

[94] A. Herràez, “ Biomolecules in the Computer: Jmol to the Rescue,” *Biochem. Mol. Biol. Educ.*, vol. 34, no. 4, pp. 255–261, 2006.

[95] M. Gottschalk, H. Nilsson, H. Roos, and B. Halle, “ Protein Self-Association in Solution: The Bovine β -Lactoglobulin Dimer and Octamer,” *Protein Sci.*, vol. 12, no. 11, pp. 2404–2411, 2009.

[96] C. Beck, M. Grimaldo, F. Roosen-Runge, M. Braun, F. Zhang, F. Schreiber, and T. Seydel, “ Nanosecond Tracer Diffusion as a Probe of the Solution Structure and Molecular Mobility of Protein Assemblies: The Case of Ovalbumin,” *J. Phys. Chem. B*, vol. 122, no. 35, pp. 8343–8350, 2018.

[97] D.-M. Smilgies and E. Folta-Stogniew, “ Molecular Weight- Gyration Radius Relation of Globular Proteins: A Comparison of Light Scattering, Small-Angle X-Ray Scattering and Structure-Based Data,” *J. Appl. Crystallogr.*, vol. 48, no. 5, pp. 1604–1606, 2015.

[98] L. E. Rayner, G. K. Hui, J. Gor, R. K. Heenan, P. A. Dalby, and S. J. Perkins, “ The Solution Structures of Two Human IgG1 Antibodies Show Conformational Stability and Accommodate Their C1q and FcγR Ligands,” *J. Biol. Chem.*, vol. 290, no. 13, pp. 8420–8438, 2015.

[99] L. Medda, M. Monduzzi, and A. Salis, “ The Molecular Motion of Bovine Serum Albumin under Physiological Conditions is Ion Specific,” *Chem. Commun.*, vol. 51, pp. 6663–6666, 2015.

[100] K. Engelhardt, M. Lexis, G. Gochev, C. Konnerth, R. Miller, N. Willenbacher, W. Peukert, and B. Braunschweig, “ pH Effects on the Molecular Structure of β-Lactoglobulin Modified AirWater Interfaces and Its Impact on Foam Rheology,” *Langmuir*, vol. 29, no. 37, pp. 11646–11655, 2013.

[101] E. R. B. Smith, “ The Effect of Variations in Ionic Strength on the Apparent Isoelectric Point of Egg Albumin,” *J. Biol. Chem.*, vol. 108, no. 1, pp. 187–194, 1935.

[102] D. Yang, R. Kroe-Barrett, S. Singh, and T. Laue, “ IgG Charge: Practical and Biological Implications,” *Antibodies*, vol. 8, no. 1, pp. 1–18, 2019.

[103] T. Topală, A. Bodoki, L. Oprean, and R. Oprean, “ Bovine Serum Albumin Interactions with Metal Complexes,” *Medicine and Pharmacy Reports*, vol. 87, no. 4, pp. 215–219, 2014.

[104] N. M. Urquiza, L. G. Naso, S. G. Manca, L. Lezama, T. Rojo, P. A. Williams, and E. G. Ferrer, “ Antioxidant Activity of MethimazoleCopper(II) Bioactive Species and Spectroscopic Investigations on the Mechanism of its Interaction with Bovine Serum Albumin,” *Polyhedron*, vol. 31, no. 1, pp. 530 – 538, 2012.

[105] H. A. Alhazmi, “ FT-IR Spectroscopy for the Identification of Binding Sites and Measurements of the Binding Interactions of Important Metal Ions with Bovine Serum Albumin,” *Sci. Pharm.*, vol. 87, no. 1, pp. 1–13, 2019.

[106] X. Yu, S. Sun, L. Zhou, Z. Miao, X. Zhang, Z. Su, and G. Wei, “ Removing Metal Ions from Water with GrapheneBovine Serum Albumin Hybrid Membrane,” *Nanomaterials*, vol. 9, no. 2, pp. 1–12, 2019.

[107] C. Guo, X. Guo, W. Chu, N. Jiang, and H. Li, “ Spectroscopic Study of Conformation Changes of Bovine Serum Albumin in Aqueous Environment,” *Chin. Chem. Lett.*, vol. 30, no. 6, pp. 1302 – 1306, 2019.

[108] L. Medda, B. Barse, F. Cugia, M. Boström, D. F. Parsons, B. W. Ninham, M. Monduzzi, and A. Salis, “ Hofmeister Challenges: Ion Binding and Charge of the BSA Protein as Explicit Examples,” *Langmuir*, vol. 28, no. 47, pp. 16355–16363, 2012.

[109] F. Roosen-Runge, M. Hennig, F. Zhang, R. M. J. Jacobs, M. Sztucki, H. Schober, T. Seydel, and F. Schreiber, “ Protein Self-Diffusion in Crowded Solutions,” *Proc. Natl. Acad. Sci. U. S. A.*, vol. 108, no. 29, pp. 11815–11820, 2011.

[110] F. Roosen-Runge, M. Hennig, T. Seydel, F. Zhang, M. W. A. Skoda, S. Zorn, R. M. J. Jacobs, M. Maccarini, P. Fouquet, and F. Schreiber, “ Protein Diffusion in Crowded Electrolyte Solutions,” *Biochim. Biophys. Acta*, vol. 1804, pp. 68–75, 2010.

[111] M. Hennig, F. Roosen-Runge, F. Zhang, S. Zorn, M. W. A. Skoda, R. M. J. Jacobs, T. Seydel, and F. Schreiber, “ Dynamics of Highly Concentrated Protein Solutions Around the Denaturing Transition,” *Soft Matter*, vol. 8, no. 5, pp. 1628–1633, 2012.

[112] K. Shoji, T. Mitsuru, K. Tatsuhiko, M. Tomoaki, and A. Koichiro, “ Interaction of Bovine Serum Albumin with Detergent Cations,” *Bull. Chem. Soc. Jpn.*, vol. 46, no. 9, pp. 2735–2738, 1973.

[113] E. L. Gelamo, R. Itri, A. Alonso, J. V. da Silva, and M. Tabak, “ Small-Angle X-Ray Scattering and Electron Paramagnetic Resonance Study of the Interaction of Bovine Serum Albumin with Ionic Surfactants,” *J. Colloid Interface Sci.*, vol. 277, no. 2, pp. 471 – 482, 2004.

[114] M. N. Jones, H. A. Skinner, and E. Tipping, “ The Interaction Between Bovine Serum Albumin and Surfactants,” *Biochem. J.*, vol. 147, no. 2, pp. 229–234, 1975.

[115] M. Sharifi, J. E. N. Dolatabadi, F. Fathi, M. Rashidi, B. Jafari, H. Tajalli, and M.-R. Rashidi, “ Kinetic and Thermodynamic Study of Bovine Serum Albumin Interaction with Rifampicin using Surface Plasmon Resonance and Molecular Docking Methods,” *J. Biomed. Opt.*, vol. 22, no. 3, pp. 1 – 6, 2017.

[116] N. S. Quiming, R. B. Vergel, M. G. Nicolas, and J. A. Villanueva, “ Interaction of Bovine Serum Albumin and Metallothionein,” *J. Health Sci.*, vol. 51, no. 1, pp. 8–15, 2005.

[117] G. Dravecz, T. Z. Jánosi, D. Beke, D. Á. Major, G. Károlyházy, J. Erostyák, K. Kamarás, and A. Gali, “ Identification of the Binding Site Between Bovine Serum Albumin and Ultrasmall SiC Fluorescent Biomarkers,” *Phys. Chem. Chem. Phys.*, vol. 20, pp. 13419–13429, 2018.

[118] A. Bhogale, N. Patel, P. Sarpotdar, J. Mariam, P. Dongre, A. Miotello, and D. Kothari, “ Systematic Investigation on the Interaction of Bovine Serum Albumin with ZnO Nanoparticles using Fluorescence Spectroscopy,” *Colloids Surf., B*, vol. 102, pp. 257 – 264, 2013.

[119] S. Höhn, S. Virtanen, and A. R. Boccaccini, “ Protein Adsorption on Magnesium and its Alloys: A Review,” *Appl. Surf. Sci.*, vol. 464, pp. 212 – 219, 2019.

[120] M. Grimaldo, F. Roosen-Runge, F. Zhang, T. Seydel, and F. Schreiber, “ Diffusion and Dynamics of γ- Globulin in Crowded Aqueous Solutions,” *J. Phys. Chem. B*, vol. 118, pp. 7203–7209, 2014.

[121] S. Da Vela, M. K. Braun, A. Dörr, A. Greco, J. Möller, Z. Fu, F. Zhang, and F. Schreiber, “ Kinetics of Liquid- Liquid Phase Separation in Protein Solutions Exhibiting LCST Phase Behavior Studied by Time-Resolved USAXS and VSANS,” *Soft Matter*, vol. 12, no. 46, pp. 9334–9341, 2016.

[122] J. Möller, M. Sprung, A. Madsen, and C. Gutt, “ X-Ray Photon Correlation Spectroscopy of Protein Dynamics at Nearly Diffraction-Limited Storage Rings,” *IUCrJ*, vol. 6, no. 5, pp. 794–803, 2019.

[123] J. Zhang, X. Liu, M. Subirade, P. Zhou, and L. Liang, “ A Study of Multi-Ligand β-Lactoglobulin Complex Formation,” *Food Chem.*, vol. 165, pp. 256 – 261, 2014.

[124] S. Świątek, P. Komorek, G. Turner, and B. Jachimska, “ β-Lactoglobulin as a Potential Carrier for Bioactive Molecules,” *Bioelectrochemistry*, vol. 126, pp. 137 – 145, 2019.

[125] L. Anghel, A. Rogachev, A. Kuklin, and R. V. Erhan, “ β-Lactoglobulin Associative Interactions: a Small-Angle Scattering Study,” *Eur. Biophys. J.*, vol. 48, no. 3, pp. 285–295, 2019.

[126] G. Kontopidis, C. Holt, and L. Sawyer, “ The Ligand-binding Site of Bovine β-Lactoglobulin: Evidence for a Function?,” *J. Mol. Biol.*, vol. 318, no. 4, pp. 1043 – 1055, 2002.

[127] C. Tanford, L. G. Bunville, and Y. Nozaki, “ The Reversible Transformation of β-Lactoglobulin at pH 7.51,” *J. Am. Chem. Soc.*, vol. 81, no. 15, pp. 4032–4036, 1959.

[128] S. Sardar, M. Anas, S. Maity, S. Pal, H. Parvej, S. Begum, R. Dalui, N. Sepay, and U. C. Halder, “ Silver Nanoparticle Modulates the Aggregation of β-Lactoglobulin and Induces to Rorm Rod-like Aggregates,” *Int. J. Biol. Macromol.*, vol. 125, pp. 596 – 604, 2019.

[129] A. Tolkach and U. Kulozik, “ Reaction Kinetic Pathway of Reversible and Irreversible Thermal Denaturation of β-lactoglobulin,” *Lait*, vol. 87, no. 4-5, pp. 301–315, 2007.

[130] E. M. Dumay, M. T. Kalichevsky, and J. C. Cheftel, “ High-Pressure Unfolding and Aggregation of β-Lactoglobulin and the Baroprotective Effects of Sucrose,” *J. Agric. Food Chem.*, vol. 42, no. 9, pp. 1861–1868, 1994.

[131] M. K. Braun, M. Grimaldo, F. Roosen-Runge, I. Hoffmann, O. Czakkel, M. Sztucki, F. Zhang, F. Schreiber, and T. Seydel, “ Crowding-Controlled Cluster Size in Concentrated Aqueous Protein Solutions: Structure, Self-and Collective Diffusion,” *J. Phys. Chem. Lett.*, vol. 8, pp. 2590–2596, 2017.

[132] F. Zhang, G. Zocher, A. Sauter, T. Stehle, and F. Schreiber, “ Novel Approach to Controlled Protein Crystallization through Ligandation of Yttrium Cations,” *Journal of Applied Crystallography*, vol. 44, no. 4, pp. 755–762, 2011.

[133] A. Sauter, M. Oelker, G. Zocher, F. Zhang, T. Stehle, and F. Schreiber, “ Nonclassical Pathways of Protein Crystallization in the Presence of Multivalent Metal Ions,” *Cryst. Growth Des.*, vol. 14, no. 12, pp. 6357–6366, 2014.

[134] A. Sauter, F. Roosen-Runge, F. Zhang, G. Lotze, A. Feoktystov, R. M. J. Jacobs, and F. Schreiber, “ On the Question of Two-Step Nucleation in Protein Crystallization,” *Faraday Discuss.*, vol. 179, pp. 41–58, 2015.

[135] B. Sohmen, “Real-time Observation of Nonclassical Protein Crystallisation induced by Multivalent Ions,” Master Thesis, Universität Tübingen, 2016.

[136] C. Beck, M. Grimaldo, F. Roosen-Runge, R. Maier, O. Matsarskaia, M. Braun, B. Sohmen, O. Czakkel, R. Schweins, F. Zhang, T. Seydel, and F. Schreiber, “ Following Protein Dynamics in Real-Time During Crystallization,” *Cryst. Growth Des.*, vol. 19, no. 12, pp. 7036–7045, 2019.

[137] R. A. Kekwick and R. K. Cannan, “ The Hydrogen Ion Dissociation Curve of the Crystalline Albumin of the Hen’s Egg,” *Biochem. J.*, vol. 30, no. 2, pp. 227–234, 1936.

[138] J. H. Wang, C. B. Anfinsen, and F. M. Polestra, “ The Self-Diffusion Coefficients of Water and Ovalbumin in Aqueous Ovalbumin Solutions at 10°,” *Journal of the American Chemical Society*, vol. 76, no. 19, pp. 4763–4765, 1954.

[139] S. J. Gibbs, A. S. Chu, E. N. Lightfoot, and T. W. Root, “ Ovalbumin Diffusion at Low Ionic Strength,” *J. Phys. Chem.*, vol. 95, no. 1, pp. 467–471, 1991.

[140] W. Kauzmann, “ Volume Changes in Ovalbumin and Bovine Serum Albumin on Adding Acid,” *Biochim. Biophys. Acta*, vol. 28, pp. 87 – 91, 1958.

[141] L. G. Longsworth, “ The Influence of pH on the Mobility and Diffusion of Ovalbumin,” *Ann. N. Y. Acad. Sci.*, vol. 41, no. 4, pp. 267–286, 1941.

[142] E. Johnson, D. Berk, R. Jain, and W. Deen, “ Diffusion and Partitioning of Proteins in Charged Agarose Gels,” *Biophys. J.*, vol. 68, no. 4, pp. 1561–1568, 1995.

[143] L. Ianeselli, F. Zhang, M. W. A. Skoda, R. M. J. Jacobs, R. A. Martin, S. Callow, S. Prévost, and F. Schreiber, “ Protein-Protein Interactions in Ovalbumin Solutions Studied by Small-Angle Scattering: Effect of Ionic Strength and the Chemical Nature of Cations,” *J. Phys. Chem. B*, vol. 114, no. 11, pp. 3776–3783, 2010.

[144] D. Scott, T. Patel, D. Besong, J. Stetefeld, and D. Winzor, “ Examination of the Discrepancy between Size Estimates for Ovalbumin from Small-Angle X-Ray Scattering and Other Physicochemical Measurements,” *J. Phys. Chem. B*, vol. 115, no. 36, pp. 10725–10729, 2011.

[145] T. Matsumoto and J. Chiba, “ Rheological and Small-Angle X-Ray Scattering Investigations on the Shape and Ordered Arrangement of Native Ovalbumin Molecules in Aqueous Colloids,” *J. Chem. Soc., Faraday Trans.*, vol. 86, pp. 2877–2882, 1990.

[146] T. Matsumoto, J. Chiba, and H. Inoue, “ Effect of pH on Colloidal Properties of Native Ovalbumin Aqueous Systems,” *Colloid Polym. Sci.*, vol. 270, no. 7, pp. 687–693, 1992.

[147] T. Matsumoto and H. Inoue, “ Association State, Overall Structure, and Surface Roughness of Native Ovalbumin Molecules in Aqueous Solutions at Various Ionic Concentrations,” *J. Colloid Interface Sci.*, vol. 160, no. 1, pp. 105 – 109, 1993.

[148] M. Halwer, G. C. Nutting, and B. A. Brice, “ Molecular Weight of Lactoglobulin, Ovalbumin, Lysozyme and Serum Albumin by Light Scattering,” *J. Am. Chem. Soc.*, vol. 73, no. 6, pp. 2786–2790, 1951.

[149] P. A. Charlwood and A. Ens, " Effect of pH on the Sedementation of Serum Albumins and Ovalbumin," *Can. J. Chem.*, vol. 35, no. 1, pp. 101–103, 1957.

[150] J. Creeth and D. Winzor, " Physicochemical Studies on Ovalbumin. 4. Characterization of an Iodine-Modified Derivative by Electrophoresis and Sedimentation," *Biophys. J.*, vol. 83, no. 3, pp. 566–574, 1962.

[151] P. D. Jeffrey, L. W. Nichol, D. R. Turner, and D. J. Winzor, " The Combination of Molecular Covolume and Frictional Coefficient to Determine the Shape and Axial Ratio of a Rigid Macromolecule. Studies on Ovalbumin," *J. Phys. Chem.*, vol. 81, no. 8, pp. 776–781, 1977.

[152] H. McKenzie, M. Smith, and R. Wake, " The Denaturation of Proteins: I. Sedimentation, Diffusion, Optical Rotation Viscosity and Gelation in Urea Solutions of Ovalbumin and Bovine Serum Albumin," *Biochim. Biophys. Acta*, vol. 69, pp. 222 – 239, 1963.

[153] A. Glazer, H. McKenzie, and R. Wake, " The Denaturation of Proteins: II. Ultraviolet Absorption Spectra of Bovine Serum Albumin and Ovalbumin in Urea and in Acid Solution," *Biochim. Biophys. Acta*, vol. 69, pp. 240 – 248, 1963.

[154] S. Ngarize, H. Herman, A. Adams, and N. Howell, " Comparison of Changes in the Secondary Structure of Unheated, Heated, and High-Pressure-Treated β-Lactoglobulin and Ovalbumin Proteins Using Fourier Transform Raman Spectroscopy and Self-Deconvolution," *J. Agric. Food Chem.*, vol. 52, no. 21, pp. 6470–6477, 2004.

[155] R. D. Shannon, " Revised Effective Ionic Radii and Systematic Studies of Interatomic Distances in Halides and Chalcogenides," *Acta Crystallogr., Sect. A: Cryst. Phys., Diffr., Theor. Gen. Crystallogr.*, vol. 32, no. 5, pp. 751–767, 1976.

[156] P. D'Angelo, A. Zitolo, V. Migliorati, G. Chillemi, M. Duvail, P. Vitorge, S. Abadie, and R. Spezia, " Revised Ionic Radii of Lanthanoid(III) Ions in Aqueous Solution," *Inorg. Chem.*, vol. 50, no. 10, pp. 4572–4579, 2011.

[157] B. Hammouda, *Probing Nanoscale Structures - the SANS Toolbox.* Mater. Sci., 2008.

[158] J. Baruchel, J. L. Hodeau, M. S. Lehmann, J. R. Regnard, and C. Schlenker, *Neutron and Synchrotron Radiation for Condensed Matter Studies – Volume 1 – Theory, Instruments and Methods.* Berlin New York Ulis, France: Springer-Verlag Les Editions de Physique, 1993.

[159] H. Schober, " Neutron Applications in Earth, Energy and Environmental Sciences: Neutron Scattering Instrumentation," pp. 37–104, Springer US, 2009.

[160] C. D. Dewhurst, I. Grillo, D. Honecker, M. Bonnaud, M. Jacques, C. Amrouni, A. Perillo-Marcone, G. Manzin, and R. Cubitt, “ The Small-Angle Neutron Scattering Instrument D33 at the Institut Laue–Langevin,” *J. Appl. Crystallogr.*, vol. 49, no. 1, pp. 1–14, 2016.

[161] S. R. Kline, “ Reduction and Analysis of SANS and USANS Data using IGOR Pro,” *J. Appl. Cryst.*, vol. 39, no. 6, pp. 895–900, 2006.

[162] F. Mezei, “ Neutron Spin Echo: A new Concept in Polarized Thermal Neutron Techniques,” *Z. Phys. A: At. Nucl.*, vol. 255, no. 2, pp. 146–160, 1972.

[163] R. Cywinski, *Neutron and X-ray Spectroscopy: Neutron Spin Echo Spectroscopy*, pp. 427–456. Dordrecht: Springer Netherlands, 2006.

[164] H. Börner, J. Brown, C. J. Carlile, R. Cubitt, R. Currat, A. J. Dianoux, B. Farago, A. Hewat, J. Kulda, E. Lelièvre-Berna, G. McIntyre, S. Mason, R. P. May, A. Oed, J. R. Stewart, F. Tasset, J. Tribolet, I. Anderson, D. Dubbers, R. S. Eccleston, M. Johnson, C. C. Wilson, G. Lander, H. Rauch, R. B. Von Dreele, and W. Waschkowski, *Neutron Data Booklet.* Institut Laue Langevin, Grenoble, France, 2 ed., 2003.

[165] M. Monkenbusch, R. Schätzler, and D. Richter, “ The Jülich Neutron Spin-Echo Spectrometer Design and Performance,” *Nucl. Instrum. Methods Phys. Res., Sect. A*, vol. 399, no. 2, pp. 301 – 323, 1997.

[166] B. Farago, P. Falus, I. Hoffmann, M. Gradzielski, F. Thomas, and C. Gomez, “ The IN15 Upgrade,” *Neutron News*, vol. 26, no. 3, pp. 15–17, 2015.

[167] F. Mezei, “ Neutron Spin Echo: The Principles of Neutron Spin Echo,” (Berlin, Heidelberg), pp. 1–26, Springer Berlin Heidelberg, 1980.

[168] W. G. Williams, *Polarized Neutrons.* Claredon Press Oxford, 1988.

[169] F. Mezei, C. Pappas, and T. Gutberlet, *Neutron Spin Echo Spectrocopy - Basics, Trends, and Applications.* Springer Verlag Berlin Heidelberg, 2003.

[170] D. Richter, M. Monkenbusch, A. Arbe, and J. Colmenero, *Neutron Spin Echo in Polymer Systems*, pp. 1–221. Berlin, Heidelberg: Springer Berlin Heidelberg, 2005.

[171] B. Frick, *Neutron and X-ray Spectroscopy: Neutron Backscattering Spectroscopy*, pp. 483–527. Dordrecht: Springer Netherlands, 2006.

[172] E. Mamontov and K. W. Herwig, “ A Time-of-Flight Backscattering Spectrometer at the Spallation Neutron Source, BASIS,” *Rev. Sci. Instrum.*, vol. 82, no. 8, p. 085109, 2011.

[173] M. Hennig, B. Frick, and T. Seydel, “ Optimum Velocity of a Phase-Space Transformer for Cold-Neutron Backscattering Spectroscopy,” *J. Appl. Crystallogr.*, vol. 44, no. 3, pp. 467–472, 2011.

[174] K. Kuhlmann, *Development and Commissioning of a Prototype Neutron Backscattering Spectrometer with an Energy Resolution Enhanced by an Order of Magnitude using GaAs Single Crystals.* Doctoral thesis, Friedrich-Alexander-Universität Erlangen-Nürnberg (FAU), 2018.

[175] M. Appel, B. Frick, and A. Magerl, “ First Results with the Neutron Backscattering and TOF Spectrometer Option BATS on IN16B,” *Phys. B (Amsterdam, Neth.)*, vol. 562, pp. 6 – 8, 2019.

[176] B. Frick, H. Bordallo, T. Seydel, J.-F. Barthélémy, M. Thomas, D. Bazzoli, and H. Schober, “ How IN16 can Maintain a World-Leading Position in Neutron Backscattering Spectrometry,” *Phys. B (Amsterdam, Neth.)*, vol. 385-386, pp. 1101 – 1103, 2006.

[177] B. Frick, J. Combet, and L. van Eijck, “ New Possibilities with Inelastic Fixed Window Scans and Linear Motor Doppler Drives on High Resolution Neutron Backscattering Spectrometers,” *Nucl. Instrum. Methods Phys. Res., Sect. A*, vol. 669, pp. 7 – 13, 2012.

[178] M. Jasnin, M. Moulin, M. Haertlein, G. Zaccai, and M. Tehei, “ *In Vivo* Measurement of Internal and Global Macromolecular Motions in Escherichia Coli,” *Biophys. J.*, vol. 95, no. 2, pp. 857–864, 2008.

[179] A. M. Stadler, L. Stingaciu, A. Radulescu, O. Holderer, M. Monkenbusch, R. Biehl, and D. Richter, “ Internal Nanosecond Dynamics in the Intrinsically Disordered Myelin Basic Protein,” *J. Am. Chem. Soc.*, vol. 136, no. 19, pp. 6987–6994, 2014.

[180] M. Monkenbusch, A. Stadler, R. Biehl, J. Ollivier, M. Zamponi, and D. Richter, “ Fast Internal Dynamics in Alcohol Dehydrogenase,” *J. Chem. Phys.*, vol. 143, no. 7, p. 075101, 2015.

[181] S. Fujiwara, K. Araki, T. Matsuo, H. Yagi, T. Yamada, K. Shibata, and H. Mochizuki, “ Dynamical Behavior of Human α-Synuclein Studied by Quasielastic Neutron Scattering,” *PloS one*, vol. 11, no. 4, p. e0151447, 2016.

[182] F. Ameseder, A. Radulescu, M. Khaneft, W. Lohstroh, and A. M. Stadler, “ Homogeneous and Heterogeneous Dynamics in Native and Denatured Bovine Serum Albumin,” *Phys. Chem. Chem. Phys.*, vol. 20, pp. 5128–5139, 2018.

[183] S. Lenton, M. Grimaldo, F. Roosen-Runge, F. Schreiber, T. Nylander, R. Clegg, C. Holt, M. Härtlein, V. G. Sakai, T. Seydel, and S. C. M. Teixeira, “ Effect of Phosphorylation on a Human-like Osteopontin Peptide,” *Biophys. J.*, vol. 112, no. 8, pp. 1586 – 1596, 2017.

[184] F. Zhang, F. Roosen-Runge, A. Sauter, M. Wolf, R. M. J. Jacobs, and F. Schreiber, “ Reentrant Condensation, Liquid- Liquid Phase Separation and Crystallization in Protein Solutions Induced by Multivalent Metal Ions,” *Pure Appl. Chem.*, vol. 86, no. 2, pp. 191–202, 2014.

[185] J. Bleibel, M. Habiger, M. Lütje, F. Hirschmann, F. Roosen-Runge, T. Seydel, F. Zhang, F. Schreiber, and M. Oettel, “ Two Time Scales for Self and Collective Diffusion Near the Critical Point in a Simple Patchy Model for Proteins with Floating Bonds,” *Soft Matter*, pp. –, 2018.

[186] L. Toppozini, F. Roosen-Runge, R. I. Bewley, R. M. Dalgliesh, T. Perring, T. Seydel, H. R. Glyde, V. García Sakai, and M. C. Rheinstadter, “ Anomalous and Anisotropic Nanoscale Diffusion of hHydration Water Molecules in Fluid Lipid Membranes,” *Soft Matter*, vol. 11, pp. 8354–8371, 2015.

[187] R. Kohlrausch, “ Theorie des Elektrischen Rückstandes in der Leidner Flasche,” *Ann. Phys. (Berlin, Ger.)*, vol. 91, pp. 56–82, 1854.

[188] M. Mittag-Leffler, “ Sur la Fonction Nouvelle E_α (x),” *CR Acad. Sci., Paris*, vol. 2, no. 137, pp. 554–558, 1903.

[189] G. R. Kneller, “ Quasielastic Neutron Scattering and Relaxation Processes in Proteins: Analytical and Simulation-Based Models,” *Phys. Chem. Chem. Phys.*, vol. 7, pp. 2641–2655, 2005.

[190] I. Krasnov, T. Seydel, I. Greving, M. Blankenburg, F. Vollrath, and M. Müller, “ Strain-dependent Fractional Molecular Diffusion in Humid Spider Silk Fibres,” *J. R. Soc., Interface*, vol. 13, no. 122, p. 20160506, 2016.

[191] B. Frick, E. Mamontov, L. van Eijck, and T. Seydel, “ Recent Backscattering Instrument Developments at the ILL and SNS,” *Z. Phys. Chem. (Muenchen, Ger.)*, vol. 224, pp. 33–60, 2010.

[192] L. van Eijck, L. Gérard, B. Frick, T. Seydel, and H. Schober, “ A Case Study for Using Neutron Backscattering Instruments at Reactors in Inverted Time-of-Flight Mode,” *Nucl. Instrum. Methods Phys. Res., Sect. A*, vol. 672, pp. 64–68, 2012.

[193] J. Wuttke, A. Budwig, M. Drochner, H. Kämmerling, F.-J. Kayser, H. Kleines, V. Ossovyi, L. C. Pardo, M. Prager, D. Richter, G. J. Schneider, H. Schneider, and S. Staringer, “SPHERES, Jülich’s High-Flux Neutron Backscattering Spectrometer at FRM II,” *Rev. Sci. Instrum.*, vol. 83, no. 7, p. 075109, 2012.

[194] M. Appel and B. Frick, " Note: One Order of Magnitude Better Signal-to-Noise Ratio for Neutron Backscattering," *Rev. Sci. Instrum.*, vol. 88, no. 3, p. 036105, 2017.

[195] P. Ageron, " Cold Neutron Sources at ILL," *Nucl. Instrum. Methods Phys. Res., Sect. A*, vol. 284, no. 1, pp. 197–199, 1989.

[196] L. Mansur, T. Gabriel, J. Haines, and D. Lousteau, " R&D for the Spallation Neutron Source Mercury Target," *J. Nucl. Mater.*, vol. 296, no. 1, pp. 1 – 16, 2001.

[197] H. Bordallo, B. Frick, H. Schober, and T. Seydel, " Primary Spectrometer Neutron Optics Simulations for a new Cold Neutron Backscattering Spectrometer," *J. Neutron Res.*, vol. 16, no. 1-2, pp. 39–54, 2008.

[198] A. Meyer, R. M. Dimeo, P. M. Gehring, and D. A. Neumann, " The High-Flux Backscattering Spectrometer at the NIST Center for Neutron Research," *Rev. Sci. Instrum.*, vol. 74, no. 5, pp. 2759–2777, 2003.

[199] C. Carlile and M. A. Adams, " The Design of the IRIS Inelastic Neutron Spectrometer and Improvements to its Analysers," *Phys. B (Amsterdam, Neth.)*, vol. 182, pp. 431–440, 1992.

[200] N. Tsapatsaris, R. Lechner, M. Markó, and H. Bordallo, " Conceptual Design of the Time-of-Flight Backscattering Spectrometer, MIRACLES, at the European Spallation Source," *Rev. Sci. Instrum.*, vol. 87, no. 8, p. 085118, 2016.

[201] B. Frick, M. Appel, T. Seydel, L. van Eijck, and D. Bazzoli, "The New Backscattering Spectrometer IN16B at the ILL." unpublished.

[202] S. R. Al-Ayoubi, P. H. Schummel, A. Cisse, T. Seydel, J. Peters, and R. Winter, " Osmolytes Modify Protein Dynamics and Function of Tetrameric Lactate Dehydrogenase upon Pressurization," *Phys. Chem. Chem. Phys.*, vol. 21, no. 24, pp. 12806–12817, 2019.

[203] A. M. Stadler, E. Knieps-Grünhagen, M. Bocola, W. Lohstroh, M. Zamponi, and U. Krauss, " Photoactivation Reduces Side-Chain Dynamics of a LOV Photoreceptor," *Biophys. J.*, vol. 110, no. 5, pp. 1064 – 1074, 2016.

[204] A. M. Stadler, J. Schneidewind, M. Zamponi, E. Knieps-Grünhagen, S. Gholami, U. Schwaneberg, I. Rivalta, M. Garavelli, M. D. Davari, K.-E. Jaeger, and U. Krauss, " Ternary Complex Formation and Photoactivation of a Photoenzyme Results in Altered Protein Dynamics," *J. Phys. Chem. B*, vol. 123, no. 34, pp. 7372–7384, 2019.

[205] L. M. Bühl, "Elastic Incoherent Neutron Scattering Study of the Thermal Denaturation of Bovine Serum Albumin in Aqaueous Solution," diploma thesis, Universität Tübingen, 2018.

[206] A. Stadler, I. Digel, J. Embs, T. Unruh, M. Tehei, G. Zaccai, G. Büldt, and G. Artmann, " From Powder to Solution: Hydration Dependence of Human Hemoglobin Dynamics Correlated to Body Temperature," *Biophys. J.*, vol. 96, no. 12, pp. 5073–5081, 2009.

[207] S. Magazú, F. Mezei, P. Falus, B. Farago, E. Mamontov, M. Russina, and F. Migliardo, " Protein Dynamics as Seen by (Quasi) Elastic Neutron Scattering," *Biochim. Biophys. Acta*, vol. 1861, no. 1, Part B, pp. 3504 – 3512, 2017.

[208] K. Wood, C. Caronna, P. Fouquet, W. Haussler, F. Natali, J. Ollivier, A. Orecchini, M. Plazanet, and G. Zaccai, " A Benchmark for Protein Dynamics: Ribonuclease A Measured by Neutron Scattering in a Large Wavevector-Energy Transfer Range," *Chem. Phys.*, vol. 345, no. 2-3, pp. 305–314, 2008.

[209] C. Caronna, F. Natali, and A. Cupane, " Incoherent Elastic and Quasi-Elastic Neutron Scattering Investigation of Hemoglobin Dynamics," *Biophys. Chem.*, vol. 116, no. 3, pp. 219–225, 2005.

[210] A. L. Thorneywork, D. G. A. L. Aarts, J. Horbach, and R. P. A. Dullens, "On the Gaussian approximation in colloidal hard sphere fluids," *Soft Matter*, vol. 12, pp. 4129–4134, 2016.

[211] Z. Yi, Y. Miao, J. Baudry, N. Jain, and J. C. Smith, " Derivation of Mean-Square Displacements for Protein Dynamics from Elastic Incoherent Neutron Scattering," *J. Phys. Chem. B*, vol. 116, no. 16, pp. 5028–5036, 2012.

[212] D. Vural, J. C. Smith, and H. R. Glyde, " Determination of Dynamical Heterogeneity from Dynamic Neutron Scattering of Proteins," *Biophys. J.*, vol. 114, no. 10, pp. 2397–2407, 2018.

[213] D. Zeller, *Investigations de Nouvelles Méthodes pour Étudier la Dynamique Moléculaire par Diffusion Neutronique Élastique.* Thesis, Communaute universite Grenoble Alpes, 2019.

[214] G. R. Kneller and G. Chevrot, " Impact of Anisotropic Atomic Motions in Proteins on Powder-Averaged Incoherent Neutron Scattering Intensities," *Chem. Phys.*, vol. 137, no. 22, p. 225101, 2012.

[215] A. Tokuhisa, Y. Joti, H. Nakagawa, A. Kitao, and M. Kataoka, " Non-Gaussian Behavior of Elastic Incoherent Neutron Scattering Profiles of Proteins Studied by Molecular Dynamics Simulation," *Phys. Rev. E*, vol. 75, no. 4, p. 041912, 2007.

[216] D. Vural, L. Hong, J. C. Smith, and H. R. Glyde, “ Motional Displacements in Proteins: The Origin of Wave-Vector-Dependent Values,” *Phys. Rev. E*, vol. 91, p. 052705, 2015.

[217] H. Nakagawa, H. Kamikubo, I. Tsukushi, T. Kanaya, and M. Kataoka, “ Protein Dynamical Heterogeneity Derived from Neutron Incoherent Elastic Scattering,” *J. Phys. Soc. Jpn.*, vol. 73, no. 2, pp. 491–495, 2004.

[218] D. J. Bicout, “ Incoherent Neutron Scattering Functions for Diffusion Inside two Concentric Spheres,” *Phys. Rev. E*, vol. 62, pp. 261–271, 2000.

[219] L. Meinhold, D. Clement, M. Tehei, R. Daniel, J. L. Finney, and J. C. Smith, “ Protein Dynamics and Stability: The Distribution of Atomic Fluctuations in Thermophilic and Mesophilic Dihydrofolate Reductase Derived Using Elastic Incoherent Neutron Scattering,” *Biophys. J.*, vol. 94, no. 12, pp. 4812–4818, 2008.

[220] J. Peters and G. R. Kneller, “ Motional Heterogeneity in Human Acetylcholinesterase Revealed by a Non-Gaussian Model for Elastic Incoherent Neutron Scattering,” *J. Chem. Phys.*, vol. 139, no. 16, p. 165102, 2013.

[221] W. Doster, S. Cusack, and W. Petry, “ Dynamical Transition of Myoglobin Revealed by Inelastic Neutron Scattering,” *Nature*, vol. 337, no. 6209, pp. 754–756, 1989.

[222] K. Kuhlmann, M. Appel, B. Frick, and A. Magerl, “ Breakthrough in Neutron Backscattering Spectroscopy: Energy Resolution Improved by One Order of Magnitude Using the GaAs 200 Reflection,” *Rev. Sci. Instrum.*, vol. 90, no. 1, p. 015119, 2019.

[223] C. Beck, M. Appel, M. Grimaldo, F. Roosen-Runge, F. Zhang, B. Frick, F. Schreiber, and T. Seydel, “ Neutron Spectroscopy on Protein Solutions Employing Backscattering with an Increased Energy Range,” *Phys. B (Amsterdam, Neth.)*, vol. 562, pp. 31–35, 2019.

[224] F. Natali, M. Bee, A. Deriu, C. Mondelli, L. Bove, C. Castellano, and S. Labbe-Lavigne, “ IN13 Backscattering Spectrometer: An Instrument in Evolution,” *Phys. B (Amsterdam, Neth.)*, vol. 350, no. 1, Supplement, pp. E819 – E822, 2004.

[225] D. Vural, L. Hong, J. C. Smith, and H. R. Glyde, “ Long-Time Mean-Square Displacements in Proteins,” *Phys. Rev. E*, vol. 88, p. 052706, 2013.

[226] F. Roosen-Runge, M. Braun, M. Grimaldo, F. Schreiber, T. Seydel, and F. Zhang, “ Denaturation Process in Protein Solutions Studied by Inelastic Fixed Window Scans. Institut Laue-Langevin (ILL) ,” 2015. doi:10.5291/ILL-DATA.8-04-752.

[227] M. Grimaldo, C. Beck, M. Braun, S. Da Vela, F. Roosen-Runge, F. Schreiber, T. Seydel, B. Sohmen, and F. Zhang, " External Crowding in Protein Solutions. Institut Laue-Langevin (ILL)," 2015. doi:10.5291/ILL-DATA.8-04-759.

[228] "Studying thermal protein denaturation as a nanoscopic structure-dynamics relationship. institut laue-langevin (ill)."

[229] F. Roosen-Runge and T. Seydel, " A generalized mean-squared displacement from inelastic fixed window scans of incoherent neutron scattering as a model-free indicator of anomalous diffusion confinement," *EPJ Web of Conferences*, vol. 83, p. 02015, 2015.

[230] M. Grimaldo, H. Lopez, C. Beck, F. Roosen-Runge, M. Moulin, J. M. Devos, V. Laux, M. Härtlein, S. Da Vela, R. Schweins, A. Mariani, F. Zhang, J.-L. Barrat, M. Oettel, V. T. Forsyth, T. Seydel, and F. Schreiber, " Protein Short-Time Diffusion in a Naturally Crowded Environment," *J. Phys. Chem. Lett.*, vol. 10, no. 8, pp. 1709–1715, 2019.

[231] J. van den Berg, A. J. Boersma, and B. Poolman, " Microorganisms Maintain Crowding Homeostasis," *Nat. Rev. Microbiol.*, vol. 15, no. 5, pp. 309–318, 2017.

[232] G. Rivas and A. P. Minton, " Macromolecular Crowding *in vitro, in vivo,*and In Between," *Trends Biochem. Sci.*, vol. 41, no. 11, pp. 970–981, 2016.

[233] R. Ellis, " Macromolecular Crowding: An Important but Neglected Aspect of the Intracellular Environment," *Curr. Opin. Struct. Biol.*, vol. 11, no. 1, pp. 114–119, 2001.

[234] E. Mamontov, " Microscopic Diffusion Processes Measured in Living Planarians," *Sci. Rep.*, vol. 8, no. 1, pp. 4190–1–8, 2018.

[235] S. Diekmann and C. Hoischen, " Biomolecular Dynamics and Binding Studies in the Living Cell," *Phys. Life Rev.*, vol. 11, no. 1, pp. 1 – 30, 2014.

[236] D. I. Freedberg and P. Selenko, " Live Cell NMR," *Annu. Rev. Biophys.*, vol. 43, no. 1, pp. 171–192, 2014.

[237] S. Longeville and L.-R. Stingaciu, " Hemoglobin Diffusion and the Dynamics of Oxygen Capture by Red Blood Cells," *Sci. Rep.*, vol. 7, no. 1, pp. 10448–1–10, 2017.

[238] D. Anunciado, V. Nyugen, G. Hurst, M. Doktycz, V. Urban, P. Langan, E. Mamontov, and H. ONeill, " *In Vivo* Protein Dynamics on the Nanometer Length Scale and Nanosecond Time Scale," *J. Phys. Chem. Lett.*, vol. 8, no. 8, pp. 1899–1904, 2017.

[239] Y. Wang, C. Li, and G. J. Pielak, " Effects of Proteins on Protein Diffusion," *J. Am. Chem. Soc.*, vol. 132, no. 27, pp. 9392–9397, 2010.

[240] M. P. Latham and L. E. Kay, " Is Buffer a Good Proxy for a Crowded Cell-Like Environment? A Comparative NMR Study of Calmodulin Side-Chain Dynamics in Buffer and E. Coli Lysate," *PLoS One*, vol. 7, no. 10, pp. e48226–1–13, 2012.

[241] C. Le Coeur and S. Longeville, " Microscopic Protein Diffusion at High Concentration by Neutron Spin-Echo Spectroscopy," *Chem. Phys.*, vol. 345, no. 2, pp. 298–304, 2008.

[242] S. Gupta, R. Biehl, C. Sill, J. Allgaier, M. Sharp, M. Ohl, and D. Richter, " Protein Entrapment in Polymeric Mesh: Diffusion in Crowded Environment with Fast Process on Short Scales," *Macromolecules*, vol. 49, no. 5, pp. 1941–1949, 2016.

[243] M. Roos, M. Ott, M. Hofmann, S. Link, E. Rössler, J. Balbach, A. Krushelnitsky, and K. Saalwächter, " Coupling and Decoupling of Rotational and Translational Diffusion of Proteins under Crowding Conditions," *J. Am. Chem. Soc.*, vol. 138, pp. 10365–10372, 2016.

[244] A. M. Stadler, F. Demmel, J. Ollivier, and T. Seydel, " Picosecond to Nanosecond Dynamics Provide a Source of Conformational Entropy for Protein Folding," *Phys. Chem. Chem. Phys.*, vol. 18, no. 31, pp. 21527–21538, 2016.

[245] Z. Zhang and Y. Liu, " Recent Progresses of Understanding the Viscosity of Concentrated Protein Solutions," *Curr. Opin. Chem. Eng.*, vol. 16, pp. 48–55, 2017.

[246] M. Feig, I. Yu, P.-H. Wang, G. Nawrocki, and Y. Sugita, " Crowding in Cellular Environments at an Atomistic Level from Computer Simulations," *J. Phys. Chem. B*, vol. 121, no. 34, pp. 8009–8025, 2017.

[247] S. R. McGuffee and A. H. Elcock, " Diffusion, Crowding & Protein Stability in a Dynamic Molecular Model of the Bacterial Cytoplasm," *PLoS Comput. Biol.*, vol. 6, no. 3, p. e1000694, 2010.

[248] T. Ando and J. Skolnick, " Crowding and Hydrodynamic Interactions Likely Dominate in vivo Macromolecular Motion," *Proc. Natl. Acad. Sci. U. S. A.*, vol. 107, no. 43, pp. 18457–18462, 2010.

[249] J. A. Dix and A. Verkman, " Crowding Effects on Diffusion in Solutions and Cells," *Annu. Rev. Biophys.*, vol. 37, no. 1, pp. 247–263, 2008.

[250] M. Haertlein, M. Moulin, J. M. Devos, V. Laux, O. Dunne, and V. T. Forsyth, “ Methods in Enzymology: Chapter 5- Biomolecular Deuteration for Neutron Structural Biology and Dynamics,” vol. 566, pp. 113–157, Elsevier, 2016.

[251] B. Alberts, A. Johnson, J. Lewis, P. Walter, M. Raff, and K. Roberts, “Molecular Biology of the Cell 4th Edition: International Student Edition,” 2002.

[252] H. Durchschlag, “ Thermodynamic Data for Biochemistry and Biotechnology: Specific Volumes of Biological Macromolecules and Some Other Molecules of Biological Interest,” pp. 45–128, Springer, 1986.

[253] U. Von Stockar and J.-S. Liu, “ Does Microbial Life Always Feed on Negative Entropy? Thermodynamic Analysis of Microbial Growth,” *Biochim. Biophys. Acta, Bioenerg.*, vol. 1412, no. 3, pp. 191–211, 1999.

[254] P. Lindner and R. Schweins, “ The D11 Small-Angle Scattering Instrument: A New Benchmark for SANS,” *Neutron News*, vol. 21, no. 2, pp. 15–18, 2010.

[255] T. Narayanan, M. Sztucki, P. Van Vaerenbergh, J. Léonardon, J. Gorini, L. Claustre, F. Sever, J. Morse, and P. Boesecke, “ A Multipurpose Instrument for Time-Resolved Ultra-Small-Angle and Coherent X-Ray Scattering,” *J. Appl. Crystallogr.*, vol. 51, no. 6, pp. 1511–1524, 2018.

[256] S. Da Vela, F. Roosen-Runge, M. W. Skoda, R. M. Jacobs, T. Seydel, H. Frielinghaus, M. Sztucki, R. Schweins, F. Zhang, and F. Schreiber, “ Effective Interactions and Colloidal Stability of Bovine γ-Globulin in Solution,” *J. Phys. Chem. B*, vol. 121, no. 23, pp. 5759–5769, 2017.

[257] G. Wang, Z. Varga, J. Hofmann, I. E. Zarraga, and J. W. Swan, “ Structure and Relaxation in Solutions of Monoclonal Antibodies,” *J. Phys. Chem. B*, vol. 122, no. 11, pp. 2867–2880, 2018.

[258] J. F. Brady and G. Bossis, “ Stokesian Dynamics,” *Annu. Rev. Fluid Mech.*, vol. 20, no. 1, pp. 111–157, 1988.

[259] R. J. Phillips, J. F. Brady, and G. Bossis, “ Hydrodynamic Transport Properties of Hard-Sphere Dispersions. I. Suspensions of Freely Mobile Particles,” *Phys. Fluids*, vol. 31, no. 12, pp. 3462–3472, 1988.

[260] J. Skolnick, “ Perspective: On the Importance of Hydrodynamic Interactions in the Subcellular Dynamics of Macromolecules,” *J. Chem. Phys.*, vol. 145, no. 10, pp. 100901–1–10, 2016.

[261] R. Verberg, I. de Schepper, and E. Cohen, “ Diffusion of Concentrated Neutral Hard-Sphere Colloidal Suspensions,” *Phys. Rev. E*, vol. 61, no. 3, pp. 2967–2976, 2000.

[262] A. J. Banchio, G. Nägele, and J. Bergenholtz, “ Collective Diffusion, Self-Diffusion and Freezing Criteria of Colloidal Suspensions,” *J. Chem. Phys.*, vol. 113, no. 8, pp. 3381–3396, 2000.

[263] M. Medina-Noyola, “ Long-Time Self-Diffusion in Concentrated Colloidal Dispersions,” *Phys. Rev. Lett.*, vol. 60, no. 26, pp. 2705–2708, 1988.

[264] J. Balbo, P. Mereghetti, D.-P. Herten, and R. Wade, “ The Shape of Protein Crowders is a Major Determinant of Protein Diffusion,” *Biophys. J.*, vol. 104, no. 7, pp. 1576 – 1584, 2013.

[265] N. Plattner, S. Doerr, G. De Fabritiis, and F. Noé, “ Complete Protein–Protein Association Kinetics in Atomic Detail Revealed by Molecular Dynamics Simulations and Markov Modelling,” *Nat. Chem.*, vol. 9, no. 10, pp. 1005–1011, 2017.

[266] A. V. Korennykh, M. J. Plantinga, C. C. Correll, and J. A. Piccirilli, “ Linkage between Substrate Recognition and Catalysis during Cleavage of Sarcin/Ricin Loop RNA by Restrictocin,” *Biochem.*, vol. 46, no. 44, pp. 12744–12756, 2007.

[267] N. P. Reynolds, J. Adamcik, J. T. Berryman, S. Handschin, A. A. H. Zanjani, W. Li, K. Liu, A. Zhang, and R. Mezzenga, “ Competition Between Crystal and Fibril Formation in Molecular Mutations of Amyloidogenic Peptides,” *Nat. Comm.*, vol. 8, no. 1, pp. 1338–1–10, 2017.

[268] E. Chelton, A. Jones, and R. Walker, “ The Chemical Composition of the Nucleic Acids and the Proteins of Some Mycoplasma Strains,” *J. Gen. Microbiol.*, vol. 50, no. 2, pp. 305–312, 1968.

[269] T. Jøssang, J. Feder, and E. Rosenqvist, “ Photon Correlation Spectroscopy of Human IgG.,” *J. Protein Chem.*, vol. 7, no. 2, pp. 165–171, 1988.

[270] J. B. Willett and J. D. Singer, “ Another Cautionary Note About R^2: Its Use in Weighted Least-Squares Regression Analysis,” *Am. Stat.*, vol. 42, no. 3, pp. 236–238, 1988.

[271] G. Nägele, “ On the Dynamics and Structure of Charge-Stabilized Suspensions,” *Phys. Rep.*, vol. 272, no. 5-6, pp. 215–372, 1996.

[272] Y. Ishihama, T. Schmidt, J. Rappsilber, M. Mann, F. U. Hartl, M. J. Kerner, and D. Frishman, “ Protein Abundance Profiling of the Escherichia Coli Cytosol,” *BMC genomics*, vol. 9, no. 1, pp. 102–1–17, 2008.

[273] A. Dinsmore, P. Dubin, and G. Grason, “ Clustering in Complex Fluids,” *J. Phys. Chem. B*, vol. 115, pp. 7173–7174, 2011.

[274] K. Johnston, J. Maynard, T. Truskett, A. Borwankar, M. Miller, B. Wilson, A. Dinin, T. Khan, and K. Kaczorowski, “ Concentrated Dispersions of Equilibrium Protein Nanoclusters That Reversibly Dissociate into Active Monomers,” *ACS Nano*, vol. 6, no. 2, pp. 1357–1369, 2012.

[275] E. Yearley, P. Godfrin, T. Perevozchikova, H. Zhang, P. Falus, L. Porcar, M. Nagao, J. Curtis, P. Gawande, R. Taing, and *et al.*, “ Observation of Small Cluster Formation in Concentrated Monoclonal Antibody Solutions and Its Implications to Solution Viscosity,” *Biophys. J.*, vol. 106, no. 8, pp. 1763 – 1770, 2014.

[276] A. Stradner, H. Sedgwick, F. Cardinaux, W. Poon, S. Egelhaaf, and P. Schurtenberger, “ Equilibrium Cluster Formation in Concentrated Protein Solutions and Colloids,” *Nature*, vol. 432, pp. 492–495, 2004.

[277] L. Porcar, P. Falus, W.-R. Chen, A. Faraone, E. Fratini, K. Hong, P. Baglioni, and Y. Liu, “ Formation of the Dynamic Clusters in Concentrated Lysozyme Protein Solutions,” *J. Phys. Chem. Lett.*, vol. 1, no. 1, pp. 126–129, 2010.

[278] Y. Liu, L. Porcar, J. Chen, W.-R. Chen, P. Falus, A. Faraone, E. Fratini, K. Hong, and P. Baglioni, “ Lysozyme Protein Solution with an Intermediate Range Order Structure,” *J. Phys. Chem. B*, vol. 115, no. 22, pp. 7238–7247, 2011.

[279] F. Cardinaux, E. Zaccarelli, A. Stradner, S. Bucciarelli, B. Farago, S. U. Egelhaaf, F. Sciortino, and P. Schurtenberger, “ Cluster-Driven Dynamical Arrest in Concentrated Lysozyme Solutions,” *J. Phys. Chem. B*, vol. 115, no. 22, pp. 7227–7237, 2011.

[280] H. Okumura, M. Higashi, Y. Yoshida, H. Sato, and R. Akiyama, “ Theoretical Approaches for Dynamical Ordering of Biomolecular Systems,” *Biochim. Biophys. Acta*, vol. 1862, no. 2, pp. 212 – 228, 2018.

[281] G. Nawrocki, P.-h. Wang, I. Yu, Y. Sugita, and M. Feig, “ Slow-Down in Diffusion in Crowded Protein Solutions Correlates with Transient Cluster Formation,” *J. Phys. Chem. B*, vol. 121, no. 49, pp. 11072–11084, 2017.

[282] O. Galkin, K. Chen, R. L. Nagel, R. E. Hirsch, and P. G. Vekilov, “ Liquid-Liquid Separation in Solutions of Normal and Sickle Cell Hemoglobin,” *Proc. Natl. Acad. Sci. U. S. A.*, vol. 99, no. 13, pp. 8479–8483, 2002.

[283] C. Ross and M. Poirier, “ Protein Aggregation and Neurodegenerative Disease,” *Nat. Med. (N.Y., NY, U.S.)*, vol. 10, pp. S10–S17, 2004.

[284] M. Heinen, F. Zanini, F. Roosen-Runge, D. Fedunova, F. Zhang, M. Hennig, T. Seydel, R. Schweins, M. Sztucki, M. Antalik, and *et al.*, “ Viscosity and Diffusion: Crowding and Salt Effects in Protein Solutions,” *Soft Matter*, vol. 8, pp. 1404–1419, 2012.

[285] A. M. Stadler, C. J. Garvey, J. P. Embs, M. M. Koza, T. Unruh, G. Artmann, and G. Zaccai, “ Picosecond Dynamics in Haemoglobin from Different Species: A Quasielastic Neutron Scattering Study,” *Biochim. Biophys. Acta*, vol. 1840, no. 10, pp. 2989 – 2999, 2014.

[286] M. Tehei, B. Franzetti, K. Wood, F. Gabel, E. Fabiani, M. Jasnin, M. Zamponi, D. Oesterhelt, G. Zaccai, M. Ginzburg, and *et al.*, “ Neutron Scattering Reveals Extremely Slow Cell Water in a Dead Sea Organism,” *Proc. Natl. Acad. Sci. U.S.A.*, vol. 104, no. 3, pp. 766–771, 2007.

[287] A. M. Stadler, J. P. Embs, I. Digel, G. M. Artmann, T. Unruh, G. Büldt, and G. Zaccai, “ Cytoplasmic Water and Hydration Layer Dynamics in Human Red Blood Cells,” *J. Am. Chem. Soc.*, vol. 130, no. 50, pp. 16852–16853, 2008.

[288] A. M. Stadler, L. van Eijck, F. Demmel, and G. Artmann, “ Macromolecular Dynamics in Red Blood Cells Investigated Using Neutron Spectroscopy,” *J. R. Soc., Interface*, vol. 8, no. 57, pp. 590–600, 2011.

[289] W. Doster and S. Longeville, “ Microscopic Diffusion and Hydrodynamic Interactions of Hemoglobin in Red Blood Cells,” *Biophys. J.*, vol. 93, no. 4, pp. 1360 – 1368, 2007.

[290] M. Bée, “ A Physical Insight into the Elastic Incoherent Structure Factor,” *Phys. B (Amsterdam, Neth.)*, vol. 182, no. 4, pp. 323–336, 1992.

[291] M. O. Dayhoff, G. E. Perlmann, and D. A. MacInnes, “The Partial Specific Volumes, in Aqueous Solution, of Three Proteins,” *J. Am. Chem. Soc.*, vol. 74, no. 10, pp. 2515–2517, 1952.

[292] P. A. Charlwood, “ Partial Specific Volumes of Proteins in Relation to Composition and Environment,” *J. Am. Chem. Soc.*, vol. 79, no. 4, pp. 776–781, 1957.

[293] A. A. Zamyatnin, “ Protein Volume in Solution,” *Prog. Biophys. Mol. Biol.*, vol. 24, pp. 107–123, 1972.

[294] J. Fitter, “ Confined Molecular Motions of Globular Proteins Studied in Powder Samples and in Solution,” *J. Phys. IV*, vol. 10, no. PR7, pp. 265–270, 2000.

[295] A. Ortega, D. Amorós, and J. de La Torre, “ Prediction of Hydrodynamic and Other Solution Properties of Rigid Proteins from Atomic- and Residue-Level Models,” *Biophys. J.*, vol. 101, no. 4, pp. 892–898, 2011.

[296] H. Berendsen, D. van der Spoel, and R. van Drunen, “ GROMACS: A Message-Passing Parallel Molecular Dynamics Implementation,” *Comput. Phys. Commun.*, vol. 91, no. 1-3, pp. 43–56, 1995.

[297] D. Svergun, S. Richard, M. Koch, Z. Sayers, S. Kuprin, and G. Zaccai, “ Protein Hydration in Solution: Experimental Observation by X-Ray and Neutron Scattering,” *Proc. Natl. Acad. Sci. U.S.A.*, vol. 95, no. 5, pp. 2267–2272, 1998.

[298] S. Perticaroli, G. Ehlers, C. Stanley, E. Mamontov, H. ONeill, Q. Zhang, X. Cheng, D. Myles, J. Katsaras, and J. Nickels, “ Description of Hydration Water in Protein (Green Fluorescent Protein) Solution,” *J. Am. Chem. Soc.*, vol. 139, no. 3, pp. 1098–1105, 2017.

[299] A. D. Nisbet, R. H. Saundry, A. J. G. Moir, L. A. Fothergill, and J. E. Fothergill, “ The Complete Amino-Acid Sequence of Hen Ovalbumin,” *Eur. J. Biochem.*, vol. 115, no. 2, pp. 335–345, 1981.

[300] N. Nemoto, A. Koike, K. Osaki, T. Koseki, and D. Etsushiro, “ Dynamic Light Scattering of Aqueous Solutions of Linear Aggregates Induced by Thermal Denaturation of Ovalbumin,” *Biopolymers*, vol. 33, no. 4, pp. 551–559, 1993.

[301] M. Weijers, R. Visschers, and T. Nicolai, “ Light Scattering Study of Heat-Induced Aggregation and Gelation of Ovalbumin,” *Macromolecules*, vol. 35, no. 12, pp. 4753–4762, 2002.

[302] N. R. Voss and M. Gerstein, “ 3V: Cavity, Channel and Cleft Volume Calculator and Extractor,” *Nucleic Acids Res.*, vol. 38, pp. W555–W562, 2010.

[303] L. J. Harris, S. B. Larson, K. W. Hasel, and A. McPherson, “ Refined Structure of an Intact IgG2a Monoclonal Antibody,” *Biochemistry*, vol. 36, no. 7, pp. 1581–1597, 1997.

[304] J. I. Loch, P. Bonarek, A. Polit, M. Jaboski, M. Czub, X. Ye, and K. Lewiski, “ β-Lactoglobulin Interactions with Local Anaesthetic Drugs Crystallographic and Calorimetric Studies,” *Int. J. Biol. Macromol.*, vol. 80, pp. 87 – 94, 2015.

[305] S. Bucciarelli, N. Mahmoudi, L. Casal-Dujat, M. Jéhannin, C. Jud, and A. Stradner, “ Extended Law of Corresponding States Applied to Solvent Isotope Effect on a Globular Protein,” *J. Phys. Chem. Lett.*, vol. 7, no. 9, pp. 1610–1615, 2016.

[306] K. D. Ratanji, J. P. Derrick, R. J. Dearman, and I. Kimber, “Immunogenicity of Therapeutic Proteins: Influence of Aggregation,” *Journal of Immunotoxicology*, vol. 11, pp. 99–109, Aug. 2013.

[307] C. Allen, D. Maysinger, and A. Eisenberg, “Nano-Engineering Block Copolymer Aggregates for Drug Delivery,” *Colloids and Surfaces B: Biointerfaces*, vol. 16, no. 1, pp. 3 – 27, 1999.

[308] F. Roosen-Runge, B. S. Heck, F. Zhang, O. Kohlbacher, and F. Schreiber, “ Interplay of pH and Binding of Multivalent Metal Ions: Charge Inversion and Reentrant Condensation in Protein Solutions,” *J. Phys. Chem. B*, vol. 117, no. 18, pp. 5777–5787, 2013. PMID: 23586503.

[309] D. Stopper and R. Roth, “ Phase Behavior and Bulk Structural Properties of a Microphase Former with Anisotropic Competing Interactions: A Density Functional Theory Study,” *Phys. Rev. E*, vol. 96, p. 042607, 2017.

[310] H. Frauenfelder, R. D. Young, and P. W. Fenimore, “ Dynamics and the Free-Energy Landscape of Proteins, Explored with the Mössbauer Effect and Quasi-Elastic Neutron Scattering,” *J. Phys. Chem. B*, vol. 117, no. 42, pp. 13301–13307, 2013.

[311] P. J. Flory, “ Molecular Size Distribution in Three Dimensional Polymers. I. Gelation,” *J. Am. Chem. Soc.*, vol. 63, no. 11, pp. 3083–3090, 1941.

[312] M. Wertheim, “ Fluids with Highly Directional Attractive Forces. I. Statistical Thermodynamics,” *J. Stat. Phys.*, vol. 35, pp. 19–34, 1984.

[313] W. G. Chapman, G. Jackson, and K. E. Gubbins, “ Phase Equilibria of Associating Fluids,” *Mol. Phys.*, vol. 65, no. 5, pp. 1057–1079, 1988.

[314] M. Kastelic, Y. V. Kalyuzhnyi, B. Hribar-Lee, K. A. Dill, and V. Vlachy, “ Protein Aggregation in Salt Solutions,” *Proc. Natl. Acad. Sci. U. S. A.*, vol. 112, no. 21, pp. 6766–6770, 2015.

[315] M. S. Wertheim, “ Fluid of dimerizing hard spheres, and fluid mixtures of hard spheres and dispheres,” *J. Chem. Phys.*, vol. 85, no. 5, pp. 2929–2936, 1986.

[316] G. D. Profio, E. Curcio, and E. Drioli, *Encyclopedia of Industrial Biotechnology: Protein Crystallization, Kinetics*, pp. 1–22. American Cancer Society, 2010.

[317] R. Schubert, A. Meyer, D. Baitan, K. Dierks, M. Perbandt, and C. Betzel, “ Real-Time Observation of Protein Dense Liquid Cluster Evolution during Nucleation in Protein Crystallization,” *Cryst. Growth Des.*, vol. 17, no. 3, pp. 954–958, 2017.

[318] G. A. Vliegenthart and H. N. W. Lekkerkerker, “ Predicting the Gas–Liquid Critical Point from the Second Virial Coefficient,” *J. Chem. Phys.*, vol. 112, no. 12, pp. 5364–5369, 2000.

[319] T. Liu, Z. Mo, S. Wang, and H. Zhang, “ Nonisothermal Melt and Cold Crystallization Kinetics of Poly(aryl ether ether ketone ketone),” *Polym. Eng. Sci.*, vol. 37, no. 3, pp. 568–575, 2004.

[320] A. T. Lorenzo, M. L. Arnal, J. Albuerne, and A. J. Müller, “ DSC Isothermal Polymer Crystallization Kinetics Measurements and the Use of the Avrami Equation to Fit the Data: Guidelines to Avoid Common Problems,” *Polym. Test.*, vol. 26, no. 2, pp. 222 – 231, 2007.

[321] J. J. Kolstad, “ Crystallization Kinetics of Poly(L-lactide-co-meso-lactide),” *Appl. Polym. Sci.*, vol. 62, no. 7, pp. 1079–1091, 1996.

[322] T. A. Land, A. J. Malkin, Y. Kuznetsov, A. McPherson, and J. J. De Yoreo, “ Mechanisms of Protein Crystal Growth: An Atomic Force Microscopy Study of Canavalin Crystallization,” *Phys. Rev. Lett.*, vol. 75, pp. 2774–2777, 1995.

[323] V. J. Bolos, R. Benitez, A. Eleta-Lopez, and J. L. Toca-Herrera, “ A Probabilistic Model for Crystal Growth Applied to Protein Deposition at the Microscale,” *Materials*, vol. 12, no. 3, p. 479, 2019.

[324] J. Tao, M. H. Nielsen, and J. J. De Yoreo, “ Nucleation and Phase Transformation Pathways in Electrolyte Solutions Investigated by in situ Microscopy Techniques,” *Curr. Opin. Colloid Interface Sci.*, vol. 34, pp. 74–88, 2018.

[325] J. Zhang, X. Wang, K. Zhou, G. Chen, and Q. Wang, “ Self-Assembly of Protein Crystals with Different Crystal Structures Using Tobacco Mosaic Virus Coat Protein as a Building Block,” *ACS Nano*, vol. 12, no. 2, pp. 1673–1679, 2018.

[326] J. M. García-Ruiz and A. Moreno, “ Investigations on Protein Crystal Growth by the Gel Acupuncture Method,” *Acta Crystallogr., Sect. D: Biol. Crystallogr.*, vol. 50, no. 4, pp. 484–490, 1994.

[327] C. Lin, Y. Zhang, J. J. Liu, and X. Z. Wang, “ Study on Nucleation Kinetics of Lysozyme Crystallization,” *J. Cryst. Growth*, vol. 469, pp. 59–64, 2017.

[328] N. E. Chayen and E. Saridakis, “ Protein Crystallization: From Purified Protein to Diffraction-Quality Crystal,” *Nat. Methods*, vol. 5, pp. 147–153, 2008.

[329] W. Huang, S. Krishnaji, O. R. Tokareva, D. Kaplan, and P. Cebe, “ Tunable Crystallization, Degradation, and Self-Assembly of Recombinant Protein Block Copolymers,” *Polymer*, vol. 117, pp. 107 – 116, 2017.

[330] R. J. Heigl, M. Longo, J. Stellbrink, A. Radulescu, R. Schweins, and T. E. Schrader, “ Crossover from a Linear to a Branched Growth Regime in the Crystallization of Lysozyme,” *Cryst. Growth Des.*, vol. 18, no. 3, pp. 1483–1494, 2018.

[331] C. Guo, J. Wang, J. Li, Z. Wang, and S. Tang, “ Kinetic Pathways and Mechanisms of Two-Step Nucleation in Crystallization,” *J. Phys. Chem. Lett.*, vol. 7, no. 24, pp. 5008–5014, 2016.

[332] M.-C. Hsieh, D. G. Lynn, and M. A. Grover, “ Kinetic Model for Two-Step Nucleation of Peptide Assembly,” *J. Phys. Chem. B*, vol. 121, no. 31, pp. 7401–7411, 2017.

[333] J. R. Luft, J. R. Wolfley, M. I. Said, R. M. Nagel, A. M. Lauricella, J. L. Smith, M. H. Thayer, C. K. Veatch, E. H. Snell, M. G. Malkowski, and G. De Titta, “ Efficient Optimization of Crystallization Conditions by Manipulation of Drop Volume Ratio and Temperature,” *Protein Sci.*, vol. 16, no. 4, pp. 715–722, 2007.

[334] C.-Y. Zhang, Y. Liu, X.-H. Tian, W.-J. Liu, X.-Y. Li, L.-X. Yang, H.-J. Jiang, C. Han, K.-A. Chen, and D.-C. Yin, “ Effect of Real-World Sounds on Protein Crystallization,” *Int. J. Biol. Macromol.*, vol. 112, pp. 841 – 851, 2018.

[335] S. Guo, D. Pranantyo, E.-T. Kang, X. J. Loh, X. Zhu, D. Jaczewski, and K. G. Neoh, “ Dominant Albumin-Surface Interactions under Independent Control of Surface Charge and Wettability,” *Langmuir*, vol. 34, no. 5, pp. 1953–1966, 2018.

[336] H. Koizumi, S. Uda, K. Tsukamoto, M. Tachibana, K. Kojima, J. Okada, and J. Nozawa, “ Crystallization Technique of High-Quality Protein Crystals Controlling Surface Free Energy,” *Cryst. Growth Des.*, vol. 17, no. 12, pp. 6712–6718, 2017.

[337] J. Lu, X.-J. Wang, and C.-B. Ching, “ Batch Crystallization of Soluble Proteins: Effect of Precipitant, Temperature and Additive,” *Prog. Cryst. Growth Charact. Mater.*, vol. 45, no. 3, pp. 201 – 217, 2002.

[338] C. Gögelein, D. Wagner, F. Cardinaux, G. Nägele, and S. U. Egelhaaf, “ Effect of Glycerol and Dimethyl Sulfoxide on the Phase Behavior of Lysozyme: Theory and Experiments,” *Chem. Phys.*, vol. 136, no. 1, p. 015102, 2012.

[339] C. N. Nanev, “ Recent Insights into the Crystallization Process; Protein Crystal Nucleation and Growth Peculiarities; Processes in the Presence of Electric Fields,” *Crystals*, vol. 7, no. 10, p. 310, 2017.

[340] Y. Zhang, J. Zhao, J. Di, H. Jiang, Q. Wang, J. Wang, Y. Guo, and D. Yin, “ Real-Time Monitoring of the Solution Concentration Variation During the Crystallization Process of Protein-Lysozyme by Using Digital Holographic Interferometry,” *Opt. Express*, vol. 20, no. 16, p. 18415, 2012.

[341] A. Nakamura, J. Ohtsuka, T. Kashiwagi, N. Numoto, N. Hirota, T. Ode, H. Okada, K. Nagata, M. Kiyohara, E.-i. Suzuki, A. Kita, H. Wada, and M. Tanokura, “ In-Situ and Real-Time Growth Observation of High-Quality Protein Crystals Under Quasi-Microgravity on Earth,” *Sci. Rep.*, vol. 6, no. 1, p. 22127, 2016.

[342] Y. Tsarfati, S. Rosenne, H. Weissman, L. J. W. Shimon, D. Gur, B. A. Palmer, and B. Rybtchinski, “ Crystallization of Organic Molecules: Nonclassical Mechanism Revealed by Direct Imaging,” *ACS Cent. Sci.*, vol. 4, no. 8, pp. 1031–1036, 2018.

[343] P. G. Vekilov, “ Dense Liquid Precursor for the Nucleation of Ordered Solid Phases from Solution,” *Cryst. Growth Des.*, vol. 4, no. 4, pp. 671–685, 2004.

[344] M. R. Duff, J. M. Borreguero, M. J. Cuneo, A. Ramanathan, J. He, G. Kamath, S. C. Chennubhotla, F. Meilleur, E. E. Howell, K. W. Herwig, D. A. A. Myles, and P. K. Agarwal, “ Modulating Enzyme Activity by Altering Protein Dynamics with Solvent,” *Biochemistry*, vol. 57, no. 29, pp. 4263–4275, 2018.

[345] G. Kontopidis, C. Holt, and L. Sawyer, “ Invited Review: β-Lactoglobulin: Binding Properties, Structure, and Function,” *J. Dairy Sci.*, vol. 87, no. 4, pp. 785–796, 2004.

[346] K. Sakurai, T. Konuma, M. Yagi, and Y. Goto, “ Structural Dynamics and Folding of β-Lactoglobulin Probed by Heteronuclear NMR,” *Biochim. Biophys. Acta*, vol. 1790, no. 6, pp. 527 – 537, 2009.

[347] K. Lieutenant, P. Lindner, and R. Gahler, “ A New Design for the Standard Pinhole Small-Angle Neutron Scattering Instrument D11,” *J. Appl. Crystallogr.*, vol. 40, no. 6, pp. 1056–1063, 2007.

[348] F. Zhang, M. Braun, S. Da Vela, M. Grimaldo, O. Matsarskaia, F. Roosen-Runge, F. Schreiber, R. Schweins, T. Seydel, and B. Sohmen, “ Kinetics of Two-Step Nucleation in Protein Crystallization Studied by Real-Time SANS. Institut Laue-Langevin (ILL),” 2015. doi.ill.fr/10.5291/ILL-DATA.9-13-620.

[349] M. Grimaldo, C. Beck, M. Braun, O. Czakkel, F. Roosen-Runge, A. Sauter, F. Schreiber, T. Seydel, and F. Zhang, “ Real Time Study of Protein Dynamics During a One-Step and a Two-Step Crystallization Process. Institut Laue-Langevin (ILL),” 2015. https://doi.org/10.5291/ILL-DATA.8-04-760.

[350] B. Farago, " Recent Neutron Spin-Echo Developments at the ILL (IN11 and IN15)," *Phys. B (Amsterdam, Neth.)*, vol. 267-268, pp. 270 – 276, 1999.

[351] A. V. Frontzek, L. Paccou, Y. Guinet, and A. Hédoux, " Study of the Phase Transition in Lysozyme Crystals by Raman Spectroscopy," *Biochim. Biophys. Acta*, vol. 1860, no. 2, pp. 412–423, 2016.

[352] B. Reif, Y. Xue, V. Agarwal, M. S. Pavlova, M. Hologne, A. Diehl, Y. E. Ryabov, and N. R. Skrynnikov, " Protein Side-Chain Dynamics Observed by Solution-and Solid-State NMR: Comparative Analysis of Methyl ^{2}H Relaxation Data," *J. Am. Chem. Soc.*, vol. 128, no. 38, pp. 12354–12355, 2006.

[353] V. Agarwal, Y. Xue, B. Reif, and N. R. Skrynnikov, " Protein Side-Chain Dynamics As Observed by Solution-and Solid-State NMR Spectroscopy: A Similarity Revealed," *J. Am. Chem. Soc.*, vol. 130, no. 49, pp. 16611–16621, 2008.

[354] W. G. Martin, C. A. Winkler, and W. H. Cook, " Partial Specific Volume Measurements by Differential Sedimentation," *Can. J. Chem.*, vol. 37, pp. 1662–1670, 1959.

[355] C. Beck, M. Grimaldo, I. Hoffmann, and T. Seydel, "Effects of Salt-Induced Protein Interactions on Collective and Self Diffusion. Institut Laue-Langevin (ILL)," 2018. Beamtime: Inter-441.

[356] C. Beck, M. Braun, L. Bühl, A. Girelli, L. Grabitz, M. Grimaldo, R. Maier, O. Matsarskaia, I. Musil, S. Prevost, F. Roosen-Runge, F. Schreiber, T. Seydel, and F. Zhang, " *In Situ* Real-Time Study of the Diffusive Dynamic Arrest of Proteins during Crystallization. Institut Laue-Langevin (ILL) ," 2019. doi:10.5291/ILL-DATA.8-04-804.

[357] C. Beck, F. Baeuerle, N. Begam, M. Braun, B. Lena, P. Christodoulou, D. Dyachok, A. Girelli, M. Grimaldo, O. Matsarskaia, F. Roosen-Runge, F. Schreiber, T. Seydel, and F. I. L.-L. I. Zhang, " *In Situ* Real-Time Study of the Diffusive Dynamic Arrest of Proteins during Crystallization. Institut Laue-Langevin (ILL) ," 2018. doi:10.5291/ILL-DATA.8-04-810.

[358] C. Beck, M. Braun, L. Bühl, A. Girelli, L. Grabitz, M. Grimaldo, R. Maier, O. Matsarskaia, I. Musil, S. Prevost, F. Roosen-Runge, F. Schreiber, T. Seydel, and F. Zhang, " *In Situ* Real-Time Study of the Diffusive Dynamic Arrest of Proteins during Crystallization. Institut Laue-Langevin (ILL) ," 2019. doi:10.5291/ILL-DATA.8-04-853.